imt
institute of microtechnology
university of neuchâtel

PAUL SCHERRER INSTITUT
PSI

Diffractive and refractive lenses for hard x-rays with ultra-high efficiencies

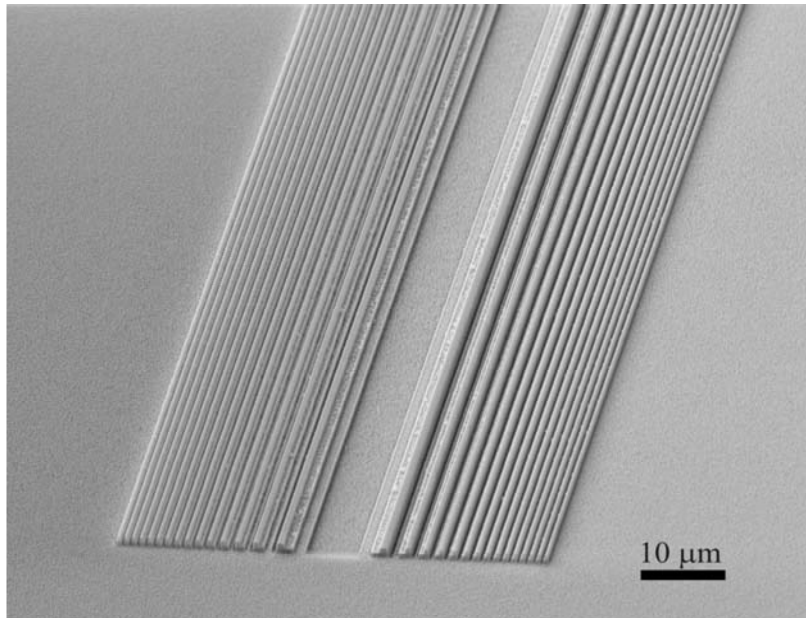

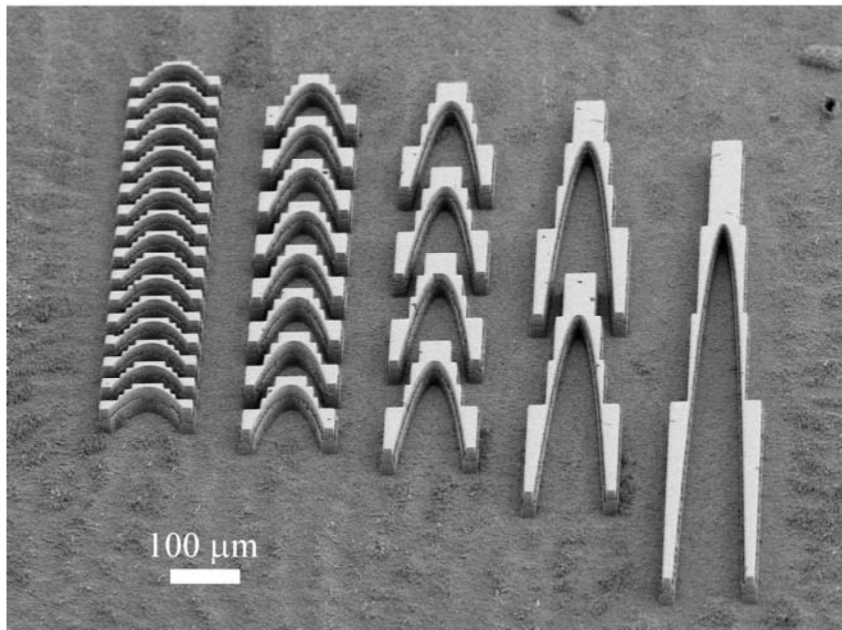

Bernd Nöhammer

Université de Neuchâtel
Institut de Microtechnique

Diffractive and refractive lenses for hard x-rays with ultra-high efficiencies

Thèse

Présentée à la faculté des sciences
Pour obtenir le grade de docteur ès sciences
par

Bernd Nöhammer

Neuchâtel, avril 2004

IMPRIMATUR POUR LA THESE

Diffractive and refractive lenses for hard x-rays with ultra-high efficiencies

M. Bernd NOEHAMMER

UNIVERSITE DE NEUCHATEL

FACULTE DES SCIENCES

La Faculté des sciences de l'Université de Neuchâtel, sur le rapport des membres du jury

MM. H.-P. Herzig (directeur de thèse),
R. Dändliker, C. David (Villigen),
F. van der Veen (Villigen), A Freund (Grenoble F)

autorise l'impression de la présente thèse.

Neuchâtel, le 29 avril 2004

La doyenne:

Martine Rahier

Abstract

Focusing of x-rays is an essential pre-requisite for many synchrotron based measurement techniques. In this work, multi-level silicon zone plates and planar refractive lenses made from diamond and silicon have been developed, aiming for focusing applications in the hard x-ray range, i.e. for photon energies between 10 and 50 keV.

The first part of the work deals with diffractive x-ray lenses (zone plates) that utilize a multi-level profile for the diffracting structures in order to obtain high diffraction efficiencies. Theoretical calculations are presented, yielding the optimal design of a multilevel profile with respect to diffraction efficiency for the general case of absorbing grating materials. A micro-fabrication process is described, enabling the fabrication of silicon zone plates with a four-level profile of high quality for grating periods down to 800 nm and a grating structure height of 1.5 µm. For good efficiencies in the hard x-ray range significantly larger grating heights of about 5-50 µm are required. This was achieved using linear zone plates with line grating structures by tilting them with respect to the x-ray beam. The tilting allowed a tuning and a strong increase of the effective grating structure height. In consequence unprecedented diffraction efficiencies of 65 % in the energy range between 10 and 17 keV could be obtained. In order to achieve 2-dimensional focusing, two crossed linear zone plates in series were used. A focal spot size and a resolution of about 2 µm were found for the resulting micro-focusing device. Outstanding features of the device are its high total focusing efficiency (above 30%) and the extremely small divergence of 2.4×10^{-4} rad of the focused beam. Linear multilevel zone plates are therefore especially suited for focusing applications, which require large efficiency and small beam divergence rather than a small spot size and high resolution.

The second part of this work deals with planar refractive lenses made from diamond and silicon. Both types of lenses were fabricated in a similar way using e-beam lithography and reactive ion etching. For both lenses the resolution is mainly determined by deviations from the ideal lens profile, which originate from the fabrication process. Theoretical considerations show that for a given fabrication process the obtainable resolution is directly proportional to the size of the lens aperture. For the comparatively large lens apertures realized within this work (100-600 µm) a resolution of the order of a few microns was achieved for both types of lenses. The potential applications of these planar refractive lenses depend on the lens material used. Silicon refractive lenses have the advantage that sophisticated methods for the structuring of silicon are available, but the disadvantage that x-ray absorption within silicon is comparatively large. Nevertheless, it was possible to reach good efficiencies of about 20-30% for large photon energies between 35-50 keV. As a consequence silicon lenses are valuable for micro-focusing applications in this x-ray range, where only very few types of lenses are available. Although much more difficult to structure than silicon, diamond has the advantage over silicon that it shows very low x-ray absorption. Therefore high efficiencies up to 80 %, even at comparatively low x-ray energies of 17.5 keV, could be reached with diamond lenses. In addition diamond has unique material properties such as a high thermal conductivity and high stability, which is of particular interest for applications in future X-ray free electron lasers (X-FEL). Such X-FELs are predicted to yield x-ray beams with peak intensities several orders of magnitude beyond those of present x-ray sources, and diamond refractive lenses are one of the few candidates for optical components, which are likely to withstand such a beam.

Acknowledgements

I would like to thank and express my deep gratitude to all people who have helped me, supported me and in one way or another contributed to this work.

In particular I want to thank Christian David, my supervisor at the Paul-Scherrer-Institute, for introducing and guiding me through the large field of x-ray science, for teaching me the secrets and tricks of micro-technology and scientific reports and also for his - finally very successful - efforts to achieve public acknowledgement of my work. I am grateful to Prof. Hans Peter Herzig, my doctoral advisor at the university of Neuchatel, for being a kind, understanding and always helpful “doctor-father”. Furthermore, I am much obliged to Friso van der Veen, Andreas Freund, and Prof. René Dändliker who gave me the honour to be part of my jury de thèse, made the effort of a careful and thoughtful revision of my dense manuscript and enabled an interesting and inspiring discussion about the difference between refractive and diffractive lenses (which - as I was motivated to calculate later on - took only 1/10000 of my PhD-time).

The fabrication of x-ray lenses was an important part of this thesis and required the knowledge, experience and assistance of many people. I would therefore like to express my deep thanks to all people of our lab (Laboratory for Micro- and Nanotechnology) for their continuous help and support and for the pleasant and amicable atmosphere. Without you this work would have been impossible. I am also grateful for the assistance of numerous people in the world near and afar, in particular for the help of Markus Kuhnke and Fabio Raimondi (Paul-Scherrer-Institute) and Hugo Rothuizen and Roland Widmer (IBM Rüschlikon).

Many thanks go to all people at the ESRF (Grenoble), in particular to Joanna Hoszowska, Eric Ziegler, Manfred Burghammer, Christian Riekel, Andrea Somogyi and Alexandre Simionovici. Doing measurements at a synchrotron is always a very tough and sleepless thing, but your extreme helpfulness and collegiality nevertheless made it possible, that for some moments I had the feeling of being on holidays.

The creation of a thesis costs quite a lot of money and I am very grateful to the Swiss people for enabling and supporting this work via the Swiss National Science Foundation.

My special thanks go to my parents and my sister for their love and moral support and for giving me the possibility to come home and have “refuge” whenever I needed it.

Last but not least, there are many people who maybe did not directly contribute, but all the more were in different ways essential for the success of this thesis. …There is no ambiguity and no particular order, so if you finally find yourself, then it is you…☺…many, many thanks to: Olaf, Günther, Bernd, Ana, Timm, Maxi, Anja, Slawo, Claudio, Philipp, Li, Sina, Bokyung, Peter (M.), Andreas, Laurent, Andre, Laura, Sung Gook, Eugen, Harald, Peter (Z.), Bettina, Marc, Matthias, Lorenz, Rene, Antonietta, Martin, Marianne, Sonya, Silvia, Brigitte, Stephi, Cyrinne, Soo-Man, Manel, Klaus, Thomas, … a beer for anyone I forgot.

ABSTRACT **5**
ACKNOWLEDGEMENTS **6**
1 INTRODUCTION **9**
1.1 THE EARLY DAYS OF X-RAY HISTORY 9
1.2 BEGINNINGS OF X-RAY SCIENCE 10
1.3 GENERATION OF X-RAYS 11
1.3.1 X-ray tubes *11*
1.3.2 Synchrotron radiation *12*
1.3.3 The second synchrotron generation *12*
1.3.4 Today's synchrotron facilities *13*
1.3.5 Future x-ray sources *13*
1.4 INSTRUMENTAL ASPECTS OF SYNCHROTRONS 14
1.5 X-RAY LENSES 15
1.6 ORGANIZATION OF THIS THESIS AND RELATED OWN PUBLICATIONS 16
2 THEORY **17**
2.1 MATERIAL PROPERTIES IN THE X-RAY RANGE 17
2.1.1 Coherent scattering of x-rays and refractive index *17*
2.1.2 A simple classical model of the origin of the refractive index *21*
2.1.3 Coherent scattering, incoherent scattering and attenuation in materials *23*
2.2 DIFFRACTIVE X-RAY LENSES (ZONE PLATES) 26
2.2.1 Construction rule of zone plates *27*
2.2.2 Resolution of a zone plate *31*
2.2.3 Depth of focus *36*
2.2.4 Efficiency and design of binary zone plates *37*
2.2.5 Multilevel zone plates *40*
2.2.6 Efficiency and optimisation of grating profiles *41*
2.3 REFRACTIVE X-RAY LENSES 55
2.3.1 The ideal lens shape *55*
2.3.2 Refractive lenses with minimized absorption *57*
2.3.3 Stacking of refractive lenses *59*
2.3.4 Transmission and efficiency of a lens with minimized absorption *61*
3 MICRO- AND NANO-FABRICATION METHODS **63**
3.1 ELECTRON-BEAM LITHOGRAPHY 63
3.1.1 General principle *63*
3.1.2 The LION LV-1 e-beam system *64*

3.1.3 E-beam resist and development ... *66*
3.1.4 Line width control ... *67*
3.1.5 PMMA-resist preparation ... *71*
3.2 THERMAL EVAPORATION OF THIN LAYERS ... 72
3.3 PLASMA ETCHING ... 72
4 FABRICATION OF MULTILEVEL ZONE PLATES ... 74
4.1 GENERAL CONSIDERATIONS ... 74
4.2 PRINCIPLE OF THE FABRICATION PROCESS ... 76
4.3 OVERLAY ... 78
4.4 REACTIVE ION ETCHING OF SILICON ... 82
4.5 FABRICATION AND LOCAL THINNING OF SILICON MEMBRANES ... 87
5 OPTICAL TESTING OF MULTILEVEL ZONE PLATES ... 92
5.1 EFFICIENCY MEASUREMENTS ... 92
5.1.1 Efficiency measurements of multilevel gratings ... *94*
5.1.2 Efficiency measurements of multilevel zone plates ... *99*
5.2 MICRO-FOCUSING USING LINEAR MULTILEVEL ZONE PLATES ... 104
5.2.1 Theory of micro-focusing ... *104*
5.2.2 Resolution tests on linear zone plates ... *118*
5.2.3 Discussion ... *125*
6 PLANAR REFRACTIVE LENSES ... 129
6.1 GENERAL CONSIDERATIONS ... 129
6.1.1 Introduction ... *129*
6.1.2 Design of planar refractive lenses ... *131*
6.1.3 Influence of shape error ... *135*
6.2 DIAMOND REFRACTIVE LENSES ... 139
6.2.1 Fabrication of diamond refractive lenses ... *139*
6.2.2 Measurements on diamond lenses ... *144*
6.3 SILICON REFRACTIVE LENSES ... 151
6.3.1 Fabrication ... *151*
6.3.2 Stacking of silicon lenses ... *155*
6.3.3 Measurements ... *157*
6.4 CONCLUSIONS AND OUTLOOK ... 163
REFERENCES ... 166

1 Introduction

1.1 The early days of x-ray history

The history of x-rays starts on the 8 November 1895, when Wilhelm Conrad Röntgen observed an unexpected phenomenon in his lab in Würzburg Germany, which he later on explained as the result of a new type of radiation. Running a discharge tube to produce cathode rays - which we nowadays know are electrons of high energy - Röntgen found, that a barium platinocyanide-coated screen far away from the tube became fluorescent. Due to the large distance the fluorescence couldn't originate from the - relatively short ranging - cathode rays. Also shielding the tube with thick material wouldn't stop the fluorescence and Röntgen finally came to the conclusion that he had observed a new type of electromagnetic radiation and called it x-rays, due to its unknown nature. In his systematic experiments Röntgen failed to change the direction of x-rays by means of refracting prisms. He also did not observe any diffraction or reflection effects, when x-rays penetrated fine metallic powders. As none of these experiments had led to any noticeable deflection of x-rays he concluded, that for all investigated materials the refractive index must be very close to unity. He also realized that these special properties of x-rays - small attenuation in materials in combination with negligible scattering - can be used with benefit to image structures inside of thick samples. Therefore, when he reported his preliminary results to the president of the Würzburg Physical-Medical Society [1], he could already present the first radiographs of human bodies. One famous example is Figure 1.1 A, showing what is commonly known as the "radiograph of Mrs Röntgen's hand".

In the following months Röntgen's discovery found a strong echo in the media. The mysterious properties of these rays - especially their large penetration depths and their unclear origin - together with the spectacular radiographs of the human body led to a veritable media hysteria. Within a few months x-rays were known all over the world, and soon were considered as a kind of mystic power, which was capable of solving more or less any problem. Due to the public interest and fascination a large number of radiographs was published in newspapers, which contained - at least from a nowadays point of view - mostly rather strange and weird samples (see for example Figure 1.1 B).

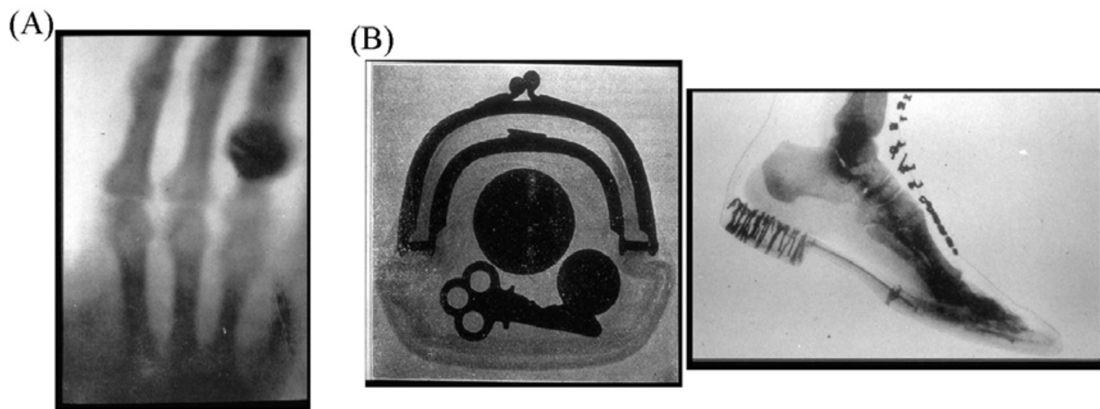

Figure 1.1: (A) One of the first radiographs of a human body made by Röntgen. (B) Radiographs of a purse with coins and a shoe in use, giving an idea of the x-ray mania in public press caused by Röntgen's discovery.

It is worth mentioning that Röntgen, who was rather a shy, reclusive person, didn't at all appreciate this kind of 'x-ray mania'. Although he was well aware of the importance of his discovery, he never failed in having a decent and realistic view of his scientific work and achievements. He also refused to make patents and published his results without claiming any proprietary rights.

One should also notice, that the x-ray mania mentioned above was one of the reasons why it took several years until the harmful and dangerous prospects of x-rays were generally recognized. Sadly, this was too late for many pioneers in the field, leading to severe burns, amputations and even the death of many of them.

1.2 Beginnings of x-ray science

Although Röntgen had already guessed that x-rays have wave properties, it took nearly two decades to clearly confirm this assumption experimentally. A first clear hint in this direction was the observation of a polarization effect for scattered x-rays by Barkla in 1906 [2]. A few years later Max von Laue, who was working at the University of Munich, had the idea of using the regular arrangement of atoms within a crystal as a diffraction grating for x-rays. He calculated, that if a beam of x-rays penetrates a crystal, parts of the beam should be diffracted in certain directions, determined by the orientation and the geometry of the crystal. Laue's assistant Walter Friedrich and Paul Knipping, a former PhD-student, finally succeeded in measuring the predicted diffraction pattern, using a crystal of copper-sulphate and long exposure times to detect the faint signal of the diffracted beam [3].

In these early days of x-ray science there was a strong relationship between the progress in the understanding x-rays and the progress in understanding the quantum-mechanical nature of light and matter. This is due to the fact, that there are many properties of x-rays, which are more or less in direct conflict with predictions, based on classical theories.

One important example is the generation of x-rays inside an x-ray tube. Soon after Röntgen's discovery Stokes [4] and Thomson [5] came up with the hypothesis that the x-rays originate from the sudden acceleration of the electrons, which occurs, when the electrons hit the atoms of the target (anode). Making the simplifying assumption, that the acceleration is opposite to the direction of the electron motion, one expects that x-rays emerging from an x-ray tube should be (at least partly) polarized, which was experimentally verified by Barkla in 1905 [6]. However, from the classical point of view one would expect that the electromagnetic waves emerging from an x-ray tube have all kind of frequencies, as the Fourier analysis of a short electromagnetic pulse will always give small but non-zero components, even for extremely high frequencies. But experimentally it is found, that only frequencies smaller than a maximum value ν_{max} are generated, where ν_{max} is directly proportional to the electric potential U applied to the tube [7]. Classically this behaviour is a miracle, but taking into account the quantum-mechanical and quantized nature of light and matter, it is easy to understand. If an electron of energy E_e causes the emission of a photon, the maximal energy E_{max} of the generated photon is equal to the original electron energy E_e, so that $E_{max}=E_e$. According to quantum mechanics the energy of a photon is proportional to its frequency [8], whereas the energy of the electron is directly proportional to the applied voltage U. This leads to

$$E_{max} = h\nu_{max} = E_e = eU \qquad (1.1)$$

where h is the Planck constant and e the electron charge.

The observation of the so-called characteristic x-ray radiation from different elements [9] is another important example, where quantum theory is essential to explain basic properties of x-rays. From the classical point of view it had always been hard to understand why atoms in gases emit characteristic frequencies of light, when energy is transferred to the atoms by means of heating or electrical discharges. It was in 1913 when Niels Bohr put forward a simple, quantum-mechanical model of atoms [10], that could give a qualitative and - in the case of hydrogen atoms - also quantitative explanation of this phenomenon. In the same year Moseley made a systematic investigation of the high frequency (x-ray) spectra of various elements and found what is nowadays known as Moseley's law: a simple relationship between the frequency of characteristic x-ray radiation and the atomic number of the corresponding element [11]. It turns out that Moseley's findings are in complete agreement with Bohr's results, assuming that the atomic number - i.e. the position of an element in the periodic table - is identical to the charge of the atomic nucleus (which at this time was reasonable to assume, but not fully proven yet).

Finally, one should also mention the Compton effect [12], as it is one of the most important examples for the link between the increase in x-ray related knowledge and the development of quantum theory. In his work Compton was able to quantitatively explain the inelastic scattering of x-rays by light elements using two basic assumptions: that electrons within light elements can be regarded as free, unbound electrons and that electromagnetic radiation consist of light quanta (photons) of certain impulse and energy. Consequently, if a photon is inelastically scattered by an electron, part of its momentum and energy will be transferred to the electron, resulting in longer wavelengths of the scattered photons than the primary photon-wavelengths. This (Compton) effect is historically important, as it is one of the most striking and direct evidences for the quantized nature of electromagnetic radiation. But it is also of considerable practical interest, as in many cases Compton scattering causes a significant loss of x-rays penetrating a material.

1.3 Generation of x-rays

Although there has always been a rapid and steady increase in x-ray related knowledge since Röntgen's discovery, for many years there were only few changes and developments concerning the method of generating x-rays.

1.3.1 X-ray tubes

The first x-ray tubes were based on low-pressure gas discharge devices and were very difficult to run in a stable and reproducible manner. It therefore was a big step forward when in 1912 W. D. Coolidge, working at the General Electric Research Laboratories in New York, developed a new type of tube, where the electrons are generated by emission from a hot filament. This enabled a strong, stable electron current and made it possible, to change the current and the applied voltage more or less independently. This "Coolidge tube" served as the standard x-ray tube for many decades without mayor changes. The maximum input power and power density of such a tube is determined by the cooling capabilities and it was soon realized, that a rotating anode would to a large extent suspend this limitation. However, due to technical problems involved in making a rotating, water-cooled and high-vacuum compatible anode, it was not until the 1960's that x-ray tubes with rotating anodes became commercially available. Compared to conventional x-ray tubes this enabled an increase of the total x-ray output power by about two orders of magnitude.

1.3.2 Synchrotron radiation

It was about the same time (early 1970's), when people started to realize that synchrotron radiation emitted from charged, relativistic particles circulating in a storage ring could be a potentially more powerful and versatile source of x-rays. The first experimental observation of synchrotron radiation had been made in 1947 at General Electrics Research Laboratory. A team under direction of Herbert Pollock was building a 70-MeV synchrotron, when during a test-run one technician by chance observed a bright arc of light (visible synchrotron radiation) coming from the electron beam [13]. However, the theoretical knowledge of radiation originating from relativistic charged particles is much older. In 1898 Liénard calculated the instantaneous power radiated by an accelerated charged particle for the general relativistic case [14]. A few years later Schott wrote a detailed essay on the same subject, including the angular and frequency power distribution as well as the polarization properties of the radiation [15]. Due to the lack of practical relevance people were not generally aware of these results, when in the early 1940's - due the development of accelerators like betatrons and synchrotrons - sources of high-energy particles became available. It was Julian Schwinger who finally re-derived the theory of electromagnetic radiation originating from relativistic charged particles and expressed the results in a convenient form for practical computations [16].

In the early days of synchrotron radiation the experiments were based on a parasitic use of accelerators, which were built for high-energy particle research. This enabled the measurement of the basic properties of synchrotron radiation, the development of the essential instrumentation (monochromators, mirrors, detectors etc.) and also the proof of principle for many experimental techniques using synchrotron radiation. However, these accelerators (also referred to as the first generation) were not optimised for this type of application and had severe drawbacks with regard to their source properties (low electron current, large cross section of the electron beam and therefore of the x-ray source) and also their running time and overall stability.

1.3.3 The second synchrotron generation

This finally led to the development of a new type of accelerators (second generation) solely dedicated to the generation of synchrotron radiation in the 1970's.

The high x-ray photon flux delivered by these 'photon factories' enabled the development of many new techniques and methods, often evolving from older ones using conventional x-ray sources. It turned out that in many of these applications the limiting factor was rather the so-called spectral brightness of the source than the total flux delivered. The spectral brightness B of a synchrotron is defined as the number of photons per second N_{photon}, emitted into a certain solid angle $d\Omega$ per unit area dA of the source within a certain spectral bandwidth dv.

$$B = \frac{N_{photon}}{d\Omega\, dA\, d\nu} \qquad (1.2)$$

The brightness of an x-ray source is often given in units (photons s^{-1} $mrad^{-2}$ mm^{-2}) assuming a bandwidth of 0.1% (see also Figure 1.2, showing the development of the peak and the average brightness of x-ray sources since the discovery of x-rays).

In order to optimise the brightness the dimensions of the x-ray source (electron beam) should be as small as possible. Due to relativistic effects synchrotron radiation is mainly emitted in the forward direction of the beam so that minimizing the angular spread of the emission is often equivalent to minimizing the angular spread of the electron beam. In consequence the

product of the angular width and the spatial width of the electron beam (the so-called emittance) has to be minimized, in order to obtain optimum brightness of a synchrotron x-ray source. This led to the development of special design of deflection magnets by Chasman and Green [17], utilizing achromatic focusing magnets to achieve electron beams with very low emittance.

1.3.4 Today's synchrotron facilities

The rapid growth of the user community, the need for sources with even higher brightness together with the strongly increased experience and knowledge of synchrotron instrumentation finally provided the justification to build a new, third generation of synchrotrons at the end of the 80's. At this time the use of undulators and wigglers as a favourable tool for the generation of x-rays was commonly acknowledged and therefore could be considered in the design of the storage rings. Contrary to conventional bending magnets, where the electron path is a circle, for undulators and wigglers the electrons move along a line, undergoing small oscillations caused by a sequence of permanent magnets with alternating fields. As the emitted light is strongly peaked in the forward direction, the emission originating from each of these oscillations adds up coherently (undulator) or incoherently (wiggler), leading to a very intense beam in the forward direction. Consequently, a modern synchrotron ring consists of a Chasman-Green lattice of deflection magnets connected by straight and empty sections, which provide the space for the incorporation of so called insertion devices (undulators and wigglers).

Third generation synchrotrons typically specialize on either the hard x-ray range (like the ESRF in Grenoble, the APS near Chicago, Spring-8 in Japan) or the soft x-ray range (e.g. the ALS in Berkeley, Elettra in Trieste, BESSY in Berlin, or also the SLS in Switzerland), whereas the intermediate region of photon energies (typically around 5 keV) is accessible by both. However, in both cases it is possible to shift the accessible photon energy range to even harder x-ray energies using super-conducting bending magnets with high magnetic fields or in-vacuum small gap undulators.

1.3.5 Future x-ray sources

Within the last three decades the brightness of state of the art x-ray sources has increased about twelve orders of magnitude compared to conventional x-ray tubes and the question arises, whether and how this development is going to continue, possibly leading to a new (fourth) generation of x-ray sources. One prominent candidate for such a device is the X-ray free electron laser (X-FEL), utilizing the self-amplification of spontaneous emission (SASE) inside a long undulator [18]. Such X-FELs are predicted to give extremely short and intense pulses, resulting in peak brightness up to 10 orders of magnitude above today's third generation synchrotrons (see also Figure 1.2). At the moment there are studies to build such SASE-based free electron lasers in Hamburg and Stanford [19, 20].

Another promising approach to overcome the limits of today's synchrotron sources is the use of so-called energy-recovery linear accelerators (ERLs) [21]. Within a conventional synchrotron bunches of x-ray generating electrons move for hours around a storage ring, until the electrons eventually get lost and hit the ring chamber walls. Within an ERL each bunch of x-ray generating electrons is only used for a very short time period. After a bunch has been accelerated to its final energy with a linear accelerator (LINAC), it once (or a few times) passes a ring similar to the storage ring of conventional synchrotrons and afterwards is deliberately removed again. Before the removal each bunch of electrons passes the linear accelerator in such way that it is out phase with respect to the accelerating electromagnetic

field. In consequence most of the electron energy is transferred back to the field and can be used to accelerate a new generation of electrons. The concept of using each bunch of electrons only for a very short time period has the advantage that Coulomb interactions between individual electrons play a minor role and only cause a small increase of the transversal size of the electron bunches. As a consequence the size of the electrons beam is mainly determined by properties of the electron source, making it possible to achieve a much smaller cross section of the beam and therefore a strong increase in brightness of the source.

However, many technological and practical problems still have to be solved, till devices like X-FELs and ERLs will come into operation. In any case it is very likely that due to the differences between third and fourth generation x-ray sources in terms of the time structure and the spectral distribution of the x-ray beam, there will be rather a complementary coexistence, than a gradual replacement of one of them.

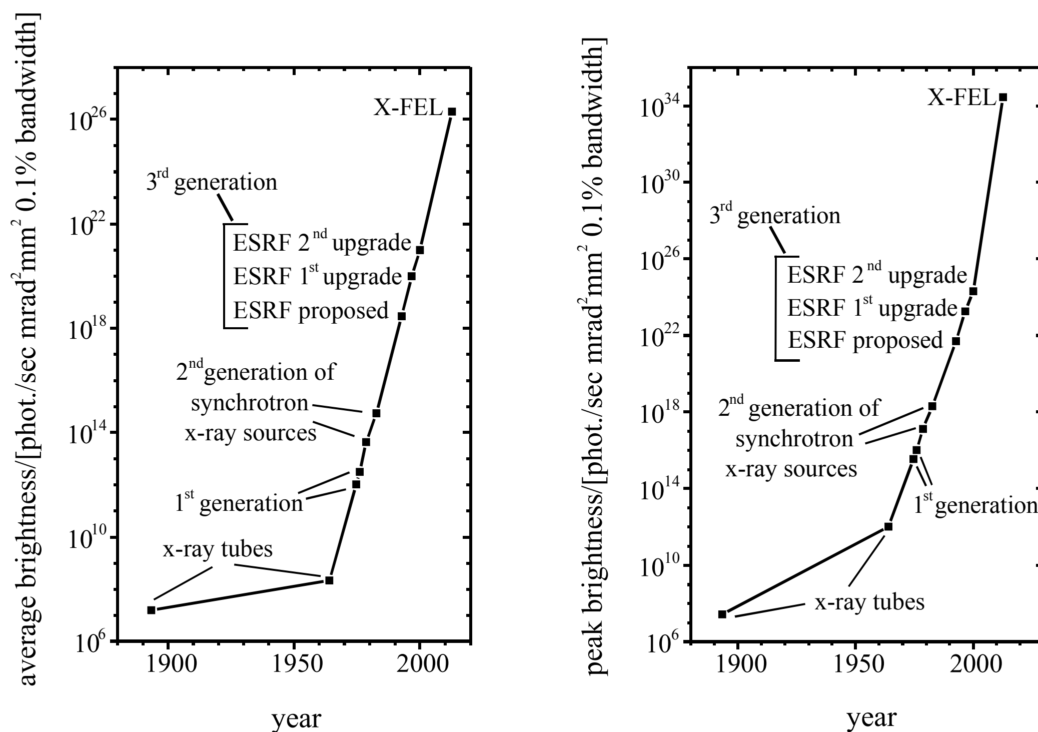

Figure 1.2: Development of the average and peak brilliance of x-ray sources since the discovery of x-rays (taken from [19]).

1.4 Instrumental aspects of synchrotrons

Although the brightness and the total flux of an x-ray beam delivered by a synchrotron are very important parameters, there are of course many other aspects and technical components of a synchrotron, which are essential for an efficient and functional experimental station (beamline). In hardly any experiment it is possible to use the direct beam from the source. One needs the possibility to cut out parts of the beam with a well-defined size, which is accomplished by a set of several horizontal and vertical slits along the x-ray beam. In most experiments one requires x-rays with a certain and tuneable photon energy. Consequently beamlines normally have a built-in crystal, multi-layer or grating monochromators allowing for the easy and automated setting of the x-ray beam energy.

1.5 X-ray lenses

Last but not least, there are quite a number of experiments, which depend on the availability of some kind of focusing device. Basically focusing is required whenever one wants to obtain structural, chemical or physical information of small regions of a sample, and this is the point where x-ray lenses come into play.

Like for conventional optics in the visible light range one can use reflection (focusing mirrors), refraction (refractive lenses) and diffraction (diffractive lenses, zone plates) in order to deflect and therefore focus light. However, there are some peculiarities originating from the fact, that for x-rays the real part of the refractive index is typically very close to unity and at the same time the imaginary part (describing absorption) comparatively large.

X-ray mirror optics take advantage of the fact that the refractive index of all materials in the x-ray range is smaller than one so that total reflection can be achieved if light falls unto a sufficiently flat surface. As the real part of the refractive index is very close to unity, a grazing incidence of the x-rays, almost parallel to the mirror surface, is required in order to obtain total reflection. Due to these small working angles x-ray mirrors are relatively hard to align and often suffer from strong aberrations. In addition very long mirrors with high shape accuracy are required making high performance mirror systems difficult to build and comparatively expensive. In consequence, spot sizes of about 1 micron can be obtained in routine operation, although spot-sizes down to 100 nm FWHM have been reported recently [22, 23, 24]. As x-ray mirrors have the advantage of being achromatic and show comparatively high efficiency, they are quite often used as x-ray focusing devices.

Refractive lenses for x-rays are a relatively new development and in fact have been considered impractical for a long time due to the small refraction effects and the strong absorption of materials in the x-ray range. Nevertheless, using many lenses in series it is possible to obtain a sufficient deflection of the beam, and therefore reasonable focal lengths [25]. And going to high photon energies, using lens materials with low atomic number and utilizing alternative approaches for the lens fabrication and design [26, 27], it is possible to keep absorption losses small. Refractive lenses for x-rays are strongly chromatic - the focal length is found to be proportional to the square of the used photon energy. However, many applications require monochromatized x-rays of a fixed energy, so that chromatic aberrations are normally negligible and do not significantly limit the applicability of refractive lenses.

Diffractive lenses (zone plates) for x-rays offer the advantage that the diffractive structures together with the support membrane can be kept very thin, so that even for soft x-rays, where absorption plays a dominant role, a sufficiently high x-ray transmission can be realized. The diffractive structures can be fabricated with high accuracy down to very small structure sizes and as a consequence zone plates achieve by far the highest resolution of all x-ray lenses [28, 29, 30, 31]. Similar to refractive lenses diffractive x-ray lenses have the disadvantage of being chromatic - the focal length is directly proportional to the photon energy. Another drawback of diffractive lenses is, that it is very difficult to obtain sufficient diffraction efficiencies for the hard x-ray range. This results from the fact, that good efficiencies require structure heights, which are often much larger than the periods of the diffracting structures, making the fabrication of zone plates with the demanded aspect ratios a non-trivial task.

There are also many other alternative methods to achieve a small spot of x-rays, like Bragg-Fresnel lenses, capillary optics and wave-guides. Consequently whole books and several reviews can be found in the literature, discussing in detail the advantages and disadvantages of all these methods and the fields of their application (see for example [32]).

For a comprehensive overview of micro-focusing techniques in the x-ray range above 1 keV the reader is referred to [33]. A review of microscopy in the soft x-ray range can be found in [34]. The development of diffractive x-ray lenses is treated in [35], containing a selection of the most important, original papers on zone plates. Finally, a short overview of different types of refractive x-ray lenses can be found in chapter 6.

1.6 Organization of this thesis and related own publications

In the context of this work diffractive lenses (zone plates) as well as refractive lenses (planar refractive lenses with minimized absorption) have been investigated, both of them aiming for applications in the hard x-ray range.

The first part of the thesis deals with the main theory of diffractive and refractive lenses (chapter 2), including the own work on the derivation and calculation of optimal multilevel grating profiles yielding maximal diffraction efficiency (see also [36]). Chapter 3 introduces and describes the micro- and nano-fabrication methods used within this work to fabricate diffractive and refractive hard x-ray lenses.

The second part of this work (chapters 4 and 5) deals with the work performed on diffractive silicon lenses (see [37]). It was already mentioned earlier, that zone plates for hard photon energies require diffracting structures with extreme aspect ratios. In chapter 4 it is shown that this requirement can be fulfilled using linear zone plates, which are tilted with respect to the x-ray beam, resulting in a strong increase of the effective height of the grating structures. Using silicon zone plates with a multilevel grating profile fabricated by means of e-beam lithography this tilting method makes it possible to obtain unprecedented diffraction efficiencies for zone plates in the x-ray range (see chapter 5).

The fabrication and testing of planar refractive lenses is described in the last part of the work (chapter 6, see also [38], [39], [40]). Refractive lenses made from silicon as well as from diamond have been investigated. Silicon has the advantage that it is easier to machine by standard micro-fabrication techniques, but shows a comparatively high absorption for the 'softer' part of the hard x-ray range. Therefore silicon planar refractive lenses are especially suited for very high photon energies (typically 30-50 keV), as there are only very few other types of lenses available in this x-ray region. Diamond is very hard to structure as a material, but has the advantage that it shows little absorption even for lower x-ray energies (down to about 10 keV). Diamond also has a high thermal conductivity, a low thermal expansion coefficient and a high stability. Therefore diamond planar refractive lenses have a realistic chance to withstand the extremely intense x-ray pulses generated by future x-ray free electron lasers, making them interesting candidates for optical systems at such fourth generation x-ray sources.

The presented results on multilevel diffractive zone plates and refractive diamond and silicon lenses represent the main part of the work performed within the PhD-study. However, some parts of the work were in very close relationship to the research at the PSI on a novel type of binary diffractive optics systems for hard x-rays. On the one hand this led to a fruitful stimulation and impact on the PhD-work, on the other hand significant contributions were made to the work on binary fresnel lenses [41, 42] and binary diffraction gratings [43].

2 Theory

The theory chapter basically consists of three parts. In the first part (chapter 2.1) the main interaction processes between matter and x-rays are described and it is shown, how this interaction can be mathematically modelled introducing a complex refractive index and a total absorption coefficient μ_{total}. The second part - chapter 2.2 - contains the main theory of diffractive x-ray lenses (zone plates), including zone plate design rules as well as calculations of the obtainable resolution and efficiency for different lens designs. In the last part - chapter 2.3 - a few basic properties of refractive x-ray lenses are shown and the concept of refractive lenses with minimized absorption is introduced.

2.1 Material properties in the x-ray range

Macroscopic phenomena like refraction, reflection and absorption of x-rays can be understood as the net result of the interaction between x-rays and individual atoms of the considered material. In chapter 2.1.1 it is therefore considered how a single atom reacts if it is irradiated with x-rays and how the resulting polarization of all atoms within a material can be described by a complex refractive index. In the following chapter (chapter 2.1.2) a simple classical model of atoms is presented leading to an approximate relationship between the real part of the refractive index and the density of a material. The last chapter of this section (chapter 2.1.3) addresses the different absorption process of x-rays within materials and shows how the attenuation of x-rays penetrating matter can be described using a total absorption coefficient μ_{total}.

2.1.1 Coherent scattering of x-rays and refractive index

The refractive index is a means to describe the net, average reaction of all individual atoms to an incoming x-ray wave. Considering a single atom, which is irradiated with x-rays of a certain frequency, the electromagnetic field will cause a time dependent distortion of the electron distribution within the atom. The resulting harmonic oscillation of the atom electrons leads to a time dependent polarization of the atom and therefore to the emission of dipole radiation of the same frequency. In consequence the emitted secondary radiation stemming from the atom will have the same energy as the primary incident x-rays. As the polarization is directly linked to the field of the incoming rays, there is a fixed phase between the incoming primary and the secondary (scattered) radiation. Consequently, the process described above is referred to as coherent scattering. For a periodic dipole moment p with $p(t)= p_a \exp(-i\omega t)$ the electric field E_s of the scattered wave in the far field region is given by [44]

$$E_s = -\left(\omega^2 / 4\pi\varepsilon_0 c^2\right) p_a \sin\theta \exp\left[-i\omega\left(t - R/c\right)\right] / R \qquad (2.1)$$

where p_a is the maximal amplitude of the dipole moment, R the distance to the position of the dipole and θ the angle between the direction of the dipole and the direction of the diffracted wave. The electrical field originating from scattering by a single atom can be written in a similar way,

$$E_s = -E_0 r_e f(\theta, E) \sin\theta \exp\left[-i\omega\left(t - R/c\right)\right] / R \qquad (2.2)$$

where E_0 is the electric field of the incoming wave and r_e the classical electron radius ($r_e = e^2 / 4\pi\varepsilon_0 m_e c^2$). The angular distribution of the radiation is described by the atomic scattering factor f. Due to symmetry reasons the field of the scattered wave only depends on the scattering angle θ and the photon energy E of the incoming x-rays.

Any harmonically oscillating charge distribution can be considered to consist of tiny oscillating dipoles, which are distributed over the space region containing this charge. This argument also applies for the irradiated atom described above. The scattered wave originating from an atom is therefore simply given by the sum of the contributions originating from such hypothetical dipoles, taking into account their position and amplitude. If the wavelength λ of the scattered wave is significantly larger than the atom diameter a, in first approximation all dipoles can be considered to have practically the same position (e.g. in the center of the atom). In this case the scattered wave field becomes identical to the one originating from a single dipole and the comparison of equations (2.1) and (2.2) leads to the conclusion that the atomic scattering factor f is only a function of the photon energy.

$$f(\lambda >> a) = f^0 = f^0(E) \qquad (2.3)$$

In addition, as the scattered wave emerging from an atom (equation (2.2)) is identical to the wave emitted by a dipole with a dipole moment p_a (equation (2.1)), we obtain

$$p_a = \left(4\pi\varepsilon_0 c^2 / \omega^2\right) r_e f_a{}^0 E_0 = \left(e^2 / m_e \omega^2\right) f_a{}^0 E_0 \qquad (2.4)$$

Analogous to normal optics in the visible light range, the coherent scattering of x-rays by atoms and molecules causes phenomena like refraction and reflection when x-rays interact with matter. This interaction can be taken into account in a quantitative way by introducing the refractive index of a material. The relationship between the local electric field E_0 and the polarization per unit volume P at a certain point is given by

$$P = \varepsilon_0 \, \chi \, E_0 \qquad (2.5)$$

where χ is the dielectric susceptibility of the material. At the same time the polarization P (according to its definition) is given by the sum of all dipole moments p_a per unit volume

$$P = \sum_a n_a p_a \qquad (2.6)$$

where n_a is the number of atoms of different kinds per unit volume (the type indicated by the index a). Combining equations (2.5) and (2.6) we obtain

$$\chi = 1/\left(\varepsilon_0 E_0\right) \sum_a n_a p_a \qquad (2.7)$$

Finally, substituting (2.4) in equation (2.7) leads to a relationship between the dielectric susceptibility of a material in the x-ray range and the atomic scattering factors of the atoms contained in the material.

$$\chi = \left(4\pi c^2 r_e / \omega^2\right) \sum_a n_a f_a = \left(r_e \lambda^2 / \pi\right) \sum_a n_a f_a \qquad (2.8)$$

The refractive index n of the material, which is equal to the root of the relative dielectric constant $\varepsilon_r = \varepsilon/\varepsilon_0$, is calculated as

$$n = \sqrt{\varepsilon_r} = \sqrt{1+\chi} \qquad (2.9)$$

Note that several approximations are involved in the derivation of equation (2.8):

1) In general (e.g. for optics in the visible light range) one has to distinguish between the effective electrical field acting on the atoms and the mean electrical field, obtained by averaging over a volume containing a sufficiently large number of atoms (see [44], page 90). However, due to the small refraction and reflection caused by matter in the x-ray range ($|\chi| \ll 1$) the difference between these two fields is negligible.

2) The simple summation over different types of atoms in equation implies, that the polarizability of isolated atoms is identical to the polarizability of atoms, which are bound to other atoms within a material. In the x-ray range this simple approximation is in most cases applicable. However, there are experimental techniques like EXAFS (Extended X-ray absorption fine structure) and NEXAFS (Near Edge X-ray Absorption Fine Structure), which use the - usually minor - effects of chemical bounds in order to study the chemical environment of atoms.

In the derivation of equation (2.8) it was assumed that the x-ray wavelength is significantly larger than the diameter of the scattering atoms. In consequence the atomic scattering factor was found to be independent of the scattering angle θ. However, considering hard x-ray photon energies (above approx. 5 keV) the corresponding wavelengths are of the same size or smaller than typical atom diameters and therefore the atomic scattering factors in general show a dependence on the scattering angle. For hard x-rays the calculations leading to equation (2.8) are therefore not necessarily applicable. But it turns out, that for many practical situations equation (2.8) is nevertheless valid, provided that certain requirements are fulfilled which are discussed below.

For hard x-rays it is always possible to find a range $\Delta\theta$ of scattering angles where the atomic scattering factor is approximately constant. It was mentioned above, that the scattered wave stemming from an irradiated atom can be considered to originate from a large number of tiny oscillating dipoles, situated at different positions of the atom. Using this model one finds, that within a range $\Delta\theta$ of diffraction angles given by $\Delta\theta < \lambda/a$ the relative phase of individual dipole contributions does not change. Within this range of diffraction angles the scattered wave is therefore identical to the wave emitted by a single dipole, which also implies that the atomic scattering factor is a constant.

Considering the important practical case of scattering angles, which are close to the original direction of the incoming x-rays (i.e. θ close to zero) this leads to

$$f(\theta \ll \lambda / a) = f^0 = f^0(E) \qquad (2.10)$$

Within this limit of nearly forward scattering ($\theta \ll \lambda/a$) equation (2.4) also applies to hard x-rays. The concept of a refractive index given by equation (2.8) is then still valid and can be used to describe interactions between matter and x-rays, where the deflection of the incoming x-ray beam is small enough, so that only scattering in the forward direction plays a role. Due to the weak interaction between x-rays and matter such small deflections are typical for many

practical applications. However, as it will be discussed in chapter 2.1.3, there are certain experimental conditions where scattering into large angles plays a significant role.

As the absolute value of χ is very small in the entire x-ray range, equation (2.9) can be approximated by

$$n = \sqrt{1+\chi} \cong 1 + \mathrm{Re}(\chi)/2 + i\,\mathrm{Im}(\chi)/2 \qquad (2.11)$$

In the x-ray range the real part of the refractive index n is in most cases smaller than one and therefore it is convenient to write the refractive index as

$$n = 1 - \delta + i\beta \qquad (2.12)$$

Finally, using equations (2.8), (2.11) and (2.12) one obtains

$$\delta = \left(r_e \lambda^2 / 2\pi\right) \sum_a n_a f_{a,1} \qquad (2.13)$$

$$\beta = \left(r_e \lambda^2 / 2\pi\right) \sum_a n_a f_{a,2} \qquad (2.14)$$

where $f_{a,1}$ is the real part and $f_{a,2}$ the imaginary part of the complex atomic scattering factor f_a. Tabulated values of $f_{a,1}$ and $f_{a,2}$ can be found for example in references [45] and [46], allowing the calculation of the decrement of the refractive index (δ) and the imaginary part (β) for each material of known composition and density.

For the derivation of equations (2.13) and (2.14) it was not necessary to have any knowledge of the origin and characteristic features of the atomic scattering factor f_a. The calculation of accurate values of f_a requires a thorough quantum mechanical treatment of the system consisting of the atom itself and the incoming x-ray wave. However there are some important features and properties of f_a, which can be understood by simple quantum mechanical and classical considerations.

In classical optics one finds that the real part of the refractive index causes a phase shift of a travelling wave. If the phase shift is different for different parts of the wave front this results in a deflection of the wave. The imaginary part of the refractive index causes an attenuation of the wave and therefore describes (photoelectric) absorption within the material (see also chapter 2.1.3). According to equations (2.13) and (2.14) the real and the imaginary part of the atomic scattering factor f_a are directly related to the real and the imaginary part of the refractive index n. This leads to the conclusion, that the imaginary part of f_a describes the x-ray absorption of a single atom, whereas the real part of f_a describes the elastic component of the scattering process, causing a change in direction of an incoming x-ray photon but no absorption of it.

For all elements there are characteristic energies - absorption edges - where the imaginary part of the atomic scattering factors becomes very large. This results from the internal structure of the atoms, as all electrons occupy a certain quantum mechanical eigenstate (quantum state) of well-defined energy. One finds, that an x-ray photon can only be absorbed if its energy is equal to the energy needed to excite one electron from its original quantum state to a quantum state of higher energy. In consequence strong x-ray absorption of an atom only occurs for well-defined photon energies, which are determined by the internal structure of the atom and therefore characteristic for each element.

2.1.2 A simple classical model of the origin of the refractive index

In the following a simple classical model of the polarizability (and therefore the refractive index) of materials is introduced. Despite of its simplicity, it basically yields the same results as the thorough, quantum mechanical treatment of the problem, and gives a good idea about the origin the refractive index and its correlation to parameters like the photon energy and the density of the regarding material. The idea of this model is to treat the bounded electrons within an atom as damped classical oscillators with natural angular frequencies ω_s and damping factors γ_s (the index s denoting a certain electron quantum state in a certain atom). If x(t) is the displacement of one electron from the equilibrium, then its motion caused by an external electric field $E(t)= E_0 \exp(-i\omega t)$ is determined by

$$d^2x/dt^2 = -eE_0/m_e \exp(-i\omega t) - \gamma_s dx/dt - \omega_s{}^2 x \qquad (2.15)$$

The solution of equation (2.15) is of the form $x(t)= x_0 \exp(-i\omega t)$ with

$$x_0 = -eE_0/m_e \frac{1}{\omega_s{}^2 - \omega^2 - i\gamma_s\omega} \qquad (2.16)$$

The dipole moment of an atom ($p(t)= p_a \exp(-i\omega t)$) is then given by

$$p_a = \sum_s -e\,x_{0,s} = e^2 E_0/m_e \sum_s \frac{1}{\omega_s{}^2 - \omega^2 - i\gamma_s\omega} \qquad (2.17)$$

By comparison of equation (2.4) and (2.17) one obtains a simple relationship between the atomic scattering factor of an atom and the atomic constants ω_s and γ_s

$$f_a = \sum_s \frac{\omega^2}{\omega_s{}^2 - \omega^2 - i\gamma_s\omega} \qquad (2.18)$$

Substituting equation (2.18) in (2.12) and (2.13)/(2.14) one obtains

$$n = 1 + \left(r_e\lambda^2/2\pi\right)\sum_a n_a \sum_s \frac{\omega^2}{\omega_s{}^2 - \omega^2 - i\gamma_s\omega} = 1 - \delta + i\beta \qquad (2.19)$$

Analysing equation (2.18) one finds, that for frequencies $\omega=\omega_s$ the imaginary part of f_a shows a more or less sharp and high peak, depending on the value of the damping factor γ_s. In the previous section it was mentioned, that such large values of f_a occur at characteristic absorption edges of atoms. In consequence the angular frequencies ω_s of the classical model simply describe the position of the corresponding absorption edges.

For many applications it is important to keep absorption as low as possible. One easy possibility to achieve this goal is to use photon energies, which are far above the absorption edges of all relevant elements ($\omega>>\omega_s$). Within this energy range the atomic scattering factor is approximately given by

$$f_a = \sum_s \frac{\omega^2}{\omega_s{}^2 - \omega^2 - i\gamma_s\omega} \cong \sum_s -1 \cong -Z_a \qquad (2.20)$$

This means that for high photon energies the atomic scattering factor becomes approximately equal to the number of electrons Z_a within an atom. Together with equation (2.19) this leads to

$$\delta \cong r_e \lambda^2 /(2\pi) \sum_a n_a Z_a \tag{2.21}$$

The sum in equation (2.21) is equal to the number of electrons per volume, i. e. equal to the electron density of the material. For most atoms (except hydrogen) the number of electrons is approximately equal to half the atomic mass number A, whereby A is defined as

$$A = m_a / u \tag{2.22}$$

with m_a being the mass of the atom and u the unified atomic mass unit. Using the approximation $Z_a \approx A/2$ we obtain

$$\delta \cong r_e \lambda^2 /(2\pi) \sum_a n_a m_a /(2u) = \left(r_e \lambda^2 /(4\pi u)\right) \sum_a n_a m_a \tag{2.23}$$

Multiplying the number of atoms per volume and the atom mass yields the mass per volume, i. e. the material density ρ leading to

$$\rho = \sum_a n_a m_a \tag{2.24}$$

and therefore

$$\delta \cong r_e \lambda^2 \rho /(4\pi\, u) \tag{2.25}$$

Finally, using the photon energy E (E= h c/λ) rather than the wavelength one obtains

$$\delta \cong \frac{\mathrm{r_e} h^2 c^2}{4\pi\, u} \rho / E^2 \tag{2.26}$$

Equation (2.26) is less accurate than (2.21), but at the same time it shows the simple dependence of the decrement of the refractive index on the material density ρ and the photon energy E. For a material with a density ρ=5g/cm^3 and a photon energy of 10 keV this results in $\delta = 2.06\ 10^{-4} \times \rho$[g/cm3]/$E^2$[keV]=1.03 10^{-5}. This demonstrates that for x-rays the decrement of the refractive index is indeed a small quantity.

Figure 2.1 shows the values of δ for gold, carbon (diamond) and silicon taken from reference [45] and the calculated values using equation (2.21). For photon energies above all absorption edges (highest absorption edge of Carbon: 280 eV; Si: 1840 eV) there is only a very small difference between the tabulated and the calculated values.

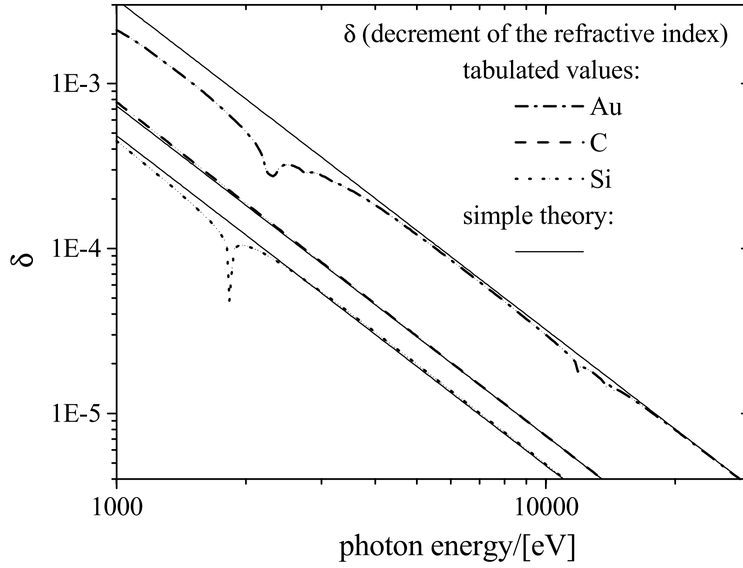

Figure 2.1: Decrement of the refractive index δ for gold, carbon (diamond) and silicon, taking the values tabulated in reference [45]. The solid line shows calculated values using the damped oscillator atom model (assuming photon energies far above all absorption edges, equation (2.21))

In the case of gold (and partly also for silicon), the condition that the photon energies have to be beyond all absorption edges is not fulfilled, as the highest absorption edge of gold is at 78.0 keV. Nevertheless one still has a quite good agreement between the literature and the calculated values of δ, provided that the photon energies are not too close to absorption edges (e.g. gold absorption edges around 2.5 keV and around 14 keV). This can be explained by the fact that compared to the total number of electrons there are only few electrons in the atomic states causing the higher absorption edges. Consequently the contribution of these electrons to the refractive index is only small. The main contribution originates from electrons having binding energies well below the photon energy and therefore equation (2.21) is still valid.

2.1.3 Coherent scattering, incoherent scattering and attenuation in materials

In the last paragraph it was shown that the refraction and reflection of x-rays is directly related to the coherent scattering of individual atoms and also how the collective action of all atoms can be described introducing the refractive index of a material. Like in conventional optics in the visible light range, the imaginary part of the refractive index describes the absorption within a material. Assuming a plane wave travelling in x-direction, which is described by $E_p = E_0 \exp\left(i(2\pi n/\lambda)x - i\omega t\right)$, we find

$$E_p = E_0 \exp\{ i\left[2\pi x(1-\delta)/\lambda - \omega t)\right] \} \exp\left(-2\pi\beta x/\lambda\right) \qquad (2.27)$$

where $E_p(x,t)$ is the electrical field of the plane wave. In consequence, the intensity I_p of the travelling wave decays exponentially within the material

$$I_p = I_0(x=0)\ \exp(-4\pi\beta x/\lambda) = I_0 \exp(-\mu_{photo} x) \quad (2.28)$$

with

$$\mu_{photo} = 4\pi\beta/\lambda \quad (2.29)$$

The parameter μ_{photo} is called the linear absorption coefficient and describes the attenuation of x-rays within materials. Note that this attenuation is directly related to the imaginary part β of the refractive index. In the two previous sections it was discussed that x-ray absorption - quantified by β - originates from the excitation of electrons into energetically higher quantum states. This process is commonly referred to as photoelectric absorption and in consequence the absorption coefficient μ_{photo} describes the attenuation of x-rays within a material due to photoelectric absorption.

In general two additional loss mechanisms for x-rays have to be considered, as both of them can lead to a significantly stronger attenuation of x-ray beams in materials than described by equation (2.28).

One of these two loss mechanisms originates from the fact that a homogeneous refractive index is incapable of describing the - on the atomic level - inhomogeneous structure of materials. It was discussed in 2.1.1 that the refractive index only accounts for scattering in the forward direction of the original x-ray wave. However, in general scattering occurs in all directions of space leading to certain scattering losses when radiation penetrates a material. For amorphous materials or gases, where the atoms are more or less randomly distributed, there is no phase correlation between the scattered waves originating from individual atoms. In consequence the total loss due to coherent (Rayleigh) scattering is simply given by the sum over all losses caused by individual atoms. The amount of light scattered by a single atom is relatively small and consequently the (additive) coherent scattering of all atoms gives only a small contribution to the overall attenuation of x-rays in materials. However, this does not hold true in situations where the contributions stemming from individual atoms add up constructively. Although each of these contributions is very small, in case of constructive interference the total amplitude of the scattered wave can be extremely large. In consequence it is possible to reach that basically all incoming x-ray photons undergo a scattering process.

Note that independent of the atom distribution within a material one has always constructive interference in the forward direction. However, the effect of this “constructive” scattering in forward direction is already taken into account by the refractive index of the material. Due to the quasi-random distribution in amorphous materials constructive interference is explicitly restricted to the forward direction. However, the situation changes, if crystals are considered, as they have a regular, non-random distribution of atoms. For crystals there is a well-defined phase correlation between the contributions of individual atoms and it turns out, that for special crystal orientations all these contributions can add up constructively (if the so-called Bragg condition is fulfilled). In such a case a large fraction of the incoming x-rays can be scattered, leading to a strong attenuation of the original x-ray beam. However, one finds, that under normal circumstances it is very unlikely that a crystal fulfils the Bragg condition. Considering x-rays of certain, fixed energy one normally has destructive interference of the individual contributions in all directions of space (except the forward direction). Consequently (at least for a perfect single crystal having no dislocations, no thermal vibrations etc.) there will be no attenuation of the x-ray beam due to coherent scattering.

The second loss mechanism leading to significant attenuation of hard x-rays in materials is the Compton effect. Contrary to photoelectric absorption, where the (total) photon energy is used to excite an electron of an atom, in the Compton process only part of the photon energy and momentum is transferred to an (quasi free) electron, whereas the rest is transferred to a secondary photon, according to the laws of energy and moment conservation. The phase of the secondary photon is related to the phase of the original atomic state of the Compton electron. Consequently, as there is no electron phase correlation between different atoms of a material, secondary Compton photons are incoherent with respect to each other. Compton scattering is therefore also often referred to as incoherent scattering.

For a single free electron Compton scattering can be described analytically by the Klein-Nishina formula [47]. For photon energies below about 100 keV the total cross section σ_{comp} of the (incoherent) Compton scattering process with a free electron is (in good approximation) given by [48, page 3-2]

$$\sigma_{comp} \cong 8\pi/3\; r_e^2 \left(1+2k_0+1.2k_0^2\right)/\left(1+2k_0\right)^2 \qquad (2.30)$$

where the parameter k_0 is defined as $k_0 = h\nu/\ m_e c^2$. The attenuation of an x-ray beam by an electron gas due to Compton scattering is related to the total cross-section via

$$I = I_0 \exp\left(-\mu_{comp} x\right) = I_0 \exp\left(-n_e \sigma_{comp} x\right) \qquad (2.31)$$

where μ_{comp} is the absorption coefficient describing x-ray attenuation due to Compton scattering and n_e the number of (free) electrons per unit volume. Equation (2.31) can be used to estimate the Compton scattering losses within materials, assuming that the electrons within the material can be regarded as free electrons. However, for the calculation of accurate values of μ_{comp} one has to take into account that the electrons are more or less strongly bound to one atom.

One finds, that Compton scattering becomes strong for high photon energies. At the same time photoelectric absorption strongly decreases with photon energy, and in consequence Compton scattering is often the main remaining loss mechanism for photon energies above 50 keV. Tabulated values of σ_{comp} and μ_{comp} for different elements, obtained by thorough quantum mechanical calculations, can be found in reference [46] and [49]. These also include tables of the "absorption" coefficient μ_{coh} due to coherent Rayleigh scattering, assuming a material with randomly distributed atoms.

Summarizing these results, the total attenuation of x-rays within a material, including photoelectric absorption, coherent scattering and incoherent scattering can be described by

$$I = I_0 \exp\left(-\mu_{total} x\right) \qquad (2.32)$$

where the total absorption coefficient μ_{total} is given by the sum over all absorption coefficients, stemming from different loss processes

$$\mu_{total} = \mu_{photo} + \mu_{comp} + \mu_{coh} \qquad (2.33)$$

Figure 2.2 shows the energy dependence of μ_{photo}, μ_{comp}, μ_{coh} and the total absorption coefficient μ_{total}, for carbon and silicon.

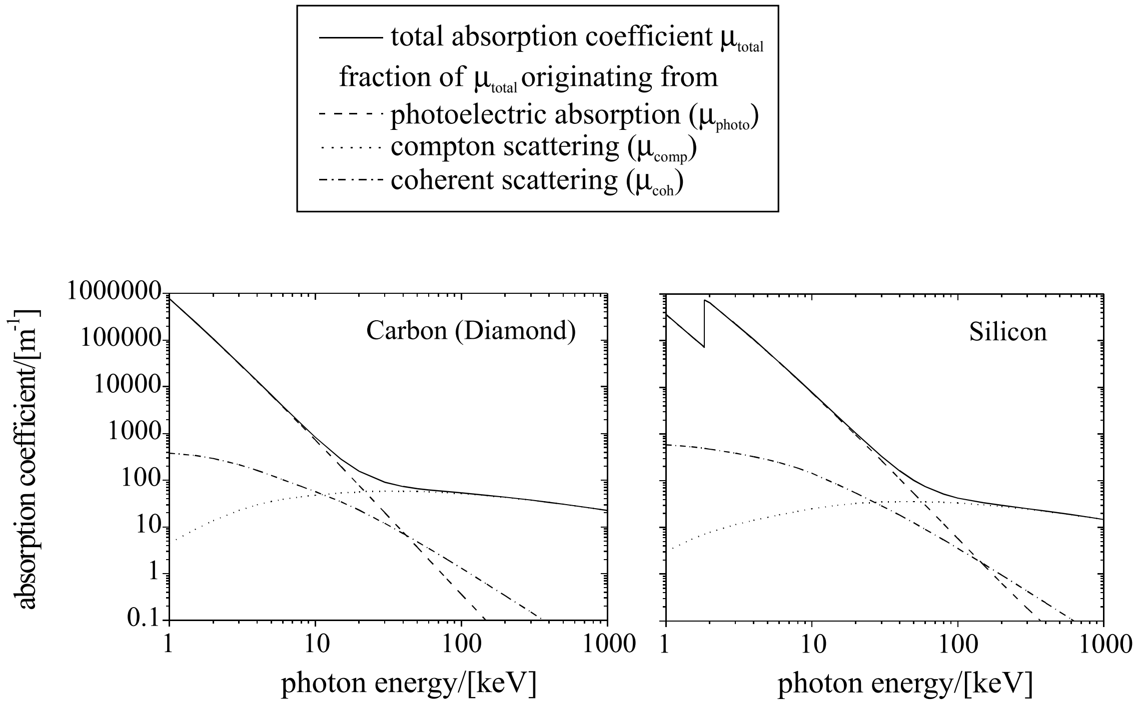

Figure 2.2: Linear (total) absorption coefficient μ_{total} of carbon and silicon (solid lines). The dashed lines show the contributions of different loss mechanisms (photoelectric absorption, Compton scattering and coherent scattering) to the total attenuation of x-rays.

For photon energies below 10 keV absorption losses are mainly caused by photoelectric absorption, whereas in the region above about 100 keV Compton scattering exceeds all other loss mechanisms. In the intermediate region both loss mechanisms play a role, whereas losses due to coherent scattering are small for all photon energies.

2.2 Diffractive x-ray lenses (zone plates)

This chapter contains the basic theory of zone plates. The first five sections deal with elementary properties and features of zone plates, like their construction rules (2.2.1), obtainable resolution (2.2.2), their depth of focus (2.2.3) and describe important properties of different zone plate types (2.2.4, 2.2.5). The last section (2.2.6) addresses the efficiency of zone plates and shows how the design of the grating structures within the zone plate has to be optimised in order to achieve maximal diffraction efficiency. The considerations include the important general case of grating materials with non-negligible absorption. A numerical and an analytical approach are presented, enabling the calculation of the optimal parameters of multilevel grating profiles (staircase profiles), which lead to maximal diffraction efficiency.

2.2.1 Construction rule of zone plates

Zone plates use the diffraction of light in order to concentrate radiation in a point (focus). In order to reach this goal a well-defined assembly of the diffracting structures within a zone plate is required. For a conventional grating one finds that the diffraction angle θ_m of a certain diffraction order m is given by

$$\sin\theta_m = m\,\lambda / b \qquad (2.34)$$

where b is the period of the grating. Changing the period of the grating will change the corresponding diffraction angle. Consequently, if a grating with an appropriate, variable grating constant b_{var} is utilized for a zone plate, it is possible to achieve that all parts of a zone plate (diffraction lens) diffract light in a certain spot (focus). One period of this grating with variable grating constant is commonly referred to as one zone of the zone plate. In chapter 2.2.4 it will be discussed, that for a special type of zone plates some authors prefer to use a different convention. However, for reasons of generality, in the following we will stick to the first definition.

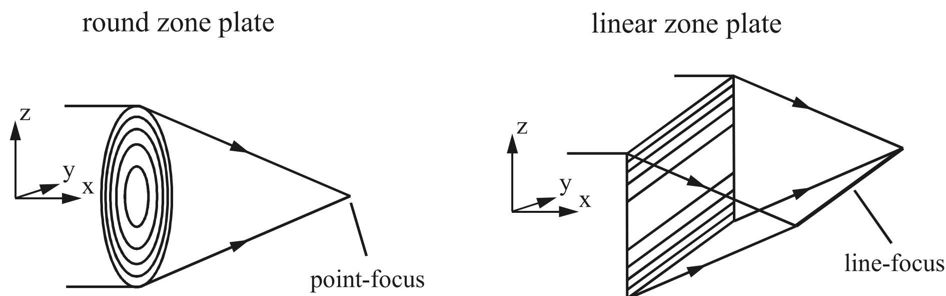

Figure 2.3: Different types of zone plates (diffraction lenses)

For ‘normal’ focusing into a spot the diffracting structures have to be arranged concentrically around the optical axis (see Figure 2.3, ‘round zone plate’). However, for certain applications it is preferable to have focusing devices, which focus only in one direction (see Figure 2.3, ‘linear zone plate’). In this case the diffracting structures show only in one direction a periodicity (e.g. the z-direction, see Figure 2.3) leading to focusing in this direction and a line focus along the perpendicular direction (y-direction).

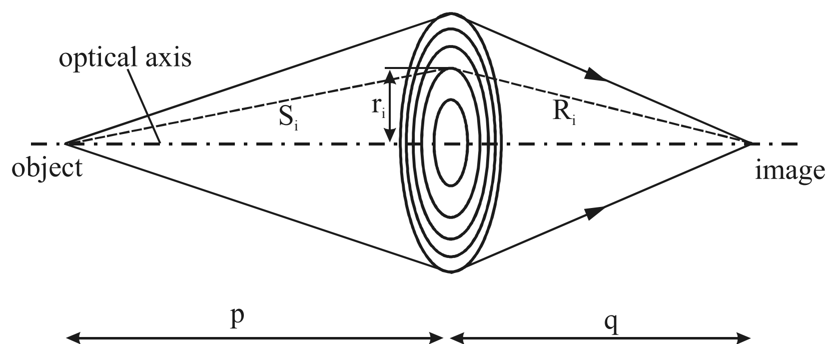

Figure 2.4: Image formation using a zone plate.

To obtain perfect focusing of a zone plate the contributions of all zones have to add up constructively in the focus or - in other words - have to be in phase with respect to each other. Constructive interference is achieved, whenever the difference in the optical path of individual contributions is an integer multiple of lambda. For the general case, where the perfect imaging of an object (with distance p to the diffraction lens) into an image (having the distance q to the lens) is required, the total light path for a certain zone is equal to (see Figure 2.4)

$$R_i + S_i = \sqrt{r_i^2 + p^2} + \sqrt{r_i^2 + q^2} \tag{2.35}$$

where r_i is the distance from the optical axis to the border of the individual zone. Normally one uses the first diffraction order, meaning that the difference in light path of two successive zones has to be one wavelength.

$$(R_{i+1} + S_{i+1}) - (R_i + S_i) = \lambda \tag{2.36}$$

For the nth zone radius r_n one finds

$$R_n + S_n = \sqrt{r_n^2 + p^2} + \sqrt{r_n^2 + q^2} = n\lambda + C \tag{2.37}$$

where C is a constant, which is determined by the radius r_0 of the first zone (equation (2.37) for the case of n=0). The radius r_0 can be chosen freely, provided that no smaller radius can be found, that fulfils equation (2.37). This requires that $(p+q) < (R_0+S_0) < (p+q+\lambda)$. Consequently equation (2.37) can be rewritten as

$$\sqrt{r_n^2 + p^2} + \sqrt{r_n^2 + q^2} = (n + \varphi)\lambda + (p + q) \tag{2.38}$$

where φ is a dimensionless parameter in the interval between 0 and 1 (again determined by r_0, using equation (2.38) for the case of n=0). As φ influences the length of the light path of all contributions it also influences their (absolute) phase. Changing φ from zero to one corresponds to a phase shift of 0 to 2π, and φ is therefore called the phase factor of a zone plate. Rearranging equation (2.38) one obtains a formula for the nth zone radius of a zone plate.

$$r_n^2 = \frac{2\tilde{n}\lambda(p+q)pq + (\tilde{n}\lambda)^2([p+q]^2 + pq) + (\tilde{n}\lambda)^3(p+q) + (\tilde{n}\lambda)^4}{(p + q + \tilde{n}\lambda)^2} \tag{2.39}$$

with

$$\tilde{n} = (n + \varphi) \qquad n = 0, 1, 2, 3 \ldots\ldots N$$

For zone plates in the x-ray range the term $\tilde{n}\lambda$ is always much smaller than the object and image distances p and q. In first approximation equation (2.39) can then be rewritten as

$$r_n^2 = 2(n + \varphi)\lambda f + (n + \varphi)^2 \lambda^2 \tag{2.40}$$

where the focal length f is defined according to the relationship for thin lenses between the focal length f, the object distance p and the image distance q:

$$1/f = 1/p + 1/q \qquad (2.41)$$

The approximate equation (2.40) is exact for the case of an indefinitely large object or image distance. For arbitrary values of p and q, it depends on the wavelength λ and the zone number n, whether equation (2.40) is a good approximation of (2.39) or not. According to Rayleigh's quarter wavelength rule [44, page 528] a phase-mismatch of π/2 of contributions from different parts of a zone plate is tolerable, without getting a significant deterioration of the imaging quality of the lens. If the n+1th zone radius of a distorted zone plate (using the design rule (2.40)) becomes equal to the nth zone radius of a perfect zone plate (using design rule (2.39)) this correspond to a phase mismatch of 2π. Consequently, applying Rayleigh's quarter wavelength rule and using equation (2.39) and (2.40) the difference of the nth zone radii should be less than a quarter of the width of this zone. The largest difference occurs at the edge of the zone plate (n=N). Therefore, applying Rayleigh's quarter wavelength rule for this case, one can show that $N < \sqrt{(p+q)/\lambda}$ has to be fulfilled, in order to get (approximate) equivalence of the two design rules (2.39) and (2.40). In fact, in most practical cases equation (2.40) can be even further simplified. Provided that $N < \sqrt{f/\lambda}$ the second term is negligible small and we get

$$r_n^2 = 2(n+\varphi)\lambda f \qquad (2.42)$$

Taking typical values for lenses in the hard x-ray range (f=1m, λ=0.1nm) leads to $N<10^5$ as a condition for the validity of equation (2.42). The number of zones N is typically of the order of 100-1000, and therefore this condition is almost always fulfilled. However, in other cases (soft x-ray region, extremely large zone plates) one should be aware of the possibility, that it can be necessary to use the more stringent design rule (2.40) or even the exact design rule given by equation (2.39) in order to get perfect imaging properties of a zone plate.

Equation (2.42) implies a few interesting and important properties of diffractive lenses. It is easy to show that one zone plate can be used for several wavelengths. If λ_0 is the design wavelength of the zone plate, the same zone plate will focus a wavelength λ' in a distance $f' = f_0 \lambda_0 / \lambda'$, where f_0 is the focal length for the design wavelength.

$$r_n^2 = 2(n+\varphi)\lambda_0 f_0 = 2(n+\varphi)\lambda'[f_0\lambda_0/\lambda'] = 2(n+\varphi)\lambda' f' \qquad (2.43)$$

$$f' = (f_0\lambda_0)/\lambda' \qquad (2.44)$$

In other words, the focal length of a zone plate is inverse proportional to the wavelength of the focused light. Consequently, the focal length changes strongly with wavelength, making zone plates highly chromatic focusing devices. It can be shown ([50], basically using Rayleigh's quarter wavelength rule again) that the spectral bandwidth Δλ/λ has to be smaller than 1/(2N) in order to make chromatic lens aberrations negligible.

Equation (2.42) is also a useful starting point to deduce several (approximate) but very useful relationships between fundamental design parameters of zone plates. Applying equation (2.42) for the Nth and N-1th zone we obtain

$$r_N^{\,2} - r_{N-1}^{\,2} = (r_N + r_{N-1})(r_N - r_{N-1}) = 2\lambda f$$

and using $(r_N + r_{N-1}) \cong D$ and $(r_N - r_{N-1}) = b_{\min}$ leads to

$$D/(2f) \cong \lambda / b_{\min} \qquad (2.45)$$

where D is the lens diameter and b_{min} the minimal grating period at the edge of the zone plate. At the same time, using equations (2.42) and (2.45) we find

$$r_N^{\,2} = (D/2)^2 \cong 2N\lambda f = 2N(b_{\min} D/2)$$

and consequently

$$N \cong 1/4\,(D/b_{\min}) \qquad (2.46)$$

Finally, one can also deduce relationships for the focusing of higher diffraction orders, taking into account that using a higher order m is mathematically equivalent to using a m-times larger wavelength in the first order.

$$r_n^{\,2} = 2(n+\varphi)m\lambda(f/m) = 2(n+\varphi)m\lambda\, f_m \qquad (2.47)$$

with

$$f_m = f_1 / m \qquad (2.48)$$

This means that for a certain zone plate (described by the radii r_n) the mth order will be focused in a distance f_l/m, where f_l is the focal length of the first order diffraction. This also applies for negative diffraction orders and consequently a zone plate acts as a converging and a diverging lens at the same time, having a set of focal points at the distances $\pm$ f_l, $\pm$ $f_l/2$, $\pm$ $f_l/3$, …$\pm$ f_m/m from the lens.

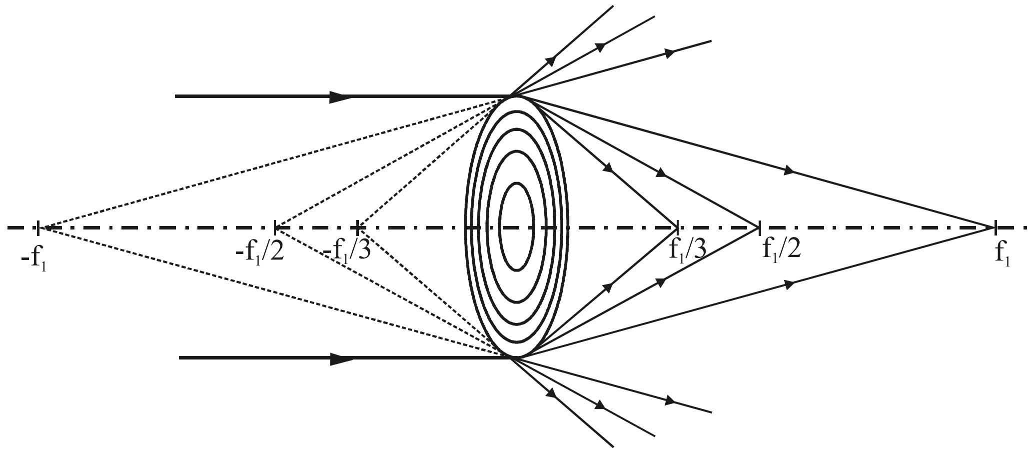

Figure 2.5: Schematic sketch of the different foci of a zone plate at the positions $\pm$ f_l, $\pm$ $f_l/2$, $\pm$ $f_l/3$, originating from the different diffraction orders of the local grating structures.

For each region within the zone plate a certain fraction η_m of the incoming photons is diffracted into the focus of the mth diffraction order. By definition this fraction is equal to the mth order diffraction efficiency η_m of the local grating structure. The fraction of incoming light ending up in a certain focus is therefore given by the diffraction efficiency of the corresponding diffraction order. In most practical cases the efficiency of the desired order (e.g. the first one) is relatively small and consequently the other orders can severely decrease the image quality. However, the clear spatial separation of individual orders makes it relatively easy to filter them out by means of apertures.

It should be noted that the arguments leading to the design rule (2.39) (and all formulas following from that) are not restricted to round zone plates. They as well apply for linear zone plates (see Figure 2.3), provided that the radius r_n denotes the distance of the nth (linear) zone from the center of the zone plate.

2.2.2 Resolution of a zone plate

If a lens is used to image a point source of x-rays (see Figure 2.6) there is a fundamental limit of the minimal width of the resulting spot one can achieve. This limit applies for any type of lens - including zone plates - and is found to result from diffraction of the incoming beam at the lens aperture.

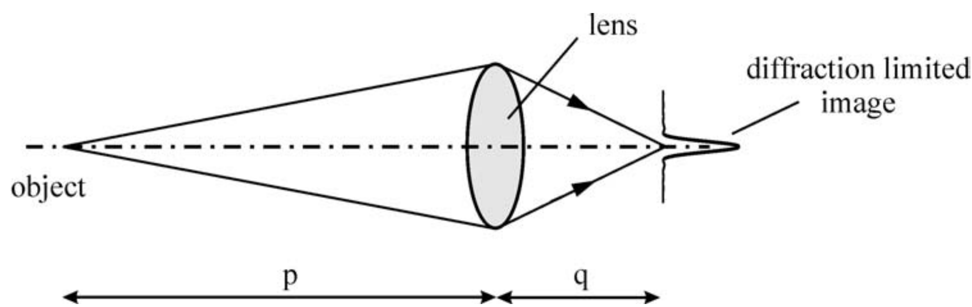

Figure 2.6: Schematic sketch of a lens, which is used to image an object (e.g. an x-ray source) into an image point. Even for an infinitely small size of the object and an aberration free lens the corresponding image point has finite width, due to diffraction at the edges of the lens. Consequently the minimal obtainable width of the image is limited by diffraction at the lens aperture.

One possibility to qualitatively understand this behaviour is to separate the influence of the lens aperture - leading to diffraction - and the influence of the lens itself - leading to a focusing of the radiation. Following this approach one can consider a lens to consist of an aperture, which is placed in front of an idealized lens, whereas the lens has no borders at all, so that all the light exiting the aperture is focused into the image plane. Without any lens a characteristic diffraction pattern of this aperture would be observed in a sufficiently large distance from the aperture. However, due to the focusing achieved by the lens this pattern is “imaged” into the image plane. The image of an indefinitely small x-ray source will therefore always have a finite width, determined by size of this diffraction pattern image.

For a rigorous, quantitative calculation of the intensity-distribution within the spot it is necessary to evaluate the so-called Fresnel-Kirchoff Integral [51, page 342], which takes into account the phase and the amplitude of the contributions stemming from different parts of the lens, making it possible to calculate the electrical field E_p at a certain point P of the image plane (see Figure 2.7).

In the x-ray range the deflection angles are always very small. Also the distance R from different contributing parts of a lens varies only very little, so that only the phase but not the amplitude of the individual contributions depends on R. The electrical field E_p is therefore (to a good approximation) determined by

$$E_p(x_2, y_2) = C_1 \iint dx_1 dy_1 \; E_1(x_1, y_1) \exp[-i\,(2\pi/\lambda)\,R] \qquad (2.49)$$

where E_1 is the electrical field just behind the lens, and C_1 a constant, that can be determined using the law of energy conservation (the photon flux behind the lens has to be equal to the photon flux in the image plane). The field E_1 is related to the field E_i of the incoming wave (in front of the lens) via

$$E_1(x_1, y_1) = \tau(x_1, y_1) \;\; E_i(x_1, y_1) \qquad (2.50)$$

where τ is the transmission function, describing the attenuation as well as the phase shift caused by the lens.

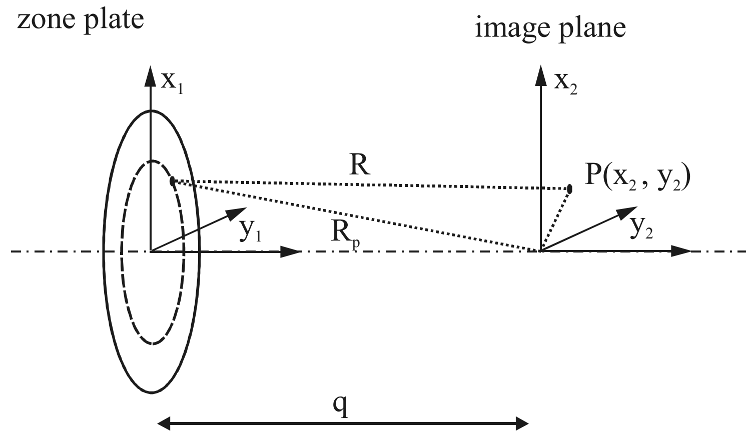

Figure 2.7: Scheme for calculating the intensity distribution of a zone plate in the focal region.

For a perfect, aberration free lens the contributions from different parts of the lens are in phase in the focal point. Therefore one has

$$E_1(x_1, y_1) \exp\left[-i \frac{2\pi}{\lambda} \mathrm{R_p}\right] = |E_1(x_1, y_1)|\, e^{-i\varphi_c}$$

where φ_c is a constant, which is identical for all positions (x_1, y_1) on the lens. Therefore (omitting unimportant phase factors) equation (2.49) can be rewritten as

$$E_p(x_2, y_2) = C_1 \iint dx_1 dy_1 \;\; |E_1(x_1, y_1)| \exp\left[i \frac{2\pi}{\lambda} (\mathrm{R_p} - \mathrm{R})\right] \qquad (2.51)$$

Assuming homogenous illumination of the lens ($|E_i|$=constant) and negligible losses of the x-rays within the lens ($|E_i|=|E_1|$; $|\tau|=1$) we obtain

$$E_p(x_2, y_2) = C_1 \, |E_i| \iint dx_1 dy_1 \ \exp\left[i \frac{2\pi}{\lambda} (\mathrm{R_p} - \mathrm{R}) \right]$$

In x-ray optics, the image distance q is always much larger than the integration and observation coordinates x_1, y_1, x_2, and y_2, making it useful to expand the radii R_p and R in a power series of the normalized coordinates x_1/q, y_1/q, x_2/q and y_2/q. Omitting all terms expect the quadratic ones (parabolic approximation, [51, page 412]) one finally gets

$$E_p = C_1 \, |E_i| \iint dx_1 dy_1 \ \exp\left[i \frac{2\pi}{\lambda} \left(\frac{x_2^{\,2} + y_2^{\,2}}{2q} - \frac{x_1 x_2 + y_1 y_2}{q} \right) \right] \qquad (2.52)$$

The integral in equation (2.52) is evaluated across the whole area of the lens. Consequently the electrical field E_p - and therefore the intensity distribution - in the image plane depends on the size and the shape of the lens aperture.

So far nothing has been assumed about the functionality or the internal structure of the lens. In principle equation (2.52) describes the focal spot of any type of lens, provided that the diameter of the lens is significantly smaller than the image distance q. However, a few assumptions, which have been made for the derivation of equation (2.52), are not necessarily true for zone plates.

First of all it was assumed that the contributions of all parts of the lens are exactly in phase in the center of the focal spot. For a zone plate the net contributions stemming from an entire zone are in phase in the focus. But in general the contributions from different parts within one zone are not in phase.

One can assume that for a sufficiently large number of zones this difference between a sum - adding up the net contributions from individual zones - and a continuous integral over the entire zone plate will become negligible. But one cannot suspect that a zone plate with only a few zones has the same properties as a conventional lens. In fact several studies show ([52], [53], [54], [55]), that the observed size and shape of the focal spot of a zone plate does not significantly differ from the one described by equation (2.52), if the number of zones is larger than about 20.

Another important property of zone plates not taken into account by equation (2.52), is the fact, that normally only a certain fraction of the incoming light is diffracted into the focus. If the diffraction efficiency η of the local grating structures is constant within the entire lens, the shape of the focal spot is identical to the spot of a lens with 100% diffraction efficiency. Solely the intensity will be decreased by a factor η compared to the lens with 100% efficiency.

However, for most zone plates the assumption of constant diffraction efficiency over the whole area of the lens is a bad approximation. Due to limitations of the fabrication process the diffraction efficiency at the edges (for small grating periods) is normally much worse than in the middle. Qualitatively this leads to a decrease of the effective diameter of the zone plate and therefore to enhanced diffraction at the corresponding effective aperture. In consequence the diffraction limited spot size of such a zone plate will be significantly larger than a zone plate with constant efficiency. At the same time the shape of the spot will be somewhat different.

Finally one should mention, that equation (2.52) only applies for an aberration-free lens. If a zone plate is distorted - e.g. due to an imperfect fabrication process - the contributions from different parts of the lens are not exactly in phase in the center of the focus. This will lead to some kind of distortion and a broadening of the diffraction limited focal spot. In case of a round zone plate one could think of having elliptical zones instead of round zones, for example due to stress within the sample. Another realistic possibility is, that due to drift during an e-beam lithography process, each zone is slightly shifted with respect to its neighbouring zones. It is found generally [56], that the aberrations resulting from distortions of a zone plate are negligible, if the deviations from the ideal zone position are smaller than about half of the minimal zone width of the zone plate. Taking into account these restrictions equation (2.52) can be used to calculate the diffraction limited spot in the focus of a zone plate.

For most applications in the x-ray range round zone plates are used. The last outermost zone of a zone plate typically defines the lens aperture. In consequence one has a round aperture of diameter D and the integration in equation (2.52) yields (see e.g. [51, page 360])

$$E_p = C_1 \left(|E_i| \; \pi D^2 / 2 \right) \; \exp\left(i \frac{2\pi}{\lambda} \tilde{r}_2^{\,2} / q \right) J_1(\tilde{r}_2) / \tilde{r}_2 \qquad (2.53)$$

with

$$\tilde{r}_2 = \pi r_2 D / \lambda q \qquad r_2 = \sqrt{x_2^{\,2} + y_2^{\,2}}$$

Taking into account that only a fraction η of the light is diffracted into the focal spot, the intensity distribution I_p is found to be

$$I_p = C_2 (\pi / 2)^2 \; \eta D^4 \; J_1^{\,2}(\tilde{r}_2) / \tilde{r}_2^{\,2} \qquad (2.54)$$

where C_2 is a constant and J_1 a Bessel function of first order.

It will be shown later on that using two crossed linear zone plates as a focusing device one automatically gets rectangular apertures. The effective aperture of such a device is a square with side length D_s. In this case the integration in equation (2.52) yields sinc-functions in both directions (x_2 and y_2) leading to

$$I_p = 4 \, C_2 \; \eta_m D_s^{\,4} \; (\sin(\tilde{x}_2) / \tilde{x}_2)^2 \; (\sin(\tilde{y}_2) / \tilde{y}_2)^2 \qquad (2.55)$$

with

$$\tilde{x}_2 = \pi x_2 D_s / \lambda q \qquad \tilde{y}_2 = \pi y_2 D_s / \lambda q$$

One important application of zone plates - and lenses in common - is to image an object of interest onto a detector plane. A simple model of such an object consists of two point sources, which are placed in the object plane and have a certain distance d with respect to each other. For an aberration-free zone plate both of these sources will produce a diffraction-limited spot in the image plane. For very small distances d the two spots will overlap, making it at some point impossible to distinguish, whether the image is produced by only one or two point

sources. In consequence the diffraction limited spot size determines the resolution of the zone plate.

For the exact calculation of the intensity distribution stemming from two closely placed point sources one has to take into account, whether these sources are mutually coherent or not. For completely incoherent sources the total intensity is simply the sum of the two individual spot intensities. In case of completely coherent sources the two wave-fields in the image plane stemming from the two sources have to be added up in phase. The total intensity is then determined by the sum of these two fields and not - like for incoherent sources - by the sum of two intensities. For strongly overlapping spots this can result in a large difference of the resulting intensity distributions. However if the overlap is small, the resulting total intensity is nearly independent of the coherence relationship between the objects. In consequence the resolution capability of a zone plate should not strongly depend on the coherence relation between the x-rays stemming from individual parts of the imaged object.

One commonly used criterion to characterize the resolution of a zone plate (and a lens in general) assumes the case of two completely incoherent point sources. According to the Rayleigh criterion the two images of the point-objects can still be resolved if the first minimum of one image coincides with the maximum of the other image. The first minimum of the Bessel function is at $\tilde{r}_2 = 3.83171$. According to the Rayleigh criterion the resolution Δr_{res} of a round zone plate is given by

$$\tilde{r}_{2,res} = \pi \Delta r_{res} D / \lambda q = 3.83171$$

and consequently

$$\Delta r_{res} = 1.22\, \lambda\ q / D \qquad (2.56)$$

For most practical cases one has $q \cong f$ and therefore, using equation (2.45) and the standard definition of the numerical aperture NA of a lens (assuming a thin lens in air or vacuum) we obtain

$$\Delta r_{res} = 0.61\ \frac{2\lambda q}{D} = 0.61 \frac{\lambda}{NA} = 0.61\, b_{\min} \qquad (2.57)$$

This means that the resolution of a diffractive lens is solely determined by the minimal grating period b_{min} at the edge of the lens. Note, that equation (2.57) applies for the case that the first diffraction order is used ($q \cong f_1$). For the general case ($q \cong f_m$, m^{th} diffraction order) the width of the diffraction limited spot (and therefore the resolution limit) is m times smaller.

Applying Rayleigh's criterion to a lens with a square aperture (where the first minimum in x-direction and y-direction is at $\tilde{x}_2 = \pi$ and $\tilde{y}_2 = \pi$) yields

$$\tilde{x}_{2,res} = \pi \Delta x_{res} D / \lambda q = \pi \qquad \tilde{y}_{2,res} = \pi \Delta y_{res} D / \lambda q = \pi$$

leading to

$$\Delta x_{res} = \Delta y_{res} = \frac{\lambda q}{D_s} = 0.5 \frac{\lambda}{NA} = 0.5\, b_{\min} \qquad (2.58)$$

Again the resolution (measured in x- or y-direction) is determined by the minimal grating period at the edges (in x- and y-direction) of the lens.

In conclusion one finds that in both cases, the resolution limit is about half the minimal grating period b_{min}.

Another common parameter characterising the focusing properties of zone plates is the width w_{FWHM} (the full width half maximum-value) of the diffraction limited focal spot. For round apertures the intensity drops to half of the maximum value at the position

$$\tilde{r}_{2,FWHM} = \pi \frac{w_{r,FWHM}}{2} D / \lambda q = 1.615$$

and therefore we find

$$w_{r,FWHM} = 0.51 \frac{2\lambda q}{D} = 0.51 \frac{\lambda}{NA} = 0.51\, b_{\min} \qquad (2.59)$$

For lenses with square apertures the situation is more complicated, as the spot doesn't have rotational symmetry. However, it turns out, that near the center of the spot (in regions of significant intensity) one has almost rotational symmetry. Consequently the FWHM-width varies only very little with direction (about 2% variation). In good approximation the width $w_{s,FWHM}$ can therefore be assumed to be constant leading to

$$\tilde{x}_{2,FWHM} \cong \pi\, w_{s,FWHM} D / \lambda q = 1.403$$

and

$$w_{s,FWHM} = 0.89 \frac{\lambda q}{D_s} = 0.45 \frac{\lambda}{NA} = 0.45\, b_{\min} \qquad (2.60)$$

In conclusion one finds, that for both types of apertures the width of the diffraction limited spot is nearly equal to the resolution limit and given by about half the minimal grating period b_{min}.

2.2.3 Depth of focus

According to the considerations in the last chapter it is possible to obtain a minimal, diffraction-limited spot at a certain image distance q from a lens. For practical applications it is therefore essential to know how exact one has to match this optimal distance q without getting a significant broadening of the spot or in other words how far an object can be outside the image plane without getting a significant decrease in resolution. This so called depth of focus d_{focus} can be easily estimated using geometrical optics. Moving a distance Δz out of the image plane this will (geometrically) increase the width of the focal spot by the order of $\Delta z \times NA$. The resulting broadening should be smaller than the diffraction limited width of the focal spot, leading to

$$\Delta z \times NA \leq w_{FWHM} \quad \text{with} \quad w_{FWHM} \cong 0.5 \frac{\lambda}{NA}$$

Consequently, assuming that the maximal tolerable distance is equal to the depth of focus one obtains

$$d_{focus} = \pm \frac{1}{2} \frac{\lambda}{NA^2} \tag{2.61}$$

2.2.4 Efficiency and design of binary zone plates

In chapter 2.2.1 it was shown, that a zone plate can be understood as a grating with variable grating constant. It was also shown that the mth diffraction order is focused in a distance f_1/m, where f_1 is the focal length of the first order diffraction. Consequently, a zone plate has a set of focal points at the distances $\pm f_1$, $\pm f_1/2$, $\pm f_1/3$, … $\pm f_m/m$ from the lens (see Figure 2.5). The considerations up to now did not require any knowledge of the local grating structures employed for the zone plate. However, the shape of the grating structures plays an essential role for the performance of a zone plate, as it determines the amount of light that is diffracted into one of these focal points, and therefore the efficiency of a zone plate. In general, the fraction of the incoming photons, which is found in the focus of the mth order is given by the mth order diffraction efficiency η_m of the local grating structure.

In most practical applications of zone plates one uses the focus that corresponds to the first diffraction order. In this case the efficiency of a zone plate is determined by the first order diffraction efficiency η_1 of the local grating structures. In chapter 2.2.6 it will be shown that the efficiency η_1 of a linear grating is given by

$$\eta_1 = |\Phi_1|^2 \tag{2.62}$$

with

$$\Phi_1 = 1/b \int_0^b dx \exp[-2\pi\, h(x)\beta / \lambda] \exp[-2\pi i\, (h(x)\delta / \lambda - x/b)]$$

where b is the grating period and h(x) the grating height at different positions of the grating. For a given shape h(x) of the diffracting structures equation (2.62) can then be used to calculate the efficiency of a zone plate.

Most of the zone plates used for practical applications in the x-ray range are binary zone plates (see Figure 2.8 A), employing a grating structure with only two different height levels. This is due to practical reasons as binary grating structures are comparatively easy to fabricate by means of standard micro-structuring techniques. Using equation (2.62) we obtain

$$\eta_1 = \frac{\sin(\pi\, b_1 / b)}{\pi^2} \left(1 + \exp\left[\frac{-4\pi\, h_1 \beta}{\lambda}\right] - 2 \exp\left[\frac{-2\pi\, h_1 \beta}{\lambda}\right] \cos[\frac{2\pi\, h_1 \delta}{\lambda}] \right) \tag{2.63}$$

where h_1 denotes the height of the binary grating and b_1 the width of the region with non-zero height. Analysing equation (2.63) one finds that one requirement for maximum efficiency of such a binary grating is to have equal widths of the two regions with different height,

meaning that $b_l = b/2$. The ratio b_l/b is commonly referred to as the duty cycle of a binary grating. Consequently a duty cycle of 0.5 is required for maximal efficiency.

The materials used for the binary grating structures are often strongly absorbing so that the light is nearly blocked out in one half of the grating period. For this case of strong absorption (β large) the exponents in equation (2.63) become very large, so that the efficiency is approximately given by $\eta_1 \cong 1/\pi^2 \cong 10.1\%$ (assuming an ideal duty cycle of 0.5). Binary zone plates are referred to as amplitude zone plates if due to absorption most of the light is blocked in one half of the grating structure. The result from above shows that such an amplitude zone plate has an efficiency of only about 10.1%.

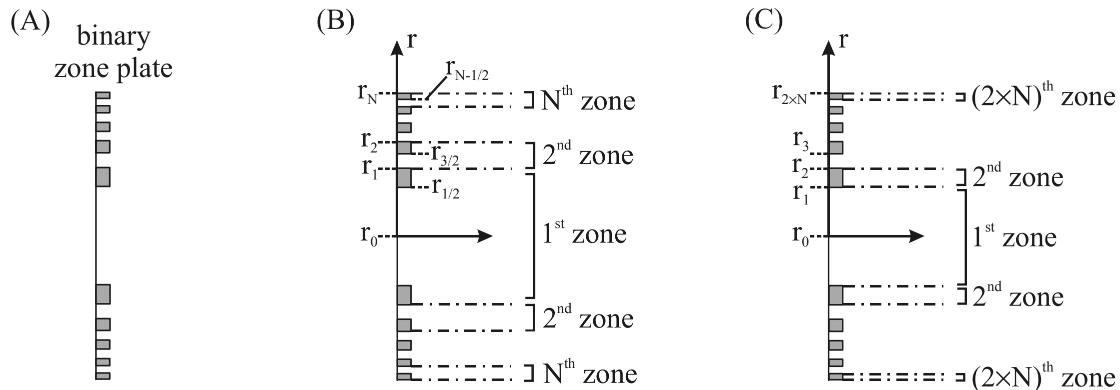

Figure 2.8: (A) Schematic sketch of a binary zone plate utilizing a grating with two different height levels. Figure (B) illustrates the nomenclature used within this work to describe the design of a binary zone plate. According to this nomenclature each period of the binary grating is referred to as one zone of the zone plate. All zones are enumerated with integer numbers n starting from the center of the lens. The boundaries of the nth zone are described by the parameters r_{n-1} and r_n. Each zone consists of two regions of different height and the boundary between these two regions is described by $r_{n-1/2}$. Figure (C) shows an alternative nomenclature, which is often used in the literature. According to this convention each region of different height is referred to as one zone of the zone plate. Again the zones are enumerated with integer numbers l and the zone boundaries are then given by r_{l-1} and r_l.

Using grating material with small absorption it is possible to achieve a significantly higher diffraction efficiency for a binary zone plate. For negligible absorption the two exponents in equation (2.63) are almost equal to zero so that basically only the cosine-term determines the efficiency. One finds that a maximal efficiency of 40.5% can be achieved, provided that the grating has a duty cycle of 0.5 and that the height h_l of the grating is chosen as $h_l = \lambda/(2\delta)$. This means that the grating structure has to introduce a phase shift of π compared to regions with zero structure height in order to yield maximum efficiency. For electromagnetic radiation in the x-ray range it is difficult it to find grating materials with negligible absorption. In praxis one speaks of a phase zone plate if in comparison to an amplitude zone plate the efficiency is significantly increased due to the phase shift introduced by the grating material.

The positions of the boundaries between the zones of a zone plate are determined by the fact that the contributions from all zones have to add up constructively in the focus. For a binary zone plate each period of the grating structure - and therefore each zone of the zone plate - consists of two sectors of different height. In principle the position of the boundary between these two sectors can be chosen freely. However, it was already discussed above, that in order to maximize the first order diffraction efficiency of a binary grating the boundary has to be in

the middle of the grating period. This corresponds to the condition, that the difference in light path between the boundary of a zone and the boundary in the middle of the zone has to be equal to half the wavelength λ. Generalizing this design rule to the positions r_n of all edges within the zone plate leads to (in analogy to the derivation of the zone plate construction rule (2.39), see chapter 2.2.1)

$$r_n^2 = \frac{2\tilde{n}\lambda(p+q)pq + (\tilde{n}\lambda)^2([p+q]^2 + pq) + (\tilde{n}\lambda)^3(p+q) + (\tilde{n}\lambda)^4}{(p+q+\tilde{n}\lambda)^2} \qquad (2.64)$$

with

$$\tilde{n} = (n+\varphi) \qquad n = j + k/2; \quad j = 0,1,2,3......N; \quad k = 0,1;$$

where N is the number of grating periods (zones) and φ the phase factor as defined in chapter 2.2.1. For integer values of n the positions r_n are identical to the positions given by the zone plate construction rule (2.39). This means that for k=0 equation (2.64) yields the borders of individual zones of the lens. For half integer values of n, i. e. for k=1, r_n gives the position of the boundary in the center of a zone (see also Figure 2.8 B). Within this work one period of the diffracting structures of a zone plate is referred to as one zone of the zone plate. However, for a binary zone plate one can think of another definition, calling each sector of different height a "zone" (see Figure 2.8 C). In this case it makes sense to numerate the boundaries of these "zones" with integer numbers l, whereas l is running from 0 to 2×N. The two different indices n and l are then simply related via l=2×n.

For most practical cases one can use approximate formulas - analogous to equations (2.40) and (2.42) - to calculate the position of the zone boundaries. The same approximations hold true for the boundaries in the center of a zone, leading to

$$r_n^2 \cong 2(n+\varphi)\lambda f + (n+\varphi)^2\lambda^2$$

and

$$r_n^2 \cong 2(n+\varphi)\lambda f$$

Considering the special case φ=0 and using the index l instead of n this leads to

$$r_l^2 \cong l\lambda f + (l\lambda)^2/4 \qquad (2.65)$$

and

$$r_l^2 \cong l\lambda f \qquad (2.66)$$

Note that equations (2.65) or (2.66) represent the standard design rules for (binary) zone plates which are typically found in literature.

2.2.5 Multilevel zone plates

Using the first diffraction order of binary zone plates a maximal efficiency of 40.5% can be achieved. In order to overcome this limitation, different grating profiles have to be utilized for a zone plate. If for each zone of a lens the contributions from different parts of the zone add up in phase in the focal point it is possible - at least in theory - to diffract 100% of the incoming light into the focus. This can be achieved using a continuous profile as shown in Figure 2.9 A. Within each zone the distance to the focus increases gradually (for increasing distance to the zone plate center) and this increase in the length of the light path is exactly compensated by the phase shift of the continuous grating structure. Note that Figure 2.9 A shows the typical case in x-ray optics, where the optical path length in material is smaller than in vacuum (refractive index smaller than unity). Consequently, the height of the grating structure has to be increased in order to compensate for a longer distance to the focus (and therefore a longer light path).

However, in praxis it is difficult to fabricate such a continuous profile with the required accuracy and one therefore often relies on an approximation of this ideal profile, using a multilevel profile as shown in Figure 2.9 B. Such multilevel gratings are the generalised case of a binary grating, having L regions with different height (e.g. L=4, in Figure 2.9 B), instead of only two for a binary grating.

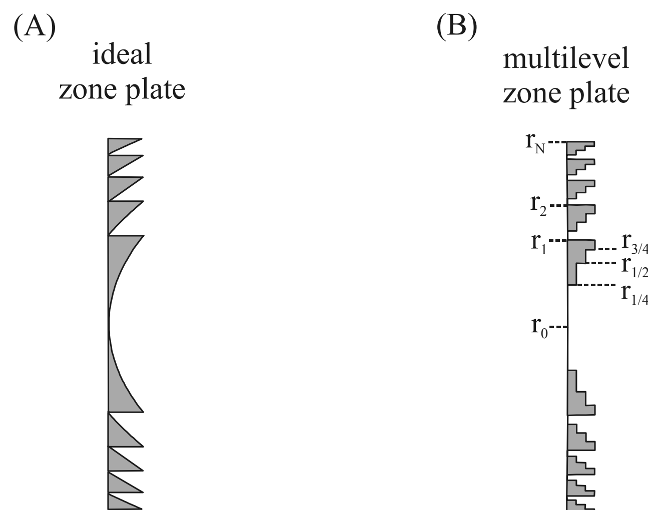

Figure 2.9: (A) Sketch of a zone plate utilizing a continuous grating profile, enabling diffraction efficiencies up to 100% in case of negligible material absorption. (B) Approximation of the ideal zone plate utilizing a multilevel grating profile. Figure B shows the special case of a multilevel zone plate having four different height levels of the grating structure. The boundaries r_n between regions of different height are labelled according to the convention used in equation (2.67).

It will be shown in the next chapter, that for a multilevel grating (provided that light absorption is negligible) the L sections of different height must have equal width in order to maximize the first order diffraction efficiency. Analogous to binary gratings this corresponds to the more general condition, that for two successive boundaries (of sections with different height) the difference in optical path has to be equal to λ/L. This leads to the general design rule for a multilevel zone plate with L levels:

$$r_n^{\,2} = \frac{2\tilde{n}\lambda(p+q)pq + (\tilde{n}\lambda)^2([p+q]^2 + pq) + (\tilde{n}\lambda)^3(p+q) + (\tilde{n}\lambda)^4}{(p+q+\tilde{n}\lambda)^2} \qquad (2.67)$$

with

$$\tilde{n} = (n+\varphi) \qquad n = j + k/L;\;\; j = 0,1,...N;\;\; k = 0,1,...(L-1)$$

For integer values of n equation (2.67) is identical to the zone plate construction rule (2.39) and yields the position of the borders of individual zones. Fractional values of n correspond to the boundaries within the zones, which separate two neighbouring sectors of different height (see also Figure 2.9 B).

2.2.6 Efficiency and optimisation of grating profiles

Obviously the task of diffracting as much light as possible in one single focal spot (corresponding to a certain diffraction order m) play an essential role for many practical applications. In consequence one has the problem of finding the optimum grating structure, maximizing the mth order diffraction efficiency. The procedures to determine this optimum strongly depend on the wavelength regime and on the design parameters of the zone plate one is looking at.

For diffractive optics in the visible light range the minimal grating period b_{min} is often of the same order of magnitude as the wavelength λ, resulting in relatively large diffraction angles. In this case the calculation of the diffraction efficiency for a certain grating requires the general solution of the Maxwell equations, taking into account the appropriate boundary conditions (see [57], chapter 2). Consequently, finding the optimum grating profile is a difficult task.

However, in the x-ray range the wavelength is always much smaller than the grating period, making it possible to use the thin element approximation [57]. Within this approximation the grating is treated as a thin element causing a certain phase shift and attenuation of the incoming wave according to the structure height $h(x_1,y_1)$ at a certain point of the zone plate. Assuming normal incidence (or small incidence angles) of the incoming wave, the relative phase shift φ (in comparison to a wave travelling in vacuum) is given by

$$\varphi(x_1,y_1) = 2\pi\,\delta\,h(x_1,y_1)/\lambda$$

and the attenuation A by (see equation (2.27))

$$A(x_1,y_1) = \exp(-2\pi\beta\,h(x_1,y_1)/\lambda)$$

The transmittance function $\tau(x_1,y_1)$, relating the electric wave field E_i of the incoming wave and the electrical field E_2 behind the diffracting structure (see equation (2.50)) is therefore given by

$$\tau(x_1,y_1) = A\,e^{-i\varphi} = \exp\left[-2\pi\beta\,\frac{h(x_1,y_1)}{\lambda}\right]\,\exp\left[2\pi i\,\delta\,\frac{h(x_1,y_1)}{\lambda}\right] \qquad (2.68)$$

As the values of δ and β are close to zero in the whole x-ray range, it is not necessary to consider reflections at the surfaces of the diffracting structures. One should also note, that

only photoelectric absorption (described by β) is taken into account by equation (2.68). However, it turns out, that in x-ray regions where absorption plays a role for the optimisation of grating profiles (when β is of the same order of magnitude or even larger than δ), photoelectric absorption is dominant and all other loss mechanisms (Compton scattering, coherent scattering) are negligible. In any case it would be easily possible to take into account other loss mechanisms (the overall absorption of x-rays described by the total absorption coefficient μ_{total}) using a modified factor β_{total} instead of β.

The thin element approximation involves the basic assumption, that a wave passing the diffracting structure is not deflected (diffracted) significantly within the structure. To quantify this condition one can consider two beams, travelling in the directions of two neighbouring diffraction orders (e.g. the 0th and 1st order), which coincide at the beginning of the diffraction grating. If the separation of the two beams after passing the grating (after a distance h_{max}, corresponding to the maximum height of the grating structure) is significantly less than the grating period b, one can expect that the thin element approximation will yield good results. This leads to the condition

$$h_{\max} \sin\theta_1 << b$$

and using equation (2.34)

$$h_{\max} << b^2 / \lambda \qquad (2.69)$$

Due to the small values of the wavelength in the x-ray range, condition (2.69) is almost always fulfilled. Only in special cases (soft x-rays in connection with extreme aspect ratios h_{max}/b of the grating structures) a more general theory, taking into account the coupling between waves of different orders (coupled wave theory), has to be used for the calculation of diffraction efficiencies [58, 59].

Applying the thin element approximation for a periodic structure (in x-direction) the electrical field E_1 behind the grating is linked to the field E_i of the incoming (plane) wave via

$$E_1 = E_i \exp\left[-2\pi\beta \frac{h(x)}{\lambda}\right] \exp\left[2\pi i\, \delta \frac{h(x)}{\lambda}\right] \qquad (2.70)$$

Assuming a grating with constant grating period b, the field E_1 will have the same periodicity and therefore can be expressed by means of a Fourier series

$$E_1 = \sum_m E_m \exp[2\pi i \text{ mx/b}] \qquad (2.71)$$

with

$$E_m = 1/b \int_0^b dx\, \mathrm{E}_1(x) \exp[-2\pi i \text{ mx/b}] \qquad (2.72)$$

Physically the factor E_m represents the complex amplitude of the mth-diffraction order (one can easily show that E_m is proportional to the electrical field of the mth order in the far field of a grating). Consequently, the mth order diffraction efficiency η_m is given by

$$\eta_m = |E_m|^2 / |E_i|^2 \qquad (2.73)$$

Using equations (2.70), (2.72) and (2.73) it is possible to calculate the diffraction efficiency of all diffraction orders for arbitrary shape of a grating (given by h(x)).

In principle this also makes it possible to find the optimum grating profile, maximising the amount of light diffracted into one single (e.g. the first) order.

Using normalized coordinates and grating parameters the diffraction efficiency η_1 of the first order is given by

$$\Phi_1 = E_1 / E_i = \int_0^1 d\underline{x} \exp[-2\pi \underline{h} / \kappa] \exp[-2\pi i (\underline{h} - \underline{x})] \qquad (2.74)$$

where

$$\eta_1 = |\Phi_1|^2 \qquad \kappa = \delta / \beta, \quad \underline{x} = x / b, \quad \underline{h} = h\delta / \lambda$$

If material absorption is negligible ($\delta >> \beta$, κ large) the first exponent in the integral of equation (2.74) is close to unity and only the phase shift caused by the grating structure (described by the second term) plays a role. In this case the absolute value of the integral and therefore also the efficiency will become a maximum, if the exponent in the second term is the same for all positions within a grating period. Physically this corresponds to the condition that the contributions from different parts of the grating are in phase with respect to each other. This leads to

$$-2\pi i (\underline{h} - \underline{x}) = \text{constant}$$

and consequently

$$h(x) = \lambda / \delta \ (x / b) \ + \text{constant} \qquad (2.75)$$

The common phase of all contributions and therefore the constant can be chosen freely, leading to different grating designs (e.g. different minimal heights at the position x=0; in fact one could add multiples of 2π to the constant for any subsection of the grating period leading to a whole set of designs). However, the simplest and typically used design has a minimal height of zero (constant=0) and a saw-tooth shape as shown in Figure 2.10.

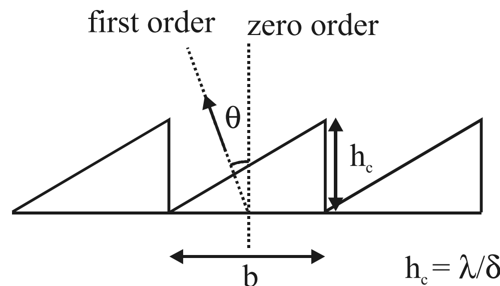

Figure 2.10: Grating design optimising the first order diffraction efficiency η_1 for negligible absorption of the grating material (η_1=100%)

For arbitrary values of δ and β it is difficult to find the optimum grating profile by use of equation (2.74). However, we could accomplish this by maximizing the 'projections' of the contributions from different parts of a grating. This 'projection method' makes use of the fact that changing the position of a grating with respect to the origin only changes the phase φ of the complex parameter Φ_1 in equation (2.74) but not its absolute value. Consequently, one may restrict the search for optimum solutions to grating profiles having amplitudes with a fixed phase φ_0.

Now, due to the restriction to a certain phase φ_0 one can take advantage of the fact, that maximising the amplitude of Φ_1 (and therefore η_1) is equivalent to maximising the projection $P[\varphi_0]$ of Φ_1 in the 'phase-direction' φ_0, if this projection is defined as

$$P[\varphi_0]\Phi_1 = |\Phi_1| \cos(\varphi_\phi - \varphi_0) \qquad (2.76)$$

where

$$\Phi_1 = |\Phi_1| \exp(\mathrm{i}\varphi_\phi)$$

The problem of maximising the diffraction efficiency is therefore reduced to the problem of maximising the projection $P\Phi_1$. The amplitude Φ_1 is given by (see equation (2.74))

$$\Phi_1 = \int_0^1 \Delta\Phi_1 \qquad (2.77)$$

with

$$\Delta\Phi_1 = \exp[-2\pi \underline{\mathrm{h}} / \kappa] \exp[-2\pi i\, (\underline{\mathrm{h}} - \underline{\mathrm{x}})]\, d\underline{x}$$

Maximising the projection of a sum is equivalent to maximising the projection of each summand within a sum

$$P\sum_j \Phi_j \rightarrow MAX \quad \Leftrightarrow \quad P\Phi_j \rightarrow MAX$$

and applying this rule to the integral (infinite sum) in equation (2.77) we obtain

$$P\Delta\Phi_1 \rightarrow MAX$$

leading to

$$\mathrm{P}\Delta\Phi_1 = \exp[-2\pi \underline{\mathrm{h}} / \kappa] \cos[-2\pi\, (\underline{\mathrm{h}} - \underline{\mathrm{x}}) - \varphi_0]\, \mathrm{d}\underline{\mathrm{x}} \rightarrow MAX \qquad (2.78)$$

This means that the contributions $\Delta\Phi_1$ stemming from different parts of the grating can be optimised independently (according to equation (2.78)), yielding the grating profile $h(\underline{x})$, that maximizes the first order diffraction efficiency of a grating for arbitrary values of δ and β. Physically meaningful gratings are restricted to structure heights $h(x) \geq 0$ (otherwise the first exponent in equation (2.78) is larger than unity meaning, that a wave is not attenuated but amplified when it passes the grating). The optimum height can then be found by differentiating (2.78). However, one has to keep in mind, that the border of the possible

solution interval (the position h=0) has to be considered separately. The optimum height h($\underline{x}$) is therefore given by

$$\partial/\partial\underline{h}\left(P\Delta\Phi_1(\underline{h})\right)=0 \qquad \text{or} \qquad \underline{h}(\underline{x})=0 \qquad (2.79)$$

depending on which of the two solutions for h($\underline{x}$) yields a larger projection $P\Delta\Phi_1$. For regions with non-zero height, differentiation of equation (2.78) yields

$$\tan\left[2\pi(\underline{h}-\underline{x})+\varphi_0\right]=-1/\kappa \qquad (2.80)$$

Consequently the argument of the tangent is a constant, leading to

$$\underline{h}(\underline{x})=\underline{x}-\varphi_0/2\pi-\underline{x}_1 \quad \text{with} \quad \tan(2\pi\underline{x}_1)=1/\kappa \qquad (2.81)$$

This means, that $\underline{h}$ is proportional to $\underline{x}$, resulting in a saw-tooth like shape in regions of non-zero structure height. If the free phase factor φ_0 is set zero, then $\underline{x}_1$ simply determines the position of one of the boundaries between regions with zero and non-zero height (as $\underline{h}(\underline{x}_1)=0$, see Figure 2.11 A).

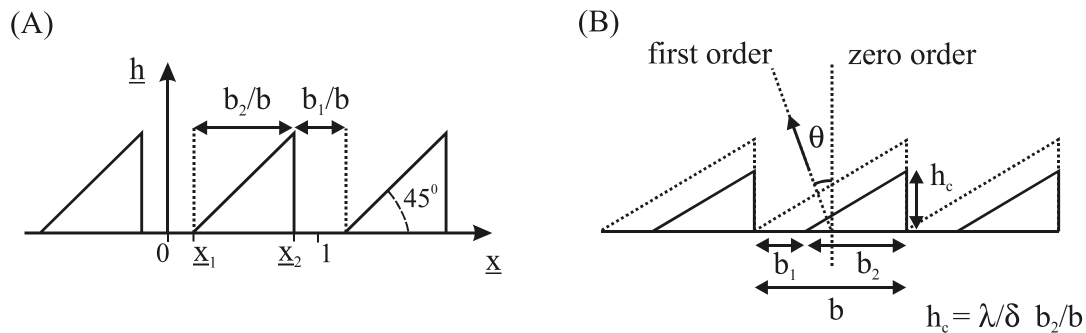

Figure 2.11: General design of a transmission grating maximising the first order diffraction efficiency in the case of absorbing grating material. (A) Using normalized coordinates (free phase factor φ_0 is set to zero). (B) Using practical coordinates and grating parameters; the dashed line shows the optimum grating profile in case of negligible absorption.

The position $\underline{x}_2$ of the second boundary can be found using the fact, that at this boundary the projections of the two different solutions for h(x) in equation (2.79) have to be equal. We get

$$\cos(2\pi\underline{x}_2)=\cos(2\pi\underline{x}_1)\exp\left[-2\pi/\kappa(\underline{x}_1-\underline{x}_2)\right] \qquad (2.82)$$

By evaluating ($\underline{x}_1$) and ($\underline{x}_2$) one can calculate the width b_1/b of the 'open' region of zero height of the optimum grating profile (see Figure 2.11 A and B). However, in praxis it is easier to vary the width and numerically determine the value of b_1/b, where the diffraction efficiency is a maximum. The results for different values of κ (δ/β), obtained with a simple Turbo Pascal program, are shown in Figure 2.12.

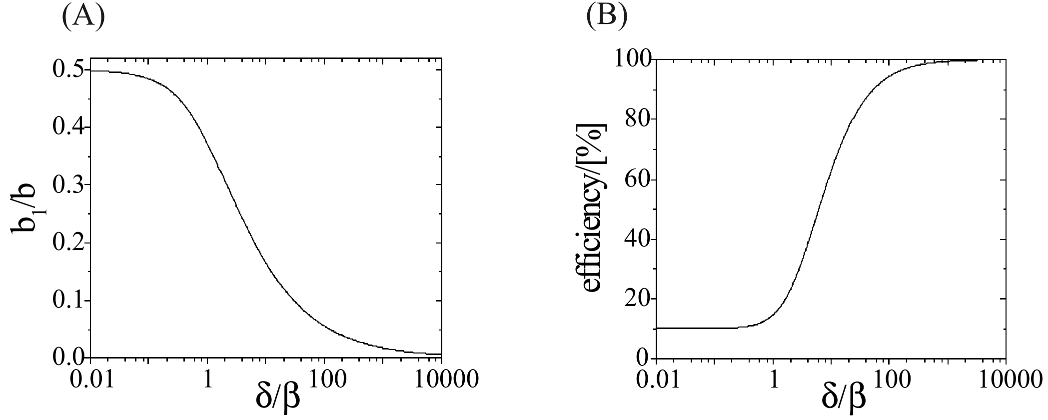

Figure 2.12: (A) Optimum value of the free design parameter b_l/b of the grating shown in Figure 2.11 in dependence of the optical properties of the grating material (described by δ/β). (B) Corresponding first order diffraction efficiency of the grating.

For low levels of absorption (δ/β large) the width b_l of the region with zero height in Figure 2.11 approaches zero, leading to the simple saw-tooth shaped design described in the beginning of this chapter, with diffraction efficiency close to 100% (see Figure 2.10). In case of strong material absorption (δ/β small) nearly one half of the grating period has zero structure height. Due the strong absorption the light is almost completely blocked in regions with non-zero height and consequently the diffraction efficiency is very close to that of an amplitude grating with duty-cycle of 0.5 (10,1%, see also chapter 2.2.4).

The results shown in Figure 2.12 (which are described by (2.80), (2.81) and (2.82)) are essentially the same as the ones reported by Tatchyn et al. [60]. Using a variational technique Tatchyn and his co-workers were able to find the optimum grating profiles for a whole set of optimisation conditions, one of them involving the problem described here (maximization of the mth order diffraction efficiency of a grating). Although their method is more generally applicable, the projection method described here has the advantage, that it is more easily implemented and used for certain problems. In particular it will be shown in the following, that the projection method makes it possible to find the optimum design of a multilevel grating maximising the first order diffraction efficiency.

In general it is difficult to fabricate continuous grating profiles with the required accuracy (e.g. the profile shown in Figure 2.12, maximising the first order diffraction efficiency). Consequently one often relies on an approximation using multilevel profiles (staircase profiles) as shown in Figure 2.13. One reason why most zone plates in the x-ray range are binary zone plates is the fact that grating structures with only two different height levels are comparatively easy to fabricate by means of standard lithography and micro-structuring techniques. The fabrication of multilevel grating structures with more than two height levels is more difficult, but can be achieved using several lithography steps, which are aligned with respect to each other (see e.g. [57] or also chapter 4 about the fabrication of multilevel silicon zone plates).

In the case of negligible absorption of the grating material the highest first order diffraction efficiency of a multilevel grating is obtained, when the L distinct steps of the staircase profile have equal width (w_j=w_k; j,k=1,..,L) and the heights h_j of the steps follow the ideal profile for zero absorption, leading therefore to h_j= [(j-1)/L] λ/δ (see Figure 2.13 A).

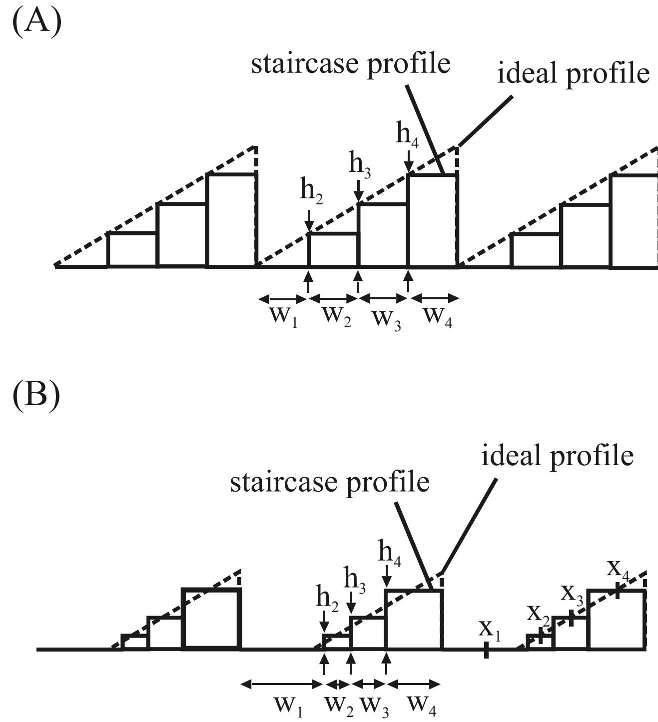

Figure 2.13: Staircase profiles (with L=4 distinct steps) giving maximum first order diffraction efficiency in case of negligible absorption (A) and in the general case of absorption (B).

However, in case of non-negligible absorption the design of a multilevel profile obviously has to be changed (e.g. using steps of different width, see Figure 2.13 B) in order to obtain a good approximation of the ideal profile - and therefore high efficiencies.

Applying equation (2.74) to a staircase profile with L steps, the first order diffraction efficiency η_1 is found to be

$$\eta_1 = \left| \sum_{j=1}^{L} \Phi_j \right|^2 \qquad (2.83)$$

where

$$\Phi_j = \exp\left[-2\pi \underline{h}_j \beta / \delta\right] \exp\left[-2\pi i(\underline{h}_j - \underline{x}_j)\right] \frac{\sin(\pi \underline{w}_j)}{\pi}$$

and the normalized heights ($\underline{h}_j$), widths ($\underline{w}_j$) and middle-positions ($\underline{x}_j$) of the steps are denoted as

$$\underline{h}_j = h_j \delta / \lambda \quad \underline{w}_j = w_j / b \quad \underline{x}_j = x_j / b$$

In order to find the optimum multilevel profile (the optimum heights and widths of the grating) one has to maximize the absolute value of the sum in equation (2.83). This makes the analytical treatment of the problem rather complex as the efficiency is determined by a complicated sum over functions of all staircase parameters.

In a first attempt [36] we therefore used a numerical approach applying a local search algorithm [61] in order to find the optimum values for the grating parameters with respect to diffraction efficiency.

The principle of the algorithm is to make small random trial changes of the actual profile, where the change is only allowed to take place if the new profile (the new set of parameters $\underline{h}_j$ and $\underline{w}_j$) has a higher diffraction efficiency than the previous one. By repeating this step until a large number n_{trial} ($n_{trial} > 100$) of subsequent trial changes fails to improve the diffraction efficiency, an optimum set of values of $\underline{h}_i$ and $\underline{w}_i$ will be finally reached.

In general one would suspect that this type of algorithm is trapped in local maxima and as a consequence will never yield reasonable results for the design parameters of the grating. However, the numerical results show that the total number of maxima is rather small and therefore it is sufficient to repeat the whole algorithm a few (typically 20) times with different, randomly chosen starting parameters for the grating in order to obtain a parameter set, that can be regarded as the global optimum with respect to diffraction efficiency.

Only for very large numbers of steps ($L>20$) the algorithm described above runs into troubles. On the one hand the computational time to find one local maximum strongly increases with the number of steps. On the other hand also the number of local maxima increases. Consequently, at some point the calculations take very long (many hours or even days), especially if one wants to find solutions for many different values of δ/β. The problem can be (at least) partly solved by using non-random starting parameters (e.g. one can use a solution for one value of δ/β as a very good set of starting parameters to find the solution for another value of δ/β close to the original one). One can also benefit from using some analytically derived knowledge of the solution (e.g. it will be shown later on, that for all steps with non-zero height there is a linear dependence between the height $\underline{h}_j$ and the middle positions $\underline{x}_j$). In any case, very large numbers of steps are rather of theoretical than practical interest, as staircase profiles with more than 20 levels are difficult to fabricate and at the same time do not significantly improve the optical performance (e.g. one already gets - theoretically - $\eta_1=99.4\%$ for a 16-level grating profile).

Figure 2.14 shows numerical results using the local search algorithm for the case of a staircase profile with four levels. For low values of absorption (high values of δ/β) one obtains the staircase profile shown in Figure 2.13 A, having steps with equal width and normalized heights of 0, 1/4, 1/2 and 3/4. Going to higher values of absorption, the widths (as well as the heights) of the second and the third step decrease and finally approach zero. The width of the first and the fourth step both increase and for values δ/β near zero, they both approach a value equal to half of the grating period b. Therefore, in the limit of infinite absorption a conventional binary amplitude grating is obtained. These results for high values of absorption can be qualitatively understood by the fact that the staircase profile always has to provide an optimum approximation of the ideal profile in terms of diffraction efficiency. For the ideal grating in the case of strong absorption the main contributions to the diffraction efficiency come from regions of the grating with small height. Therefore, it is important to get a good approximation of the region with zero height (provided by the first step with $w_1 \approx b_1$) and a short region with small height at the beginning of the saw-tooth (provided by the second and third step, which therefore tend to have rather small widths and heights for the case of high absorption).

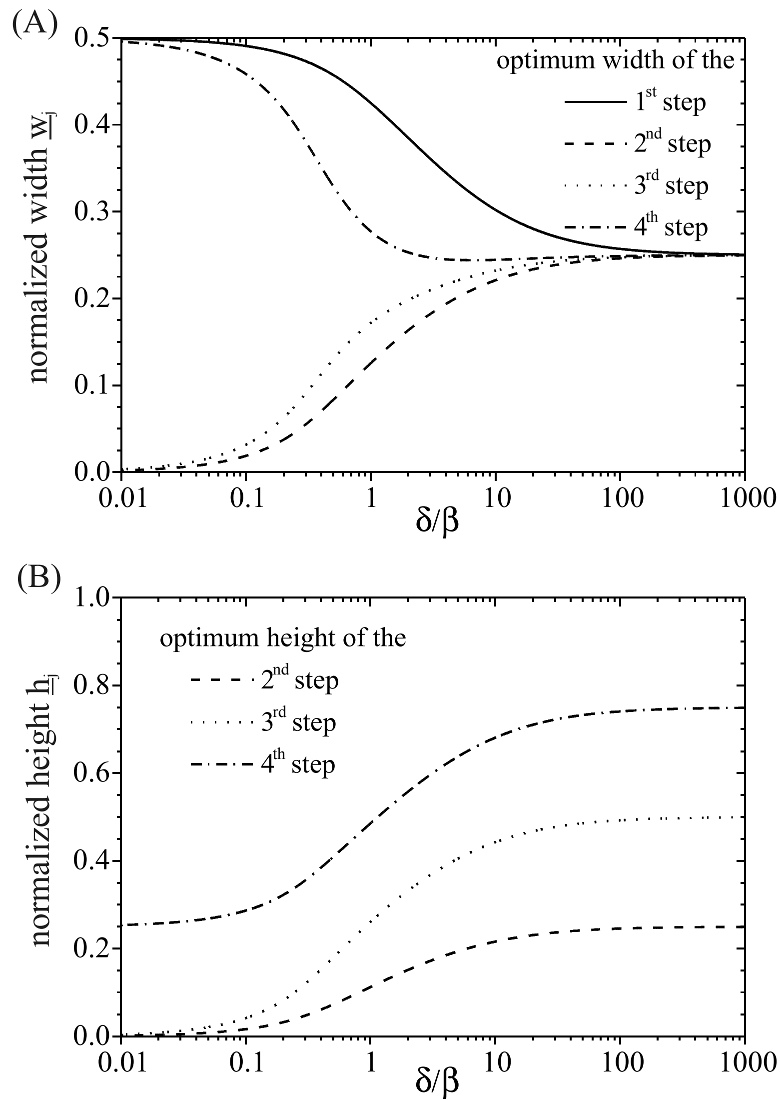

Figure 2.14: Optimum widths and heights of a staircase profile with four levels (steps) resulting in maximal first order diffraction efficiency.

In Figure 2.15 the diffraction efficiency of a four-step profile using optimal values for $\underline{h}_j$ and $\underline{w}_j$ is depicted. In addition the diffraction efficiencies of the ideal continuous profile, the ideal two-step profile, and a four-step profile using the conventional design rule optimised for zero absorption are plotted for comparison.

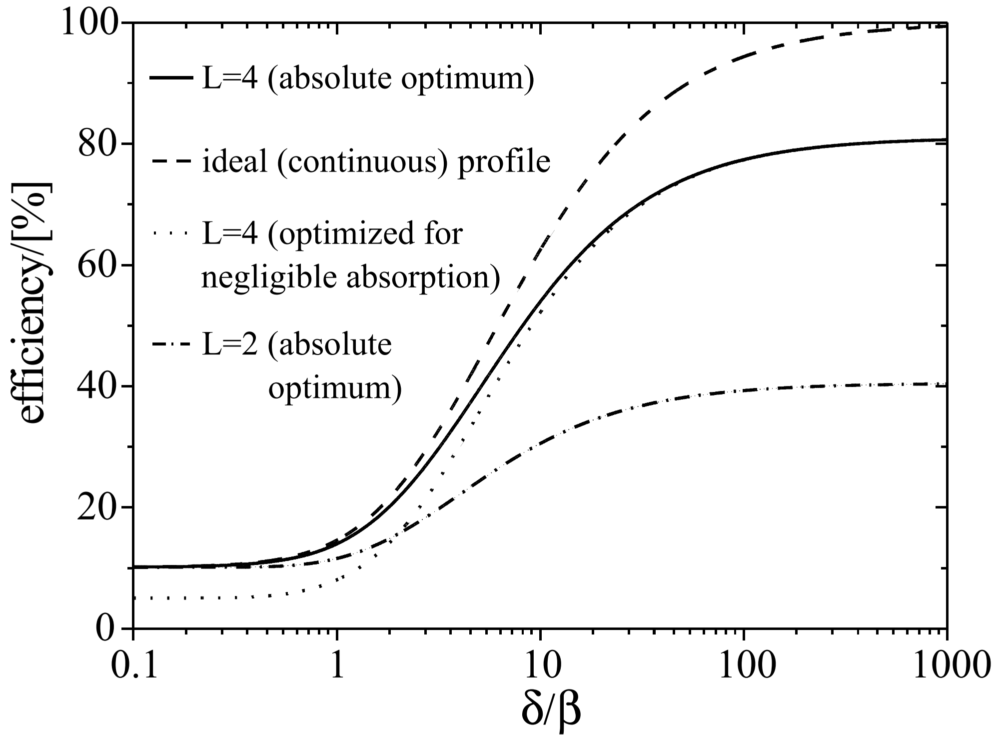

Figure 2.15: First order diffraction efficiency of a four-level grating (L=4) featuring optimum values for all step heights and widths (solid line). For comparison the efficiency of the ideal continuous profile (dashed line), the ideal two-level grating (L=2, dashed-dotted line) and a four-level profile optimised for zero absorption (dotted line) is shown.

For high values of δ/β, the two different four-level profiles nearly have the same diffraction efficiency, whereas for values of δ/β below 10 a significant difference can be observed. Therefore, the optimal design of the staircase profile has to be used in this case in order to guarantee maximum diffraction efficiency (e.g. at $\delta/\beta=2$ the optimum four-step profile gives 22% diffraction efficiency in comparison to only 16% for a four-step profile optimised for zero absorption). However, for small values of δ/β, the four-step profile optimised for zero absorption (having steps of equal width) is obviously a very bad approximation of the ideal profile (where nearly half of the grating period has zero height). Consequently, for values of δ/β below 2 even a simple two-level profile (with optimal design parameters) has a higher efficiency than the four-level profile optimised for no absorption.

Using different step numbers L of the staircase profile similar results are found (see e.g. Figure 2.16 showing the case of a staircase profile with 16 levels). For high values of δ/β (typically $\delta/\beta > 10$) the anticipated profile optimised for zero absorption ($\underline{h}_j = (j-1)/L$ and $\underline{w}_j = \underline{w}_k$) is obtained. For the case of high absorption, the staircase profile gives a good approximation of the ideal continuous profile in regions with small or zero structure height and a less perfect approximation in regions of large structure heights as expected.

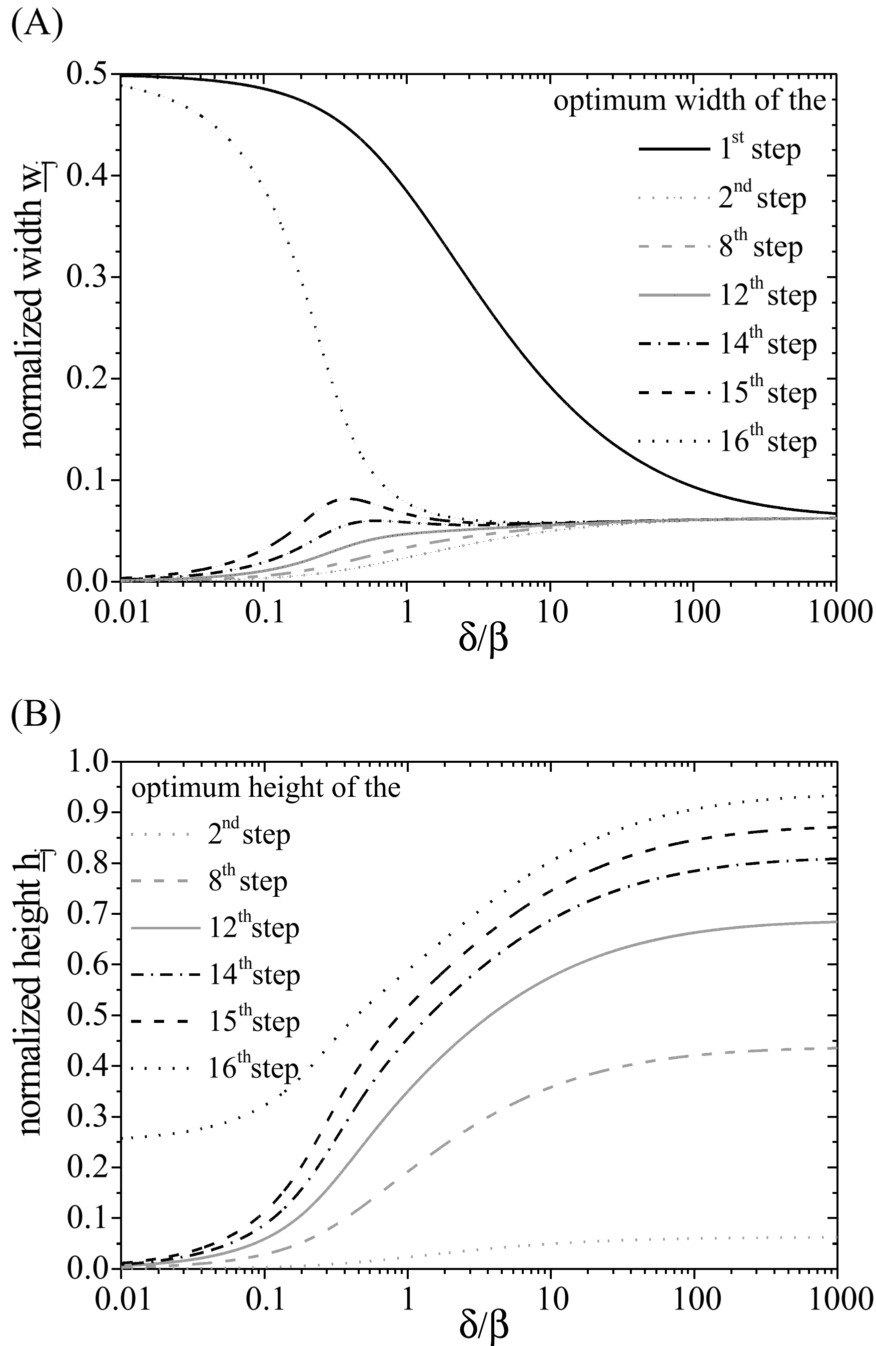

Figure 2.16: Optimum heights and widths of selected steps for a multilevel profile with L=16 levels.

Figure 2.17 shows the first order diffraction efficiencies of optimised profiles with different step numbers L. For small values of absorption, a larger number L of steps leads to a strongly improved diffraction efficiency whereas for strong absorption, very little difference is found between all profiles. This is due to the fact that for all profiles, the normalized width of the region with zero height approaches 1/2, going to small values of δ/β. Consequently, in the limit of infinite absorption all of the staircase profiles will have the same optical properties as a binary amplitude grating.

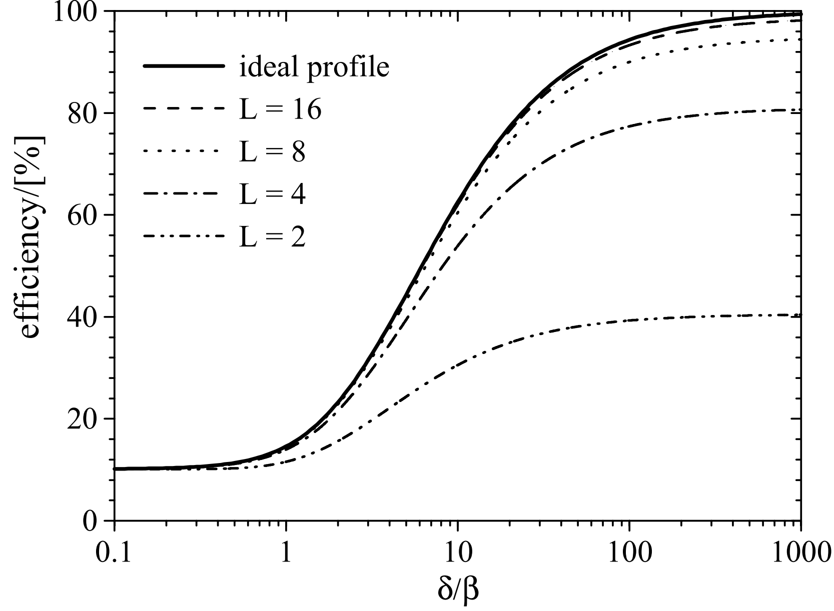

Figure 2.17: First order diffraction efficiency for the ideal (continuous) profile and for several optimised multilevel gratings with different number L of steps.

In the following it is shown that using the projection method it is possible to find analytical expressions for the optimum widths and heights of a staircase-profile. The analytical treatment has the advantage that it yields general information about the staircase profile, which one could not easily find by just making numerical calculations (e.g. the fact, that for all steps with non-zero height there is a linear dependence between the height $\underline{h}_j$ and the center positions $\underline{x}_j$). At the same time it is also a useful tool to check the numerical results shown above. Finally, using these analytical expressions it should be relatively easy to calculate the optimum profile even for extremely large numbers L of staircase levels.

According to equation (2.83) the first order diffraction efficiency η_1 is determined by a sum over amplitudes Φ_j, where Φ_j represents the contribution from the jth step of the staircase profile to the total amplitude Φ with

$$\eta_1 = |\Phi|^2 = \left|\sum_{j=1}^{L} \Phi_j\right|^2$$

and

$$\Phi_j = \exp[-2\pi \underline{h}_j \beta / \delta] \, \exp[-2\pi i(\underline{h}_j - \underline{x}_j)] \, \frac{\sin(\pi \underline{w}_j)}{\pi}$$

Maximum efficiency is obtained if the projection of Φ is a maximum. Analogous to the optimisation of the ideal continuous profile one therefore has

$$P\Phi \rightarrow MAX \qquad \text{and} \qquad P\Phi_j \rightarrow MAX$$

Optimising the height $\underline{h}_j$ of the jth step yields (analogous to equation (2.79))

$$\partial/\partial \underline{h}_j \left(P\Phi_j(\underline{h}_j)\right) = 0 \qquad \text{or} \qquad \underline{h}_j(\underline{x}_j) = 0 \qquad (2.84)$$

depending on which of the two solutions for $h_j(\underline{x})$ yields a larger projection $P\Phi_j$. Using equation (2.84) in the region of non-zero height yields

$$\underline{h}_j = \underline{x}_j - \varphi_0 / 2\pi - \varphi \qquad \text{with} \qquad \tan(2\pi\varphi) = 1/\kappa \qquad (2.85)$$

Consequently, one has a linear dependence between the heights $\underline{h}_j$ and the center positions $\underline{x}_j$ for all steps with non-zero height. In the region with non-zero height $\underline{h}_j$ the projection $P\Phi_j$ has to be larger than the projection one would get, if the step had zero height. This leads to the condition

$$\cos\left(2\pi\underline{x}_j + \varphi_0\right) \le \cos(2\pi\varphi)\exp\left(-2\pi\underline{y}_j / \kappa\right) \qquad (2.86)$$

Setting the free (projection) phase factor φ_0 zero and analysing equation (2.86) for different values of κ (δ/β) one finds, that (analogous to the case of the ideal continuous profile) the grating consists of two parts, one part (step) with zero height and the other part (all other steps) with non-zero height. Consequently, without loss of generality one has (see also equation (2.85))

$$\underline{h}_1(\underline{x}_1) = 0 \qquad \text{and} \qquad \underline{h}_j(\underline{x}_j) = \underline{x}_j - \varphi_0 / 2\pi - \varphi \quad j = 2,...,L \qquad (2.87)$$

For the optimisation of the widths $\underline{w}_j$ one has to take into account that an increase Δw in width of one step has to be exactly compensated by the decrease in width of another step. "Cutting" Δw from one step and adding Δw to a neighbouring step the projection PΦ is decreased by (see equation (2.78))

$$\Delta P\Phi_j = \exp\left[-2\pi\underline{h}_j / \kappa\right]\cos\left[-2\pi(\underline{h}_j - \underline{x}_j - \underline{w}_j/2) - \varphi_0\right]\Delta w$$

and increased by

$$\Delta P\Phi_{j+1} = \exp\left[-2\pi\underline{h}_{j+1} / \kappa\right]\cos\left[-2\pi(\underline{h}_{j+1} - \underline{x}_{j+1} + \underline{w}_{j+1}/2) - \varphi_0\right]\Delta w$$

For a set of $\underline{h}_j$, $\underline{w}_j$ and $\underline{x}_j$ yielding maximum diffraction efficiency the total change of the projection has to be zero, leading to

$$\Delta P\Phi_j - \Delta P\Phi_{j+1} = 0 \qquad (2.88)$$

Applying equation (2.88) in regions with non-zero height yields

$$\cos\left[2\pi\left(\frac{w_j}{2} - \varphi\right)\right] = \cos\left[2\pi\left(\frac{w_{j+1}}{2} + \varphi\right)\right]\exp\left[-(\underline{w}_j + \underline{w}_{j+1})\pi / \kappa\right] \qquad (2.89)$$

$$j = 2,3,.....(L-1)$$

Taking into account that $\underline{h}_1$=0, equation (2.88) yields (using the two steps with j=1 and j=2)

$$\cos\left[2\pi(\underline{h}_2 - \frac{\underline{w}_2}{2} + \varphi)\right] = \cos\left[2\pi(\frac{\underline{w}_2}{2} - \varphi)\right]\exp[-2\pi\underline{h}_2 / \kappa] \qquad (2.90)$$

and (using the two steps with j=1 and j=L)

$$\cos\left[2\pi(\underline{h}_2 - \underline{w}_1 - \frac{\underline{w}_2}{2} + \varphi)\right] = \cos\left[2\pi(\frac{\underline{w}_L}{2} + \varphi)\right]\exp\left[-2\pi\underline{h}_L / \kappa\right] \qquad (2.91)$$

In principle equations (2.89), (2.90) and (2.91) can be used to calculate all parameters of an optimised multilevel grating. Starting with a randomly chosen width $\underline{w}_{2,\text{trial}}$ of the second step, the numerical solution of equation (2.89) yields a set of widths $\underline{w}_3$, $\underline{w}_4$,…$\underline{w}_L$. Equation (2.90) then gives the height $\underline{h}_2$ of the second step, and using the fact that there is a linear dependence between the middle positions and the height of all steps with non-zero height (equation (2.87)) one can also calculate the height of all other steps ($\underline{h}_3$, $\underline{h}_4$, … $\underline{h}_L$). Finally equation (2.91) determines the width of the first step $\underline{w}_1$.

Obviously this procedure will always yield a full set of grating parameters ($\underline{w}_1$, ….. $\underline{w}_L$, $\underline{h}_1$,….$\underline{h}_L$) independent of the starting value $\underline{w}_{2,\text{trial}}$ of the width of the second step. However, one also has to match the condition that the normalized grating period is equal to one, leading to

$$\sum_{j=1}^{L} \underline{w}_j = 1 \qquad (2.92)$$

If the sum over all widths is larger than one, the next starting value $\underline{w}_{2,\text{trial}}$ should be chosen smaller (or otherwise larger than the first one). By varying $\underline{w}_{2,\text{trial}}$ one will finally end up with a set of grating parameters, that fulfils equation (2.92) and represents the global optimum, giving maximum first order diffraction efficiency.

2.3 Refractive x-ray lenses

2.3.1 The ideal lens shape

For a long time refractive lenses for the x-ray range have been considered as impractical due to the strong absorption of all materials and the comparatively small refraction caused by them. However, about a decade ago it was realised, that in the hard x-ray range absorption of materials with low atomic numbers is sufficiently small to make refractive x-ray lenses feasible [25, 62, 63]. Compared to conventional optics in the visible light range, the decrement of the refractive index is much smaller and therefore one has to use lenses with strong curvatures or many lenses in series to obtain reasonable focal lengths (see Figure 2.18 B). As the refractive index is normally smaller than unity in the x-ray range, a focusing lens needs to have a concave shape.

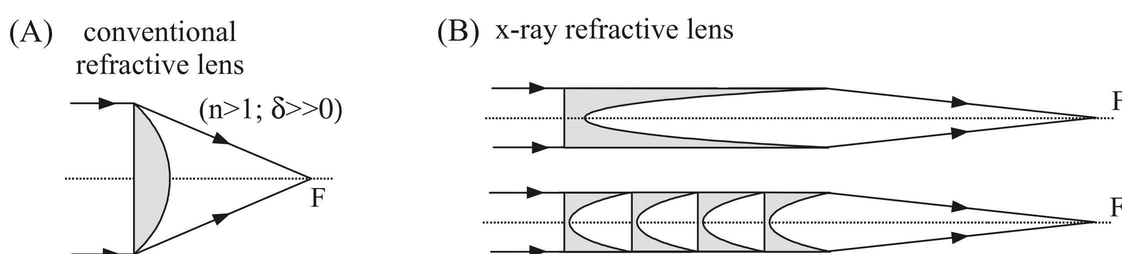

Figure 2.18: (A) Sketch of a conventional refractive lens in the visible light range. (B) Schematic picture of a refractive x-ray lens. Due to the small values of the decrement of the refractive index δ, strong curvatures or many lenses in series have to be used in order to obtain reasonable focal lengths.

The optimum x-ray lens shape, leading to the perfect focusing of a plane wave (an infinitely far away point source) can be determined using Fermat's principle (see also Figure 2.19 A).

For all rays reaching the focus the optical path length has to be the same leading to

$$f/c = (1-\delta)h(x)/c + 1/c\sqrt{(f-h(x))^2 + x^2}$$

Rearranging this equation we obtain

$$h(x)^2 - 2h(x)f/(2-\delta) + x^2/(2\delta-\delta^2) = 0 \quad (2.93)$$

Using a transformed coordinate $x' = x/\sqrt{(2\delta-\delta^2)}$ the height h(x') is given by

$$h(x')^2 - 2h(x')f/(2-\delta) + (x')^2 = 0$$

It can be easily shown (see also Figure 2.19 B), that the ideal shape h(x') in transformed coordinates describes a circle with radius r given by $r = f/(2-\delta)$. Consequently, the ideal shape in untransformed coordinates is an ellipse (characterized by a major axis a_1 and minor axis b_1) where

$$a_1 = r = f/(2-\delta) \tag{2.94}$$

and

$$b_1 = r\sqrt{(2\delta-\delta^2)} = a_1\sqrt{(2\delta-\delta^2)} \tag{2.95}$$

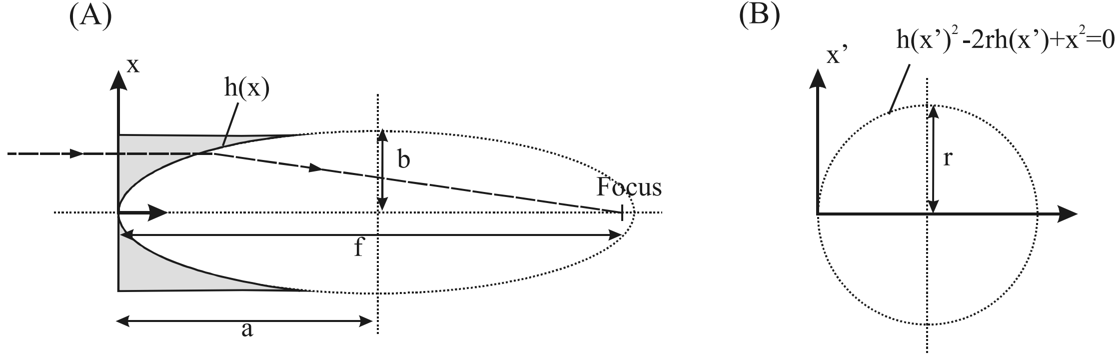

Figure 2.19: (A) Calculation of the ideal lens shape h(x) for a refractive x-ray lens using Fermat's principle. (B) Ideal lens shape h(x') using a transformed coordinate x'.

In the x-ray range the decrement of the refractive index δ is always very small leading to

$$a_1 \cong f/2 \qquad b_1 \cong \sqrt{2\delta} f/2 \tag{2.96}$$

Note that b_1 determines the maximum aperture (diameter) D_{max}, which can be realized using a single refractive x-ray lens where

$$D_{max} = 2b_1 \cong \sqrt{2\delta} f \tag{2.97}$$

Using typical values (f=1m, $\delta=7.8\times10^{-7}$ - assuming silicon and a photon energy of E=25 keV) we find D_{max}=1.2mm. It will be shown later on (see chapter 6.2 and 6.3) that refractive lenses with large apertures D get relatively close to this value. However, in praxis always many lenses in series are used, leading to a significant increase of the value of D_{max}, and consequently one always has $D \ll D_{max}$.

If the lens aperture D is significantly smaller than the maximum aperture, it is possible to approximate the optimum lens shape (the ellipse) by a parabola. Using equation (2.93) one obtains

$$h(x) \cong x^2/(2f\delta) \tag{2.98}$$

Equation (2.98) represents the standard lens shape of refractive x-ray lenses reported in literature [27, 64]. Applying equation (2.98) as a design rule for the fabrication of (parabolic) refractive lenses, the deviations from the ideal (elliptical) lens shape will cause a certain broadening Δw of the focal spot. It can be shown (basically using equation (2.93) and simple geometrical optics) that this broadening is of the order

$$\Delta w \cong D^3 / (2 f^2 \delta) = D \left(D / D_{max} \right)^2 \qquad (2.99)$$

The broadening Δw of the focal spot will be negligible if $\Delta w/D \ll w/D$, where w/D is the relative width w/D of the focal spot, leading to

$$\left(D / D_{max} \right)^2 \ll w / D \qquad (2.100)$$

It proves to be hard to achieve relative widths w/D of the focal spot that are significantly smaller than about 1/100 and consequently condition (2.100) is very often fulfilled.

If the difference in optical performance between lenses of parabolic and of elliptical shape is negligible (equation (2.98) applies), then one can use one lens to focus a whole range of x-ray photon energies without getting significant aberrations. However, the focal length will change due to the dispersion of the lens material. Using Equation (2.98) results in

$$h(x) \cong x^2 / (2 f(E) \delta(E)) = \text{constant}$$

and therefore

$$f(E) \propto 1 / \delta(E)$$

The decrement of the refractive index δ is in good approximation inverse proportional to the square of the photon energy (see equation (2.26)) leading to

$$f(E) \propto E^2 \qquad (2.101)$$

This means, that contrary to refractive lenses for visible light, refractive lenses in the x-ray range are highly chromatic focusing devices.

2.3.2 Refractive lenses with minimized absorption

For all refractive x-ray lenses absorption in the lens material is one of the limiting factors for the optical performance. The lens thickness (and therefore absorption) strongly increases with the distance to the optical axis. Consequently, in lenses with large apertures most of the light passing the lens near its edges is absorbed.

One possibility to overcome this problem of absorption is shown in Figure 2.20 B. Removing parts (rectangles) of a refractive lens, which cause a multiple M_1 of 2π in phase shift (compared to vacuum) doesn't change the optical properties of the lens, but significantly decreases the mean thickness of the lens. Consequently, by removing the corresponding lens regions one obtains a lens with minimized absorption.

The resulting lens structure consists of a quasi-periodic array of lens-sectors of similar (more or less triangular) shape. Therefore it can be considered as a special type of diffraction lens. In fact, one obtains a conventional diffractive lens (see Figure 2.20 C) when the individual sectors of such a lens are moved into one common plane (in general this requires a slight change of the size and shape of the sectors in order to achieve optimum optical performance). The difference in the optical path between two subsequent lens-sectors is $M_1 \times \lambda$. Consequently the lenses shown in Figure 2.20 B and C are diffracting lenses, using the M_1^{th} diffraction order.

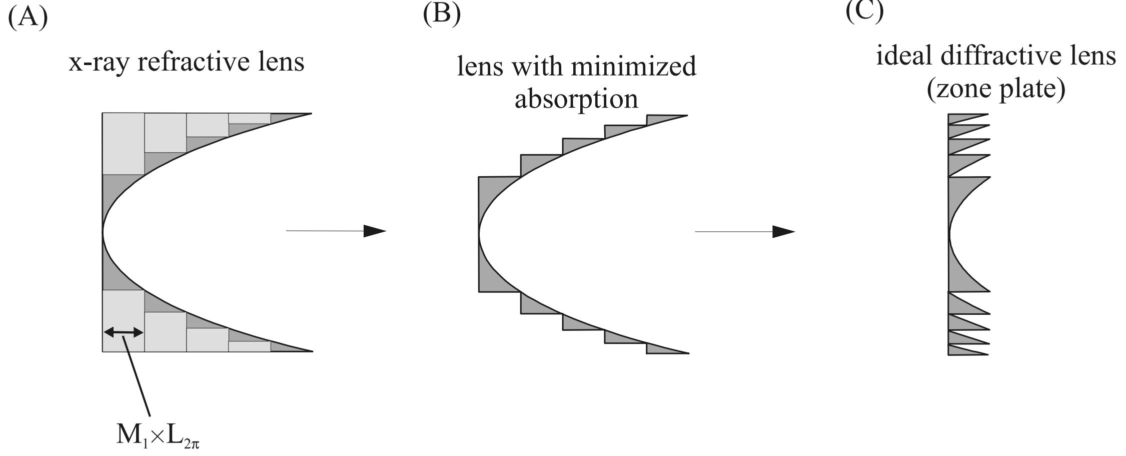

Figure 2.20: (A) Schematic sketch of a refractive x-ray lens. (B) Refractive lens with minimized absorption. Lens B is obtained from lens A by cutting away bars that cause a multiple of 2π in phase shift. (C)

In praxis the number of lens-sectors is small (and M_1 large). Therefore the optical behaviour of a lens with minimized absorption is always similar to a normal refractive lens, as each of these sectors deflects (refracts) the incoming light into a small region around the focus. The distance between this focal region and the lens will change with energy according to equation (2.101). However, optimum focusing (minimal width of the focus) will only be achieved if the waves stemming from different sectors add up in phase in the focal point. This condition is only matched if the removed rectangles (in Figure 2.20 A and B) cause a multiple of 2π in phase shift and consequently optimum lens performance can only be expected for certain x-ray energies/wavelengths. If λ_1 is the design wavelength and $M_1\times L_{2\pi}(\lambda_1)$ the thickness of the removed rectangles, optimum performance for a different wavelength λ'_1 requires that

$$M_1(\lambda_1)L_{2\pi}(\lambda_1) = M'_1(\lambda'_1)L_{2\pi}(\lambda'_1)$$

where M_1' has to be an integer value. This leads to

$$M_1\lambda_1/\delta(\lambda_1) = M'_1\,\lambda'_1/\delta(\lambda'_1) \qquad (2.102)$$

and using equation (2.26)

$$M_1E_1 \cong M'_1\,E'_1 \qquad (2.103)$$

Equations (2.102) and (2.103) yield the energies where (at least in theory) diffraction limited focusing can be achieved. Applying Rayleigh's quarter-wavelength rule one can estimate how accurate one has to match one of these energies (the allowed spectral range ΔE/E) to ensure optimum optical performance.

If h_{max} is the maximum thickness of the lens (and therefore more or less the maximum thickness of the removed rectangles) this leads to

$$L_{2\pi}(\lambda_1)\frac{\Delta E/2}{E}\left(h_{\max}/L_{2\pi}(\lambda_1)\right) \le L_{2\pi}(\lambda_1)/4$$

And using the parabolic approximation of the lens shape (equation (2.98))

$$\frac{\Delta E}{E} \leq 4 f \lambda_1 / D^2 \qquad (2.104)$$

For typical lens parameters (f=1m, D=400µm, λ_1=0.05nm) one finds ΔE/E<1/800.

The same consideration also applies for the tolerable uncertainty of the decrement of the refractive index δ and - as δ is proportional to the material density ρ - for the uncertainty of the material density ρ leading to

$$\frac{\Delta \delta}{\delta} \leq 4 f \lambda_1 / D^2 \quad \text{and} \quad \frac{\Delta \rho}{\rho} \leq 4 f \lambda_1 / D^2 \qquad (2.105)$$

Consequently one needs to know E_1, δ and ρ with considerable accuracy in order to ensure an optimum design and performance of a lens.

However, equations (2.104) and (2.105) assume diffraction limited focusing and in praxis (due to a finite size of the x-ray source and lens shape errors/aberrations) this is hardly ever achieved. The width of the focal spot is normally considerably larger than in the diffraction limited case, and therefore conditions (2.104) and (2.105) can be relaxed accordingly.

2.3.3 Stacking of refractive lenses

For the x-ray range one has to use refractive lenses with extreme curvatures and/or many lenses in series to obtain reasonable focal lengths. In first approximation the optical behaviour of a stack (array) of lenses can be calculated using paraxial optics, assuming small deflection and refraction angles (see e.g. [51]). In praxis, the length of such a stack is always much smaller than the focal length f_1 of one lens. The total focal length f of the lens array is then (to a good approximation) K times smaller than the focal length of one lens ($f= f_1/K$), where K is the number of lenses in the stack.

In the paraxial approximation it should be sufficient to use lenses with parabolic shape (instead of e.g. elliptical shape) for the lens array. However, it was already shown earlier that (at least for one single lens) this can lead to non-negligible aberrations. Consequently, the question arises, what kind of lens-shape one has to choose, in order to avoid aberrations for an array of K individual lenses.

Although it is not easy to answer this question in general, in the following it will be shown that one can find a shape very close to the ideal one, if the stack consists of closely packed lenses with minimized absorption (see Figure 2.21).

Due to the small values of the decrement of the refractive index δ a significant deflection of the x-ray beam within a lens array will only occur at the (strongly) curved surfaces. For each of these surfaces Snell's law applies (see e.g. [51]).

$$n_1 \sin\theta_1 = n_2 \sin\theta_2$$

For a stack of lenses in air (vacuum) this leads to

$$\sin\theta_1 = (1-\delta)\sin\theta_2 \qquad (2.106)$$

The lens array shown in Figure 2.21 B will have identical optical properties as the array shown in Figure 2.21 A, provided that for all surfaces Snell's law has the same form as in equation (2.106). This requires that

$$n_{j+1} / n_j = (1-\delta)$$

and therefore

$$n_j = (1-\delta)^j \cong 1 - j\delta \qquad j = 0,1,2,...K \qquad (2.107)$$

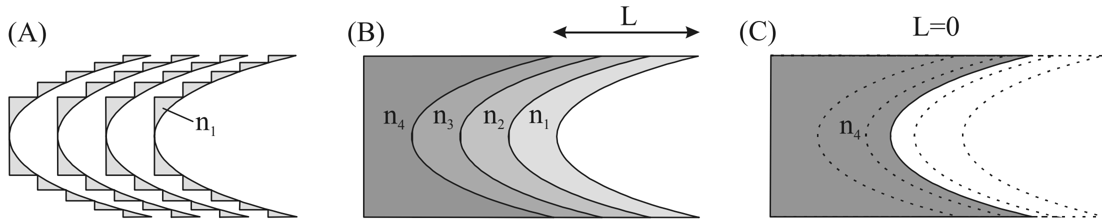

Figure 2.21: (A) Schematic sketch of a stack (array) of refractive lenses with minimized absorption. The lens-shape leading to (almost) aberration free imaging with this lens array can be found using the (approximate) optical equivalence of the lenses shown in (A), (B) and (C).

If the length of the stack (more accurately L, see Figure 2.21 B) is small compared to the overall focal length, the optical properties should be more or less independent from the actual value of L. Consequently, the optical behaviour of the lenses shown in Figure 2.21 B and Figure 2.21 C should be almost the same.

For the single lens in Figure 2.21 C the optimum lens shape is an ellipse, where the effective decrement of the refractive index δ_K of the lens material is given by (see equation (2.107))

$$\delta_K = (1-n_K) \cong K\delta \qquad (2.108)$$

and the major axis a_1 and minor axis b_1 of the ellipse by

$$a_1 = f/(2-\delta_K) \quad \text{and} \quad b_1 = a_1\sqrt{(2\delta_K - \delta_K{}^2)} \qquad (2.109)$$

Due to the (approximate) equivalence of all lenses in Figure 2.21, the optimal lens shape for Figure 2.21 C (described by equation (2.109)) can be also be used for a stack of lenses with minimized absorption (Figure 2.21 A), resulting in an almost aberration free focusing device.

The broadening Δw of the focal-spot due to the (remaining) aberrations can be estimated using simple ray tracing. One finds that the relative broadening $\Delta w/D$ is of the order of

$$\Delta w / D \cong \left(D / D_{\max}(\delta_K)\right)^2 L / f = \left(D / D_{\max}(\delta)\right)^2 L/(Kf) \qquad (2.110)$$

It is useful to compare this result to the relative broadening $\Delta w_{para}/D$ one expects, using a parabolic instead of an elliptical lens shape (e.g. in Figure 2.21 C). Applying equation (2.99) we find

$$\Delta w_{para} / D \cong \left(D / D_{\max}(\delta_K)\right)^2 = \left(D / D_{\max}(\delta)\right)^2 / K \qquad (2.111)$$

Obviously the broadening due to the parabolic approximation is much bigger (the length L of the lens is typically a factor 100 smaller than the focal length f). However, it was already mentioned earlier, that even the broadening due the parabolic approximation is often tolerable.

Using typical lens parameters (L=1cm, f=1m, K=20, D=400µm, $D_{max}(\delta)$=1.2mm - assuming Si and a photon energy of 24.8keV) we obtain Δw=20nm which is about a factor 100 less than the typical width of an experimentally obtained focal spot.

2.3.4 Transmission and efficiency of a lens with minimized absorption

The theoretical transmission T of a lens with minimized absorption can be calculated by averaging over the transmission of different lens regions. This leads to (see also [64])

$$T = 1 / D \int dx \exp[-\mu_{total} d(x)] \qquad (2.112)$$

where d(x) is the lens thickness measured along the x-ray beam, D the lens diameter and μ_{total} the total absorption coefficient. Note, that a lens with minimized absorption is a special kind of diffractive lens with a blazed grating profile, which follows the shape of a conventional refractive lens. For negligible absorption one has complete equivalence to a normal refractive lens so that all light is focused into one single point, meaning that all light is diffracted into one single order. In the general case of absorption this is not necessarily the case. However, one can show that for reasonable transmissions of a lens with minimized absorption only a very small fraction of the light is found in other diffraction orders. As a consequence the fraction of the incoming x-rays that ends up in the focus - i. e. the efficiency η of the lens - is almost equal to the fraction of x-rays that is transmitted through the lens, leading to

$$\eta \cong T \qquad (2.113)$$

If a lens with minimized absorption consists of many segments, most of these segments have almost a triangular shape. The quasi-periodic array of these segments acts as a grating with variable grating constant. In order to estimate the difference between η and T it is therefore useful to consider the case of a blazed grating with triangular shape.

Using equations (2.70) - (2.73) one can calculate the fraction of transmitted light that is diffracted into the blazed diffraction order of such a grating. Figure 2.22 shows the resulting ratio η/T calculated for different transmission values T of a grating with triangular shape.

Note that even for a transmission of only 50 % more than 95 % of the transmitted light is diffracted into the blazed diffraction order. As a consequence the difference between the efficiency and the transmission was found to be negligible and smaller than 1 % for all types of lenses with minimized absorption considered within this work.

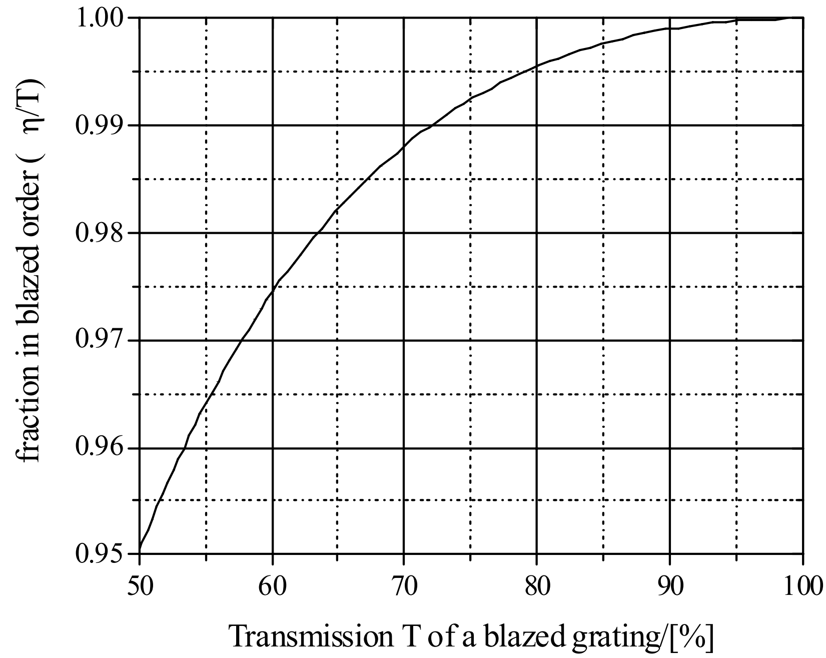

Figure 2.22: Influence of the absorption within a grating of triangular shape on the diffraction efficiency of the blazed diffraction order. Even for low transmission values of the grating most of the transmitted light ends up in the blazed diffraction order. The corresponding values of η/T are calculated using equations (2.70) - (2.73). Note that the resulting values of η/T are independent on whether the blazed grating uses the first, second or a higher diffraction order.

3 Micro- and Nano-fabrication methods

The fabrication of the two types of x-ray lenses described in this work (zone plates and planar refractive lenses) requires many types of lithography and structuring techniques. A general introduction and a detailed description of micro-fabrication methods can be found for example in reference [65]. The following chapter intends to give a short overview of the used techniques and equipment and to provide a detailed description of special aspects and features of these methods, which cannot easily be found elsewhere.

3.1 Electron-beam lithography

3.1.1 General principle

One key part (and the first step) of many types of micro-fabrication processes is the predefinition of the size and shape of the microstructures by means of lithography techniques. Most of these techniques use some kind of resist - a thin layer of material on a substrate - that is locally modified using photons (e.g. visible light, ultra violet, x-rays), ions or (in case of electron-beam lithography) electrons. By selectively removing the modified regions (positive resist) or the unmodified regions (negative resist) using a suitable solution (developer), one obtains a structured resist-layer. The resulting resist-mask can then be transferred to the underlying sample by several types of etching or also deposition techniques.

Figure 3.1 shows a schematic sketch of these different process steps in the case of e-beam lithography.

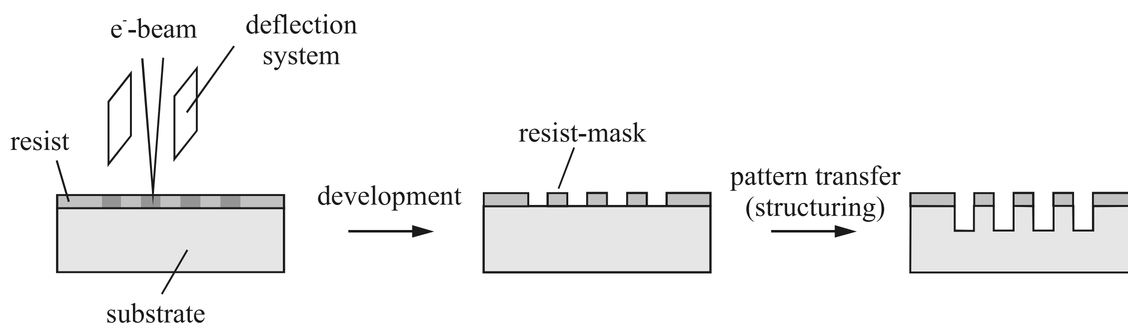

Figure 3.1: Principle of electron-beam lithography

In order to modify (expose) different regions of the resist the e-beam is normally deflected by means of magnetic or also electric forces. This makes it possible to address each part of the resist individually and consequently enables the exposure of basically any kind of pattern within the resist. This large freedom in the mask-pattern design is one of the big advantages of e-beam lithography systems. The sequential exposure of individual regions makes e-beam lithography a relatively slow lithography tool, e.g. compared to conventional photolithography, were visible or ultraviolet light in connection with a photo-mask is used to expose the whole pattern in one single step, which at the same time means that one is restricted to the pattern determined by the photo-mask. However, for scientific applications, where normally a small quantity of samples and therefore a relatively small total area has to be patterned, the lithography speed does not play a mayor role.

E-beam lithography enables the fabrication of extremely small structures. Structure sizes in the order of 10 nm are feasible. This high resolution is of special importance for the

fabrication of zone plates as they require a positioning and shape accuracy of the grating structures, which is in the order 10 nm and which could hardly be achieved by other lithography techniques.

Such high resolutions require a restriction to small deflections of the beam and consequently only a small area (field) of the sample (typically a field of about 100×100 μm^2) can be exposed. The exposure of larger areas is obtained by splitting the pattern into appropriately small sub-fields and by moving the sample after the exposure of each of these fields. This method is therefore commonly referred to as field-stitching. Due to errors of the deflection system or the sample stage one will always have some overlap or a gap between these fields (a stitching error). These errors occur periodically with a period given by the size of the stitch-field. Especially for the fabrication of diffracting optical elements such periodic errors can cause troubles as they result in unwanted diffraction orders ("ghosts") of the optical device.

3.1.2 The LION LV-1 e-beam system

Within this work the LION LV-1 (from Leica Microsystems, Jena) was used as a tool for e-beam lithography (LION stands for Lithography for integrated optics and nanostructures).

High-resolution e-beam lithography requires the positioning of samples with an accuracy of about 10 nm. In the LION e-beam system this is achieved using a highly frequency stabilized Helium-Neon laser in connection with an interferometric stage. Several types of sample holders can be automatically transferred and placed onto this stage, enabling the exposure of more or less any kind of sample, provided that it is sufficiently thin and flat.

During exposures the deflection of the beam is normally controlled by a built-in pattern generator, allowing the exposures of various types of data formats (gds, bitmaps, etc.). All exposures using these data formats include the concept of field stitching and consequently will always be accompanied by a certain stitching error. However, the LION-LV1 is also capable of doing exposures in a different (for e-beam systems unique) modus, making it possible to avoid this field-stitching problem. The main characteristic of this so-called continuous-path-control (CPC) mode is the fact, that instead of moving the e-beam across the sample, the sample (stage) is mechanically moved underneath the e-beam. This enables the exposure of practically any type of curve without discontinuities, provided that certain limits are not exceeded (e.g. maximum speed and acceleration of the stage). In general the mechanical movement cannot be controlled with the required accuracy in the nanometre range. However, the difference between the target and the actual value of the stage position is measured continuously and compensated by means of magnetic deflection of the beam. The remaining deviations from the ideal curve (e-beam path) are in the range of 10 nm and of non-periodic character and consequently the main problem of field stitching (periodic discontinuities) is avoided in the CPC-modus.

In the CPC-modus so-called Bez-data files (BEZ=short for Bezier) are used to define the properties of the curves one wants to expose. Bez-data files are simply text-files were all curve parameters are written in ASCII-text-format. This makes it very easy to automatically generate Bez-files by means of self-written programs, as basically any programming language offers simple possibilities to produce and handle text-files.

The name of this special type of data-format originates from the fact, that the shape and the size of all exposed curves are defined (mathematically described) by means of Bezier-curves [see e.g. 66]. In literature one can find several different types of Bezier-curves, characterized

by different definitions and potential applications. Within the LION-software rational Bezier-curves (of 1st, 2nd and 3rd order) are used to define the path of the electron beam.

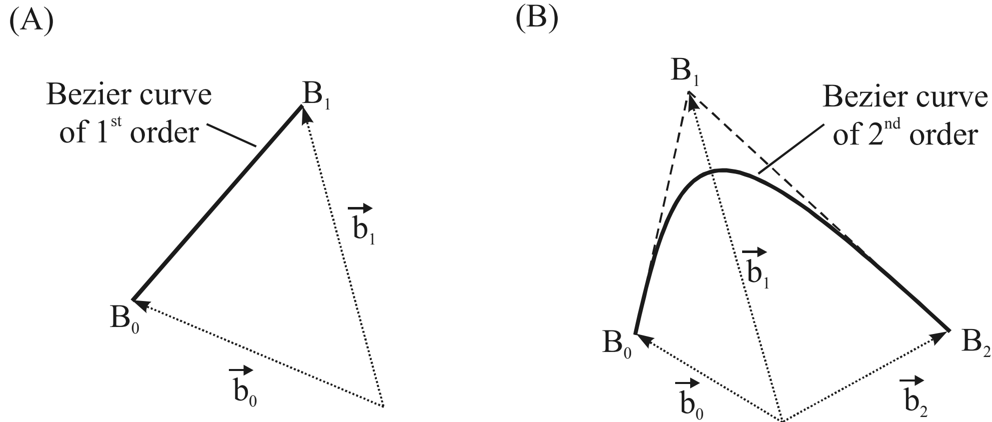

Figure 3.2: Schematic sketches of rational Bezier-curves of first order (shown in A) and of second order (shown in B).

A rational Bezier-curve of first order is simply a line between a starting point B_0 and an end-point B_1 (see Figure 3.2 A). A parametric description of such a line is given by

$$\vec{r}(t) = \vec{b_0}(1-t) + \vec{b_1}t \qquad 0 \le t \le 1 \qquad (3.1)$$

In principle the possibility to write such lines in the CPC-mode would already be sufficient, as any type of curve (area) can be approximated (filled) using a sufficiently large number of lines. However, to keep the data files small and compact it is convenient to have the possibility to expose Bezier-curves of higher orders. In particular this is the case for Bezier-curves of 2nd order, as they represent all possible types of conic sections (ellipses, parabolas, hyperbolas).

In parametric description a Bezier-curves of 2nd order is defined by

$$\vec{r}(t) = \frac{\vec{b_0}(1-t)^2 + 2g\vec{b_1}(1-t)t + \vec{b_2}t^2}{(1-t)^2 + 2g(1-t)t + t^2} \qquad 0 \le t \le 1 \qquad (3.2)$$

For t=0 and t=1 equation (3.2) yields the starting point B_0 and the endpoint B_2 of the curve as shown in Figure 3.2 B. The point B_1 represents a “guiding point” for the curve, as it defines the direction of the tangents in the starting point and the end point (see Figure 3.2 B). The factor g determines the type of conic section described by equation (3.2). For g=1 the denominator in equation (3.2) is equal to one for all values of t and r(t) describes a parabola.

Many applications require the exposure of circles (or also parts of circles). Applying equation (3.2) to the point P in Figure 3.3 (parameter t=0.5) one finds that the g factor for the section of a circle is given by

$$g = \cos(\varphi / 2) \qquad (3.3)$$

Due to technical reasons the Bezier-data format of the LION-LV1 is restricted to g values larger than zero and therefore only sections of a circle with $\varphi<180^0$ can be exposed. Consequently, in order to expose a full circle it has to be divided into (at least) three parts.

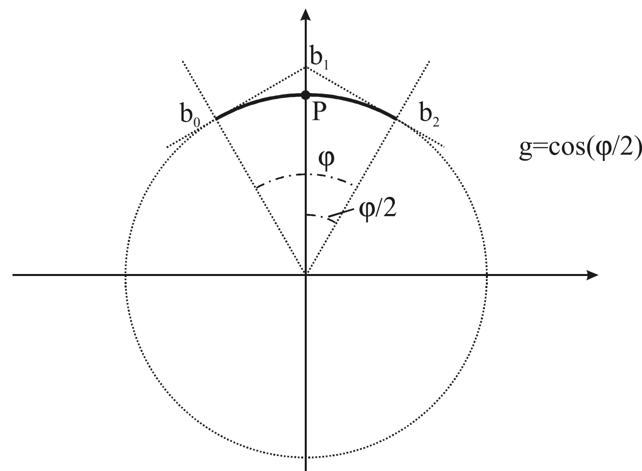

Figure 3.3: Calculation of the g-factor for the section of a circle

It will be shown later on that the fabrication of refractive lenses with minimized absorption requires the exposure of (sections) of ellipses. In this case the appropriate factor g can be found using the fact, that g doesn't change if a linear transformation is applied to the underlying coordinate system of a Bezier-curve. By stretching (or compressing) the ellipse along one of its axis, it is always possible to turn a section of an ellipse into a section of a circle. The g-factor in this transformed coordinate system (calculated using equation (3.3)) is then identical to the one of the (untransformed) elliptical Bezier-curve.

3.1.3 E-beam resist and development

E-beam lithography uses the fact that the chemical properties of a resist are changed by local irradiation with electrons. Most of the energy transferred to the resist (and therefore most of the chemical modification) does not directly originate from the incoming electron-beam (primary electrons) but from secondary electrons of low energy (up to 50 eV). These are produced, when the primary beam penetrates the resist and transfers small amounts of its energy to electrons, which are bound within the resist material. For e-beam lithography systems the energy of the primary electrons typically lies in the range between 1 keV and 100 keV. For the LION-LV1 the primary electron energy can be set to values between 1 keV and 20 keV. For all exposures within this work the energy was set to 2.5 keV.

The mean free path of the secondary electrons in organic materials is in the order of 10 nm, and is one of the fundamental limiting factors for the resolution of e-beam lithography. The amount of chemical change within the resist is proportional to the number of incoming electrons per unit area and consequently the dose D (charge per unit area) is commonly used to quantify, how much a certain area of resist was exposed. Due to the finite size of the electron beam and the finite range of the secondary electrons there will always be a gradual change of the dose between exposed and unexposed regions of the resist. At the same time the fabrication of structures with well-defined size requires a sharp edge between regions were all resist and no resist is removed after the development process. Consequently, for electron-beam lithography resists with large contrast are needed (meaning that a small change in dose determines whether the resist is removed or not).

One commonly used resist meeting this requirement is PMMA (polymethyl methacrylate, also known as acrylic glass or Plexiglas). PMMA is an organic polymer with a typical degree of polymerisation (the average number of monomers within one molecule) in the order of 10000. The exposure of PMMA with electrons leads to a decrease of the mean molecule length and in consequence the exposed regions become solvable in an appropriate developer (positive resist). Within this work PMMA with a molecular weight of 600k was used (AR-P 661.09 from Allresist GmbH), which was diluted with chlorobenzene, giving a solution with 2.25% solid content of PMMA.

All samples were developed using a HAMATECH (Steag-Hamatech HME 500) developing machine, enabling a fully automated and highly reproducible processing of exposed PMMA-resist. A 1:3 solution of methylisobutylketone (MIBK) and isopropyl alcohol (IP) was typically used to develop the sample. In a second step the sample was then rinsed with pure isopropyl alcohol (in order to stop the development process) and afterwards dried by rotating the sample with high speed.

The minimal dose (the critical dose D_c) leading to a complete removal of exposed PMMA-regions depends on several parameters, like the energy E_p of the primary electrons, the degree of polymerisation of the PMMA, the thickness d of the PMMA-resist, the duration t_d of the developing step and the composition of the developer. For the typical parameters used within this work (E_p=2.5 keV, d=100nm t_d=30 sec, MIBK:IP=1:3) one finds, that the critical dose is about 14 $\mu C/cm^2$.

3.1.4 Line width control

The fabrication of diffracting optical elements typically requires the exposure of curves (e.g. circles for zone plates) with different, well-defined line width [67]. Using the LION-LV1 e-beam system in the CPC-modus it is possible to control the line width by adjusting the writing speed v_s of an exposed curve (and therefore the applied dose) and also by using a certain, adjustable defocus d_f of the electron beam (see Figure 3.4). Suitable parameters to obtain a certain line width can always be found making test exposures. However, in praxis it is much more convenient to have an analytical model, especially if a continuous range of line widths has to be exposed (e.g. a zone plate).

A simple mathematical model can be found assuming uniform irradiation within the (circular) defocused e-beam spot in connection with a resist of infinite contrast [67]. The dose D_s of a sample area, which is hit by such an e-beam spot increases with time according to (see also Figure 3.4)

$$dD_s / dt = I_b / r^2\pi = 4I_b / \left(d_f{}^2\theta^2\pi\right)$$

where I_b is the current, d_f the defocus and θ the aperture angle of the electron beam. The exposure time t_e of a certain part of the sample depends on the stage speed v_s and on the distance x to the center of the exposed curve, leading to

$$t_e = 2\sqrt{r^2 - x^2} / v_s$$

The distribution of the dose D(x) is therefore given by

$$D(x) = t_e(dD_s / dt) = 2I_b\sqrt{1-(x/r)^2} / (v_s r\pi) \qquad (3.4)$$

During the development the resist will be removed for regions where the dose D(x) exceeds the critical dose D_c. Consequently, the width w of the line is determined by

$$D_c = D(w/2) = 2I_b\sqrt{1-(w/2r)^2}\,/(v_s r\pi)$$

leading to

$$w = 2r\sqrt{1-(D_c r v_s \pi/4I_b)^2} = d_f\theta\sqrt{1-(\pi D_c v_s d_f \theta/4I_b)^2} \qquad (3.5)$$

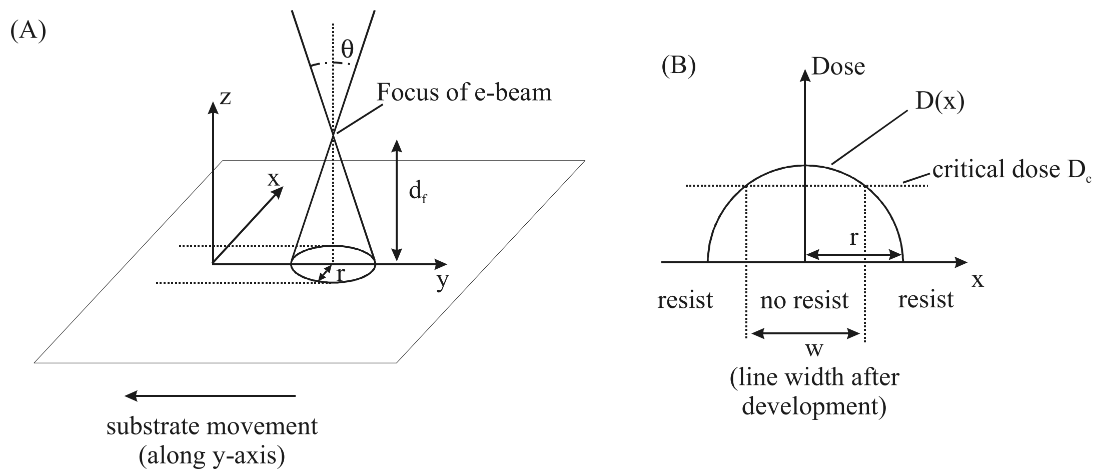

Figure 3.4: (A) Schematic sketch of a curve-exposure in the CPC-mode of the LION-LV1. (B) Resulting line-with after development, assuming a homogenous irradiation with electrons within a circular defocused spot.

The CPC-modus of the LION-LV1 only allows for the exposure of lines with constant stage speed v_s. The number of electrons (or more accurately the charge Q) reaching the sample along such a line of length l is given by

$$Q = I_b(l/v_s)$$

Obviously the charge per unit length is a means of quantifying the amount of chemical change due to the exposure for a curve. This makes it useful to define a line dose D_l (the charge per unit length=Q/l; usually given in nC/cm) leading to

$$D_l = I_b/v_s \qquad (3.6)$$

Using the CPC-mode it is possible either to specify the speed of the stage movement or (provided that the current has been properly measured and set within the software) the line dose of a curve. Within this work only the latter possibility was used. Consequently, each curve was defined by its defocus d_f, its line-dose D_l and its Bezier-parameters (starting point, end point and for rational Bezier-curves of first order also the guiding point and the g-factor). Rewriting equations (3.4) and (3.5) for this practical case one finds

$$d_f = w / \left(\theta \sqrt{1 - (\frac{\pi}{4} d_f \theta \frac{D_c}{D_l})^2} \right) = w / (k_e \theta) \qquad (3.7)$$

and

$$D_l = \frac{\pi}{4} D_c w / \left(k_e \sqrt{1 - k_e^{\,2}} \right) \qquad (3.8)$$

defining the "exposure factor" k_e by

$$k_e = \sqrt{1 - (\frac{\pi}{4} d_f \theta \frac{D_c}{D_l})^2} \qquad 0 < k_e < 1$$

For large values of the line dose (k_e close to unity) the width w of the line is nearly equal to the diameter of the defocused beam. For small values of the line dose the factor k_e becomes imaginary, resulting from the fact, that even in the center of the exposed curve the dose is smaller than the critical dose. Consequently, no line at all appears after the development process (w=0).

The practical application of equations (3.7) and (3.8) requires the knowledge of only two parameters, the aperture angle θ of the electron beam and the critical dose D_c. Both can be easily determined by means of short test exposures.

Many physical phenomena influencing the line width are not included in the model described above, resulting in more or less pronounced deviations of the calculated and experimental line-width. This is especially true for thin lines, as equation (3.7) predicts an infinitely small width w for zero defocus. Consequently, neither the finite size of the focused electron-beam nor the finite range of the secondary electrons is taken into account by the model. The model also neglects the influence of the finite resist-thickness, the development process and the subsequent pattern transfer. However, for thick lines all these effects play a minor role resulting in a good agreement between model and experiment (difference less than 10 %) for line-widths above 300 nm [67].

A better agreement (especially for small line widths) can be achieved using an empirical method. The basic idea is to avoid unnecessary defocusing of the electron beam, as for small line-widths the experimental width always exceeds the width predicted by equation (3.7). Consequently, one leaves the line dose D_l unchanged (determined by equation (3.8)) but tries to find a different, empirical formula for the defocus d_f, resulting in a better agreement to the experiment for small values of w. Using the original formula ((3.7)) for the line width w one can write

$$w = k_e d_f \theta + \Delta w \qquad (3.9)$$

where Δw is a correction term, taking into account (at least some of) the discrepancies between reality and the original simple model. Rearranging equation (3.8) one finds

$$w = \frac{4 D_l}{\pi D_c} \left(k_e \sqrt{1 - k_e^{\,2}} \right) \qquad (3.10)$$

Exposing a set of lines with different line doses D_l and zero defocus, at some point the theoretical line width given by equation (3.10) will be equal to the experimental one ($w_{exp,0}$).

Consequently, using equation (3.9) one has the condition that $w=\Delta w=w_{exp,0}$ in this case. The width in equation (3.10) depends on the factor k_e, and therefore different values of k_e will result in different values of $w_{exp,0}$ ($w_{exp,0}=w_{exp,0}(k_e)$).

For large line-widths equation (3.9) has to approach equation (3.7). In conclusion one therefore finds

$$\Delta w \to 0 \qquad \text{for} \quad w >> w_{\exp,0}$$

and

$$\Delta w = w_{\exp,0} \qquad \text{for} \quad w = w_{\exp,0}$$

In principle, one could think of many functions fulfilling these two conditions and realising a smooth transition between these two border cases. Even using very simple functions (e.g. $\Delta w=w_{exp,0}/2$) one can achieve, that the difference in line width between theory and experiment is significantly less than the line width $w_{exp,0}$ (e.g. using $\Delta w=w_{exp,0}/2$ the error will be less than $w_{exp,0}/2$ for all lines). Within this work an exponential function was used to realize such a smooth transition leading to

$$\Delta w = w_{\exp,0} \exp\left(-k_f (w - w_{\exp,0})\right) \qquad (3.11)$$

and rewriting equation (3.9)

$$d_f = \left[w - w_{\exp,0} \exp\left(-k_f (w - w_{\exp,0})\right)\right] / k_e \theta \qquad (3.12)$$

The free fit parameter k_f can be used to minimize the deviations in line width between theory and experiment for a specific set of resist and development parameters (resist type and thickness, type of developer, development time, etc.). The remaining error in line width is typically in the order of 10 nm for thin lines ($w<300$nm) and in the order of 5% for thick lines ($w>300$nm). Equation (3.12) is only valid for positive values of the defocus d_f. In consequence $w_{exp,0}$ represents the minimal line width that can be exposed using this kind of empirical model.

One phenomenon, which has been neglected up to now, but sometimes has a strong influence on the size and shape of exposed patterns, is the so-called proximity effect. The proximity effect results from the fact that a certain fraction of the primary electrons is backscattered by the substrate underneath the resist. This leads to an additional irradiation of the resist in the vicinity of the original electron beam, whereas the range and the number of backscattered electrons strongly depend on the energy of the primary electrons and on the substrate material. Due to the proximity effect the dose at a certain point is influenced (increased) by exposed regions in its vicinity, leading to a distortion and enlargement of the exposed patterns. However, the LION-LV1 e-beam system is capable of performing exposures with electron beams of very low energy ($E_p=2.5$keV for all exposures within this work), resulting in only very short-range proximity effects. Consequently, the line width of an exposed curve (nearly) does not depend on the density of other lines in its vicinity, provided that a sufficiently stable exposure regime is used (meaning that a small change in dose should only result in small change of the size of the resist-pattern). Analysing equation (3.7) and equation (3.12) one finds, that such a stable regime requires values of the factor k_e close to one. In praxis values of k_e in the range between about 0.9 and 0.95 give good results.

3.1.5 PMMA-resist preparation

One pre-requisite for e-beam lithography is the ability to fabricate resist-layers of uniform and well-defined thickness. In praxis this is commonly achieved using the spin-coating technique, were a resist/solvent mixture is applied onto a sample and then distributed by rotating the sample. The thickness of the resulting, highly uniform layer only depends on the type of mixture used and the chosen rotational speed, provided that certain practical conditions are fulfilled (application of a sufficiently large amount of the resist/solvent mixture; reasonable acceleration in order to reach the final rotational speed within a time period were the actual thickness of the resist layer is still much larger than its final thickness). Theoretical consideration in connection with practical testing [68] shows that the final thickness h_r depends on the rotational frequency f via

$$h_r = C_r (f)^{-\gamma_s} \qquad (3.13)$$

The constant C_r depends on the resist/solvent-mixture used and includes physical parameters like the viscosity of the mixture. The factor γ_s describes the (main) frequency dependence of h_r. One often has $\gamma_s \approx 1/2$.

Figure 3.5 shows experimental results for the resist thickness as a function of the rotation speed obtained for the PMMA-resist used within this work.

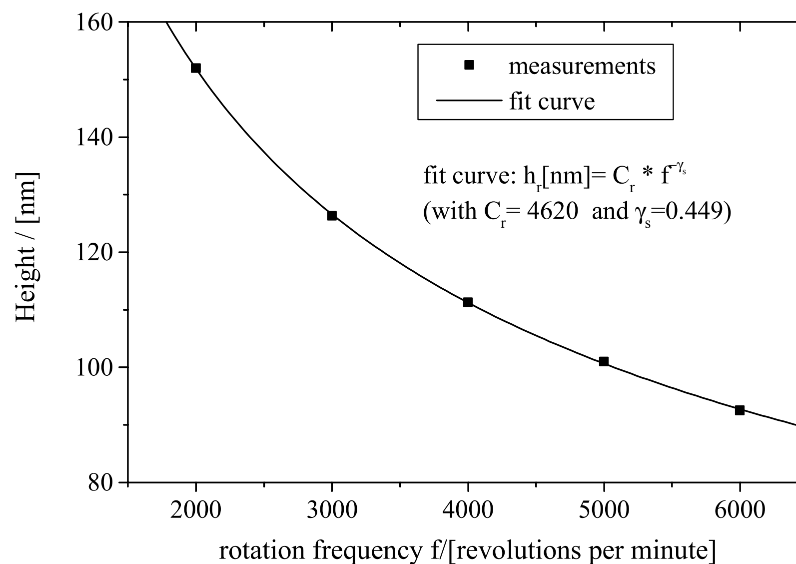

Figure 3.5: Thickness of a PMMA-resist as a function of the rotation frequency of the spin-coating process. The thickness of the PMMA-layer was determined using a surface profilometer (Tencor Alpha-step 200).

Within this work a spin-coater from Karl Süss Technique (CT60) was used to prepare the PMMA-layers for the electron-beam lithography. After the spin-coating process all samples were put onto a hot plate (HT-302, ATV Technologie Gmbh) for about five minutes. The chosen temperature (about 170^0 Celsius) was close to the glass transition temperature of PMMA, enabling the relaxation of strain within the PMMA-layer and the outgassing of residual solvent.

3.2 Thermal evaporation of thin layers

One important step for many micro-fabrication techniques is the deposition of thin layers of various metals and dielectric materials. One simple method of fabricating such layers is to evaporate materials in a vacuum using electrically heated evaporation boats. The heating of the material within such a boat (which is often associated with the melting of the material) leads to the emission of atoms (molecules, clusters) in all directions. The low pressure of the vacuum chamber (typically about 10^{-6} mbar) prevents collisions with atoms of residual gas in the chamber, so that the atoms undergo a ballistic motion till they hit some part of the vacuum chamber or a properly placed substrate, finally leading to the formation of a thin layer of the corresponding material.

The method of thermal evaporation is restricted to materials having a boiling point (or sublimation point), which is well below the melting point of the evaporation boat. Consequently the boats are typically made of materials like W and Ta as they both have very high melting points. Another restriction originates from the fact, that some materials form alloys with the boat material causing a fast degradation and finally the destruction of the boat.

Within this work an evaporation system from Balzers (BAE 250T) was used for the fabrication of thin layers of chromium, aluminium, silicon and palladium. Two thermal evaporation boats can be simultaneously mounted in the BAE 250 T enabling the fabrication of several layers (of two different materials) without intermediate venting of the system. A built in, mechanical shutter makes it possible to accurately control the duration of the evaporation process. The thickness of the deposited layers can be controlled using a built-in film thickness monitor. Like in most evaporation systems this monitor is based on the frequency change of a piezoelectric oscillator, caused by the additional mass in the oscillating system, when a layer is evaporated onto one of the surfaces of the oscillator.

3.3 Plasma etching

Many micro-fabrication techniques involve the use of a resist-mask, which is then transferred into the substrate by means of etching or also the deposition of material. One commonly used etching method to remove material in unprotected regions (regions with no resist) is the plasma etching technique. Plasma etching, which is also referred to as reactive ion etching (RIE), utilizes the reactive atoms, molecules and ions originating from a plasma, which is generated in a suitable gas mixture of low pressure (in the order of a few mTorr) by means of a radio-frequency gas discharge between two electrodes. If the size (area) of these two electrodes is different this results in the formation of a constant electric potential between the plasma and the electrodes (the so-called self-bias voltage, see [69]). In consequence, positively charged molecules and atoms will be accelerated towards the sample (which is normally placed on the smaller, negatively charged electrode). This directional beam of reactive ions results in an anisotropy of the etching process (anisotropic etching) with an enhanced etch rate along the direction of the beam and therefore perpendicular to the sample surface. Besides reactive ions the plasma also generates a certain amount of neutral reactive atoms and molecules (radicals). These radicals are not influenced by electric fields and therefore cause an isotropic removal of the sample material (isotropic etching, see also Figure 3.6).

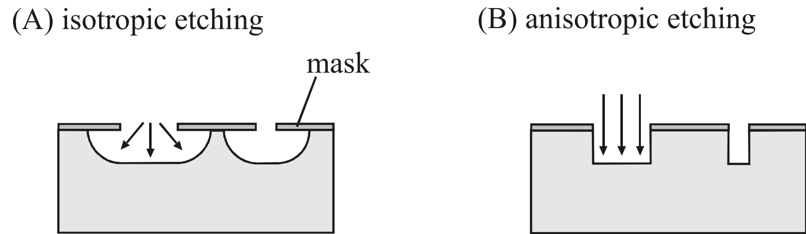

Figure 3.6: Schematic sketch of different etch profile obtained by plasma etching showing the case of non-directional (isotropic) etching (A) and the case of directional (anisotropic) etching (B). In praxis the anisotropic etch characteristic shown in (B) is achieved using etch processes with high bias-voltages in connection with etch gas mixtures that lead to the deposition of a passivation polymer layers on the sample surface.

In any case the etching result always strongly depends on the mixture of etch gases that is used for the etch process. Simple processes typically use only one type of reactive gas (maybe in connection with an inert carrier gas) and often have a low anisotropy, especially if only a small self-bias voltage is generated within the system (isotropic etching, see Figure 3.6 A). More sophisticated processes normally utilize several types of gases, where some components cause an etching of the material, whereas other components lead to the deposition of a passivation layer (e.g. a polymer) on the surface of the sample. In connection with the etching anisotropy caused by a high-bias voltage this can lead to an equilibrium state between the deposition and etching of material at sidewalls (regions perpendicular to the surface), whereas other parts (regions parallel to the sample surface) are still etched (anisotropic etching, see Figure 3.6 B). Other important parameters influencing the etching result are the gas pressure, the gas flow (commonly specified in standard cubic centimetre per second - sccm), the supplied RF-power and the substrate temperature.

Within this work several types of plasma etching/reactive ion etching machines were used for different kind of applications. For the etching of thin chromium layers and partly for the etching of polymers and silicon a BMP Plasmafab 100 from BMP was used. The two electrodes of the BMP are of equal size, leading to a negligible bias-voltage and consequently a more or less isotropic etching characteristic of the machine. Four gas lines (Cl_2, CO_2, O_2, SF_6), each of them equipped with a gas flow controller, enable the processing of many different types of materials (e.g. a chlorine based process with Cl_2:CO_2=1:1 was used as a standard technique for transferring a PMMA-mask into a chromium mask, removing the chromium in unprotected regions with no PMMA-resist).

Structuring processes requiring highly anisotropic etching characteristics (enabling the fabrication of structures with high aspect ratios) were performed with an Oxford Plasmalab 100 from Oxford Instruments. Using high RF input powers and low gas pressures it is possible to achieve the necessary high self-bias voltages (typically several hundred Volts). The provided gas lines (SF_6, CHF_3, O_2, $CBrF_3$, Ar; He as a cooling gas) make the Oxford suited for materials, which can be etched by fluorine-based processes (e.g. Si and Ta) as well as oxygen based processes (e.g. PMMA, photo-resist). A special feature of the Oxford is the fact, that liquid nitrogen is used for the cooling of the system. For special applications this opens up the possibility to perform etching processes at temperatures down to about 150 Kelvin.

4 Fabrication of multilevel zone plates

4.1 General considerations

It was already mentioned earlier that most diffractive x-ray lenses (zone plates) used for practical applications are binary zone plates (having a simple grating design with only two different height levels of the grating structure). This is mainly due to practical reasons, as the fabrication of binary zone plates by means of micro-lithography techniques requires only one single lithography step, making the fabrication process relatively simple. Another reason to favour binary zone plates is the fact, that using more sophisticated grating designs does not necessarily result in a better performance (higher diffraction efficiencies) of the lens. In fact the theoretical considerations in chapter 2.2.6 showed, that for high levels of absorption (small δ/β) all grating profiles (including the binary and the optimum profile) yield more or less the same diffraction efficiency. However, in the hard x-ray range, where absorption is often negligible small (large δ/β), the use of different grating designs (e.g. multilevel gratings) offers the potential to strongly increase the diffraction efficiency.

One important issue for the fabrication of any type of diffractive optical element in the hard x-ray region is the fact that (although the ratio δ/β is large) the absolute value of δ is very small. Consequently, the diffracting structures have to be very high in order to achieve the necessary phase shift for an optimum performance of the device. For zone plates the required phase shift is typically of the order of 2π corresponding to a structure height of about 1-100 microns (depending on the grating material and the chosen hard x-ray energy). At the same time grating periods in the sub-micron range are required to achieve a sufficient deflection of the incoming x-rays. This results in the demand to fabricate diffracting structures with (sometimes extremely) high aspect ratios.

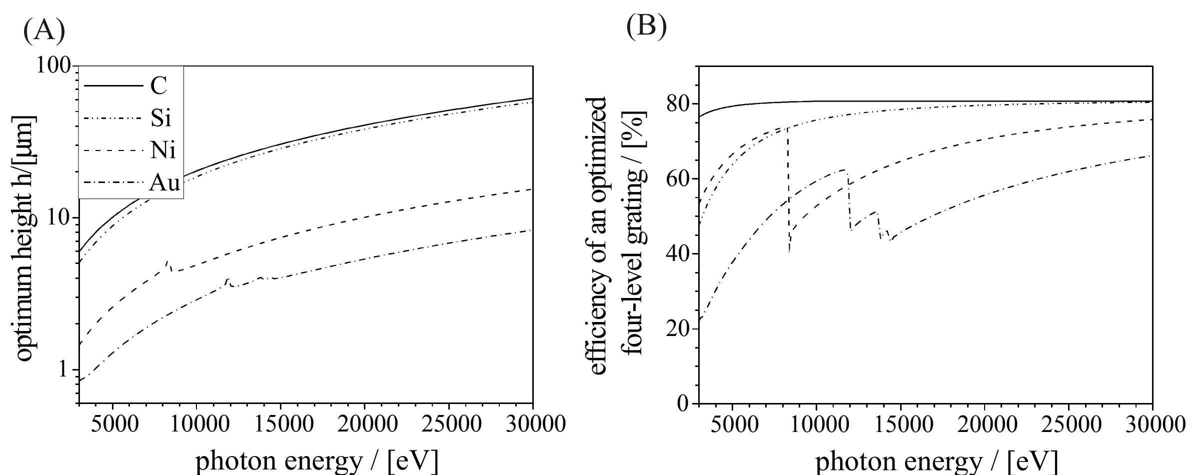

Figure 4.1: (A) Calculated optimum height of a four-level grating resulting in maximum first order diffraction efficiency, shown for different types of materials. The height was calculated using the results from chapter 2.2.6 together with the optical data (δ/β) from reference [45]. (B) Resulting first order diffraction efficiency for an optimal four-level grating.

Such high aspect ratios can be partly avoided using materials with high density (e.g. Au, Ni) as they have a comparatively high decrement of the refractive index δ (see equation (2.26)), resulting in less extreme structure heights. Consequently, the first multi-level zone plates, which have been reported recently [70, 71, 72], were nickel and gold zone plates, designed for photon energies between about 5 and 8 keV. These zone plates were made by means of x-ray lithography and subsequent electroplating, resulting in diffraction efficiencies up to 55% (at 7 keV), for zone plates having a minimum period of 2 μm.

However, materials like gold or nickel have the disadvantage that only for certain regions in the hard x-ray range absorption can be neglected (see Figure 4.1 A). The situation is different for materials with low atomic number (e.g. C, Si), where the energetically highest absorption edges are well below the hard x-ray region (e.g. at 1.8 keV for Si), resulting in efficiency values close to the theoretical limit of 81%. Unfortunately these elements typically also have a low density and consequently extreme optimum structure heights (typically above 10 μm) are required (see Figure 4.1 B).

Both problems, extreme aspect ratios and material absorption, can be avoided using linear zone plates made of silicon in connection with a technique that has been patented by the Paul-Scherrer-Institut, Switzerland ([73], see also Figure 4.2). The principle of this technique is to tilt the zone plate with respect to the x-ray beam, resulting in a strong increase (typically factors up to 20) of the effective light-path length h_{eff} through the grating structures. A change of the tilt angle enables the tuning of the effective height of the grating structures and consequently it is possible obtain optimum efficiencies over a large range of x-ray energies.

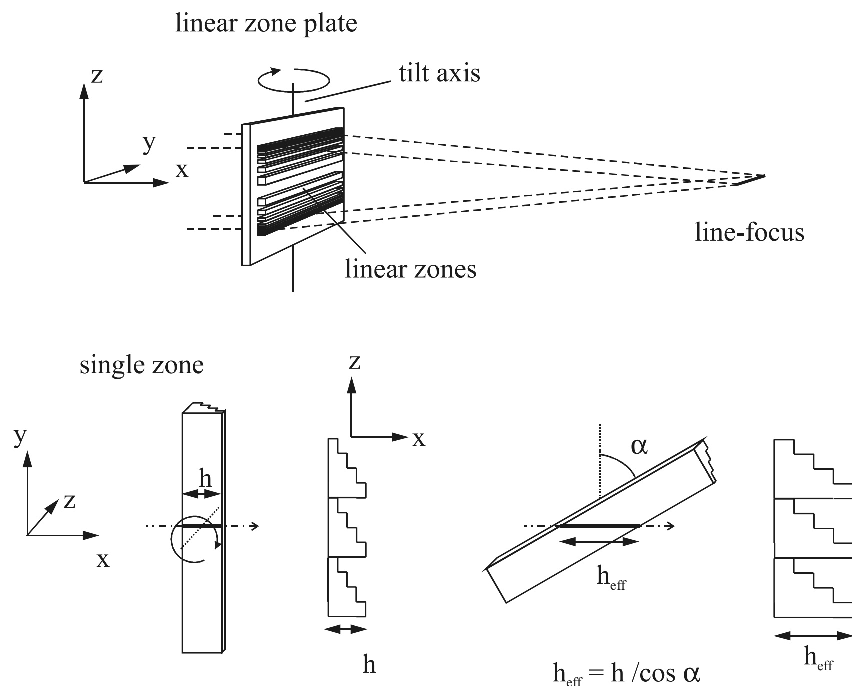

Figure 4.2: Illustration of the tilting method used within this work, enabling a strong and adjustable increase of the effective height of the multilevel grating structures within a linear zone plate.

Obviously this tilting technique is not restricted to linear zone plates, but can be used for any kind of diffracting optical element, provided that this element has linear diffracting structures, which are parallel with respect to each other (see [41], [42] and [43]).

Note, that the tilting only changes the effective height but not the shape of the grating. Consequently the widths and heights of the individual grating levels can only be optimised for one single value of δ/β of the grating material. However, for many materials absorption is negligible for a large range of x-ray energies, so that the profile optimised for zero absorption can be used without a significant loss in diffraction efficiency. In the case of silicon for example one finds that this loss in diffraction efficiency becomes negligible (less than one percent) for x-ray photon energies above 5keV.

Tilting a linear zone results in a tilted line focus (see Figure 4.2). In general this will cause aberrations, when a linear zone plate is used in an optical set-up. However, for the photon energies and the lenses used within this work the depth of focus was sufficiently large so that the tilt of the line focus had no influence on the optical performance of the lenses.

Linear zone plates act as cylindrical lenses, focusing only in one direction, and consequently two lenses have to be used in series in order to obtain 2-dimensional focusing. Compared to a conventional zone plate this has the disadvantage that losses (absorption, unwanted diffraction orders) within two optical systems have to be considered. However, it will be shown later on that this disadvantage can be counterbalanced by the possibility to match such a focusing device to the asymmetry of synchrotron sources (see chapter 5.2.1).

These evident advantages of linear multilevel zone plates made from silicon, were the motivation to develop a suitable fabrication process. The different steps of this development, finally resulting in the successful fabrication of zone plates with unprecedented diffraction efficiencies are shown in the chapters 4.2- 4.5. Chapter 5 describes the optical testing of the resulting lenses, including efficiency measurements (see chapter 5.1) and resolution tests (see chapter 5.2).

4.2 Principle of the fabrication process

The fabrication process used within this work is based on a micro-fabrication technique that has been developed and patented by the Paul-Scherrer-Institut (Switzerland) [74]. It allows the fabrication of more or less arbitrarily shaped multilevel structures using a special kind of metal mask in connection with plasma etching of suitable sample materials (e.g. Si, SiO_2 etc.). The principle of this process is shown in Figure 4.3 and Figure 4.4.

In the first part of the process e-beam lithography is used to fabricate a combined Al/Cr-mask as shown in Figure 4.3. PMMA-resist is first spun on a silicon sample and structured by means of e-beam lithography. The resulting PMMA-mask is then transferred into a thin chromium-layer using plasma etching. After a second exposure an aluminium layer is thermally evaporated onto the sample. Finally, parts of this aluminium layer are removed in a lift-off process, where acetone is used to dissolve the PMMA underneath the aluminium layer.

In the second part (see Figure 4.4) of the process the obtained Al/Cr layers act as an etch mask for the reactive ion etching of silicon using a fluorine containing plasma. Parts of this Al/Cr-mask are selectively removed between subsequent steps of silicon etching, resulting in different etch times for different regions of the sample. Consequently, a structure profile with four levels is obtained after three subsequent steps of silicon etching.

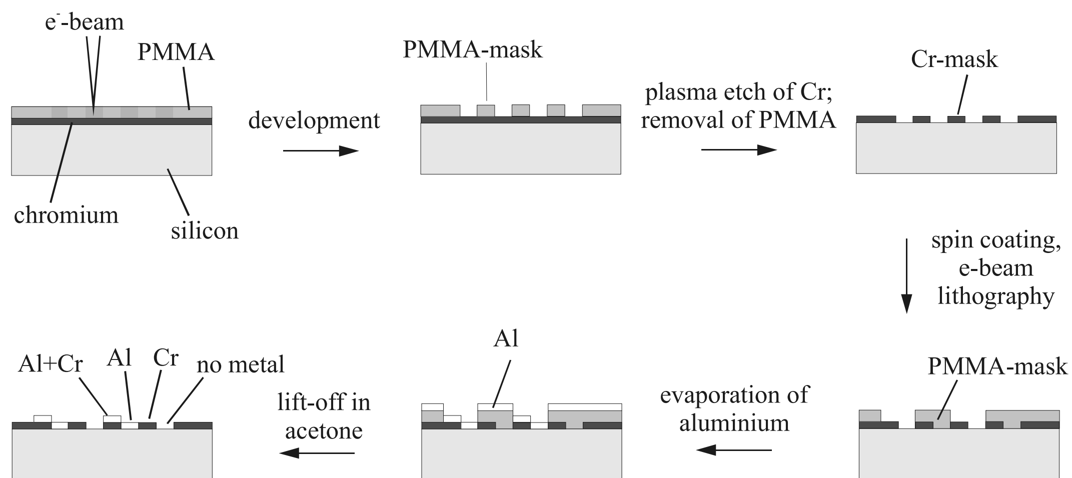

Figure 4.3: Fabrication process of a combined Al/Cr-mask using electron beam lithography

One main advantage of this process is the fact, that thin layers of chromium and aluminium are sufficient (typically in the 10 nm range) to withstand the subsequent etch (structuring) processes. Consequently, all lithography steps that are required to obtain the combined Al/Cr-mask can be performed on flat sample. This is in contrast to conventional fabrication techniques, where one lithography step (to define the mask) is followed by one structuring step (to remove or add structure material) and both procedures are then repeated several times, in order to achieve a multi-level structure (see e.g. [57]). In the latter case some lithography steps have to be performed on already structured samples, leading to considerable practical problems, especially if the fabrication of structures with high aspect ratios is required.

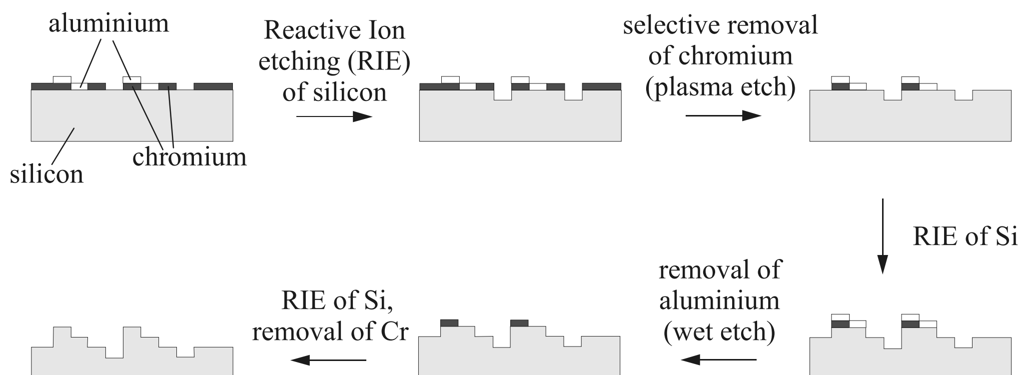

Figure 4.4: Principle of the reactive ion etching process used within this work for the fabrication of multilevel zone plates.

4.3 Overlay

One prerequisite for the successful fabrication of multilevel zone plates is a distinct sequence of different mask regions (see Figure 4.3). Consequently, the two electron-beam exposures, defining the position of the chromium containing part and the aluminium containing part of the mask, have to be aligned with respect to each other.

Such aligned exposures (overlay exposures) are commonly accomplished using suitable alignment marks, whose position is detected by sweeping the mark with the electron beam and measuring the amount of secondary electrons, which are emitted from the sample.

Within the LION-LV1 lithography tool alignment marks are swept along lines. Using built in, automated analysis routines it is then possible to evaluate the position of an alignment mark boundary, provided that the region within the alignment mark yields a significantly different amount of secondary electrons than the region outside. Consequently, sweeping a mark in different positions and directions it is possible to determine the coordinates of the alignment mark (see Figure 4.5). The coordinate system defined by two of these marks can then be used to perform two exposures at the same position of a sample.

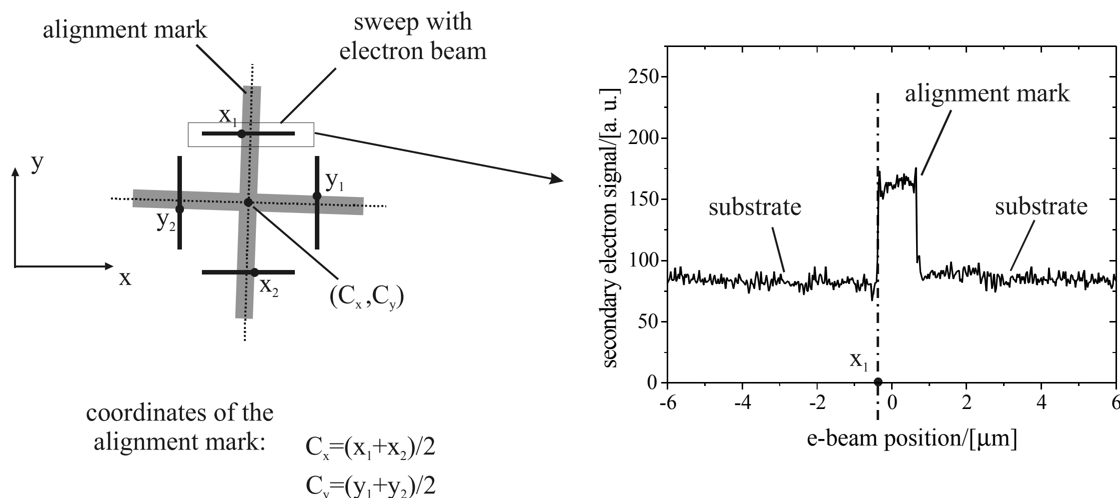

Figure 4.5: Principle of the automated detection of alignment marks within the LION-LV1 lithography system. Sweeping a mark with the electron beam in different positions and directions yields a set of coordinates (x_1, x_2, y_1, y_2) that can be used to determine the position (C_x, C_y) of the center of the alignment mark. Not that in general the coordinate system defined by the alignment marks is tilted with respect to the coordinate system (x,y) of the sample stage. The resulting tilt of individual marks requires a careful choice of sweep positions, sweep directions and evaluation strategy in order to obtain highly accurate coordinate values of the alignment mark center.

The high positioning accuracy of the sample stage and the high accuracy of the sweeping procedure enable aligned exposures with an overlay error (difference in position of the two exposures) in the 10 nm range. However, in praxis several conditions have to be fulfilled in order to get at least close to this value.

One important prerequisite is the fabrication of alignment marks of high quality. To ensure a reproducible detection of the mark boundaries the mark material has to provide either a significantly higher or a significantly smaller yield of secondary electrons than the sample.

Within this work pure silicon samples or silicon samples coated with a thin chromium layer were used. Both types of substrates consist of materials with low atomic number, resulting in comparatively small yield of secondary electrons. This made materials with high atomic number - having a high yield of secondary electrons - favourable for the fabrication of alignment marks.

In a first attempt it was therefore tried to fabricate tantalum alignment marks by means of e-beam lithography and sputtering of a thin (approximately 20 nm) tantalum layer. The subsequent lift-off process resulted in alignment marks with a strong secondary electron signal and therefore in a strong contrast between regions with and without tantalum (see Figure 4.6). However, the boundaries of the tantalum marks were extremely rough, making the marks unsuitable for the automated position detection by means of sweep-routines. This roughness supposedly originates from a connection between the tantalum layer on the PMMA and the tantalum-layer on the substrate, so that the tantalum on the PMMA-mask is not completely removed during the lift-off process.

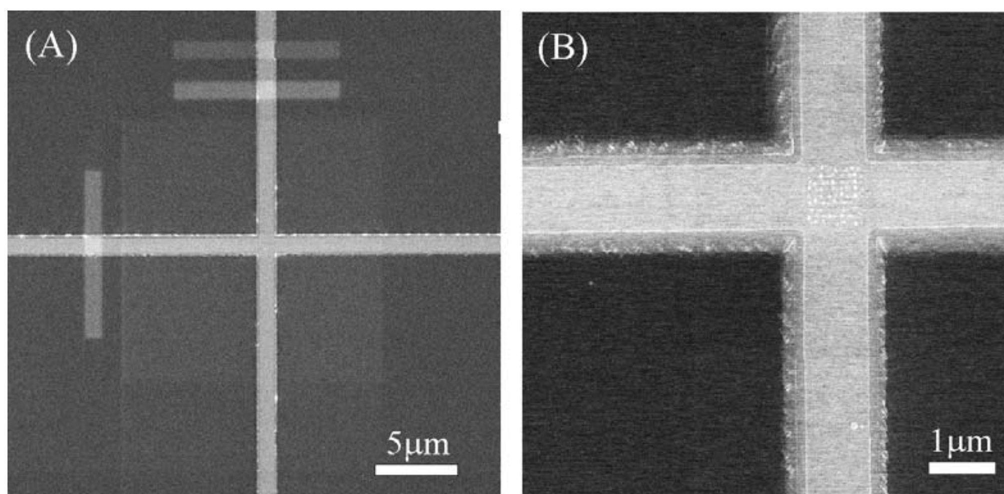

Figure 4.6: SEM-pictures of tantalum alignment marks with a PMMA-layer (A) and without any PMMA (B) covering the alignment mark. The bright rectangular stripes in the left picture represent PMMA-regions that have been exposed by the electron beam for a long time, resulting in an increased yield of secondary electrons – and therefore increased brightness.

Such an incomplete lift-off process is a problem that often occurs in connection with sputtering, as the sputtering process involves a homogenous, non-directional deposition of material. In the following it was therefore tried to use the thermal evaporation of a suitable material instead of sputtering, as in this case the deposited material originates only from a small area (the evaporation boat) in space. This results in a vertical deposition of material onto the sample and consequently normally avoids problems with the lift-off process.

One suitable material for the fabrication of alignment marks by means of thermal evaporation is palladium. Compared to other materials like gold, palladium has the advantage that it is compatible to electronic grade silicon, meaning that small amounts of palladium do not interfere with standard fabrication processes for micro-electronic devices. This is different for materials like gold, where even a small amount of material can completely change the electronic properties of silicon, leading to a malfunction of electronic devices. Consequently samples containing gold are not allowed in areas of a clean room, which are used for the fabrication of electronic devices.

One disadvantage of palladium is its comparatively high melting and evaporation point (1825 K and 3200 K respectively), making it difficult to handle in thermal evaporation systems. Consequently, a special tungsten evaporation boat was used where the palladium is heated up within a small aluminium oxide or boron nitride jar (a so called liner). It turned out that boron nitride liners cause troubles as the heated, liquid palladium is sprayed in tiny drops, which are emitted into the vacuum chamber of the evaporation system. However, using aluminium oxide liners and by carefully heating up the evaporation boat to the minimal required temperature, it was possible to successfully evaporate thin layers of palladium.

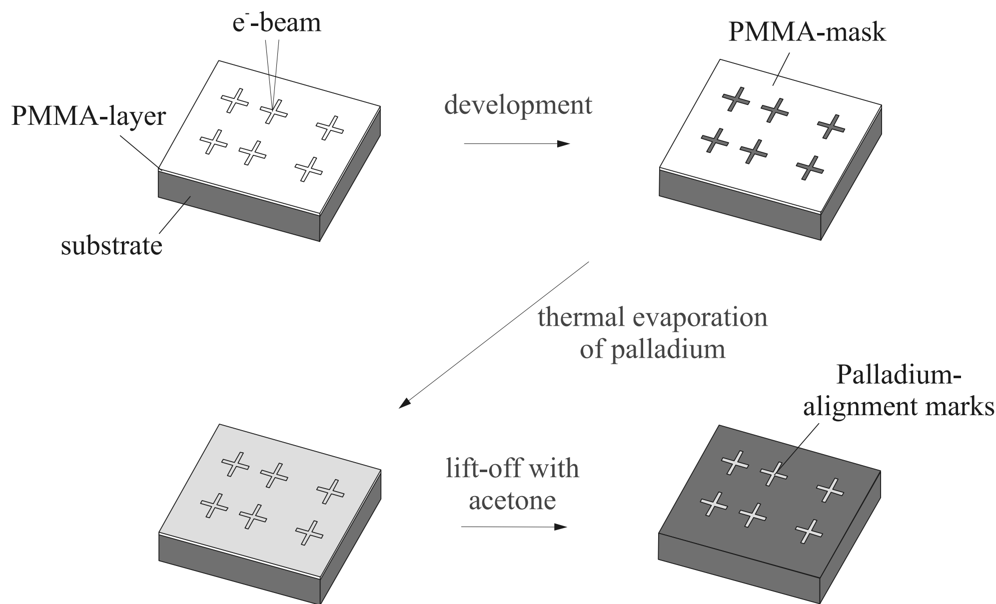

Figure 4.7: Fabrication process of palladium alignment marks

Figure 4.7 shows in detail the resulting process for the fabrication of palladium alignment marks. In a first step an approximately 150 nm thick layer of PMMA (see also Figure 3.5) was spun on the sample. The PMMA-layer was then structured using e-beam lithography. In a next step a thin adhesion layer of chromium (about 5 nm) together with an approximately 15 nm thick layer of palladium were thermally evaporated onto the sample. Afterwards most of this chromium/palladium layer was removed by a lift-off process in acetone, resulting in the formation of palladium alignment marks of high quality (see Figure 4.8). To ensure a successful and complete lift-off the samples had to be left in the acetone bath for a relatively long time (typically one night). In addition a mild ultrasonic treatment was used to facilitate the lift-off process. Occasionally the lift-off process was incomplete, so that some of the alignment marks could not be used for overlay procedures. However, this problem could be easily solved, as alignment marks are very small compared to the total size of the sample, making it possible to use a redundant design with several sets of alignment marks. Figure 4.8 shows SEM-pictures of the resulting palladium marks, revealing the small roughness of the mark boundaries and the good contrast of the secondary electron signal between the alignment mark and the substrate underneath.

One other important issue for the achievement of high overlay accuracies was the mounting of the samples during the two overlay exposures. For the overlay exposures a titanium adapter-plate was used, onto which the samples were fixed by means of clips made from tungsten wire. Immoderate tightening of the screws holding these clips resulted in stress and consequently a distortion of the sample. Test measurements of the positions of several sets of

alignment marks showed, that a strong sample fixation leads to mark displacements up to several 100 nm. Consequently, overlay errors in the same order of magnitude have to be expected. However, the problem could be solved to a large extent by carefully fixing the sample, applying as little force with the clips as possible.

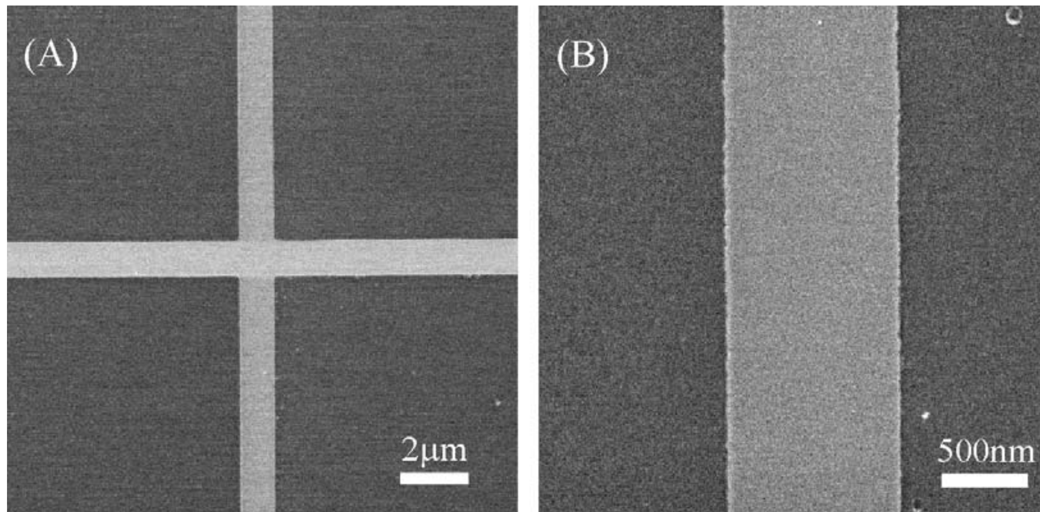

Figure 4.8: (A) SEM-picture of a palladium alignment mark fabricated by e-beam lithography and thermal evaporation of palladium. (B) Close-up of the alignment mark revealing the small roughness of the alignment mark boundaries.

Another problem interfering with the goal of a stable and accurate overlay exposure is the fact, that a PMMA-layer on a sample decreases the yield of secondary electrons and significantly lowers the contrast between an alignment mark and the substrate underneath. In particular it is a problem, that the irradiation of the PMMA during sweeping an alignment mark modifies the PMMA and leads to an increase of the secondary electron signal (see also Figure 4.6 A). This makes it very difficult to find parameters that enable a stable automated detection of alignment marks.

Obviously the only possibility to fully avoid these problems is to get rid of the PMMA covering the alignment marks. This was accomplished using reactive ion etching of the PMMA in an oxygen plasma (Oxford; 10 sccm O_2, 20 mTorr, 200 Watt, resulting bias voltage: approx. 570 Volt, etch time for 150 nm PMMA: 2 min). During the etch process parts of the PMMA-layer were protected by covering the sample with small pieces of a silicon wafer. A gap of typically 0.5 mm was left between the substrate and such a “protection cover” to avoid damage to the sample. The high anisotropy of the etch process resulted in a relatively small transition region (approx. 1 mm) between protected regions and regions, were the PMMA was totally removed.

Using this kind of process it was finally possible to reach an overlay accuracy of about 100 nm. Besides distortions of the substrate a significant part of the remaining overlay error was supposedly caused by thermal drift of the sample holder during the exposure. Tests showed, that the position of an alignment mark drifts up to 100 nm per hour. At the same time the exposure of one zone plate typically took up to about 20 minutes. Consequently, the effect of thermal drift was normally not tremendous but under unfortunate circumstances could nevertheless badly influence the result of an overlay exposure. It was therefore essential to check regularly, that the built in temperature stabilization system of the LION-LV1 e-beam system was working properly. It was also avoided to start an exposure just after the sample

was transferred into the chamber of the e-beam system in order to allow the sample to settle and get in thermal equilibrium with the whole system (the exposure was typically started two hours after this transfer).

It will be shown later on, that the fabrication of multilevel zone plates of high quality requires overlay accuracies in the order of 30 nm. Taking into account the typical alignment errors mentioned above it is hardly possible to fulfil this condition for a single exposure. Fortunately the required time to expose one zone plate is relatively short and the exposed areas are small compared to total sample area, enabling a sufficiently large number of trial exposures. Due to the nature of linear zone plates only displacements perpendicular to the direction of the linear grating structures play a role. Consequently, it was sufficient to expose a set of five or six zone plates next to each other. By deliberately displacing each zone plate by a different amount for one of the two overlay exposures, a sufficiently small overlay error could be achieved for at least one of the zone plates.

This trial and error strategy requires, that the coordinate systems of the two overlay exposures are only displaced but not tilted with respect to each other. In most cases this tilt could be kept sufficiently small using a comparatively large distance (5-6 mm) between the two alignment marks defining the coordinate system of an exposure.

4.4 Reactive ion etching of silicon

One important step for the fabrication of multilevel silicon zone plates is the structuring of silicon by means of reactive ion etching. The etching process has to be highly anisotropic in order to achieve grating profiles with high aspect ratios.

Within this work a Oxford Plasmafab 100 Reactive Ion Etching system was used for this purpose. The necessary anisotropy of the etching process is obtained using a mixture of basically two gases. One of them, sulphur-hexafluoride (SF_6), strongly etches silicon due to its high content of fluorine, whereas the other gas - freon-23 (CHF_3) - leads to the deposition of a polymer-like protection layer on the silicon, resulting in very low etch rates despite of its high fluorine content. Using a mixture of both gases it is possible to achieve a balance between the etching of silicon and the deposition of a protection layer, resulting in an anisotropic etching process.

The first etch tests were based on a standard recipe for the Oxford RIE-system, used within our group, if anisotropic etching of silicon samples is required. The characteristics of the corresponding process are a high bias voltage (approximately 600 Volt), high input power (200 Watt), low gas pressure (20 mtorr), a balanced mixture of SF_6 (4 sccm) and CHF_3 (40 sccm) and a small amount of oxygen (5 sccm O_2).

One problem encountered during the first etch tests was the fact, that the selective removal of the chromium as well as the aluminium part of the etch mask did not work properly.

In the case of aluminium it had already been observed in earlier experiments that a aluminium mask can not be removed by means of wet etching once it has been used as an etch mask for reactive ion etching in the Oxford RIE-system. This etch resistivity is obviously caused by some kind of protection layer on the aluminium stemming from the RIE-process. It was found that this layer is removed if the sample is put into 80 ^{0}C hot water for about 5 minutes, as after this treatment the aluminium mask is again removable by means of wet etching.

The first etch tests revealed a similar phenomenon for the selective removal of the chromium part of the etch mask. Analogous to the case of aluminium it was found that chromium can

not be removed by means of plasma etching once it has been used as an etch mask in the Oxford RIE-system. This etch problem could be solved in the same way as for the aluminium mask - by putting the sample into hot water for a few minutes. However, in contrast to aluminium masks only a few chromium masks exhibited this kind of etch resistivity. Further investigations led to the astonishing result that a sapphire disc, which is conventionally used within the Oxford-system to place small samples onto it, was at the origin of these problems. Only samples that had been placed on this disc showed an abnormal etch resistivity of the chromium mask. It was therefore easy to avoid this kind of problem by using a silicon wafer coated with chromium instead of the sapphire disc.

Already the first etch test showed that the standard recipe for anisotropic silicon etching mentioned above is not suited to achieve grating structures of high quality. Its etch characteristic turned out to be too isotropic, resulting in a relatively strong horizontal etch component (under-etching). Consequently, in the subsequent tests the SF_6 content of the etch gas was successively decreased, whereas all other process parameters were kept constant. It was found that a maximum content of 1 sccm of SF_6 is tolerable for good etch results (see Figure 4.9).

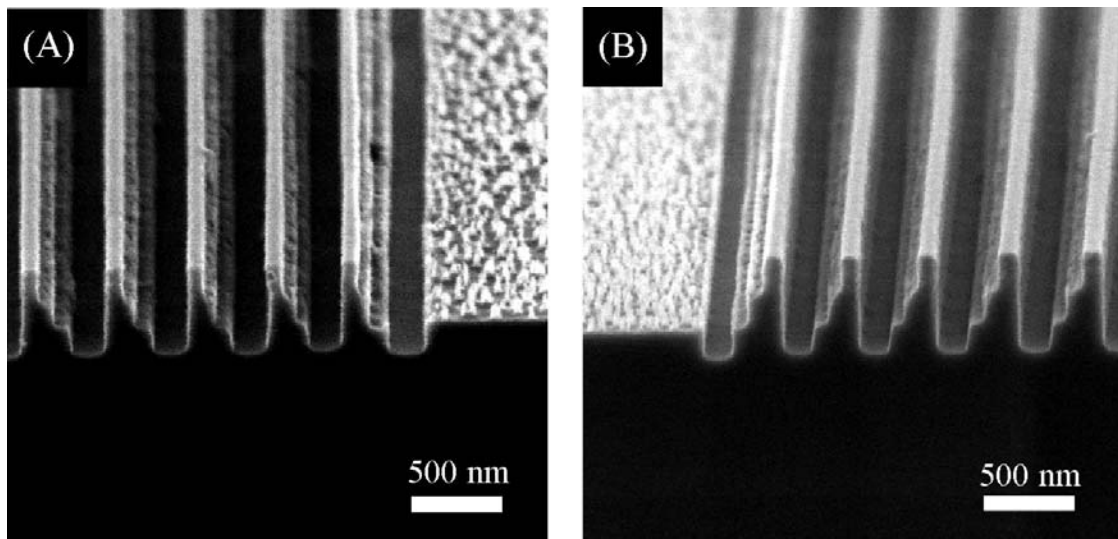

Figure 4.9: Sem-pictures showing the cross-sections of two test-gratings. Both gratings were etched with the same RIE-process parameters apart from a different content of SF_6 in the etch gas. In picture A (etched with 2 sccm of SF_6) still a significant under-etching can be observed, whereas the grating structures in B (etched with 1 sccm of SF_6) nearly perfectly resemble the ideal four level profile.

In order to further improve the etch process other parameters like the oxygen content of the etch gas, the gas pressure, and the supplied power were varied. However, none of these tests lead to an improvement of the etch characteristics of the process. The best etch results were finally obtained utilizing a multi-step process, where for one etch-step 1sccm of SF_6 and for the subsequent step no SF_6 at all is used. The reason to apply such a process instead of a single step - with a SF_6 content between 0 and 1 sccm - was the fact, that such low SF_6 gas flows are difficult to set in a reproducible manner using the built-in gas flow controllers.

The four-level grating structures shown in Figure 4.9 B already closely resemble the ideal multilevel profile optimised for zero absorption, so that high diffraction efficiencies should be feasible with such a grating. However, the structure height is comparatively small (approx.

600 nm). Consequently a strong tilting of the zone structures would be required in order to obtain optimum diffraction efficiencies for photon energies beyond 10 keV. It will be shown later on that several practical reasons limit the increase in effective height, which can be achieved by tilting, to a factor of about 20. Considering the optimum silicon grating height in this energy region (e.g. 24 µm at 12.4 keV photon energy, see Figure 4.1) this results in the requirement to fabricate grating structures with a height above 1 µm.

Subsequent etch tests showed that the original mask design, using a Cr-layer of 25 nm and an Al-layer of 35 nm thickness, was not suited to withstand a significantly prolonged etch process. Especially, the aluminium layers, which are part of the etch mask, undergo strong erosion during the reactive ion etching of silicon. Consequently, in order to achieve a structure a height of about 1.5 µm it was necessary to use very thick aluminium layers (above 70 nm). Chromium was found to be much more resistant to the silicon RIE etch process, so that the original thickness of the chromium layer of the mask could be retained.

For some etch tests even a layer of 70 nm aluminium was not sufficient, resulting in a failure of the aluminium mask and consequently in the formation of grating structures of bad quality (see Figure 4.10 A). Much better results were obtained with a slightly modified process, using a thin chromium layer (20 nm) on top of the aluminium layer (50 nm). The chromium layer protects the aluminium during the first structuring step of silicon and is then removed in the subsequent processing step - where all unprotected chromium layers are removed by means of plasma etching (see also Figure 4.3 for comparison). The aluminium-layer has to withstand only one single (the second) structuring step of silicon. Consequently, a relatively thin etch mask (25 nm Cr and 50+20 nm of Al/Cr) is sufficient to obtain structure height of 1.5 µm (see Figure 4.10 B).

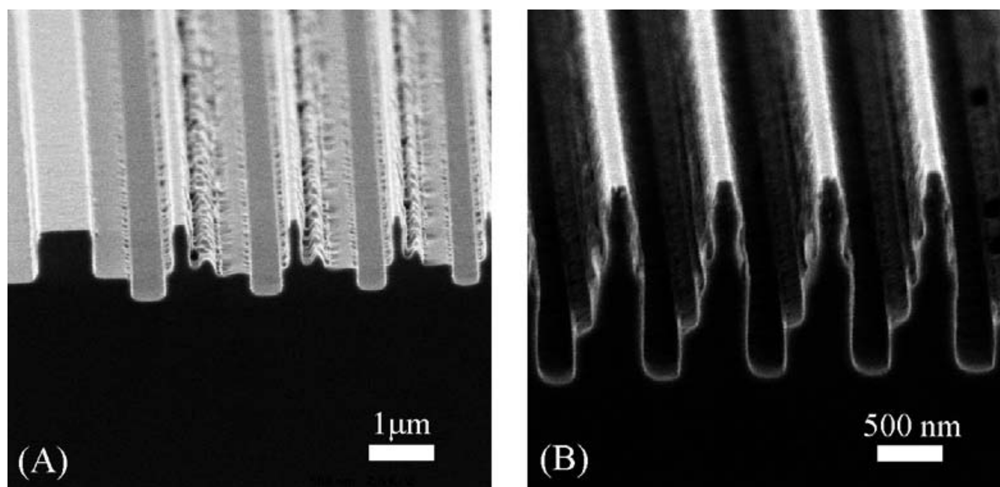

Figure 4.10: (A) Grating after a RIE structuring test, where the 70 nm thick aluminium layer of the mask failed due to mask erosion. (B) Grating with improved mask design using a 20 nm thick chromium protection layer on top of a (in this case only) 50 nm thick Aluminium layer.

In order to obtain high quality grating structures for small grating periods down to about 800 nm it is necessary to take into account the isotropic component of the etch process as well as the horizontal (parallel to the sample surface) mask-erosion at the edges of the mask, both leading inevitably to some under-etching. This under-etching can be compensated using an improved mask design, where the widths of different mask regions are modified accordingly. Assuming that the amount of under-etching is the same for each of the three RIE-structuring processes one obtains mask-designs like the one shown in Figure 4.11 A. Figure 4.11 B

shows a test grating utilizing this kind of pre-compensating mask design for the optimisation of the etch result. The chromium part and the aluminium+chromium part of the etch-mask had slightly different grating periods (800 and 808 nm). Consequently, at a certain point the two mask parts were ideally aligned, whereas for all other positions the two masks were displaced with respect to each other period. Considering Figure 4.11 B one finds, that within a region of approximately eight subsequent periods the grating structures closely resemble the ideal four-level profile. This corresponds to the requirement to reach an alignment accuracy of about 30 nm in order to obtain high quality grating structures for grating periods down to 800 nm.

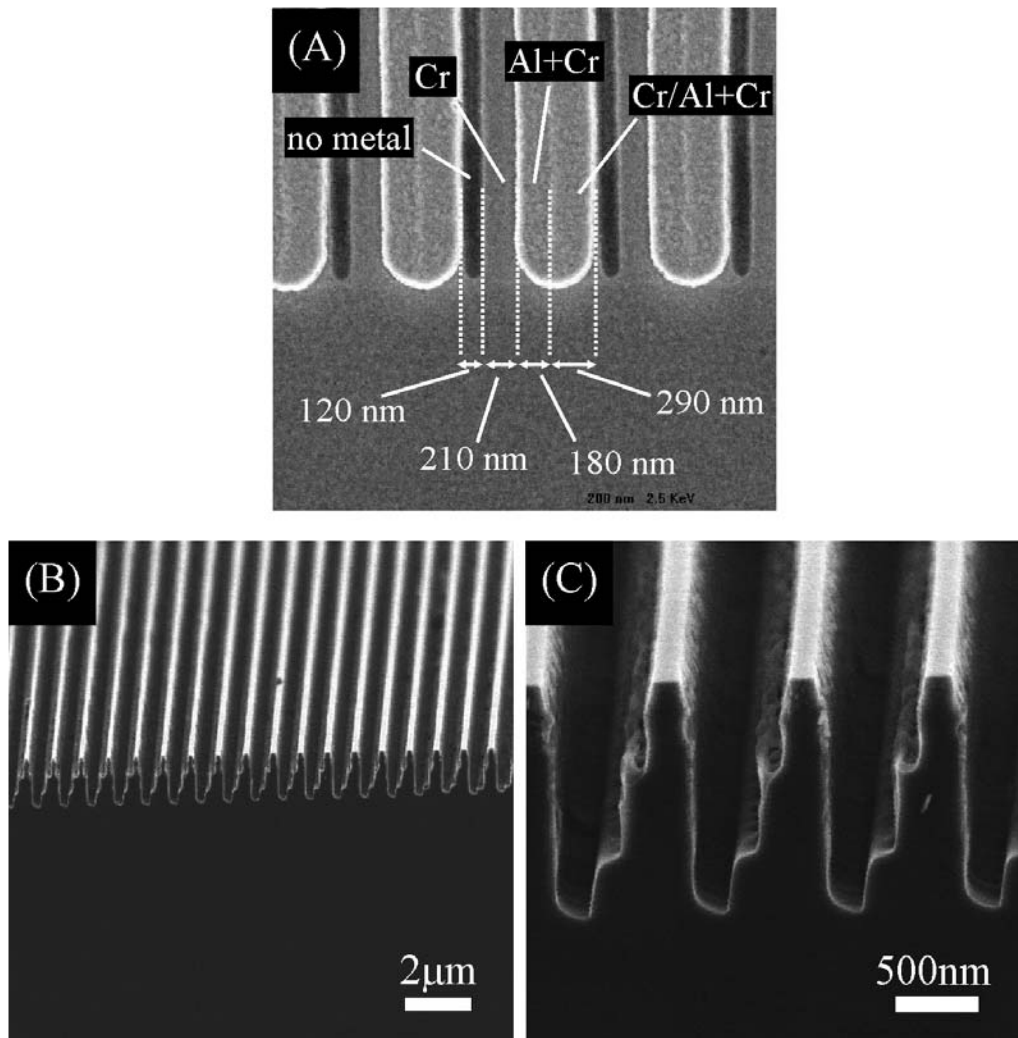

Figure 4.11: (A) Compensation of under-etching using an improved mask design. The measured widths of different mask regions are close (±10 nm) to the ideal calculated widths, assuming an under-etching of 13.3 nm for each RIE-structuring step. (B) Cross-section of a grating using the mask design shown in picture A. In order to see the influence of an overlay error the chromium part and the aluminium+chromium part of the mask had slightly different periods (800 and 808 nm), so that only at a certain point both parts were perfectly aligned with respect to each other. One finds, that approximately eight subsequent grating structures are of high quality, corresponding to a tolerable displacement (overlay error) of about ±30 nm. (C) Close-up of picture B showing a region with grating structures of high quality.

Using a pre-compensating mask design in connection with the improved RIE-structuring process mentioned above finally made it possible to successfully fabricate linear four-level zone-plates made of silicon. Figure 4.12 shows a SEM-picture of such a zone plate, having a diameter of 48 µm, a minimal outermost period of 800 nm and a focal length of 187.5 mm (at the design photon energy of 12.4 keV). Figure 4.13 shows the cross section of a test zone plate with a very similar design, giving an impression of the grating structure profile across such a zone plate.

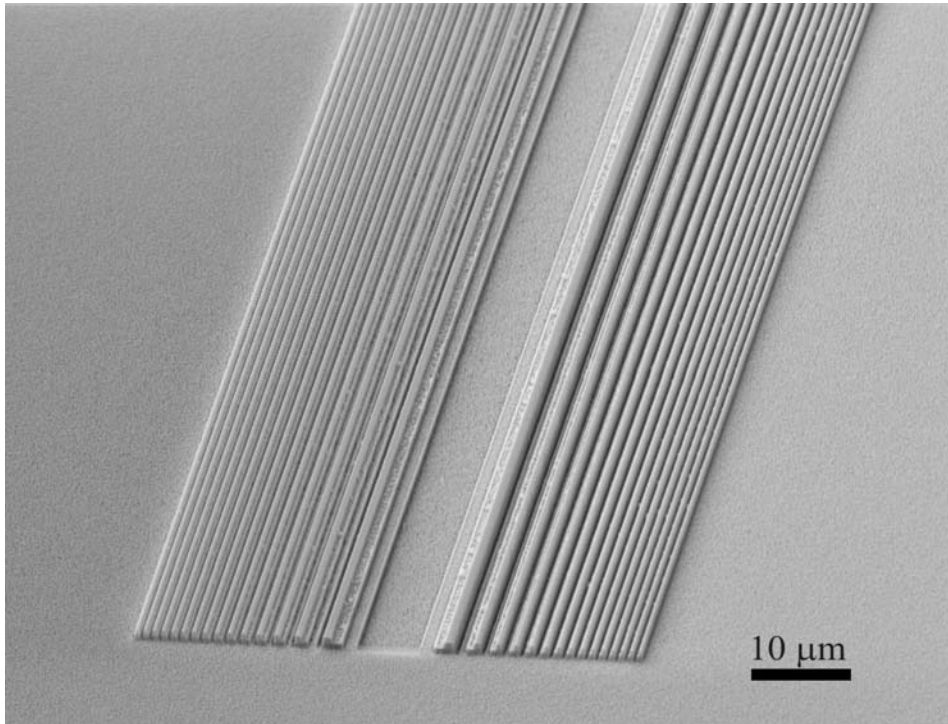

Figure 4.12: SEM-picture of a linear zone plate; the zone plate parameters are: diameter = 48 µm, outermost zone width = 800 nm, focal length = 187.5 mm (at the design energy of 12.4 keV); length of zone plate = 2 mm;

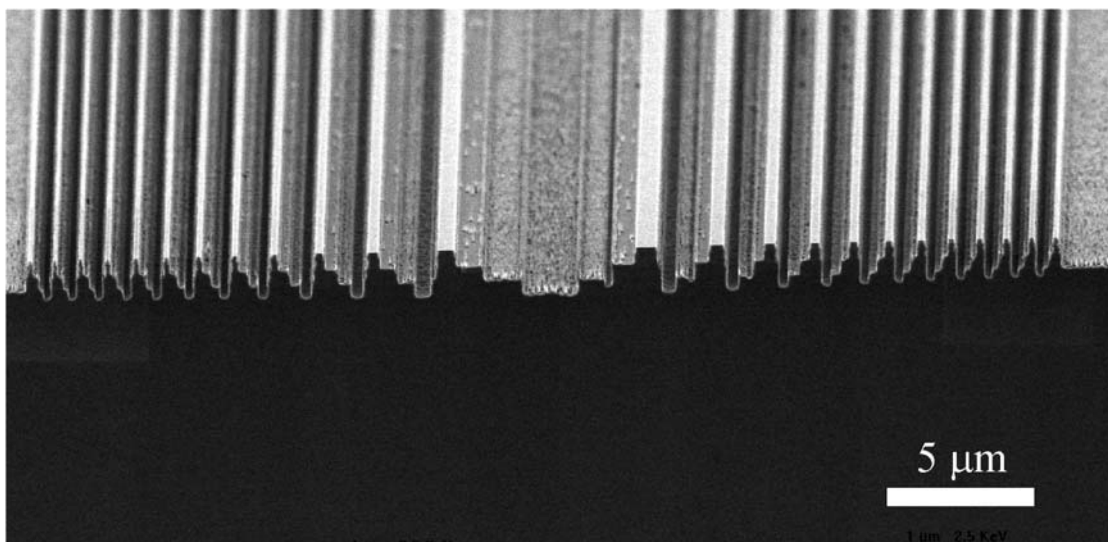

Figure 4.13: Cross section of a test zone plate having similar design parameters like the zone plate shown in Figure 4.12.

4.5 Fabrication and local thinning of silicon membranes

Although x-ray absorption of silicon is comparatively small in the hard x-ray region, it is nevertheless necessary to fabricate linear zone plates on very thin silicon substrates (i.e. membranes) in order to keep absorption sufficiently low. Later on in this chapter it will be shown that the tolerable membrane thickness is typically in the micron range.

Figure 4.14 gives the details of the fabrication process used within this work to fabricate silicon membranes. In a first step a standard photolithography process is used to form a photo-resist mask on a silicon wafer. The resulting pattern is then transferred into the wafer by means of reactive ion etching, leading to the formation of silicon membranes of the desired thickness.

The etch process was performed in collaboration with external labs (ETH Zurich, IBM Rüschlikon) using deep reactive ion etching (DRIE) of silicon. DRIE-systems utilize a highly optimised etch process (Bosch-process [75]), enabling high etch rates, low surface roughness and accurate control of the sidewall angles (anisotropy).

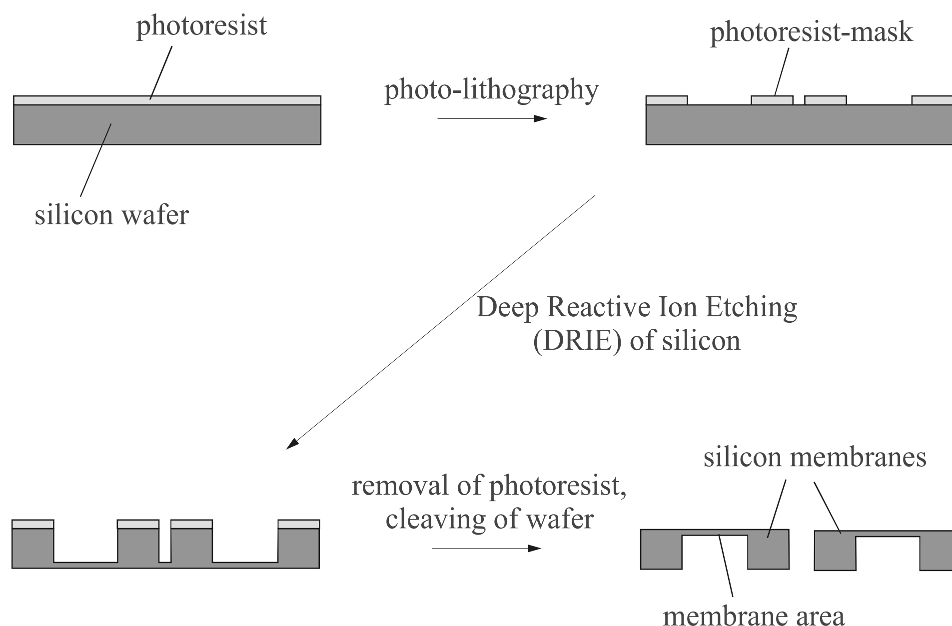

Figure 4.14: Fabrication process of silicon membranes

After removing the remaining photo resist and performing a controlled cleaving of the wafer, one finally obtains a set of individual silicon membranes that can be directly used for the fabrication of linear silicon zone plates.

Two different membrane designs were used within this work (see Figure 4.15 A). Figure 4.15 B demonstrates that the finite size of the membranes results in an ultimate limit of the tilt angle α one can use to increase the effective size of the grating structure.

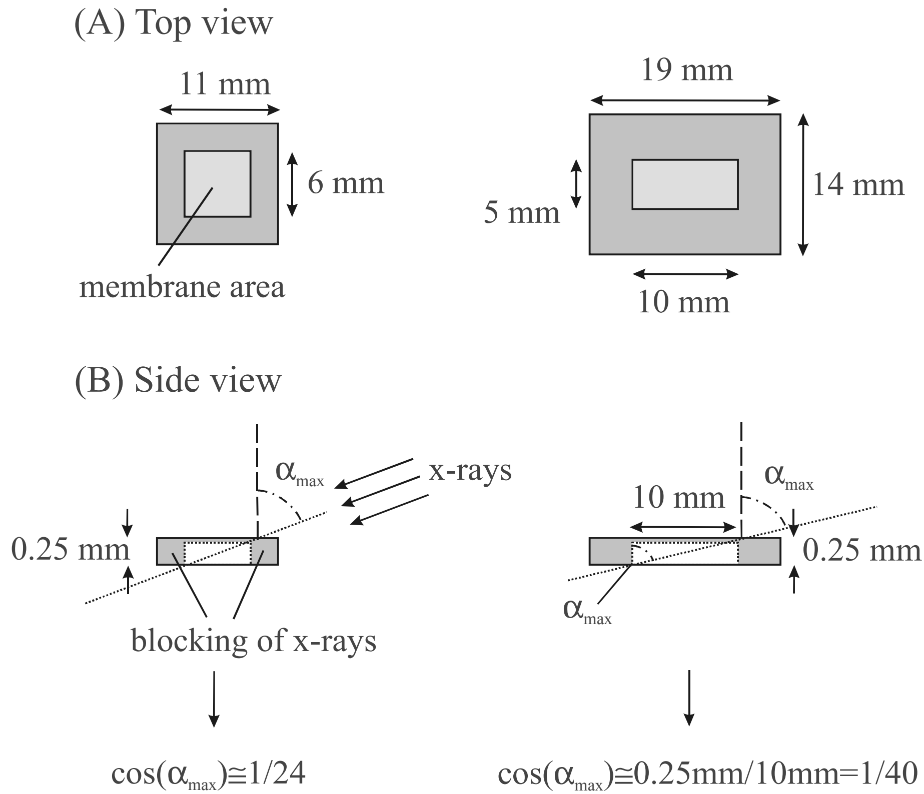

Figure 4.15: (A) Sketch of the two different silicon membrane designs used within this work. (B) Side view of the membranes illustrating the fact, that the ultimate tilt angle α_m is determined by the substrate thickness and the length of the membrane area.

It was mentioned in the last chapter, that this tilting limit is one of the reasons to fabricate zone plates with grating structure heights well above 1 μm. However, in praxis there is another important reason to make the structures as high as possible.

Note, that if the effective height of a grating is increased using the tilting method, this will at the same time increase the effective thickness of the membrane. Consequently, the membrane thickness must not significantly exceed the height of the grating structures for otherwise absorption will play a significant role.

Figure 4.16 gives the transmission of a membrane for different ratios r_m of the membrane thickness and the grating structure height. The values are calculated assuming, that for each photon energy the four-level zone plate is tilted to the optimum angle, resulting in maximum diffraction efficiency. One finds that the thickness of the silicon membrane should be at most twice the height of the four-level grating structure (r_m<2). If this condition is fulfilled, the transmission will be above 75% for all photon energies beyond 10 keV.

For a structure height of 1.5 μm this corresponds to the requirement to fabricate silicon membranes with a thickness below 3 μm.

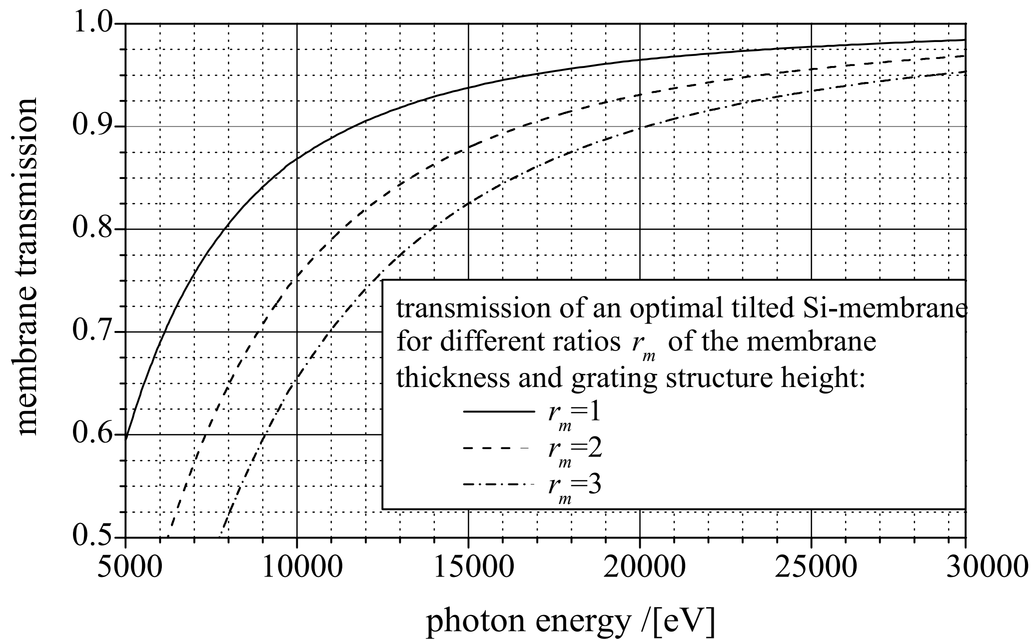

Figure 4.16: Calculated transmission of a tilted silicon membrane, containing a four-level zone plate with a grating structure height h. For the calculation it is assumed that the membrane is tilted to the optimum angle leading to a maximal diffraction efficiency of the zone plate. The resulting transmission is shown for different ratios r_m of the membrane thickness d and the structure height h (r_m=d/h).

The thickness of the silicon membranes fabricated by the process shown in Figure 4.14 is typically in the ten-micron range. This results from the comparatively inhomogeneous DRIE-etch process, where membranes can be nearly etched through at one side of the wafer, whereas at the other side the remaining membrane thickness is still up to 40 µm. Within one membrane the thickness variations are significantly smaller - typically about 10 µm. This opens up the possibility to further thin individual membranes using an additional etch process.

For the overlay exposures it is of advantage to have thick membranes, as external forces less easily bend thick membranes, avoiding unnecessary overlay errors induced by membrane distortions. Consequently, the additional thinning of silicon membranes was performed after the selective etching of chromium, following the first RIE-structuring step of silicon (see also Figure 4.4). After this etching of chromium most of the membrane region is mask-free and consequently no metal layer interferes with the transmission measurement described below, which was used to control the membrane thickness during the thinning process.

The thinning of membranes was performed by means of plasma etching (BMP) using SF_6 as an etch gas. The samples were placed onto a special holder, where the membrane could be put up-side down and flooded (rinsed) with helium during the etch process. Consequently only the backside of the membrane is etched, whereas the topside - eventually containing a zone plate or a grating structure - is protected. The etch rate of the corresponding BMP-process is about 2.5 µm/min.

A precise control of the thinning procedure requires a means of determining the actual membrane thickness at different positions of the membrane. For this purpose a simple optical set-up was built in order to measure the membrane transmission T of red light stemming from a Helium-Neon laser (λ_0=632.8nm). The transmitted light flux and the flux of the direct beam were determined with a diode.

Figure 4.17 represents the corresponding calibration curve, which was used to determine the thickness of membranes having a transmission above the detection limit of about $T=10^{-5}$. This corresponds to a maximum membrane thickness of about 40 µm. The experimental transmission data values in Figure 4.17 were obtained by subsequent etching of a test-membrane. The etch depth was monitored with a reference silicon sample that was processed (etched) together with the membrane.

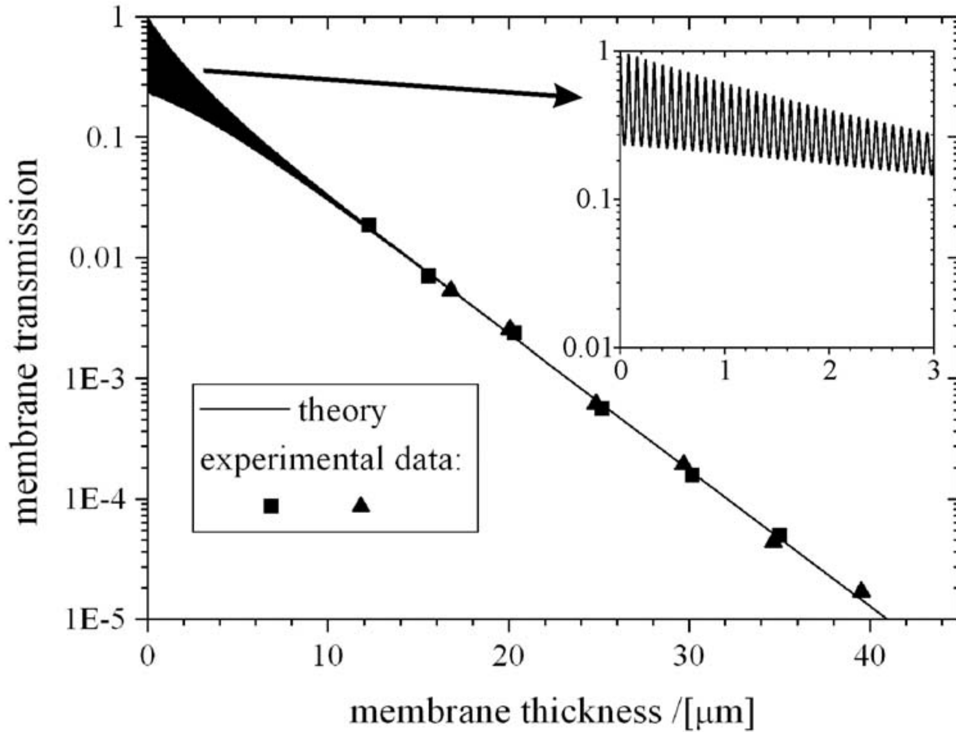

Figure 4.17: Transmission of a silicon membrane at the wavelength of a standard helium neon laser (λ_0=632.8nm). The transmission was calculated using equation (4.2), equation (4.3) and the experimentally obtained value of the imaginary part of the refractive index (see below). Due to interference effects a strong oscillation of the membrane transmission is found for small membrane thickness.

For thick membranes most of the light travelling from one membrane surface to the other is absorbed, so that for theoretical considerations multiple reflections at the membrane surfaces can be neglected. The difference in transmission of two membranes of thickness d_1 and d_2 is therefore simply given by the additional light absorption of silicon within a distance d_1-d_2. This leads to (see also equation (2.28))

$$T(d_1)/T(d_2) = \exp[-4\pi\beta(d_1 - d_2)/\lambda_0] \qquad (4.1)$$

According to equation (4.1) one can use the slope of the regression line of the experimental data values in Figure 4.17, in order to determine the imaginary part of the refractive index β.

The obtained value for β (β=0.013, silicon, for λ_0=632.8nm) is in good agreement with the different values reported in literature [76, 77]. Using the tabulated value of the real part of the refractive index n_r (n_r=3.88, [76]), it is then possible to calculate the theoretical transmission

of a silicon membrane (see also Figure 4.17). If multiple reflections are taken into account, an incoming plane wave at one surface of the membrane results in an infinite number of plane waves exiting the membrane at the other surface. By adding up these waves and assuming normal incidence of the laser light one obtains

$$T(d) = \frac{(1-R)^2 \exp(-\mu_{Si} d)}{1 - 2R\exp(-\mu_{Si} d)\cos(4\pi n_r d/\lambda_0) + R^2 \exp(-2\mu_{Si} d)} \quad (4.2)$$

with

$$\mu_{Si} = 4\pi\beta/\lambda_0$$

The factor R represents the reflectivity of a single silicon surface. Due to the comparatively small value of the imaginary part of the refractive index we find

$$R = \left|\frac{(n-1)}{(n+1)}\right|^2 \cong \left|\frac{(n_r-1)}{(n_r+1)}\right|^2 = 0.348 \quad (4.3)$$

For thin membranes multiple reflections play an important role. In consequence it is of importance whether the waves, which are reflected at the different surfaces of the membrane, are in phase or out of phase with respect to each other. One finds that constructive interference occurs, if the membrane thickness d is a multiple of half the laser wavelength in silicon ($d_i = i\lambda_0/(2n_r)$, i=0,1,2..). In between destructive interference is obtained, resulting in the strong oscillation of the transmission shown in Figure 4.17. The period of this oscillation is about 80 nm, so that in praxis - due to the comparatively strong variation of the membrane thickness - regions of constructive as well as destructive interference can be found within the spot of the laser. Consequently, in the experiment this oscillation cannot be observed as only an average transmission value is measured.

Using Figure 4.17 as a reference for the thinning process of silicon membranes it was possible to achieve a membrane thickness down to about 15 µm. According to Figure 4.16 such membranes are still not thin enough to guarantee sufficiently small x-ray absorption of the membrane.

In principle a further thinning is prevented by the inherent thickness variations of silicon membranes. However, the problem can be circumvented utilizing a localized thinning technique. For this purpose a chromium protection layer is thermally evaporated onto the backside of a membrane. During the evaporation process a thin, flexible metal stripe is placed closely above a region of the membrane containing a fully processed zone plate of high quality. The resulting chromium-free and therefore unprotected membrane area can then be further thinned by means of plasma etching.

In praxis the size of the unprotected membrane region was about 1mm×2.5mm, providing enough space for at least one zone plate of high quality. The variation of the membrane thickness within a region of this size was typically less than 2 µm. Consequently, applying this local thinning technique it was possible to obtain membranes with a thickness down to about 3 µm.

5 Optical testing of multilevel zone plates

This chapter contains the experimental data obtained during two beam times at the European Synchrotron Radiation Facility (ESRF) in Grenoble (France). The goal of these experiments was to test the optical performance of silicon multilevel zone plates that had been fabricated with the process described in the last chapter.

In the first run (see section 5.1) various efficiency measurements were made changing the tilt angle as well as the used photon energy. Besides zone plates, multilevel-gratings with different periods were tested. As a zone plate can be understood as a grating with variable grating periods these measurements on gratings provide an additional knowledge and understanding of the optical performance of multilevel zone plates.

The second beam time (see section 5.2) was dedicated to resolution tests of multilevel zone plates. As linear multilevel zone plates act as cylindrical lenses, focusing in only one direction, two crossed lenses in series have to be used in order to achieve 2-dimensional focusing into a focal spot. The resulting focusing device was built up and tested with respect to its resolution (size of the focal spot) and its (overall) efficiency.

5.1 Efficiency measurements

The efficiency measurements of multilevel zone pates and gratings were performed at the BM05 optics beamline of the ESRF (experiment MI-563, March 2002).The optics beamline BM05 utilizes a bending magnet for the generation of x-rays. The primary and secondary slits are then used to produce an x-ray beam of well-defined size and shape (typically 1mm×1mm during the experiment). In addition the resulting x-ray beam is monochromatized using a double crystal Si(111) monochromator, yielding x-rays in an energy range from 6keV-60keV with an energy resolution $\Delta E/E$ of about 10^{-4}.

Figure 5.1 shows a schematic sketch of the experimental set-up used for the measurements. Besides the built-in slits of the beamline (primary and secondary slits) two additional slits were used within the optical set-up. Both slits allowed an independent setting of the middle position of the slit-gap and the gap-size in horizontal (y-direction) and vertical (z-direction) direction. One slit (slit1) was placed close to the tested multilevel gratings/zone plates and was used to pick out a certain, well-defined part of a grating or a zone plate. Another slit (slit2) was placed in a distance of about 1m from the tested multilevel optical devices. This slit was used to collect a certain fraction of the x-rays that are diffracted/focused by multilevel optical devices, finally enabling the determination of the corresponding diffraction efficiency. The x-rays passing slit2 were detected with a diode placed behind the slit. An x-ray camera was placed behind the diode, enabling the visualization of all optical components along the x-ray beam and therefore the alignment of all these components with respect to an optical axis.

For a bending magnet the effective size of the x-ray source in the vertical (z-) direction is much smaller than in the horizontal (x-) direction. If a linear zone plate is used to focus the x-rays from such a source the resulting line focus represent an (1-dimensional) image of the source. A large source results in a large source image and consequently a large width of the resulting line focus. For the efficiency measurements the width of the line focus should not exceed certain limits (a few microns are tolerable) and therefore it is of advantage to focus in the direction, where the source size is small. Consequently, the linear zone plates and

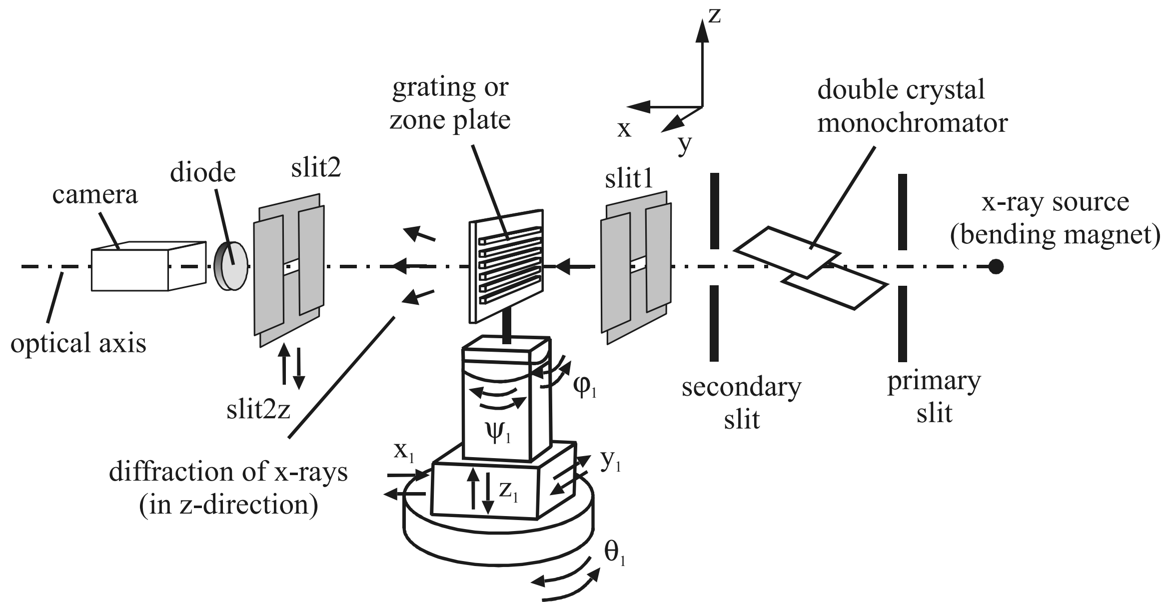

Figure 5.1: Schematic sketch of the set-up used to determine the diffraction efficiency of multilevel gratings and zone plates. Basically two slits are used to determine a x-ray beam of well-defined size (using slit1) and to measure the fraction of light that is diffracted or focused by a grating or a zone plate (using slit2). The sample is mounted on a goniometer-head and can be automatically moved in any direction of space (the motors x_1, y_1 and z_2 for a movement in x, y and z-direction; the motors φ_1, ψ_1, and θ_1 for a movement around the x-, y- and z-axis, respectively).

gratings were oriented in such way, that diffraction (focusing) occurred in the vertical direction.

The silicon membranes containing multilevel optical devices were fixed onto a sample holder, which was made of optical components and mounting systems from LINOS Photonics GmbH&Co Kg. The sample holder allowed a manual tilting of the membranes around the z-axis (which is the tilt resulting in an increase of effective grating structure height). Using an alignment microscope one could achieve that the center of the grating structures lies on this tilt axis and that at the same time the grating structures were exactly perpendicular to the tilt axis. The sample holder was then mounted onto a goniometer head, which was used to perform a rotation of the multilevel optical devices around the x- and y-axis (tilt angles φ_1 and ψ_1, respectively, see also Figure 5.1). The goniometer head was fixed onto a built-in mechanical stage at BM05 allowing additional movements of the sample in x, y, and z-direction and a rotation around the z-axis (angle θ_1). The high precision of all mechanical components of the set-up ensured that the manual tilt axis of the sample holder was basically identical to the motorized tilt around the z-axis (angle θ_1) of the mechanical stage.

A thorough measurement of the optical properties of multilevel optical device requires an accurate alignment of the grating structures with respect to the x-ray beam. For this purpose a built in alignment laser at BM05 was used, which could be calibrated to have the same position and direction as the x-ray beam. Using the mirror like reflection of the silicon membrane, one could reach that the (not tilted) membrane area lies perpendicular to the x-ray beam (alignment of the angles ψ_1, and θ_1).

The alignment of the angle φ_1 (grating structures along y-axis) could be achieved by putting a water level on top of the sample holder. The same procedure was used for slit1 and slit2 in

order to ensure that the grating structures and the slits used for the measurements are aligned with respect to each other.

5.1.1 Efficiency measurements of multilevel gratings

In the first part of the experiment at BM05 several gratings with different grating period were tested. The efficiency was measured by creating an x-ray beam of small diameter and determining the fraction of the beam-intensity that is diffracted in a certain order. The distance between the sample and slit2 was set to 1 m during the measurements of all gratings. For a typical grating period and photon energy (1 µm, 12.4 keV) the separation between two neighbouring orders is 100 microns. Consequently, in order to clearly separate the different orders the vertical gap of slit1 and slit2 have to be significantly smaller than this separation between two orders. Typical settings used in the experiment, leading to good results are 20 µm for the vertical gap of slit1 and 50 µm for the vertical gap of slit2.

In horizontal direction the tolerable size of the x-ray beam is determined by the fact that the whole beam should undergo diffraction and therefore hit a region within a grating. The largest applied tilt angle was about 88^0 corresponding to an increase of effective grating structure height by a factor of about 30 ($1/\cos[88^0]$). At the same time this means, that the effective length of the grating structures for the measurement (effective length in y-direction) is decreased by the same factor. All gratings had a length of 2 mm, leading to an ultimate limit of 70 µm for the tolerable horizontal size of the x-ray beam. In praxis the horizontal gap size of slit1 was therefore set to values below 40 µm. The corresponding gap of slit2 was set to about twice this value in order to ensure, that the whole beam in horizontal direction was collected.

All test gratings were designed in such way that at one position of the grating the two overlay exposures were perfectly aligned with respect to each other, leading to an optimal grating profile and therefore maximum first order diffraction efficiency for this grating position. This was accomplished in the same way as for the test grating shown in Figure 4.11 B, where the two gratings defining the chromium part and the aluminium/chromium part of the etch-mask have slightly different grating period. A small difference of 0.1% in grating period was chosen for all test gratings. This ensured that the size of the region with optimum quality of the grating structure was larger than the vertical size of the x-ray beam used for the measurement.

For the measurements a grating was centred in y-direction with respect to the beam whereas in vertical direction the position of optimal grating performance, giving maximum first order diffraction efficiency, was determined. All measurements, determining the diffraction efficiencies for different tilt angles, photon energies and diffraction orders, were then performed using this optimum region of the grating. Due to the precise alignment of the gratings with respect to the x-ray beam and the vertical tilt axis, a change of the tilt angle θ_1 had no observable influence on the y- and z-position of this optimal grating region. Consequently, a whole set of measurements at different tilt angles could be made without the necessity to realign the grating.

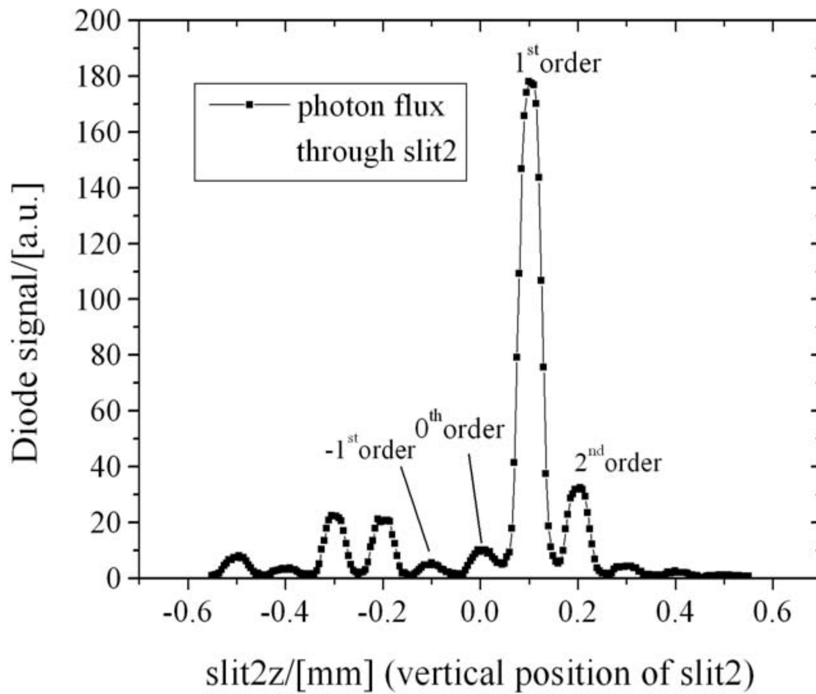

Figure 5.2: Typical example of the data sets, which were used to determine the diffraction efficiencies of different orders of four-level gratings. Figure 5.2 shows the data for the case of optimal tilt angle θ_1 leading to maximum first order diffraction efficiency. Experimental parameters: tilt angle $\theta_1 = 86.5^0$, photon energy = 12.4 keV, grating period 1 µm.

Figure 5.2 shows one of the obtained data-sets using a grating of 1 µm period, a photon energy of 12.4 keV and a tilt angle of $\theta_1=86.5^0$. The different peaks, representing the different diffraction orders, are clearly separated.

For a proper evaluation of the data additional reference measurements were made, determining the flux (diode signal) I_{dir} of the direct beam as well as the flux I_{mem} of the beam penetrating the membrane in a non-patterned region very close to the grating. The ratio of the peak value I_m of the mth order and the flux I_{mem} directly gives the fraction of light diffracted into this order and consequently the diffraction efficiency.

Note, that the efficiency calculated in such way does not account for membrane absorption. The efficiency including membrane absorption is obtained using the ratio I_m/I_{dir}. However, the membrane thickness and the resulting x-ray absorption will vary from grating to grating, making it more useful to compare the efficiencies one would obtain, if the gratings were placed on an infinitely thin membrane.

Figure 5.3 shows a full dataset of diffraction peaks, obtained for many different tilt angles of a grating with 1 µm period. The diode signal is normalized using the value of I_{mem} for the corresponding tilt angle so that the peak values directly represent the diffraction efficiency of a certain order. For low tilt angles most of the light is not diffracted and remains in the zero order, whereas for high tilt angles it is possible to achieve that most of the light is diffracted into the first order.

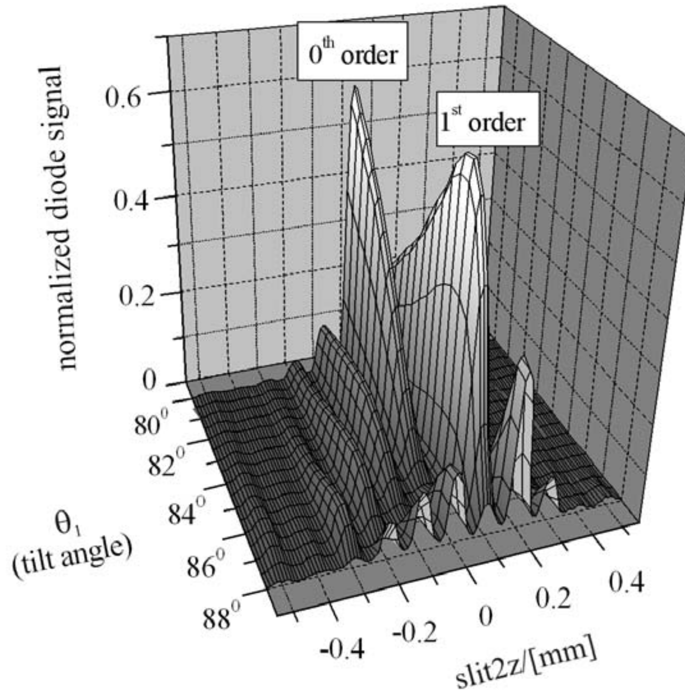

Figure 5.3: Measured diffraction peaks for different tilt angles θ_1 of a grating (experimental parameters: grating period = 1 µm, photon energy = 12.4 keV, distance of grating to slit2 = 1m). The diode signal is normalized using the signal of the direct, not diffracted beam, so that the peak values directly correspond to the diffraction efficiency of a certain order.

Figure 5.4 shows some of the corresponding diffraction efficiencies, which are obtained evaluating different peaks of the curves in Figure 5.3. The theoretical curves are obtained taking into account, that the grating structure was etched 1.5 µm deep and using the tabulated values of δ and β [45] for silicon at the photon energy of 12.4 keV. The required theoretical expression for the diffraction efficiency η_m of the mth order is obtained combining the equations (2.70), (2.72) and (2.73) (see also equation (2.83), representing the special case m=1):

$$\eta_m = \left| \sum_{j=1}^{L} \Phi_j \right|^2 \qquad (5.1)$$

where

$$\Phi_j = \exp\left[-2\pi \underline{h}_j \beta / \delta\right] \exp\left[-2\pi i(\underline{h}_j - m\underline{x}_j)\right] \frac{\sin(\pi m \underline{w}_j)}{\pi m}$$

and using normalized heights ($\underline{h}_j$), widths ($\underline{w}_j$) and middle-positions ($\underline{x}_j$) of the L different steps

$$\underline{h}_j = h_j \delta / \lambda \quad \underline{w}_j = w_j / b \quad \underline{x}_j = x_j / b$$

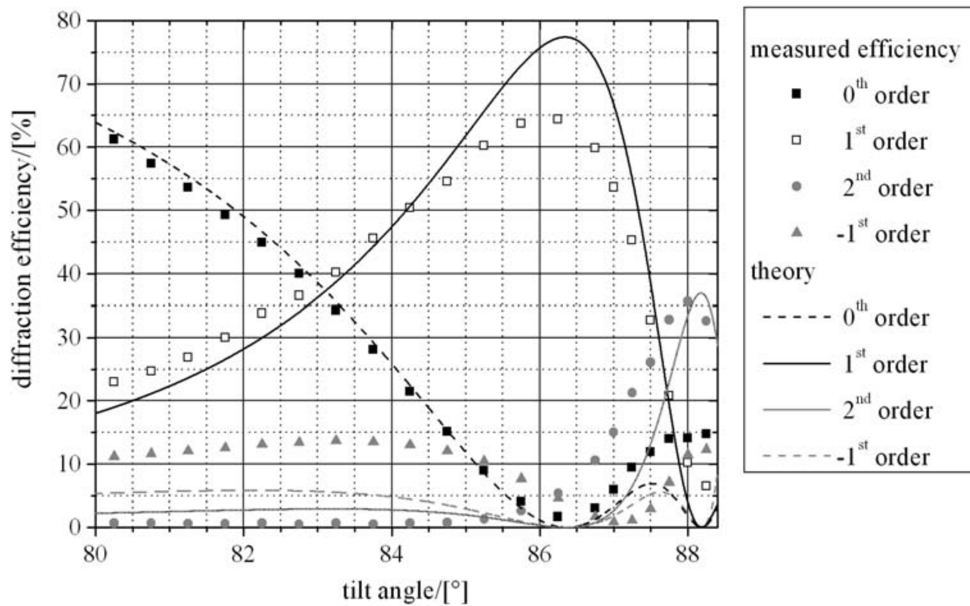

Figure 5.4: Diffraction efficiencies of various orders obtained evaluating the data shown in Figure 5.3. The solid curves are the corresponding theoretical efficiencies, which are calculated using equation (5.1), assuming a four-level grating with 1.5 μm height and taking into account the tabulated values of δ and β for silicon [45] at the chosen photon energy (12.4 keV).

Figure 5.4 shows that there is a good qualitative agreement between the calculated and measured diffraction efficiencies of low orders. Especially for the zero and first order the theoretical curves closely match the measured data. These two orders are the most important ones, because the first order efficiency gives the amount of light that is diffracted into the focus-spot and the zero order gives the main contribution to the diffuse background (unwanted photon flux) in regions close to the focus.

Especially for higher orders considerable discrepancies between experiment and theory are found, which can be attributed to the fact that local features of the ideal multilevel profile are only badly reproduced by the actual profile. However, these features (especially the sharp transitions between two neighbouring steps) determine the high frequency Fourier components of the wave-field behind the grating and consequently mainly determine the diffraction efficiencies of higher orders.

Figure 5.5 shows the first order diffraction efficiency of the same grating (1 μm period) obtained for different photon energies. For all tested energies in the range between 10 keV and 16.5 keV it was possible to tune the tilt angle and the corresponding grating structure height to an optimum value resulting in maximum diffraction efficiencies. The obtained efficiency values (around 65%) are already close to the theoretical limit (81.1%).

For the design of multilevel zone plates of high efficiency it is of importance to know about the smallest grating period where high diffraction efficiencies are still feasible. Therefore several gratings with different grating periods were tested, using the same photon energy of 12.4 keV for the tests.

In Figure 5.6 the measured first order diffraction efficiencies are depicted. For the two gratings with 0.8 μm and 1 μm grating period the same optimum efficiency of about 65% can

be reached, whereas for a grating period of 0.64 µm only 52% are feasible. In conclusion one finds, that grating periods of about 0.8 µm represent the ultimate lower limit, where diffraction efficiencies close to the theoretical limit can still be obtained. This is in good agreement with SEM-inspection of test-gratings, which showed that only for grating-periods above approximately 0.8 µm the fabrication of gratings of good quality is feasible.

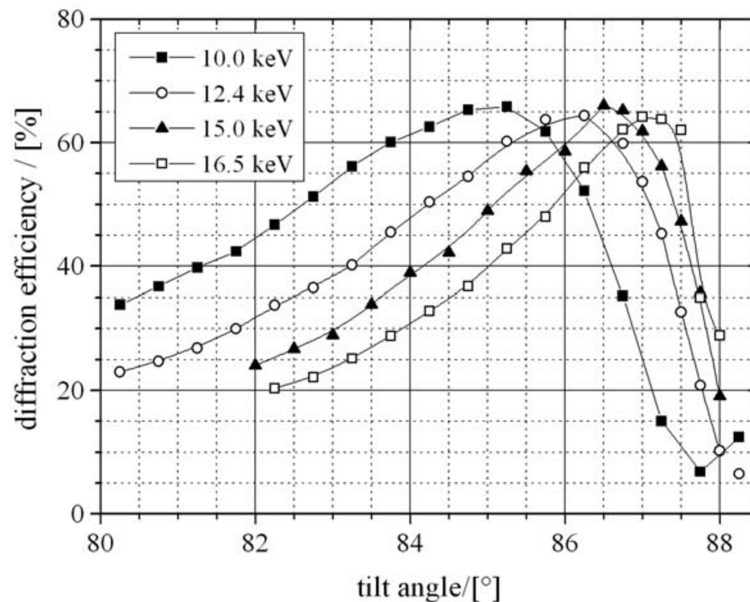

Figure 5.5: Measured first order diffraction efficiency of a grating with 1 µm period, shown for different x-ray energies. For all tested energies a maximal efficiency of approximately 65% was obtained, provided that the tilt angle θ_1 was set to its optimum value.

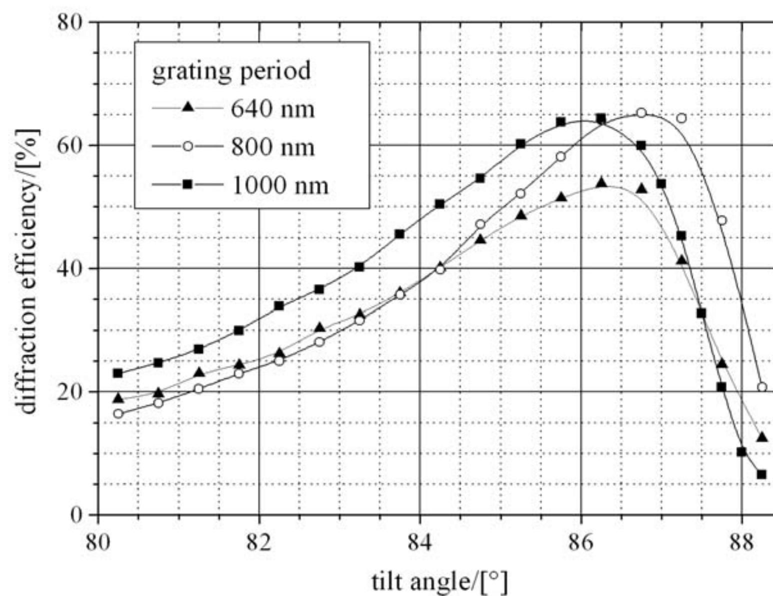

Figure 5.6: Measured first order diffraction efficiencies at 12.4 keV photon energy for gratings with different grating period, showing that for grating periods above about 800 nm high efficiencies close to the theoretical limit can be obtained.

Although the optimum efficiency for the two gratings with 0.8 µm and 1 µm is almost the same, at the same time a significant difference of their optimum tilt angle is observed. This can be explained by a different behaviour of the RIE-structuring process for different grating periods, as the etch depth for large grating periods is found to be slightly bigger than for small grating periods.

5.1.2 Efficiency measurements of multilevel zone plates

The measurements on zone plates were made with the same set-up as for the gratings. Also the alignment of the zone plates with respect to the x-ray beam could be achieved using the same procedure as described before. However, some experimental parameters had to be adjusted for a proper efficiency measurement.

The gratings structures of the zone plates were horizontally orientated, leading to a focusing in the vertical direction. As a whole zone plate should be used for the focusing, the vertical gap of slit1 was chosen in such way that the zone plate and also a membrane region nearby is homogeneously illuminated. For a zone plate with 200 µm diameter the vertical gap of slit1 was chosen to be approximately 350 µm, assuring that no other zone plates on the membrane were illuminated with x-rays. Like for the measurements on gratings, the x-ray beam in the horizontal direction the x-ray beam was strongly confined (horizontal gap of slit1 = 20 µm) and centred with respect to the zone plate. Consequently, even for strong tilt angles no light passed on the left or right side of the zone plate. For the efficiency measurements slit2 is used to collect all light that is diffracted into the focus. The gap in horizontal direction was therefore chosen significantly larger than the gap of slit1 (100 µm). In the vertical direction the gap of slit2 can be set freely within certain limits. The gap should be significantly larger than the width of the focal spot so that at least for one vertical position slit2z of the slit all focused x-rays pass slit2. At the same time the gap should not be too large so that the background signal passing slit2, stemming from the zero and higher diffraction orders, is kept sufficiently low. Typical gap settings meeting this requirement lay between 20 and 50 µm.

For such large gaps the focusing of the beam onto slit2 is not critical. However, in order to achieve highly reliable and accurate measurements it was made sure that the position of slit2 coincided with the focal plane of the lens. The distance between zone plate and slit2 could be set with a sufficient accuracy using a measuring tape and the theoretically calculated image distance q. For example having a focal length of 0.75 m (at the design wavelength of 12.4keV) and a distance of about 40 m to the x-ray source, equation (2.41) yields q=764mm. The setting of the distance q could then be confirmed by scanning slit2 through the focus, setting the vertical gap of slit2 to a very small value (approximately 2 µm). The width of the resulting peak gave some measure of the width of the focal line and could be used to find the optimal distance between the zone plate and slit2.

The actual efficiency measurements then were carried out with a technique that had already been used successfully for the testing of linear zone plates with binary (two-level) grating structures [42, 78]. Basically the efficiency is determined by scanning a slit through the focus of the zone plate. Figure 5.7 A and B show an overview and a close-up of the resulting diode signal.

(A) overview

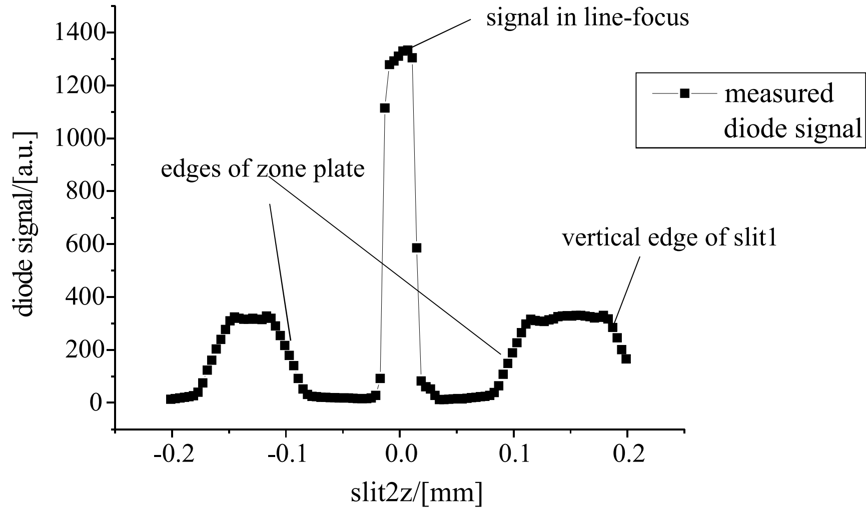

(B) close-up of focal region

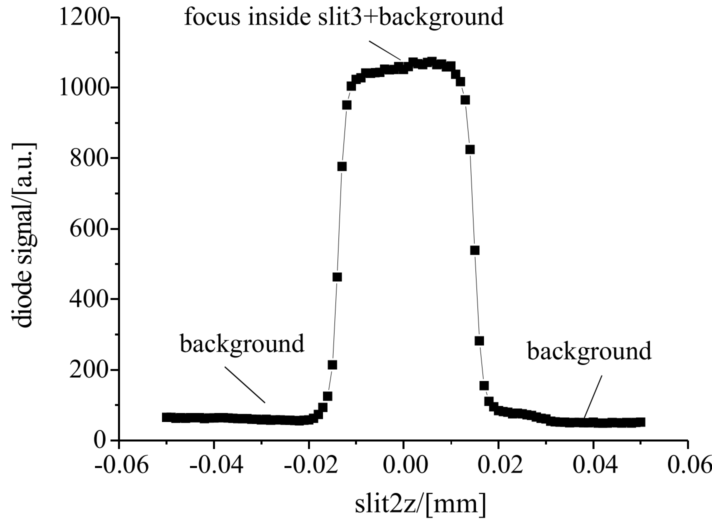

Figure 5.7: Experimental data for efficiency measurements, obtained by scanning slit2 through the focal plane of a zone plate. Figure (A) gives an overview of the resulting diode signal for different vertical positions of slit2. Figure (B) is a close-up of the focal region in (A). The area underneath the peak can be used to determine the diffraction efficiency of the zone plate, making simple, additional reference measurements.

For an infinitely small line-focus and perfectly sharp slits a rectangular peak would be obtained for Figure 5.7, having a width g_{s3} that is equal to the vertical gap size of slit2. Due to the finite width of the focal line and imperfections of slit2 in reality the peak is somewhat smeared. However, such a smearing will hardly change the integral underneath the peak. Consequently one finds with high precision

$$\int I_{diode} d(slit2z) = I_{diode}\ g_s \tag{5.2}$$

where g_s represents the width of the vertical gap of slit2. The diode signal I_{diode} depends on the photon flux Φ of the beam illuminating the zone plate, the diffraction efficiency η of the zone plate and the diameter D of the zone plate.

$$I_{diode} = C_1 \Phi \eta \mathrm{D} \tag{5.3}$$

The factor C_1 is a (unknown) constant of the set-up. Making a reference measurement, where the zone plate is moved out of the beam but using the same settings for slit2, we find for the resulting diode signal I_{ref}

$$I_{ref} = C_1 \Phi \, g_s \tag{5.4}$$

Combining all three equations one finally finds

$$\eta_{abs} = 1/(I_{ref}\mathrm{D}) \int I_{diode} d(slit2z) \tag{5.5}$$

The efficiency η_{abs} given by equation (5.5) takes into account that parts of the light illuminating the zone plate will be absorbed in the silicon membrane, and consequently η_{abs} represents the absolute efficiency of the zone plate.

The influence of membrane absorption can be determined making an additional reference measurement after the first one, where the sample is placed in such way that a membrane region close to the zone plate is illuminated by the x-ray beam. Analogous to equation (5.4) the resulting diode signal I_{mem} is then given by

$$I_{mem} = C_1 \Phi_{mem} \, g_s \tag{5.6}$$

where Φ_{mem} is the photon flux of the illuminating beam behind the membrane. The membrane transmission T is then determined by

$$T = \Phi_{mem} / \Phi = I_{mem} / I_{ref} \tag{5.7}$$

Consequently, the (ideal) diffraction efficiency η_{ideal} one would obtain for zero absorption of the membrane is given by

$$\eta_{ideal} = \eta_{abs} / T = 1/(I_{mem}\mathrm{D}) \int I_{diode} d(slit2z) \tag{5.8}$$

Obviously the efficiency η_{ideal} determined by equation (5.8) characterizes the quality of the grating structures, as it gives the fraction of light passing these structures that is diffracted into the focal spot. For a simple comparison to other results - e.g. the measurement on gratings described in the last chapter - it is therefore more useful to use the ideal efficiency η_{ideal}. One should also note that for some experiments it might be less important to maximize the flux in the focus than to minimize the other, unwanted diffraction orders. In this case the ideal efficiency η_{ideal} and not the absolute efficiency η_{abs} will be the main figure of merit.

The above procedure requires no knowledge of the gap-width g_s of slit2. The parameter g_s neither appears in equations (5.5) nor in equation (5.8). In fact both formulas are also valid if the gap of slit2 varies in the vertical direction, provided that g_s denotes the corresponding mean value of the gap width.

Figure 5.8 depicts the measured efficiencies η_{ideal} of a zone plate for different tilt angles and energies. As for the gratings, the tilt angle θ_1 of the zone plate could be changed without

loosing the centring with respect to the beam, enabling the automatic measurement of the efficiency for many different tilt angles, without the requirement to do a manual realignment.

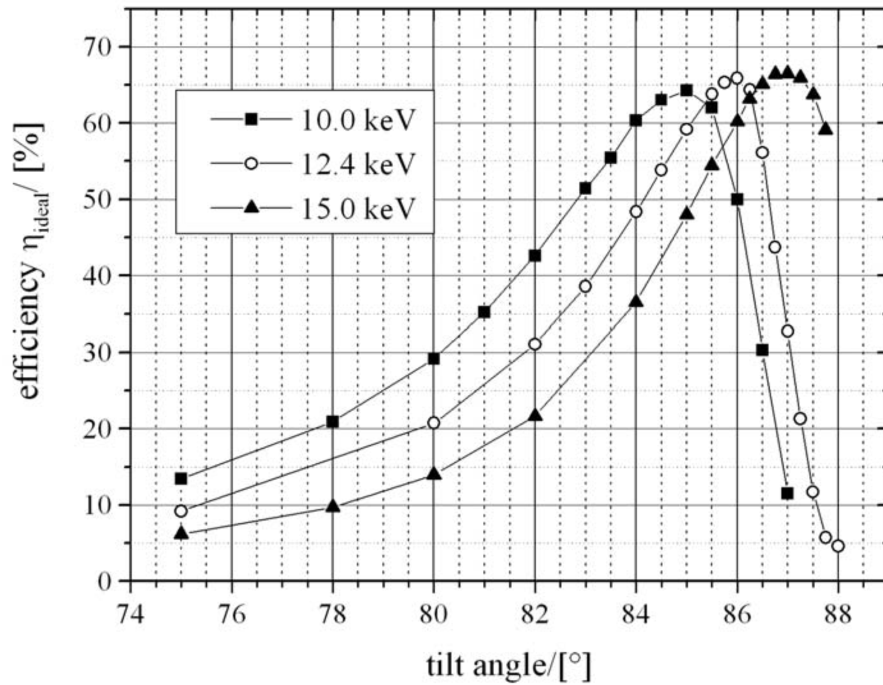

Figure 5.8: Measured diffraction efficiencies at 12.4 keV of a linear multilevel zone plate with 190 µm diameter, 800 nm minimal outermost period and 1.5 µm grating structure height. For all tested photon energies unprecedented efficiencies of about 65% could be reached, tuning the tilt-angle of the zone plate to its optimum value.

The zone plate was placed on a membrane that had been thinned with the local thinning process described in chapter 4.5, resulting in a membrane thickness of about 3.5 µm. Nevertheless the remaining membrane absorption had a noticeable effect on the absolute efficiency η_{ideal}. Figure 5.9 shows the corresponding efficiencies, using the same data as for Figure 5.8, but taking into account absorption losses.

Figure 5.8 and Figure 5.9 show that for all three tested photon energies it was possible to tune the tilt angle and the corresponding effective height to optimum values resulting in maximal efficiency. The achieved efficiency values for η_{ideal} (65%) are higher than any value reported so far for x-ray diffractive optical elements. At least for the hard x-ray range above 10 keV this holds true, even if membrane absorption is considered (Figure 5.9).

Note, that the optimum tilt angle for η_{ideal} is always slightly smaller than for η_{abs}. This can be explained by the fact, that if the optimum tilt angle for η_{ideal} is moderately decreased, this hardly affects the ideal efficiency but at the same time leads to a significant increase in transmission, so that a net increase of the absolute efficiency η_{abs} is obtained.

The efficiency data presented here were obtained using one particular zone plate. However, several other zone plates have been tested during other beam times and at other beam lines of the ESRF, basically always leading to the same result. For all zone plates of high quality (which can be checked making an SEM-inspection after the lithography as well as after the subsequent structuring process) an efficiency η_{ideal} of about 65% (±2%) can be reached. The

respective optimum tilt angle changes with energy, but the obtained optimum diffraction efficiency is basically the same for all energies in the tested energy range (10-15 keV). These findings also match very well to the results of the last chapter, where it was shown that for all grating periods above 800 nm efficiencies of about 65% can be obtained.

This also means, that for a zone plate with a minimal outermost period of 800 nm - like the one described above - one would expect that all regions of the zone plate give the same, strong contributions to the total amount of light that is diffracted into the focus.

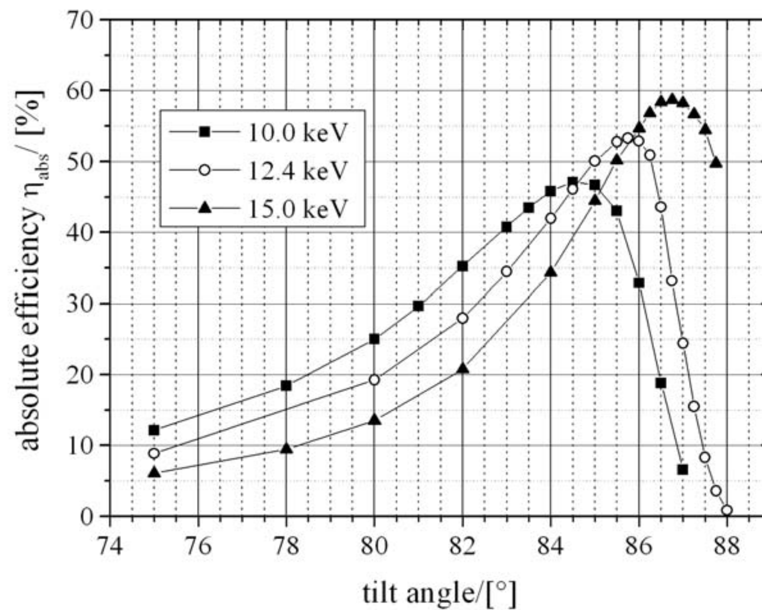

Figure 5.9: Measured diffraction efficiencies of a zone plate taking into account membrane absorption. For low photon energies (10 keV) the membrane thickness of approximately 3.5 μm leads to a significant decrease of the absolute efficiency in comparison to the ideal efficiency shown in Figure 5.8.

In fact this could be experimentally verified by closing down slit1 in vertical direction and illuminating different parts of the zone plate. The resulting flux in the line focus, originating from different regions of the zone plate, showed basically no variations (less than 5%).

For most zone plates used in practical applications the efficiency for the zones at the edge of the lens is significantly smaller than for zones in the middle of the zone plate. This leads to a decrease in numerical aperture and consequently the resolution of such a zone plate is significantly smaller than one would expect from theory, where a constant efficiency is assumed within the whole zone plate (see chapter 2.2.2). However, the linear zone plates described above have an almost constant efficiency across the zone plate and so one can expect that their resolution should be close to the theoretical value. For a minimal outermost period of 800 nm the expected theoretical value of the resolution and the FWHM-width of a diffraction-limited spot are both approximately 0.5 μm. In order to test the resolution of the linear silicon zone plates in praxis, additional measurements were made, which are described in the following chapter.

5.2 Micro-focusing using linear multilevel zone plates

This chapter contains the experimental results of another beam time, where the resolution of multilevel zone pates was tested at the micro-focus beamline ID13 of the European Synchrotron Radiation Facility (experiment MI-638, February 2003).

As linear zone plates act as cylindrical lenses, focusing only in one direction, two lenses have to be used in series in order to get 2-dimensional focusing into a focal spot (see Figure 5.10).

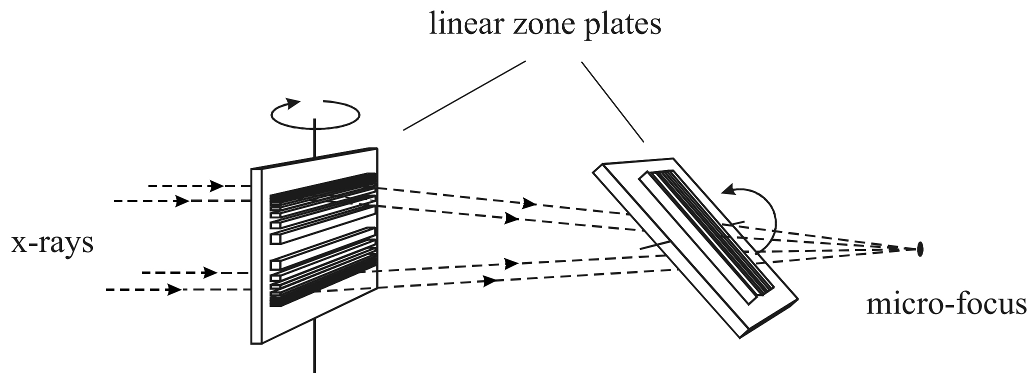

Figure 5.10: Schematic sketch of a micro-focusing device consisting of two linear zone plates.

The resulting micro-focusing device can be used for many different types of set-ups and experimental methods, whenever spatially resolved physical or chemical information of a sample is obtained using x-rays (scanning x-ray microscopy, micro-diffraction). Several types of lenses (refractive lenses, zone plates, focusing mirrors) are suitable to achieve such a micro-focus. In order to understand the advantages and disadvantages of linear multilevel zone plates compared to other types of lenses, a few theoretical considerations are necessary, which are made in the following chapter.

5.2.1 Theory of micro-focusing

5.2.1.1 Micro-focusing using a round zone plate

Figure 5.11 gives an example of a micro-focusing device using a conventional, round zone plate. The considerations in chapter 2.2.2 showed, that for negligible dimensions of the x-ray source the FWHM-size of the focal spot $w_{r,FWHM}$ is determined by diffraction at the aperture of the lens. It was found that for a zone plate having a round or also a square aperture and a minimal zone width b_{min}, the width of the diffraction limited focal spot is the same in horizontal and vertical direction and equal to about half the minimal zone width b_{min}. However, in the general case of non-negligible x-ray source size the focal spot will represent an image of the source.

For synchrotrons the x-rays emitted from different parts of the source are incoherent, as the individual relativistic electrons generating the x-ray radiation have an arbitrary phase with respect to each other. Consequently, in good approximation each electron can be regarded as an independent point source, causing a diffraction limited spot in the focal plane. The image of the source is then obtained by summing up the intensities coming from individual electrons. Due to the large number of electrons (within one second about 10^{18} individual electrons contribute to the overall intensity) this sum becomes equal to an integral, where the contributions of different parts of the source are weighted according to the brightness of the corresponding source region. At the same time this means that the intensity $I_{foc}(y,z)$ in the

image plane is a convolution of the diffraction limited spot $I_p(y,z)$ (see also equation (2.54)) and the geometrical image of the source $I_{geo}(y,z)$, leading to

$$I_{foc}(y_1, z_1) = C_1 \iint dy_2 dz_2 \, I_{geo}(y_2, z_2) \, I_p(y_2 - y_1, z_2 - z_1) \qquad (5.9)$$

The x-ray source brightness can be described by a Gaussian curve having a width s_a in the horizontal direction and a width s_b in the vertical direction (see also Figure 5.11). The geometrical image I_{geo} of such a source is also a Gaussian with widths s_y and s_z in the horizontal and vertical directions, leading to

$$s_y = s_a \, (q/p) \quad \text{and} \quad s_z = s_b \, (q/p) \qquad (5.10)$$

and

$$I_{geo}(y, z) = I_{geo,\max} \exp[-y^2 / s_y^{\,2}] \exp[-z^2 / s_z^{\,2}] \qquad (5.11)$$

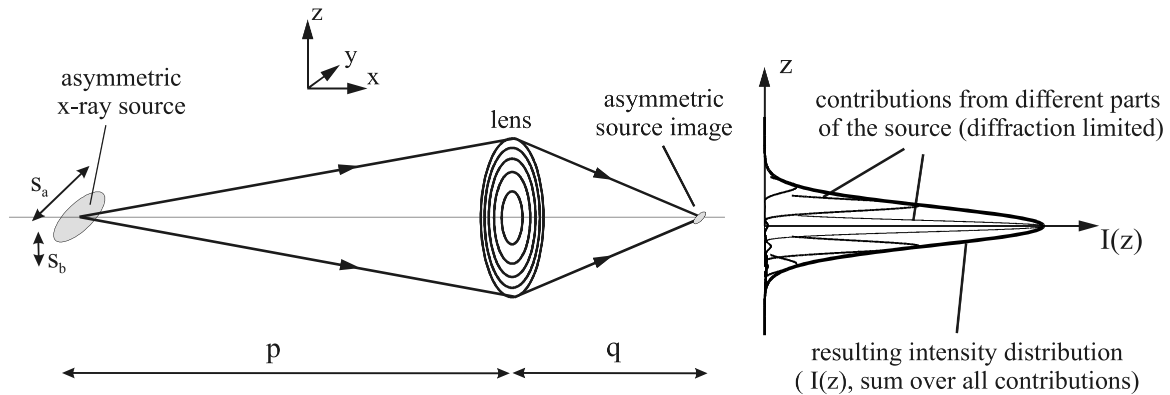

Figure 5.11: Schematic sketch of a micro-focusing device using a conventional, round lens - for example a zone plate - in order to focus the light stemming from an asymmetric x-ray source (e.g. a synchrotron).

The diffraction limited spot of a round zone plate was found to be described by Bessel functions (see equation (2.54)), so that the integral in this case would be a convolution between a Gaussian curve and Bessel function. For a lens with square aperture one would obtain a convolution between a Gaussian curve and a sinc-function. This makes general considerations complicated, as the corresponding integral (5.9) in both cases cannot be solved analytically. However, in praxis one finds, that the central part of the diffraction-limited peak I_p can always be approximated by a gauss-curve with high accuracy. Considering parts of the peak within the FWHM-region the error is typically in the order of a few percent. Therefore - provided that one is not interested in the influence of faint side-peaks of I_p - the errors induced by the Gauss-approximation should be small compared to practical errors induced by uncertainties of the experimental conditions (e.g. non-perfectly Gauss-like x-ray sources, non perfect lenses resulting in a difference between the theoretical and experimental diffraction limited peak).

The main advantage of such a Gauss-approximation is the fact, that in this case the integral in equation (5.9) can be solved analytically. The convolution of a Gauss-curve with a Gauss-

curve is still a Gauss-curve and one finds that the FWHM-widths $w_{foc,y,z}$ of the Gauss-like focal spot I_{foc} are simply given by

$$w_{foc,y} = \sqrt{w_{diff}^{\,2} + s_y^{\,2}} \qquad w_{foc,z} = \sqrt{w_{diff}^{\,2} + s_z^{\,2}} \tag{5.12}$$

where w_{diff} denotes the width of the Gauss-curve that provides the best approximation of the theoretical diffraction limited peak. One possible choice, which will be used in the following and leads to good results in terms of the approximation error, is to take a Gauss-curve whose width w_{diff} is exactly equal to the theoretical width of the diffraction limited spot. Note that equation (5.12) implies, that the asymmetric source shown in Figure 5.11 leads to different widths of the focal spot in vertical and horizontal direction. This can be understood easily as the image of an asymmetric source will be - at least in general - asymmetric.

It should be also noted that equation (5.12) is not restricted to zone plates but can be used for any kind of lens, provided that w_{diff} represents the width of the focal spot one obtains for negligible x-ray source size.

Synchrotron x-ray sources have an "asymmetry factor" m_a of about 5-20, meaning that the source-size in horizontal direction (s_a) is about 5-20 times larger than in vertical direction (s_b). In consequence the size of the geometrical image in horizontal direction is 5-20 times larger than in vertical direction. In general one has

$$s_a = m_a s_b \qquad s_y = m_a s_z \tag{5.13}$$

For the further discussion it is useful to introduce a "coherence factor" r_{coh} defined as the ratio between the diffraction limited size w_{diff} of the focal spot and the geometrical image size (using the larger size s_y in the horizontal direction).

$$r_{coh} = w_{diff} / s_y \tag{5.14}$$

Rewriting equation (5.12) yields

$$w_{foc,y} = s_y \sqrt{r_{coh}^{\,2} + 1} = w_{diff} \sqrt{1 + 1/r_{coh}^{\,2}}$$

and

$$w_{foc,z} = s_z \sqrt{(m_a r_{coh})^2 + 1} = w_{diff} \sqrt{1 + 1/(m_a r_{coh})^2}$$

One finds, that for large values of r_{coh} (r_{coh}>>1) the width of the focal spot is only determined by diffraction ($w_{foc,y}=w_{foc,z}=w_{diff}$), whereas for small values of r_{coh} (r_{coh}<<1) the focal spot represents a geometrical image of the source ($w_{foc,y}=s_y$; $w_{foc,z}=s_z$).

It turns out, that the coherence factor r_{coh} is directly linked to the degree of coherence of the illumination of the lens. To prove this result one has to compare the size of the coherently illuminated area at the position of the lens to the diameter D of the zone plate. The size of the coherently illuminated area can be quantified by the so-called transverse coherence length l_t [51]. Considering two points P_1 and P_2 that have the same distance p from the center of a light source with a source size s_a, the transverse coherence length l_t gives the maximum distance between the two points P_1 and P_2, where the electromagnetic fields in P_1 and P_2 still

have a considerable degree of coherence. The transverse coherence length $l_{t,y}$ in horizontal direction for a x-ray source with a (horizontal) source size s_a is then given by (see [51], page 551)

$$l_{t,y} = \lambda p / s_a \qquad (5.15)$$

Using equation (2.59), (5.10) and (5.14) this leads to

$$l_{t,y} / D = (\lambda q / D)(p / q s_a) \cong w_{diff} / s_y = r_{coh}$$

meaning that the ratio $l_{t,y}/D$ is basically identical to the coherence factor r_{coh}. If $l_{t,y}$ is significantly larger than the lens diameter D (i.e. $r_{coh}>>1$) one has a completely coherent illumination of the lens and diffraction limited spot is obtained ($w_{foc,y}=w_{foc,z}=w_{diff}$). Incoherent illumination of the lens is obtained, when $l_{t,y}$ is significantly smaller than the lens diameter (i.e. $r_{coh}<<1$). In this case the focal spot represents a geometrical image of the source ($w_{foc,y}=s_y$; $w_{foc,z}=s_z$).

For all focusing devices there are practical and physical reasons limiting the maximal obtainable numerical aperture and therefore the minimal, diffraction limited focal spot size w_{diff} one can achieve. For zone plates the maximal deflection of the incoming x-ray beam (and therefore the maximal numerical aperture) is determined by the minimal grating period one can fabricate, having still a good profile quality - and therefore reasonable diffraction efficiencies. In case of focusing mirrors the maximal deflection is determined by the maximum acceptable angle of incidence between the incoming x-rays and the surface of the mirror, that still provides a reasonable reflectivity. Considering refractive lenses one finds that the maximal deflection, which can be obtained by refraction is limited by the inevitable absorption within the refracting device. Consequently, for all lenses there exists a lens specific limit for the minimal obtainable spot size w_{diff}.

For all lens types it is possible to adjust the lens design in such way, that the diameter of the lens is changed without changing the diffraction limited spot size w_{diff}, of the lens. In consequence the lens diameter is an important design parameter, which can be adjusted to meet the requirements of a certain experimental set-up.

For a given, fixed value of w_{diff} - and therefore the numerical aperture - the lens diameter is directly proportional to the image distance q. At the same time one has $f \approx q$ as in praxis the distance between the x-ray source and the lens is always much larger than the focal length of the lens. Consequently, using equations (5.10) and (5.14) one finds that for constant w_{diff} the coherence factor is inverse proportional to the lens diameter ($r_{coh} \sim 1/D$). It is therefore useful to study the change in lens performance as a function of the coherence parameter r_{coh}.

Three important parameters determining the quality of a focal spot are: the total photon flux Φ_s within the spot, the peak value of the intensity I_p in the center and the FWHM-width w_{foc} of the spot in horizontal and vertical direction.

Assuming uniform illumination with x-rays at the position of the lens the photon flux Φ_s will solely depend on the lens area A_{lens} and the total efficiency η_{total} of the focusing device

$$\Phi_s \propto \eta_{total} A_{lens} \qquad (5.16)$$

Assuming a gauss curve for the intensity distribution the peak intensity is proportional to Φ_s and indirectly proportional to the spot widths in horizontal and vertical direction

$$I_p \propto \Phi_s /(w_{foc,y} w_{foc,z}) \qquad (5.17)$$

To clearly see the influence of changing the coherence factor r_{coh} - and therefore the lens diameter D - it is useful to normalize Φ_s , I_p and w_{foc} using the corresponding values of these parameters for the case that the coherence factor r_{coh} is equal to one. The total photon flux Φ_s is proportional to the square of the lens diameter leading to

$$\Phi_s(r_{coh}) = 1/r_{coh}^2 \, \Phi_s(r_{coh} = 1) \qquad (5.18)$$

For the peak intensity I_p we obtain

$$I_p(r_{coh}) = I_p(r_{coh} = 1) \; \frac{\Phi_s(r_{coh})}{\Phi_s(r_{coh} = 1)} \; \frac{w_{foc,y}(r_{coh})}{w_{foc,y}(r_{coh} = 1)} \; \frac{w_{foc,z}(r_{coh})}{w_{foc,z}(r_{coh} = 1)}$$

leading to

$$I_p(r_{coh}) = I_p(r_{coh} = 1) \; \frac{\sqrt{2}\sqrt{1+1/m_a^2}}{\sqrt{1+1/r_{coh}^2}\sqrt{1+1/(r_{coh} m_a)^2}} \; (1/r_{coh})^2 \qquad (5.19)$$

For the width of the focal spot in vertical and horizontal direction one obtains

$$w_{foc,y}(r_{coh}) = w_{foc,y}(r_{coh} = 1) \; \sqrt{1+1/r_{coh}^2} \,/\, \sqrt{2} \qquad (5.20)$$

and

$$w_{foc,z}(r_{coh}) = w_{foc,z}(r_{coh} = 1) \; \sqrt{1+1/(r_{coh} m_a)^2} \,/\, \sqrt{1+1/m_a^2} \qquad (5.21)$$

Figure 5.12 shows the resulting (normalized) total photon flux Φ_s, peak intensity I_p and focal spot width $w_{foc,y}$ for a symmetric (m_a=1; Figure 5.12 A) and asymmetric (m_a=5, Figure 5.12 B) synchrotron source. Both figures represent general correlation curves between lens parameters, which can be used to optimise a focusing device, so that all specific requirements of an experimental set-up with respect to total flux, intensity and resolution (spot size) can be met. In general the asymmetry m_a of the source will influence the result of such an optimisation process. However there are some general trends, which are independent of the source asymmetry.

(A) Symmetric x-ray source (m_a=1)

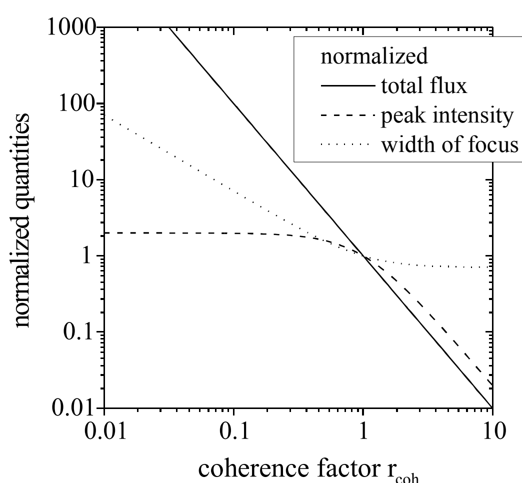

(B) Asymmetric x-ray source (m_a=5)

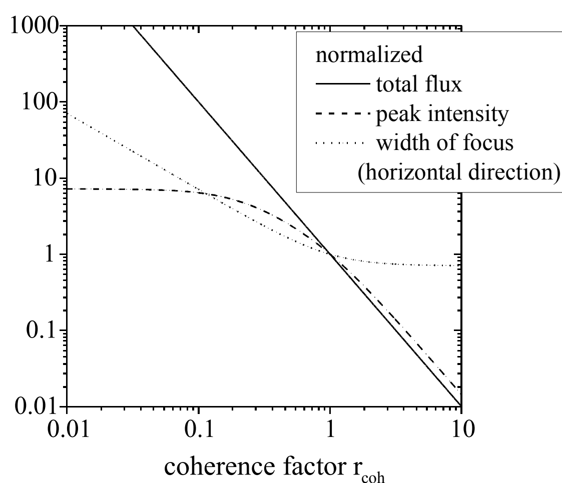

Figure 5.12: Calculated total photon flux, maximum intensity and width of a focal spot of a round lens, assuming Gauss-distributions for the brightness of the x-ray source as well as for the intensity distribution of the diffraction limited focal spot. All lens parameters are normalized using the respective value of the parameter for the case r_{coh}=1. For both figures the coherence factor r_{coh} is defined as the ratio between the diffraction limited spot-size w_{diff} and the size of the geometrical image of the source s_y measured in horizontal direction. Figure A shows the case of a symmetric x-ray source (asymmetry factor m_a=1), whereas Figure B gives one example for an asymmetric x-ray source (m_a=5).

Figure 5.12 A and B show that it does not make sense to choose a coherence factor r_{coh} significantly larger than one, as this leads to a strong decrease of the total flux and the maximum intensity in the focal spot but at the same time does not result in a significant decrease of the width of the focal spot.

If one has the requirement to maximize the intensity in the focal spot it makes sense to choose a coherence factor r_{coh} that is a little bit smaller than unity. Analysing equation (5.19) one finds that a factor r_{coh} of about $1/m_a$ is already sufficiently small to reach intensities close to the theoretical limit. In this case (for $r_{coh}=1/m_a$) the illumination of the lens is more or less coherent in the vertical direction ($l_{t,z}$ /D=1) but at the same time more or less incoherent in the horizontal direction ($l_{t,y}/D=r_{coh}=1/m_a$). Due to this (partly) incoherent illumination one cannot expect to obtain a diffraction limited spot size in horizontal direction and in fact that is what can be found in Figure 5.12, as the width of the focal spot is significantly larger than for the ideal case of completely coherent illumination (r_{coh}>>1).

For many applications however it is desirable to get as much flux Φ_s into the focal spot as possible, taking into account that at the same time a certain, application specific maximal spot size in vertical and horizontal direction is not exceeded. In this case Figure 5.12 can be used to find the smallest possible coherence factor where the resulting spot size is still within the tolerable limits.

Plots analogous to Figure 5.12 are also a useful starting point to compare the performance of different types of lenses. Note, that if the coherence factor of two lenses with round aperture is the same this implies that they also have the same diameter. Consequently, the total flux in the focus of the two lenses will be identical, provided that their total efficiency is the same. This makes it relatively easy to compare the performance of two lenses having a different diffraction limited resolution w_{diff}.

To clearly see the general trends it is useful to make a (quite) rough approximation of the conclusions and results of equations (5.18) - (5.20):

1) It never makes sense to choose a coherence factor larger than one as this will not improve the resolution of a lens but lead to significant loss in total flux and peak intensity.
2) For $r_{coh}\approx 1$ the peak intensity has almost reached its optimum value. At the same time one still has basically coherent illumination, so that the width of the focal spot is approximately equal to the ideal diffraction limited spot size.
3) Values of r_{coh} smaller than one represent the case of incoherent illumination, where an decrease of the coherence factor r_{coh} by a factor k will increase the total flux by a factor k^2 and at the same time increase the width of the focal spot by a factor k.

According to 1) ad 2) it is sufficient to consider the case $r_{coh}\approx 1$ if one wants to compare peak efficiencies of two lenses. Choosing $r_{coh}\approx 1$ for both lenses results in the same lens diameter and therefore the same flux within the focal spot (assuming the same total efficiency for both lenses). If the resolution limit of one lens is a factor k smaller than for the second one, the width of the peak of the first lens will be k times smaller than of the second lens. In consequence the maximum achievable peak intensity of the first lens will be roughly a factor k^2 higher than for the second lens (see equation (5.17)).

Similar results are found for the obtained flux, assuming again, that one lens has a factor k smaller resolution limit than the other lens. If the coherence factor of the high-resolution lens is chosen a factor k smaller than for the other lens this will result in the approximately the same resolution of both lenses (see point 3 above). At the same time the lens diameter of the high-resolution lens will be a factor k larger, resulting in a factor k^2 larger flux within the focus.

In conclusion one finds, that the lens with smaller resolution limit has a k^2 better performance with respect to both, total flux as well as peak intensity in the focus. This means that even for a lens having a comparatively small total efficiency this disadvantage can be more than compensated if the lens has a very small resolution limit.

The same kind of argumentation basically holds true for all types of lenses, including the multilevel zone plates presented within this work. In the last chapter it was shown that multilevel zone plates have extremely high efficiencies, so that the total efficiency of a focusing device using these lenses should be very high. However, compared to other lenses like binary wet etched silicon lenses [41, 42] or focusing mirrors they have a relatively large diffraction limited focal spot size. Consequently for many applications multilevel zone plates are not necessarily the optimal devices with respect to the achievable maximal photon flux and intensity. However, it will be shown later on that there are certain cases where the experimental restrictions lead to a limitation of the tolerable numerical aperture of the focusing device so that the argument above does not apply any more (see chapter 5.2.3).

5.2.1.2 Micro-focusing with linear zone plates

Up to now it was assumed that a micro-focusing device consist of a conventional lens with a certain focal length and a certain diameter. However, using linear multilevel zone plates for micro-focusing applications, the focusing in vertical and horizontal direction is achieved by two individual lenses, providing additional freedom in the design of the resulting focusing device. In principle the focal length of both lenses can be chosen freely, provided that their focal planes coincide (see Figure 5.13). To optimise the performance in terms of total flux, peak intensity and focal spot size the numerical aperture of both lenses has to be maximised.

It was shown before that for all lenses there is a lens specific physical limit NA_{lens} for the numerical aperture and consequently changing the focal length f will directly influence the diameter D of the lens.

$$D_i / 2 = f_i \, NA_{lens} \qquad i = 1,2 \tag{5.22}$$

For a zone plate the maximal achievable numerical aperture is determined by the minimal technically achievable outermost zone width $(b_{min})_{lens}$ that still provides reasonable diffraction efficiencies. Consequently equation (5.22) implies that for both zone plates the same outermost zone width $(b_{min})_{lens}$ is used.

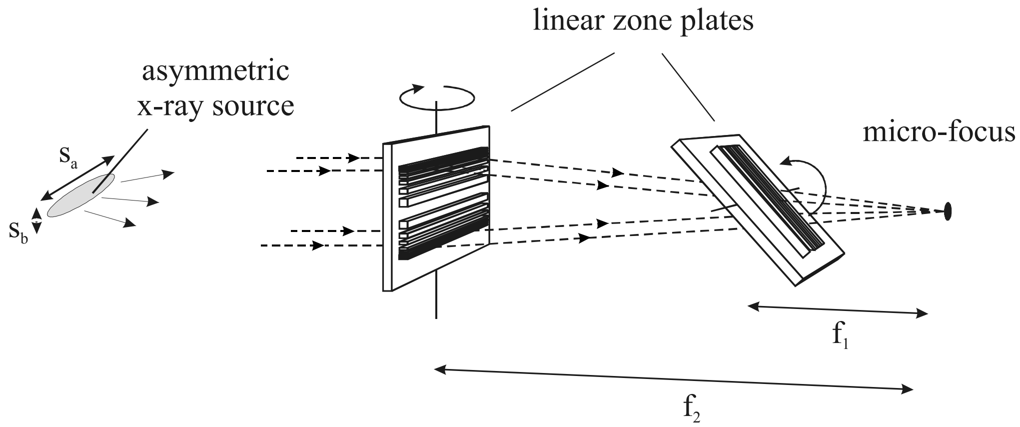

Figure 5.13: Schematic sketch of a micro-focusing set-up consisting of two linear zone plates. In principle the focal lengths of the two zone plates can be chosen freely. For minimal size of the resulting micro-focus the focal planes of the two lenses have to coincide.

Using geometrical optics and taking into account equation (5.22) one finds that the effective aperture at the position of the second lens (having a focal length f_2) is always a square, independent of the choice of f_1. Consequently, the diffraction limited spot of such a device will be identical to spot of a conventional zone plate, having a square shaped aperture and a numerical aperture NA_{lens}. This leads to (see equation (2.60))

$$w_{diff,c} = 0.89 \frac{\lambda f_2}{D_2} = 0.45 \frac{\lambda}{NA_{lens}} = 0.45 \, (b_{\min})_{\text{lens}} \tag{5.23}$$

For conventional lenses the performance can be compared using plots analogous to Figure 5.12. The performance of focusing devices having an independent focusing in horizontal and vertical direction can be easily included in such a comparison, if the relative gain in performance of such a device compared to a conventional zone plate, having the same minimal outermost zone width $(b_{min})_{lens}$, is known. In consequence it is useful to compare the performance of a conventional round zone plate with a focusing device consisting of two linear zone plates, taking into account that all lenses have the same numerical aperture NA_{lens}.

For a conventional zone plate an asymmetric x-ray source will lead to an asymmetric image of the source and consequently an asymmetric focal spot. It will be shown in the following that this is not necessarily true for the focusing device shown in Figure 5.13. A proper choice of the two focal lengths f_1 and f_2 makes it possible to obtain a symmetric image of the source.

The fact that a symmetric focal spot can be achieved using such a device is an advantage for most practical applications. However, it is not straightforward to find a useful criterion for

comparing an asymmetric spot (originating from a conventional zone plate) with a symmetric spot (produced by two crossed linear zone plates). Even in the general case of freely chosen values of the focal lengths f_l and f_2 the asymmetry of the two focal spots is not the same (unless the two focal lengths f_l and f_2 are identical), making a direct comparison difficult.

One useful criterion to compare the performance of a conventional zone plate and a focusing device using two crossed linear zone plates is to consider the area A_{foc} of the focal spot defined as.

$$A_{foc} = w_y w_z \tag{5.24}$$

On the one hand the value of $w_y w_z$ approximately determines the number of pixels per unit area that can be resolved if a sample is scanned with the micro-focus. On the other hand the product $w_y w_z$ determines the peak intensity in the focal spot (see equation (5.17)). Finally, the spot area defined by equation (5.24) is directly related to the geometric mean $\underline{w}$ of the focal widths w_y and w_z, so that the value of A_{foc} also determines the mean width of the focal spot.

$$\underline{w} = \sqrt{w_y w_z} = \sqrt{A_{foc}} \tag{5.25}$$

In principle there are two possibilities to compare the performance of two focusing devices that produce micro-spots with different asymmetries. Either one claims that both spots need to have the same area and compares the total flux in both spots, or one claims that both spots need to contain the same amount photons and compares the area of the two spots.

For a focusing device consisting of two crossed zone plates the focal lengths f_l and f_2 can be chosen freely (see also Figure 5.13). Consequently, one needs to find the optimum values of f_l and f_2, resulting in optimal performance of the device. For the calculation of the optimum focal lengths one can either optimise the flux in the spot, keeping its area constant, or minimize the spot area, keeping the flux in the spot constant. Both considerations lead to the same result. In the following it is shown that optimal performance requires a ratio of f_l and f_2 that is equal to the source asymmetry m_a.

In analogy to equation (5.10) the geometrical source image in horizontal and vertical direction are given by

$$s_{y,c} = s_a(f_1 / p) \quad \text{and} \quad s_{z,c} = s_b(f_2 / p) \tag{5.26}$$

where the subscript c denotes the fact, that two crossed lenses are used as a focusing device. The width of the focal spot is then given by

$$w_{y,c} = \sqrt{w_{diff,c}^{\;2} + s_{y,c}^{\;2}} \qquad w_{z,c} = \sqrt{w_{diff,c}^{\;2} + s_{z,c}^{\;2}} \tag{5.27}$$

and using equations (5.13) and (5.26) leads to

$$w_{y,c} w_{z,c} = \sqrt{w_{diff,c}^{\;2} + (m_a s_b f_1 / p)^2} \; \sqrt{w_{diff,c}^{\;2} + (s_b f_2 / p)^2} \tag{5.28}$$

Note, that introducing a modified focal length f_l‘ defined by f_l’$=m_a f_l$ equation (5.28) becomes symmetric with respect to f_l‘ and f_2.

Maximising the photon flux Φ in the focal spot is equivalent to maximising the product of the lens diameters D_1 and D_2 and - according to equation (5.22) - equivalent to maximising the product of f_1 and f_2. Keeping the area of the focal spot constant one finds

$$w_{y,c} w_{z,c} = \text{constant} \qquad \text{and} \qquad \phi \propto (\mathrm{f}_1 \times \mathrm{f}_2) \rightarrow \text{Max}$$

Using equation (5.28) and its symmetry with respect to f_1' and f_2 this leads to

$$f_2 = f_1' = m_a f_1 \qquad (5.29)$$

Minimising the area of the focal spot while keeping the photon flux Φ constant one has

$$\phi \propto (\mathrm{f}_1 \times \mathrm{f}_2) = \text{constant} \qquad \text{and} \qquad w_{y,c} w_{z,c} \rightarrow \text{Min}$$

Taking into account equation (5.28) this leads to the same result as found before (see equation (5.29)).

$$f_2 = f_1' = m_a f_1$$

In conclusion one finds that choosing the ratio of f_2/f_1 equal to the asymmetry m_a of the x-ray source will result in optimum performance of the focusing device with respect to both, photon flux and size of the focal spot. Note, that this choice for the focal lengths also leads to an symmetric micro-spot ($w_{y,c}$=$w_{z,c}$; see equations (5.27) and (5.28)), which for most applications represents an important advantage in comparison to focusing devices using only one conventional lens. If the ratio of the two focal lengths f_1 and f_2 is fixed and given by the asymmetry m_a of the x-ray source it is relatively simple to compare the performance of a round zone plate with a focusing device consisting of two crossed linear zone plates.

For a round zone plate the diffraction limited size $w_{diff,r}$ of the focal spot is given by

$$w_{diff,r} = 1.02 \frac{\lambda f}{D} = 0.51 \frac{\lambda}{NA_{lens}} = 0.51\, (b_{\min})_{\text{lens}} \qquad (5.30)$$

where the subscript r denotes the fact that one has a conventional round zone plate. In the following it proves to be useful to introduce a factor $k_{r,c}$ defined as the ratio between the diffraction limited spot size $w_{diff,r}$ of a round zone plate and the diffraction limited spot size $w_{diff,c}$ obtained by using two crossed linear zone plates. As the numerical aperture and the corresponding minimal zone width b_{min} is the same for both types of lenses we therefore obtain (see equations (5.23) and (5.30))

$$k_{r,c} = w_{diff,r} / w_{diff,c} = 0.51 \frac{\lambda}{NA_{lens}} / 0.45 \frac{\lambda}{NA_{lens}} = 1.15$$

Using equations (5.12) - (5.14) one finds

$$w_{y,r} w_{z,r} = s_{y,r}{}^2 \sqrt{r_{coh}{}^2 + 1}\ \sqrt{r_{coh}{}^2 + (1/m_a)^2} \qquad (5.31)$$

Rearranging equation (5.28) leads to

$$w_{y,c} w_{z,c} = s_{y,r}{}^2 \left(\sqrt{(1/k_{r,c})^2 r_{coh}{}^2 + (f_1/f)^2}\right)^2 \qquad (5.32)$$

where f is the focal length of the round zone plate. Claiming that the area of both spots has to be the same ($w_{y,r}w_{z,r}=w_{y,c}w_{z,c}$) one obtains

$$(f_1/f)^2 = \sqrt{r_{coh}{}^2+1}\ \sqrt{r_{coh}{}^2+(1/m_a)^2} - (1/k_{r,c})^2 r_{coh}{}^2 \qquad (5.33)$$

The gain in photon flux G_{signal} is given by the ratio of the flux Φ_c in the focus of the focusing device using two crossed zone plates and the flux Φ_r in the spot of the conventional zone plate. The area of both foci is the same. Consequently, the ratio $I_{p,c}/I_{p,r}$ of the peak intensities of the two foci will the same as the ratio Φ_c/Φ_r. This leads to

$$G_{signal} = \Phi_c / \Phi_r = I_c / I_r \qquad (5.34)$$

If the total efficiency η_{total} of both focusing devices is the same, then the area of the two lens apertures solely determines the photon flux within the focal spot. Taking into account the possibility of different total efficiencies one finds

$$G_{signal} = \frac{\eta_{total,c}}{\eta_{total,r}} \frac{D_1 D_2}{(D/2)^2 \pi} = \frac{4}{\pi} \frac{\eta_{total,c}}{\eta_{total,r}} \frac{f_1 f_2}{f^2} = \frac{4m_a}{\pi} \frac{\eta_{total,c}}{\eta_{total,r}} \left(\frac{f_1}{f}\right)^2$$

Together with equation (5.33) this leads to

$$G_{signal} = \frac{4m_a}{\pi} \frac{\eta_{total,c}}{\eta_{total,r}} \left(\sqrt{r_{coh}{}^2+1}\sqrt{r_{coh}{}^2+(1/m_a)^2} - (r_{coh}/k_{r,c})^2\right) \qquad (5.35)$$

Figure 5.14 shows the resulting gain in signal assuming equal total efficiencies of both focusing devices. For small values of the coherence factor r_{coh} (incoherent illumination) both focusing devices basically achieve the same photon flux (G_{signal}~1). The small difference (a factor $4/\pi$) results from the difference in the aperture shape of a device using crossed linear zone plates and a conventional round zone plate.

This behaviour in the case of incoherent illumination can be easily understood as for small values of r_{coh} the focal spot basically represents a geometrical image of the source. Starting from $f_1=f_2$ and increasing one of the focal lengths (and therefore one of the diameters) of the linear zone plates will increase the photon flux but also increase the focal spot size by the same amount. Consequently, changing the ratio f_1/f_2 does not improve the gain G_{signal} in photon flux and intensity. However, there is a significant difference between the two focusing devices. For the conventional zone plate the photon flux is found within an asymmetric spot whose asymmetry is given by the asymmetry m_a of the x-ray source, whereas for two crossed linear zone plates a symmetric focal spot is achieved, provided that the appropriate ratio of f_1/f_2 was chosen.

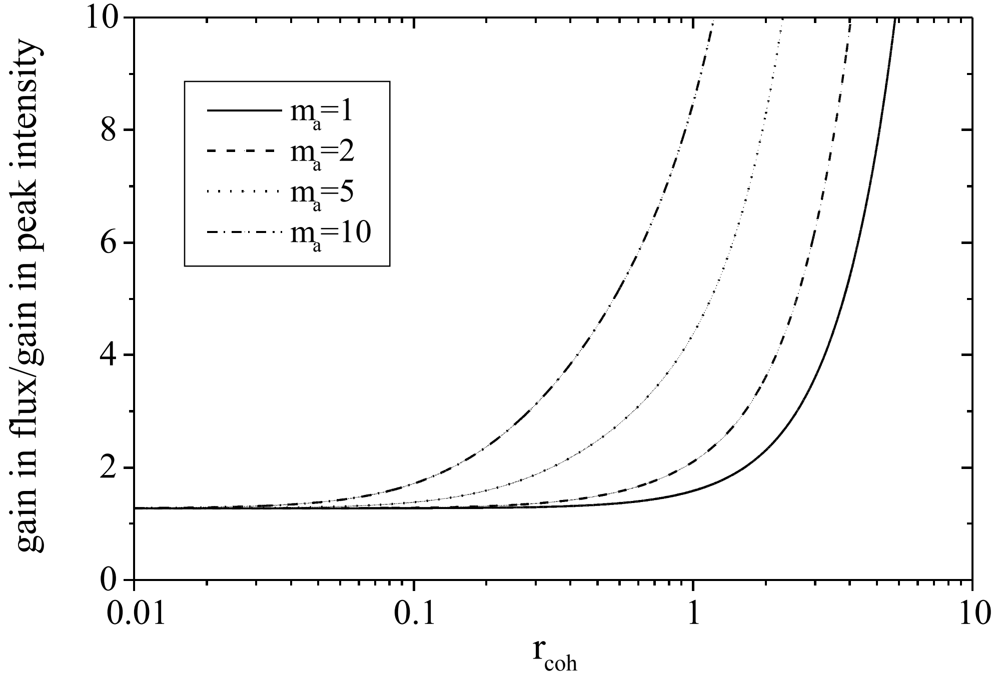

Figure 5.14: Calculated gain in photon flux and peak intensity using a focusing device consisting of two crossed linear zone plates instead of a conventional round zone plate. For the calculation it is assumed that both focusing devices have to achieve the same size of focal spot area, that all lenses have the same outermost zone width b_{min} and that both devices feature the same total efficiency.

For large values of the coherence factor r_{coh} a large increase of the gain in flux/intensity is found. Analysing equation (5.35) one finds that for r_{coh}>>1 the gain G_{signal} is proportional to m_a and r_{coh}^2. The strong increase of the gain results from the fact, that the area of diffraction limited spot of a round zone plate is about 30% larger than for two crossed linear zone plates. In order to get very close to the theoretical resolution limit of a round zone plate the diameter of the round zone plate has to be made extremely small. However due to the higher diffraction limited resolution of two crossed zone plates it is easy to achieve the same spot size even using reasonable diameters of the linear zone plates.

It was shown in chapter 5.2.1.1 that for focusing devices it never makes sense to use coherence factors r_{coh}, which are significantly smaller than one, as this does not significantly improve the resolution but strongly decreases the photon flux and the intensity in the focal spot. One finds that for the border case r_{coh}=1 (more or less coherent illumination) the gain in flux and intensity is approximately equal to the asymmetry m_a of the x-ray source (G_{signal}~m_a, see e.g. Figure 5.14).

An alternative possibility to compare a conventional zone plate and a focusing device consisting of two crossed zone plates is to claim that the photon flux within both focal spots has to be the equal and to compare the resulting areas of the two micro-spots. The gain in resolution G_{res} is then given by the ratio of the two focal spot areas leading to

$$G_{res} = \frac{w_{y,c} w_{z,c}}{w_{y,r} w_{z,r}} \qquad (5.36)$$

The photon flux is determined by the diameters of the round and two linear zone plates, as well as by the total efficiency of the two focusing devices, leading to

$$\frac{\phi_c}{\phi_r} = 1 = \frac{\eta_{total,c}}{\eta_{total,r}} \frac{D_1 D_2}{\pi (D/2)^2} = \frac{4 m_a \eta_{total,c}}{\pi \eta_{total,r}} \frac{f_1^2}{f^2}$$

Using equations (5.31) and (5.32) one obtains

$$G_{res} = \sqrt{r_{coh}^2 + 1} \sqrt{r_{coh}^2 + (1/m_a)^2} \Bigg/ \left[(r_{coh} / k_{r,c})^2 + \frac{\pi \eta_{total,r}}{4 m_a \eta_{total,c}} \right] \qquad (5.37)$$

Figure 5.15 shows the resulting gain in resolution assuming the same total efficiency for both focusing devices.

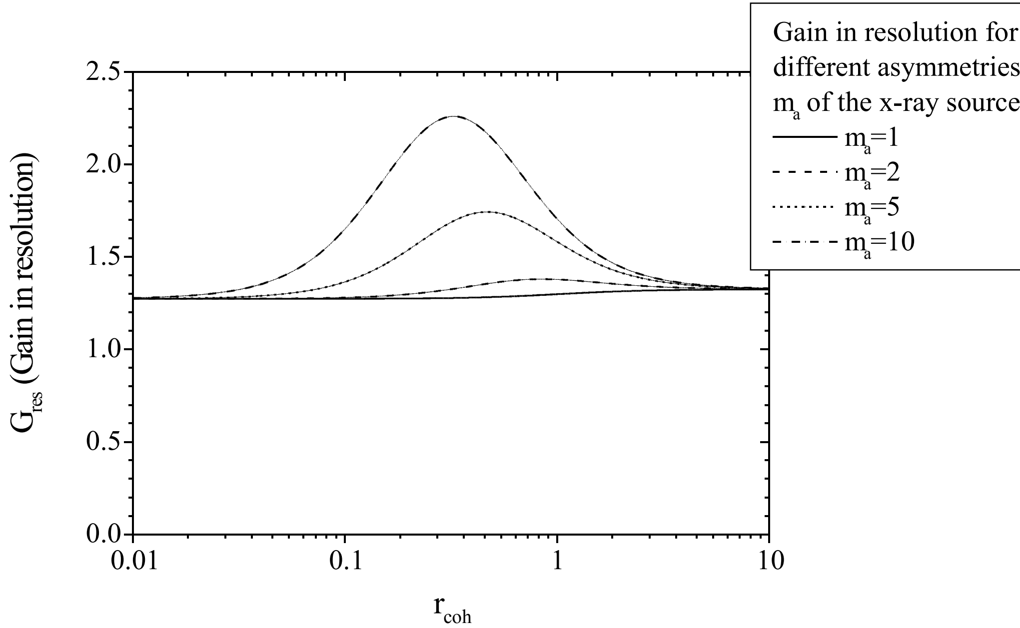

Figure 5.15: Calculated gain in resolution using a focusing device consisting of two crossed linear zone plates instead of a conventional round zone plate. For the calculation it is assumed that both focusing devices have to achieve the same flux in the spot, that all lenses have the same outermost zone width b_{min} and that both devices feature the same total efficiency. The gain in resolution G_{res} is then defined as the ratio of the corresponding spot areas stemming from the round zone plate and the focusing devices using two crossed linear zone plates.

Again, for small values of r_{coh} (incoherent illumination) little difference is found between the two focusing devices (G_{res}~$4/\pi$). For very large values of the coherence factor r_{coh} the gain in resolution is determined by the ratio $r_{r,c}$ (G_{res}~$k_{r,c}^2$=1.33). A significantly higher gain in resolution can be achieved for values of r_{coh} close to unity, provided that the source asymmetry m_a is large.

In praxis it is unlikely that both focusing devices have exactly the same total efficiency. Consequently, it is interesting to know about the maximal tolerable ratio $\eta_{total,r}/\eta_{total,c}$ of the efficiencies where two crossed linear zone plates still have the same performance as a conventional zone plate with respect to obtainable photon flux and resolution. Considering equation (5.35) for the case that both devices have the same efficiency ($\eta_{total,c}$=$\eta_{total,r}$) one obtains a certain gain G_0 in photon flux and peak intensity using two crossed linear zone plates instead of a round zone plate (see also Figure 5.14). This gain G_0 then gives the maximal tolerable ratio $\eta_{total,r}/\eta_{total,c}$ where the performance of two crossed linear zone plates is still the same as for a round zone plate.

If two linear zone plates are used in series one has to consider diffraction and absorption losses in two optical devices. The total efficiency $\eta_{total,c}$ of two linear zone plates in series is then given by $\eta_{total,c}=\eta_{1,c}\eta_{2,c}$, where $\eta_{1,c}$ and $\eta_{2,c}$ are the efficiencies of the first and the second linear zone plate. Consequently, the efficiency of a round zone plate will be higher than for two crossed linear zone plates, considering the special case that both types of lenses reach the same efficiencies. Note however, that the tilting technique, enabling an increase and optimisation of the grating structure height, can only be applied for linear zone plates, so that in praxis it will be more difficult to reach high efficiencies for round zone plates than for linear zone plates. At the same time one has to take into account the gain G_0 in flux and intensity mentioned above, which is obtained using two crossed linear zone plates instead of a round zone plate. Figure 5.14 shows that for the case of incoherent illumination ($r_{coh}<<1$) this gain G_0 in signal is comparatively small. However, for the case of coherent illumination of the lens ($r_{coh}\approx1$) the gain G_0 in flux and intensity is found to be approximately equal to the asymmetry m_a of the x-ray source.

In conclusion one finds, that there are basically two parameters determining the performance of a focusing devices: the diffraction limited spot size and the degree of coherence of the lens illumination, described by the parameter r_{coh}. Chapter 5.2.1.1 showed the consequences of using two different round zone plates for the same focusing application, if one of these lenses yields a k times smaller diffraction limited spot size than the other one. A k-times smaller diffraction limited spot size corresponds to a k times larger numerical aperture and therefore a k times larger "light collecting angle". It was therefore (roughly) found, that the lens with better resolution has a k^2 better performance with respect to both, total flux as well as peak intensity in the focus. This gain in total flux can then compensate for an eventually lower efficiency of the lens with higher resolution. Chapter 5.2.1.2 showed the consequence of using two crossed linear zone plates instead of a round zone plate assuming that both lenses have the same minimal outermost grating period and that the total efficiency of both devices is the same. It was found, that for incoherent illumination ($r_{coh}<<1$) the use of two crossed zone plates instead of a round zone plate does not result in a significant gain G_0 in photon flux and intensity of the focal spot. For coherent illumination ($r_{coh}\approx1$) the gain G_0 is found to be approximately equal to the asymmetry m_a of the x-ray source. In both cases one has the advantage, that the focal lengths of the two crossed lenses are adjusted to the asymmetry of the x-ray source, leading to a symmetric focal spot for such a focusing device instead of the asymmetric spot achieved with a conventional round zone plate.

5.2.2 Resolution tests on linear zone plates

Figure 5.16 shows a schematic sketch of the experimental set-up at the beamline ID13 of the European Synchrotron Radiation Facility, which was used to test the resolution of a micro-focusing device consisting of two linear multilevel zone plates.

The set-up is very similar to the one used to determine the efficiency of linear zone plates. Basically it only contains two additional components: another zone plate (lens1), which is used for the focusing of the beam in horizontal direction, and an order selecting aperture (pinhole), which is used to block most of the light that is not diffracted into the micro-focus.

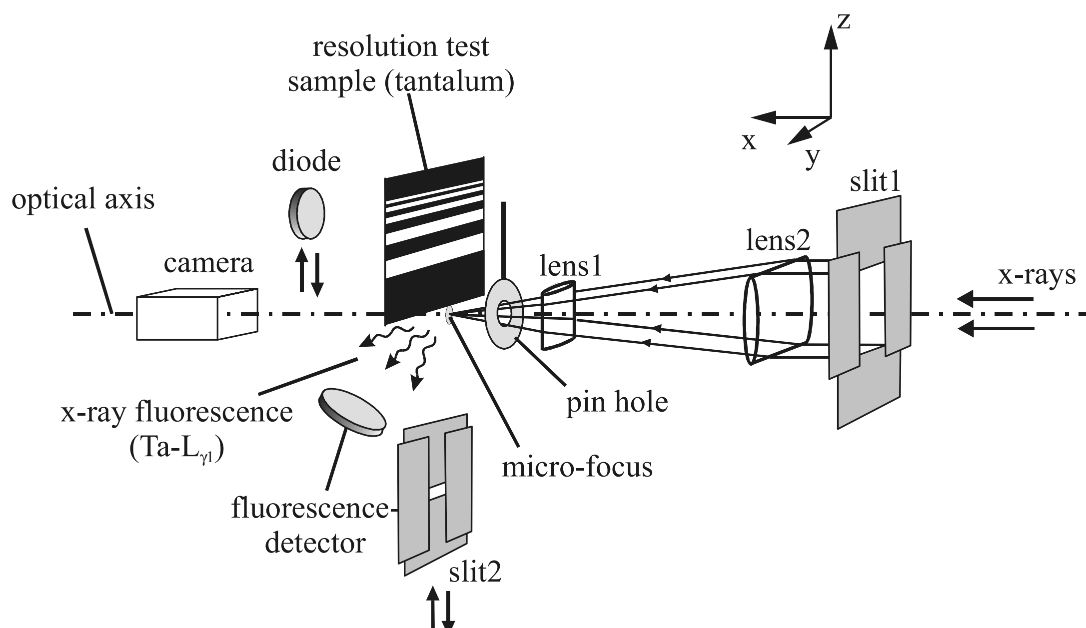

Figure 5.16: Schematic sketch of the experimental set-up for testing the resolution of a micro-focusing set-up consisting of two crossed linear multilevel zone plates. The resolution and the size of the focal spot are determined by scanning a tantalum containing test object through the focal spot, measuring the resulting tantalum x-ray fluorescence with a suitable detector.

Both lenses are mounted as described before, using sample holders consisting of components from LINOS Photonics GmbH&Co Kg. The holders were then fixed onto a motorized goniometer heads and built-in stages of ID13, enabling the adjustment of the position and orientation of both zone plates with respect to each other as well as with respect to the incoming x-ray beam.

At the micro-focus beam-line ID13 an undulator is used for the generation of x-rays. The beam is monochromatized by means of a silicon (111) double crystal monochromator. A constant photon energy of 12.7 keV was used, enabling high diffraction efficiencies of the zone plates as well as a strong absorption - and therefore good contrast - of the tantalum resolution test sample.

The undulator at ID13 has an x-ray source size of about 140µm×25µm, leading to a source asymmetry m_a of about 5.6. For the given distance between the lenses and the x-ray source ($p \approx 35$m) the transverse coherence lengths in horizontal and vertical direction at the position of the focusing device are found to be 25 µm and 140 µm, respectively. In order to achieve more or less coherent illumination of both linear zone plates - and therefore a resolution close to the diffraction limit - the diameters of the zone plates would have to be of about the same

size as the transversal coherence lengths or even smaller. Especially in horizontal direction this would result in a very small lens diameter and therefore a very small aperture of the focusing device. It was therefore decided to accept a certain loss in resolution and also to accept a certain asymmetry of the focal spot of the focusing device in order to increase the flux collected by the focusing device. Consequently, diameters of 200 µm and 50 µm were chosen for the two zone plates. The zone plates had focal lengths of 750 mm and 187.5 mm at the design photon energy of 12.4 keV, leading to a numerical aperture of about 1.3×10^{-4} in vertical as well as in horizontal direction.

Taking into account the size of the x-ray source, its distance to the focusing device (approx. 35m) and the focal lengths of the two zone plates, the size of the geometrical source image is found to be 0.76µm×0.56µm. Equation (5.27) then yields $w_{c,z}$=0.67µm and $w_{c,y}$=0.84µm for the theoretical spot widths in vertical and horizontal direction. The theoretical widths of the spot are nearly two times larger than the diffraction limited spot size, which is a direct result from the rather incoherent illumination of the device. In fact the coherence factor r_{coh} is found to be significantly smaller than one (r_{coh}=0.28). According to the considerations in chapter 5.2.1 this will reduce the gain in flux and intensity G_{signal} of the focal spot, which one can achieve using two linear zone plates instead of a round zone plate. For the given parameters of the focusing device a gain G_{signal} of approximately 2 of is found in comparison to a conventional round zone plate, assuming the same total efficiency for both focusing devices.

For the measurements the distance between the zone plates and the resolution test-sample/slit2 was first set manually using a tape measure, taking into account the calculated image distances of both zone plates. The obtained positioning accuracy was larger than the theoretical depth of focus, which is found to be approximately 3 mm using equation (2.61). Consequently, later on no refocusing was required in order to achieve optimal resolution of the device. Both zone plates were then aligned with respect to the x-ray beam using the procedure described in chapter 5.1. For both zone plates the tilt angle influencing the effective height of the grating structures was set to the theoretical value (86^0), leading to optimal diffraction efficiency.

For the second lens having a comparatively large diameter (D_2=190µm) the efficiency was measured by scanning slit2 through its focal plane while the first lens was moved out of the beam. Using the evaluation technique described in chapter 5.1.2 the ideal efficiency was found to be 65% and the absolute efficiency 59%, taking into account absorption losses within the membrane. By changing the tilt angle and measuring the resulting photon flux in the focus the chosen tilt angle (86^0) could also be confirmed to be optimal with respect to the achievable efficiency.

Due to the comparatively small diameter of the first zone plate (D_1=50µm) it was not possible to obtain a reliable efficiency measurement of this lens. However, later on its high diffraction efficiency could be confirmed indirectly by measuring the overall efficiency of the focusing device.

Using the x-ray camera the two lenses were centred with respect to each other, leading to a focusing in both directions within their overlap region and consequently to the formation of a micro-focus. In order to reduce the background signal in the focal plane the gaps of slit1 were closed down according to the diameters of the two lenses. The remaining zero and higher diffraction orders were then blocked out using an order-selecting aperture (pinhole of about 20 µm diameter), which was placed in a distance of about 2 mm from the resolution test object.

The resolution test object was a silicon membrane (of about 20 µm thickness) with a 350 nm thick, sputtered tantalum layer. Within the membrane region the tantalum layer had been patterned by means of e-beam lithography and reactive ion etching. The test-object was fixed onto a piezoelectric scanner, enabling very small and controlled movements in y- and z-direction (smallest step size about 25 nm). The scanner itself was mounted onto conventional mechanical motor stages, enabling the course adjustment of the position of the test object with respect to the micro-focus.

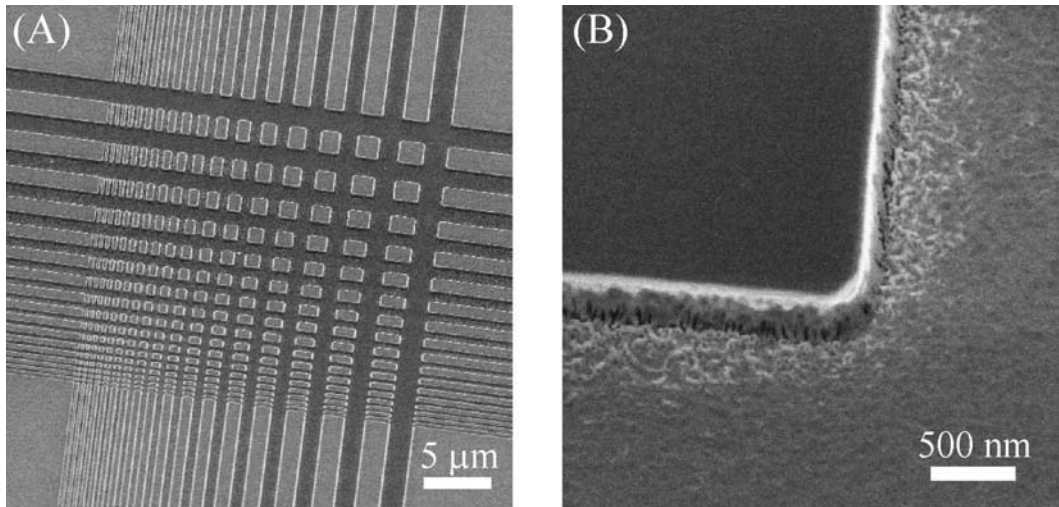

Figure 5.17: SEM-viewgraphs of resolution test structures made from tantalum. (A) Crossing region between two binary test gratings having a variable grating period. (B) Close-up of two straight, perpendicular edges (so-called knife-edges) which are used to determine the shape of the focal spot in two orthogonal (e.g. horizontal and vertical) directions.

Basically two types of tantalum test-structures were used to determine the resolution of the micro-focusing device. One of them is a binary grating with variable grating period ranging from 400 nm to 4 µm (see Figure 5.17 A). Another type of structure simply consists of large regions containing tantalum or no tantalum with a sharp transition (a so-called knife-edge) between these two regions (see Figure 5.17 B).

The characteristic x-ray fluorescence ($L_{\gamma 1}$ line of Ta; photon energy = 10,9 keV) of tantalum was measured using an energy sensitive x-ray detector, resulting in a strong imaging contrast between regions with tantalum (more than 10^4 counts/sec) and without tantalum (about 10^2 counts/sec).

Figure 5.18 shows the corresponding detector signal obtained by scanning a binary tantalum grating with variable grating constant through the micro-focus. If the size of the focal spot is significantly smaller than the grating period a strong oscillation of the fluorescence signal is observed. Going to smaller grating periods the oscillations become smaller and smaller and below a certain grating period completely cease. A maximal fluorescence signal (I_{max}) is obtained if the center of the focal spot coincides with the center of a bar (half period) containing tantalum. Minimal fluorescence (signal I_{min}) occurs for the case that the center of the focal spot coincides with the center of the neighbouring half period containing no tantalum. The difference between these two extreme values divided by their sum represents a kind of normalized modulation depth of the signal and is commonly referred to as the visibility v_{signal} of the test grating structure.

$$v_{signal} = (I_{\max} - I_{\min}) / (I_{\max} + I_{\min}) \quad (5.38)$$

Plotting the visibility versus the spatial frequency (e.g. number of lines/mm) of the grating the so-called modulation transfer function (MTF) of the focusing device is obtained, which in conventional optics is commonly used to characterize the optical performance of a lens system.

Optimal focusing of the device was obtained by maximizing the visibility of horizontally and vertically orientated test gratings. The optimal distance between lens1 and the test-sample was determined using a test grating with vertical lines. In a second step the position of lens2 was adjusted to give maximal visibility of a test grating with horizontal lines.

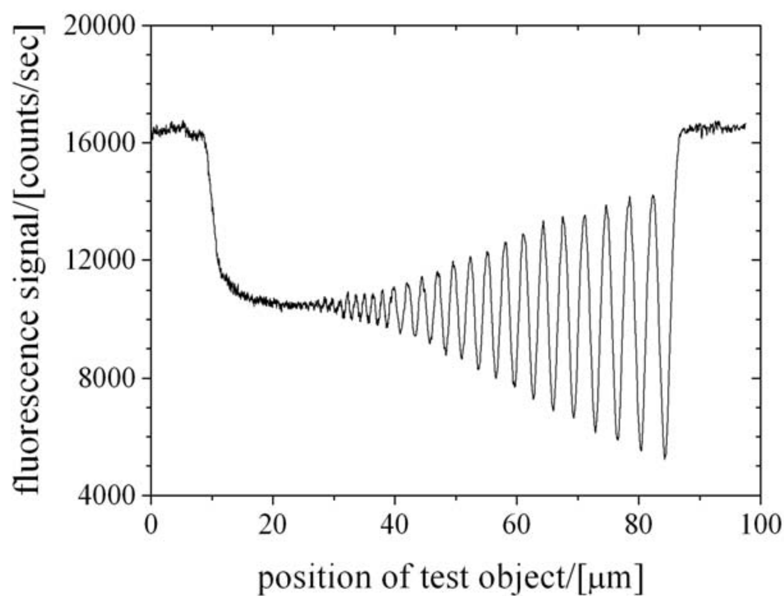

Figure 5.18: Tantalum fluorescence signal obtained by scanning a grating with variable grating constant across a focal spot. If the width of the micro-focus is significantly smaller than the grating period this leads to strong variations of the fluorescence signal, depending on whether the binary tantalum grating is fully hit by the focal spot or not. Going to smaller grating periods (regions in the left part of the figure) these oscillations gradually decrease and finally cease, meaning that the corresponding grating period cannot be resolved any more.

It was found that the optimum positions of the test-object and the zone plates were practically identical to the ones one would expect from theory, taking into account the focal length of the two lenses and the image distance p to the x-ray source. The observed differences (less than 2 mm) can be attributed to the comparatively large focal depth d_{focus} of the focusing device ($d_{focus} \approx$ 3mm, see equation (2.61)) and the uncertainty of determining the distances with a tape measure.

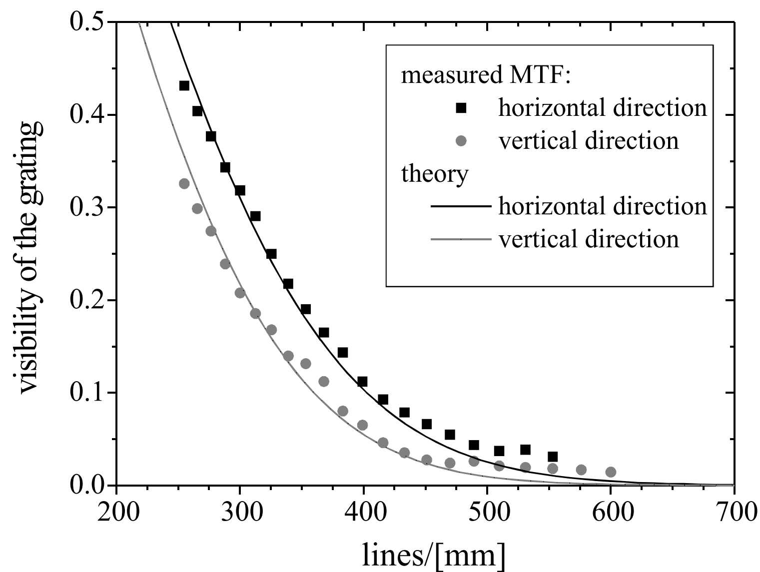

Figure 5.19: Measured and theoretical visibility of a binary tantalum grating shown for different spatial frequencies (lines/mm) of the grating. The obtained curves are referred to as the modulation transfer functions (MTF) of the focusing device. The theoretical curves are obtained assuming a tantalum grating with a duty cycle of 0.5 (equal width of regions with and without tantalum layers) and a gaussian focal spot, having a FWHM-size of 2.1 μm and 2.35 μm in horizontal and vertical direction, respectively.

Figure 5.19 shows the measured modulation transfer function of a well-focused optical device consisting of two crossed linear zone plates. The corresponding visibilities were determined by scanning subsequently a horizontally and a vertically orientated test grating with variable grating constant across the micro-focus, leading to a fluorescence signal equivalent to the one shown in Figure 5.18. In order to ensure a highly precise positioning, the piezoelectric scanner was used for the movement of the resolution test sample. As the position as well as the width of each period is known, the obtained data could be used to evaluate the visibility for different grating periods but also to calibrate the movement of the piezoelectric-scanner (absolute position as a function of the input voltage).

Figure 5.19 shows that for gratings with less than about 500 lines/mm a significant visibility is observed for the horizontal as well as for the vertical direction. The maximal spatial frequency of a grating leading to a non-zero visibility is commonly referred to as the cut-off frequency. Consequently, one finds that the cut-off frequency of the modulation transfer functions shown in Figure 5.19 is about 500 lines/mm and approximately the same in the vertical and the horizontal direction. At the same time this means that gratings with a period down to about 2 μm have significant visibility and therefore can be resolved using this focusing device.

For the fabrication of the binary resolution test gratings special care was taken that for each period the two halves containing tantalum and no tantalum have the same width (duty cycle equal to 0.5). At the same time it could be achieved that the transition region between these two different regions is always much smaller than the grating period itself. Consequently the optical behaviour of such a grating should be close to the behaviour of an ideal grating, with infinitely sharp transitions between regions of tantalum and no tantalum and a duty cycle of 0.5. Assuming a gauss-like micro-focus and calculating the fraction of the total flux within the focal spot, which penetrates regions with tantalum, it is possible to model the fluorescence signal one anticipates for the grating described above. Calculating the maximal and the minimal fluorescence signal for different ratios of the width of the focal spot and the

grating period one obtains the modulation transfer function. The solid lines in Figure 5.19 show the resulting theoretical curves, which were calculated using a simple turbo pascal program.

For the calculation of the MTF only the width of the focal spot along the direction of the grating periodicity plays a role, as changing the width in the perpendicular direction does not influence the result. This enables an independent evaluation of the theoretical FWHM-widths of the spot in vertical and horizontal direction, which lead to the best approximation of the measured MTF-data values.

Knife-edge scans are another possibility to characterize the focal spot and directly measure its FWHM-widths in horizontal and vertical direction. Figure 5.20 shows the corresponding fluorescence signal, if a sharp edge between two regions with and without tantalum is scanned across the micro-focus. The fluorescence signal is determined by the fraction of the spot that lies within the region with tantalum. Making a small change of the position of the resolution test object, a small part of the focal spot will either be moved out or included in the tantalum-containing region. Consequently, the change in fluorescence (i.e. its derivative) is proportional to the intensity within this small part of the spot. Note that like for the MTF-measurements the width of the focal spot in the direction of the knife-edge does not play a role. In case of a gauss-like shape of the spot the derivative of the fluorescence signal directly represents the shape of a cut through the focal spot, which is made perpendicular to the direction of the knife-edge.

Even a small noise in the fluorescence signal will lead to considerable noise of the corresponding derivate of the signal. However, by averaging consecutive data values it is possible to obtain a very accurate image of the spot shape. Figure 5.20 shows, that the shape of the spot closely resembles a Gauss-curve. The FWHM-widths of the obtained Gauss-fits could therefore be used to determine the spot-widths in horizontal and vertical direction. Using the Gauss-fit shown in Figure 5.20 a spot width of 1.9 μm in horizontal direction was found. The width of the spot in vertical direction was found to be 2.2 μm, evaluating the data from another knife-edge scan in vertical direction. Both values are in very good agreement with the indirectly obtained focal spot widths, which provided the best agreement between the theoretical and the measured modulation transfer function (see Figure 5.19).

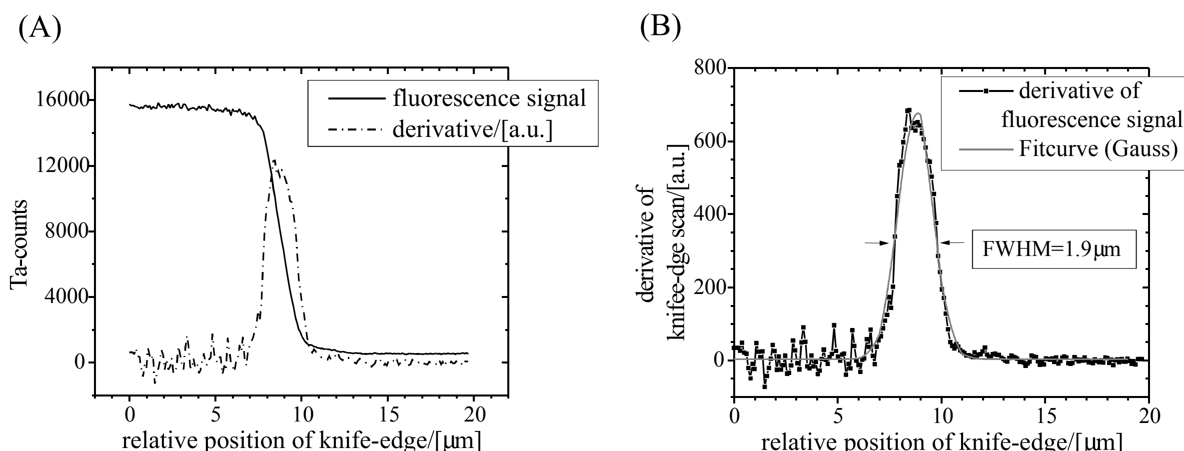

Figure 5.20: (A) Fluorescence signal obtained by horizontally scanning a knife-edge across a focal spot. (B) Evaluating the derivative of the scan one obtains the shape of the focal spot in perpendicular direction to the knife-edge. Figure B shows that the resulting spot-shape closely resembles a Gauss-curve.

Note, that the experimentally determined width of the focal spot (approx. 2 μm in horizontal as well as in vertical direction) is significantly larger than one would expect from theory. The minimal outermost period b_{min} of both linear zone plates was 800 nm, leading to a diffraction limited spot size of about half this value. Taking into account the size of the x-ray source (140μm×25μm), its distance to the focusing device (approx. 35m) and the focal lengths of the two zone plates, the size of the geometrical source image is found to be 0.76μm×0.56μm. Consequently, using equation (5.27) one obtains $w_{c,z}$=0.67μm and $w_{c,y}$=0.84μm for the theoretical spot widths in horizontal and vertical direction.

There are several possible reasons for the discrepancy between the theoretical and the experimental spot width. One possible explanation is a non-perfect focusing of the two linear zone plates, meaning that either the distance between the two lenses was not fully optimised or that the test-object was not exactly placed in the focal plane. However, due to the large focal depth of the focusing device (approx.3 mm) such a defocusing can - at most - partly explain the observed broadening of the focal spot.

In principle also a non-perfect alignment of the zone plates with respect to each other or with respect to the x-ray beam can lead to an increased width of the focal spot. However, due to symmetry reasons any alignment error $\Delta\varphi$ will only in the second order effect the width of the focal spot. At the same time - due to the used alignment procedure - the errors of all relevant tilt angles are small and should not exceed a value of about 10^{-2} rad. Making simple estimations and ray tracing one finds that the broadening should be of the order of $\Delta\varphi^2 \times D_1$ where D_1 is the (larger) diameter of the two linear lenses. Consequently, only extreme alignment errors in the order of 10^{-1} rad could explain the observed broadening of the focal spot.

One effect, which was experimentally verified to influence the resolution and the width of the focal spot, is vibrations within the optical set-up. Vibrations of the focusing device itself (the two lenses) and also the resolution test object are very unlikely to play any role as this would require oscillation amplitudes in the micron range. Experience shows that this is far beyond what one finds in praxis, even for non-optimised mechanical set-ups within a beam-line.

However it was experimentally found that vibrations within the silicon double monochromator strongly affected the resolution of the focusing device. These vibrations were caused by the cooling system which pumps liquid nitrogen through cooling elements that are placed on the back of the monochromator crystal, in order to remove the large amount of heat energy (in the order of 1 kW) produced by the incoming x-ray beam. The effect of the monochromator vibrations also could be observed directly using the x-ray camera and observing the change in the position of inhomogeneities within the x-ray beam. A characteristic 'jumping' of the position of the x-ray beam was observed, having amplitudes in the 10-micron range and frequencies in the order of a few hertz. This movement of the beam corresponds to a change in direction of the incoming beam and consequently lead to an erratic change of the position of the focal spot. Taking into account the distance between the monochromator and the focusing device (approx. 5 m) and the observed amplitude of the beam movement (in the 10 micron range) one finds that this monochromator vibrations are very likely to have a considerable effect on the mean, effective focal spot size. In fact it was found that by decreasing the frequency and pumpage of the liquid nitrogen pump the vibrations could be reduced, leading to a significant increase in the resolution of the focusing device. However, for practical and safety reasons the pumping power could only be decreased to certain limit, so that the effect of the vibrations on the resolution could not be completely eliminated.

A short test was performed in order to affirm the high efficiency of the focusing device. Measuring the diode signal with pinhole (flux in micro-focus) and without pinhole (total flux in focal plane, including all diffraction orders) we found an ideal efficiency of 40.2 %. The ideal efficiency of the focusing device is determined by the product of the ideal efficiencies of the first and the second zone plate. Consequently, taking into account the measured efficiency of lens2 (65%) it is also possible to calculate the ideal efficiency η_1 of lens1 (η_1= 40.2/65×100%=62%).

The absolute efficiency can be estimated considering the fact that both membranes had been thinned to approximately the same thickness, using the local thinning technique described in chapter 4.5. For lens2 the membrane absorption losses were in the order of 10% of the incoming beam. The absorption in air is found to be negligible (less than 2%) so that the absolute efficiency η_{abs} of the focusing device should be approximately 20% below its ideal efficiency (η_{abs}≈0.8×40%=32%).

5.2.3 Discussion

Using linear multilevel zone plates it is possible to build a micro-focusing device with very high efficiency. Another advantage is the small background signal caused by such a focusing device as a large fraction of the photon flux in the focal plane is contained in the focal spot. Consequently relatively large pinholes can be used, while it is still possible to block out most of the unwanted diffraction orders. For some applications it might be even possible to work without any order-selecting aperture.

Experimentally a spot size of about 2 microns was found, theoretically a spot size beneath 1 micron should be feasible, provided that experimental problems (like vibrations within the beam-line set-up) can be eliminated. In consequence linear zone plates are interesting candidates for micro-focusing applications where rather large photon flux than high resolution is required.

Such a micro-focus is a prerequisite for many experimental methods, where spatially resolved physical or chemical information of a sample is obtained using x-rays. One example is the element mapping of materials and of geological and biological samples, where the relative content of different elements within the focal spot is determined by measuring the element-specific (characteristic) x-ray fluorescence with an energy-selective detector. Scanning the micro-focus across the sample it is then possible to obtain a 2-dimensional or - in combination with tomography - even a 3-dimensional element map of the sample [79, 80, 81]. Micro-focusing devices are also useful to determine the x-ray absorption within different regions of a sample. Performing measurements at different photon energies the absorption contrast will change according to element specific absorption edges. Again this opens up the possibility to perform an - at least qualitative - element mapping. If photon energies close to the absorption edge of a specific element are used and by studying the bond-specific fine structure of the corresponding absorption spectrum it is possible to obtain information about the binding environment as well as the geometry of the absorbing atom. The use of a micro-focus for such EXAFS (Extended X-ray absorption fine structure) and NEXAFS (Near Edge X-ray Absorption Fine Structure) studies then offers the possibility to investigate different and very small regions of the sample.

One simple method to determine the absorption of different sample regions is to place an x-ray detector (e.g. a diode) behind the sample and measure the resulting x-ray transmission. Obviously for the absorption measurements there is no need to have a position sensitive detector, as only the total amount of light penetrating the sample is of interest for the measurement. However, it was found recently that the intensity distribution of the penetrating

light, measured in a plane that has a sufficiently large distance from the focal plane/sample, contains additional, valuable information about the internal structure of the sample. Basically one finds, that a gradient in the refractive index of the sample will lead to a shift of the center of the defocused focal spot. Consequently, using a segmented detector (e.g. a CCD-camera) and by properly combining the signal of different detector-regions it is possible to obtain differential phase contrast images of the sample. Depending on the chosen detector-regions and the evaluation strategy of the integrated signals, several different types of phase contrast are achievable. Consequently, one obtains an additional, novel set of imaging techniques within the large field of micro-focus based scanning x-ray microscopy [82].

For all micro-focusing applications mentioned up to now there are basically two properties of the focal spot, which are of relevance: the total photon flux within the spot and the minimal achievable focal spot size. In chapter 5.2.1 it was shown that a small efficiency of a micro-focusing device does not necessarily result in a bad performance of the device, provided that large numerical apertures and therefore small diffraction limited focal spot sizes are feasible. Consequently - despite of their extremely high efficiency - multilevel zone plates are not necessarily the optimal devices for these kind of micro-focusing applications.

One example of a promising competitor are linear binary silicon zone plates [41, 42] which can be used in exactly the same fashion as silicon multilevel zone plates. The main difference results from the fact, that these wet-etched lenses have binary (two-level) grating structures, so that their diffraction efficiency is significantly smaller than for multilevel lenses. The maximal theoretical efficiency is 40%, experimentally efficiencies of about 25% are found for high-resolution zone plates with a minimal grating period of 200 nm. Due to the high anisotropy of the wet-etching process extreme aspect ratios of the silicon grating structures are feasible. The large structure heights in connection with tilting of the zone plates makes it possible to use these lenses for extremely high photon energies (up to about 30 keV) and nevertheless obtain efficiencies close to theoretical limit [41]. At the same time it is possible to fabricate grating structures of high quality for very small grating periods down to 200 nm. This is a factor 4 smaller than what can be achieved for linear multilevel zone plates. The considerations in chapter 5.2.1 (see page 110) showed that a four times larger numerical aperture can compensate for an approximately 16 times smaller total efficiency of a focusing device. Assuming an efficiency of 25% for a binary lens the total efficiency of a focusing device consisting of binary lenses is approximately 6%. The total efficiency of a device consisting of multilevel zone plates was found to be larger than 30%. As the device consisting of binary zone plates has an approximately 16 times larger light collecting power, its performance with respect to the total flux and peak intensity in the focal spot is roughly a factor 3 better than for device using multilevel zone plates (comparing two devices that produce a micro-focus of the same size). However, the better performance of the binary lenses results from their larger numerical aperture and it will be shown later on that there are certain applications, which have an explicit limit for the maximal tolerable numerical aperture. Obviously in such a case it is not possible to compensate for the low efficiency of binary lenses by using lenses with larger numerical aperture.

X-ray mirrors are another type of focusing devices, which compete with linear multilevel for micro-focusing applications. They can reach comparatively large efficiencies, similar to the ones obtained with multilevel lenses. However, this requires sophisticated and expensive fabrication techniques in order to reach the necessary quality of the mirror surface with a roughness in the nm range. At the same time the incidence angle between the incoming x-rays and the mirror has to be extremely small (a few mrad) in order to achieve a sufficient reflectivity. Due to these shallow working angles a small change in the orientation of the mirror already leads to a strong change of the effective diameter and shape of the mirror,

making the alignment of x-ray mirrors a very critical and difficult procedure. The small incidence angles also require the use of very long mirrors, making it difficult to achieve the necessary accuracy of the mirror shape across the full mirror length. In consequence x-ray mirrors often suffer from strong aberrations because of both - deviations form the ideal mirror shape as well as misalignment with respect to the x-ray beam.

But there are also several undeniable advantages of x-ray mirrors. One of them is the fact that x-ray mirrors - contrary to all other types of x-ray lenses - are achromatic, so that the used x-ray wavelength can be changed without any need to refocus the sample or the focusing device. Another advantage is the fact that x-ray mirrors with comparatively large numerical apertures can be built. The maximum achievable numerical aperture is determined by the critical angle of total reflection $\theta_{critical}$ of the mirror material. Applying Snell's law one finds that the critical angle is approximately given by $\theta_{critical} \approx (2\delta)^{1/2}$ so that for materials with large density and therefore large δ (e.g Au, Pt) a critical angle of about 1/200 mrad can be reached (considering a photon energy of 12.4 keV). Assuming that the maximal numerical aperture is equal to about half the critical angle the theoretical, diffraction limited resolution is found to be about 20 nm and independent of the photon energy (using equation (2.26)). In praxis spot sizes of about 1 micron are obtained in routine operation. However, spot-sizes down to 100 nm FWHM have been reported recently [22, 24], using a so-called Kirkpatrick-Baez set-up, where two individual mirrors are used for the focusing in vertical and horizontal direction, respectively. In most cases the achieved spot size is significantly larger than the theoretical, diffraction limited spot size, meaning that the spot size of an x-ray mirror is typically determined by distortions and shape errors of the mirror and not by the diffraction at the lens aperture. For applications where the flux within the focal spot is the main figure of merit such a broadening of the focal spot does not play a role, provided that the resulting spot size does not exceed the experimentally given limits. However, the underlying distortions of the x-ray wave will destroy some of the original coherence of the lens illumination and there are certain applications (see the considerations below) where the coherence of the focal spot plays an essential role.

Finally, one should also mention the possibility to use refractive lenses for micro-focusing applications. A steady development and improvement of the fabrication techniques and lens materials nowadays makes it possible to achieve spot sizes down to about 100 nm [26, 83, 84]. However, for the x-ray energy range addressed with silicon multilevel zone plates (approximately 8-16 keV) x-ray absorption still plays a dominant role resulting in low total efficiencies of these devices. Using materials with very low atomic numbers (e.g. C, Be, B) the efficiency can be significantly improved. But the highly accurate structuring of these materials is a non-trivial task, making it difficult to achieve the required shape accuracy - despite of the large number of different approaches to fabricate such lenses (see also chapter 6 about refractive lenses).

In summary one finds, that binary silicon zone plates as well as focusing mirrors are superior to multilevel zone plates with regard to the maximal obtainable numerical aperture. This results in a significantly larger light collecting power and consequently for both devices the maximum obtainable photon flux for a certain fixed focal spot size will be larger than for multilevel zone plates. However, it was already mentioned earlier that a large numerical aperture is not necessarily tolerable for all kind of applications.

One obvious practical advantage of having small numerical apertures - like the ones obtained with multilevel zone plates - is the fact that a small numerical aperture results in a large focal depth of the device, which enables the investigation of thick samples and makes the focusing

process comparatively easy. But in fact there are also some applications having an explicit limit for the maximum tolerable numerical aperture.

One example is the study of small-angle x-ray scattering from small samples [85, 86] where focusing devices can be used to increase the total flux hitting the sample. The minimum scattering angle θ_{min} that can be detected is determined by the angular spread of the incoming beam. Consequently the numerical aperture NA of the focusing device must not exceed this minimum scattering angle. If the numerical aperture NA of a focusing just meets this requirement ($NA=\theta_{min}$) the only way of increasing the flux as well as the intensity in the spot is to increase the total efficiency of the device. The multilevel zone plates described within this work are therefore especially suited for this kind of application as they have very high efficiencies and at the same time very small numerical apertures (about 10^{-4}).

The minimum detectable scattering angle θ_{min} determines the maximum size a_{max} of internal structures of a sample, which can be resolved by small angle scattering. For a zone plate with $NA=\theta_{min}$ one finds that a_{max} is approximately equal to half the minimal outermost grating period b_{min} of the lens. For the multilevel zone plates described within this work, having an outermost grating period of 800 nm, this leads to an upper limit of about 0.5µm for the size of x-ray scattering objects, which can be investigated by small angle scattering.

X-ray wave-guiding experiments [87, 88, 89] are another example of set-ups, where one can profit from using focusing devices but where at the same time the possibility to freely choose the aperture and the numerical aperture of the focusing device can be limited, if it is preferable to use only one single mode of the wave-guide. Using a focusing device within such a set-up several conditions have to be met in order to reach that most of the focused light is coupled into one single wave-guide mode. Independent of the type of wave-guide there is always a certain limit of the tolerable angular spread of the incoming x-ray beam and therefore also of the numerical aperture of the focusing device. For the simplest case of a planar wave-guide having a constant gap w between two totally reflecting, parallel surfaces the maximal tolerable numerical aperture is determined by the angular mode spacing $\Delta\theta$ between two neighbouring modes [90], where $\Delta\theta$ is approximately given by $\Delta\theta=\lambda/(2w)$. If the numerical aperture exceeds this limit this will lead to the excitation of several neighbouring modes of the wave-guide. Note, that for the special case of a single mode wave-guide there is no real limitation of the numerical aperture, as in any case only one single mode can be excited. However, increasing the numerical aperture beyond a certain limit - which is determined by the angular "width" of this mode - will increase the photon flux at the entrance of the wave-guide but not increase the amount of light coupled into the single mode.

Besides the numerical aperture also the coherence of the illumination of the focusing device plays an essential role. Coherent illumination of the focusing device leads to a coherent field-distribution within the focus and implies that the focus basically contains only one fundamental mode of the electromagnetic field (and vice versa). For incoherent illumination of the device the focus contains several fundamental modes of the electromagnetic field. Incoherent illumination of the focusing device will therefore either lead to the excitation of several modes of the wave-guide or - in the best case - decrease the fraction of incoming light, which is coupled into the desired mode of the wave-guide. In consequence it does not make sense to increase the lens aperture beyond the limits given by the coherently illuminated area of the x-ray source, as only a coherent fraction of photons can be coupled into one single mode of a wave-guide.

6 Planar refractive lenses

In the following chapter the fabrication and optical testing of diamond and silicon planar refractive x-ray lenses is reported. The first part (chapter 6.1) gives a short introduction to the topic of refractive x-ray lenses in general and planar refractive lenses in particular, but also deals with general design considerations and the influence of shape errors on the performance of planar refractive lenses. Chapters 6.2 and 6.3 contain the work done on diamond and on silicon refractive lenses, respectively. Finally, in chapter 6.4 possible applications of such planar refractive lenses are pointed out and their advantages and disadvantages in comparison to other types of x-ray lenses are discussed.

6.1 General considerations

6.1.1 Introduction

About decade ago it was realized that it is feasible to fabricate x-ray refractive lenses with reasonable efficiencies and focal lengths [63]. Using many refractive lenses in series can circumvent the problem of small refractive effects in the x-ray range, so that extreme curvatures of the lens shape are omitted and nevertheless reasonable focal lengths are obtained. At the same time one finds that in the hard x-ray region above approximately 10 keV absorption becomes sufficiently small, so that reasonable transmissions of refractive lenses can be achieved, provided that suitable lens materials with low atomic numbers (e.g. Li, C, Be, Al, Si, etc.) are used.

The first refractive lenses were made using rather simple fabrication methods like drilling holes into suitable materials (Be, Al) [25], or utilizing bubbles enclosed in liquids or polymers [91]. However, in both cases the lenses have spherical shape, instead of the ideal parabolic one, leading inevitably to strong aberrations. More recently aluminium refractive lenses have been fabricated using a pressing technique in order to obtain a lens shape close to the ideal one. In consequence these so called parabolic compound refractive lenses show a greatly improved performance in terms of resolution and imaging quality [92]. The use of aluminium for the fabrication of these lenses has the drawback that absorption plays a dominant role for energies below about 15 keV. In consequence considerable efforts have been made to transfer this fabrication process to more suitable materials (e.g. Be, B, C), which recently led to the successful fabrication of beryllium lenses [93]. However, beryllium is highly toxic and therefore dangerous to handle and its large brittleness makes the machining of such lenses very difficult. In consequence it is reasonable to restrict their use to applications where they offer a significant advantage in comparison to aluminium lenses - e.g. in the lower part of the hard x-ray region where absorption plays a dominant role.

A different approach to overcome the problem of absorption has been reported by Aristov et. al. [27], who used a planar fabrication technology to obtain planar silicon lenses with minimized absorption. The idea of this type of lens is to omit passive parts of a lens, which merely cause a multiple of 2π in phase shift (see Figure 2.20 in chapter 2.3.2). Shifting the phase of a plane wave by 2π resembles the same wave again. Consequently, removing a bar within a lens that causes a multiple of in phase shift will have no direct optical effect. This means that the optical behaviour of the two lenses shown in Figure 2.20 is identical. Note however that this equivalence only holds true for certain wavelengths, as the phase shift of materials strongly depends on the used x-ray photon energy (see chapter 2.3.2). Following

this approach of Aristov et. al. planar refractive lenses made from diamond and silicon were fabricated within this work.

The principle of the fabrication process is shown in Figure 6.1. In a first step e-beam lithography is used to define a mask having the desired lens shape. In a second step this mask is transferred into the underlying diamond or silicon substrate by reactive ion etching, leading to the formation of a planar refractive lens with minimized absorption.

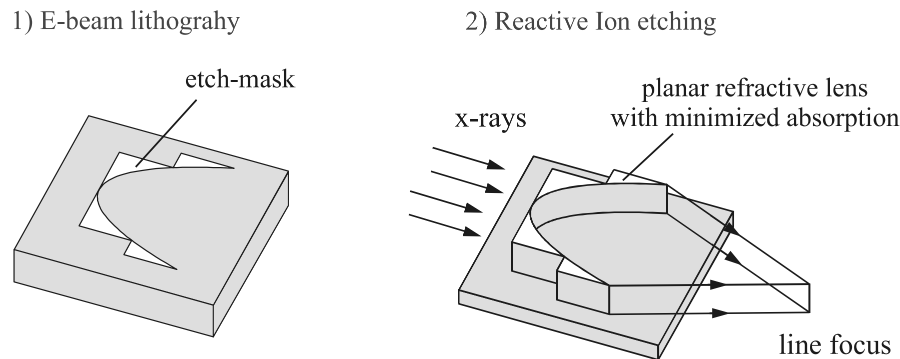

Figure 6.1: Schematic sketch of the fabrication process of planar refractive lenses.

Obviously the reactive ion etching process has to be matched to the used lens material and will mainly determine the lens quality and therefore - as will be shown later on - the performance of the planar refractive lens. The lens material also determines the optical properties of the lens with respect to x-ray absorption and the obtainable refraction/deflection of the x-ray beam. In consequence the potential applications of such planar refractive lenses strongly depend on the lens material.

Using silicon for the fabrication of planar refractive lenses one can benefit from the fact, that silicon is widely used in micro-technology, so that there are highly specialized structuring methods available for this material. For x-ray energies above about 30 keV absorption becomes sufficiently small, so that high efficiencies become feasible for silicon lenses.

This was the reason to work on silicon lenses, which were especially designed for the use in the very hard x-ray region of photon energies between about 30 keV and 50 keV. The performance of these silicon lenses in terms of resolution and efficiency is significantly smaller than what is feasible for x-ray lenses in the soft or the lower part of the hard x-ray range. However, there are only very few types of lenses available for this extreme energy range, so that such silicon refractive lenses are nevertheless very valuable and useful focusing devices.

Diamond is a material, which in comparison to silicon is difficult to structure. Due to the typically very low etch rates of the reactive ion etching process mask erosion plays an important role, making it difficult to fabricate diamond lenses of high quality and with sufficient structure heights. But diamond offers the advantage of having very low x-ray absorption, so that even for photon energies of 12.4 keV efficiencies of about 80 % are feasible. In addition diamond has unique material properties, like an extremely high thermal conductivity, a low thermal expansion coefficient and a high thermal stability. This is of special interest in the context of future X-ray free electron lasers. The extraordinary intense x-ray beam of such a X-FEL is expected to enable a broad range of novel applications. But there are also many technical problems and practical difficulties, which have to be overcome till one can actually start to build such X-FELs and one of these problems is the fact, that no

conventional x-ray lens is likely to survive such an intense beam. The unique material properties of diamond in connection with the special geometry of planar refractive lenses, which enables effective heat dissipation, make diamond refractive lenses one of the very few promising candidates for optical systems at X-FELs.

Due the significant differences between diamond and silicon refractive lenses with respect to their fabrication and their optical properties it makes sense to treat them in two separate chapters (chapters 6.2 and 6.3). On the other hand there are many general aspects, which do not depend on the lens material, like the principal design of planar lenses, the design optimisation, and the influence of shape errors, which lead to lens aberrations and diffraction losses. These aspects will be discussed in the next two chapters (chapters 6.1.2 and 6.1.3)

6.1.2 Design of planar refractive lenses

It was shown in chapter 2.3.1 that the ideal lens shape of a plano concave lens is an ellipse. However, in praxis the ideal shape is always close to parabola, so that for design considerations it is sufficient to assume a simple parabolic shape. The lens shape h(x) is then approximately given by equation (2.98). It will be shown later on that one important parameter for the design and the performance of a refractive lens is the maximum slope of the parabola at the edges of the lens (for x=D/2). Differentiating equation (2.98) yields the slope of the tangent to h(x), whereby the slope is equal to the tangent of the inclination angle φ (see also Figure 6.2)

$$\tan(\varphi) = D/(2f\delta) \tag{6.1}$$

Up to now it has been assumed that a refractive lens with minimized absorption is designed according to Figure 6.2 A, removing passive parts of a lens in such way, that at several points the thickness of the lens approaches zero. Although such a design minimizes absorption losses, it does not take into account certain peculiarities of the fabrication process. One finds, that any kind of etch process leads to a certain lateral erosion of the etch mask as well as some kind of under-etching. Consequently, the thickness of the lens regions close to the etch mask steadily decreases during the etch process.

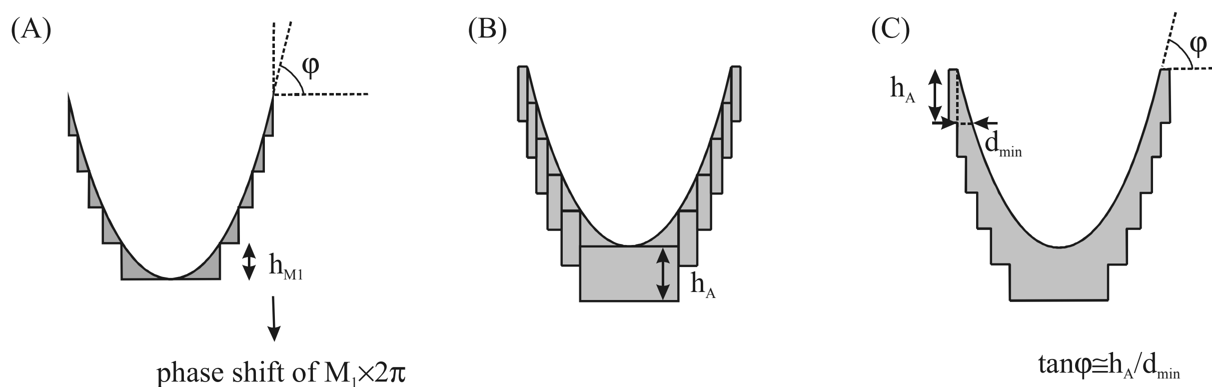

Figure 6.2: (A) Simplest form of a refractive lens with minimized absorption, obtained by removing bars causing a multiple M_1 of 2 π in phase shift. (B) Generalized form of a refractive lens with minimized absorption, obtained by adding bars of thickness h_A, in order to avoid lens regions where the thickness of the lens becomes very small. According to (C) the minimal lens thickness d_{min} is determined by the maximum slope angle φ of the refracting surface and the thickness h_A of the bars, which are added to the lens as illustrated in Figure B.

The use of a mask design like the one shown in Figure 6.2 A would therefore inevitably lead to holes within the lens at lens positions where the initial lateral thickness of the etch mask was not sufficient. Consequently it is necessary to compensate for the lateral etching component in the mask design. Basically one has to makes sure that the thickness of the lens - meaning the lateral thickness of the etch mask - is larger than a certain minimal thickness d_{min}.

This can be achieved utilizing a lens design like the one shown in Figure 6.2 B, which uses the fact that adding bars of thickness h_A to a lens does not influence the lens properties. In praxis the maximum slope of the parabolic lens shape is always much larger than unity. Consequently we obtain in good approximation

$$\tan(\varphi) \cong h_A / d_{\min}$$

Combining this result with equation (6.1) yields

$$h_A = \frac{D}{2f} d_{\min} / \delta = \frac{NA}{\delta} d_{\min} \qquad (6.2)$$

Hence the thickness h_A of the additional bars is directly proportional to the minimal tolerable thickness d_{min} and the numerical aperture of a planar refractive lens. Obviously the minimum tolerable thickness will depend on the utilized etch process and therefore also depend on the lens material. However, in spite of the completely different etch characteristics of diamond and silicon the required thickness d_{min} is approximately the same for the diamond and silicon lenses fabricated within this work, and was found to lie in the range from about 3 to 5 µm. The value of h_A given by equation (6.2) only represents a lower limit of h_a which ensures a sufficient thickness d_{min} of the lens. However, one will try to omit significantly larger values of h_A as this would only unnecessarily increase the lens thickness and therefore increase the absorption losses within the lens.

Up to now it has been implicitly assumed that one single planar refractive lens is used for the focusing of x-rays. However, normally a stack of lenses has to be used in order to obtain reasonable focal lengths. It was discussed in chapter 2.3.3 that such a stack of K individual lenses has basically the same optical properties as one single lens, whereas the effective decrement of the refractive index δ_K of this single lens is given by $\delta_K=\delta\times K$. The parabolic approximation of the lens shape of one individual lenses in the stack is then given by

$$h(x) \cong x^2 / (2 f \delta_K) \qquad (6.3)$$

Each of the lenses in the stack represents a lens with minimized absorption where bars of thickness h_{m1} and h_a have been removed and added. Due to the small deflection angles caused by refractive x-ray lenses the optical effects of K individual segments along the x-ray beam simply add up. After the x-ray beam has penetrated all K lenses the net phase jump at the border between two segments is therefore a multiple M_1 of 2 π, where

$$M_1 = K\, m_1$$

At the same time one finds

$$h_a = K\, h_A$$

In other words this means that the K individual lenses in Figure 6.3 A and the effective lens in Figure 6.3 B can be regarded to have basically the same optical behaviour. Taking this into account one finds that equation (6.2) also applies for the general case of stacked lenses. This means that with respect to absorption inside a lens it does not make a difference whether one single lens or a stack of lenses is used. The minimal tolerable lens thickness h_A measured along the beam, which is given by equation (6.2), is the same in both cases.

Up to now nothing has been said about a useful choice of the parameter M_l. It was shown in chapter 2.3.2 that for a refractive lens with minimum absorption there is a set of energies where the contributions of individual lens segments add up in phase in the focus, so that optimal performance of the lens is achieved. Increasing M_l increases the number of energies, where optimum performance can be achieved, so that it is of advantage to choose M_l as large as possible. However, large values of M_l also increase the mean thickness of the lens. In praxis it is therefore reasonable to avoid values of M_l, which significantly increase the mean lens thickness along the x-ray beam. In consequence the corresponding parameter h_{Ml} should not be significantly larger than the inevitable lens thickness defined by h_A.

As K individual lens sectors of causing a phase shift $m_l \times 2\pi$ act as one single sector introducing a phase shift $M_l \times 2\pi$ in principle it is not necessary that m_l has an integer value. However, it is reasonable to ensure that m_l is an integer value, so that for each lens the wave exiting the lens shows no jumps in phase. At the same the value of M_l is always sufficiently large so that in praxis it is no disadvantage to choose the number of lenses K in such way that m_l becomes an integer value.

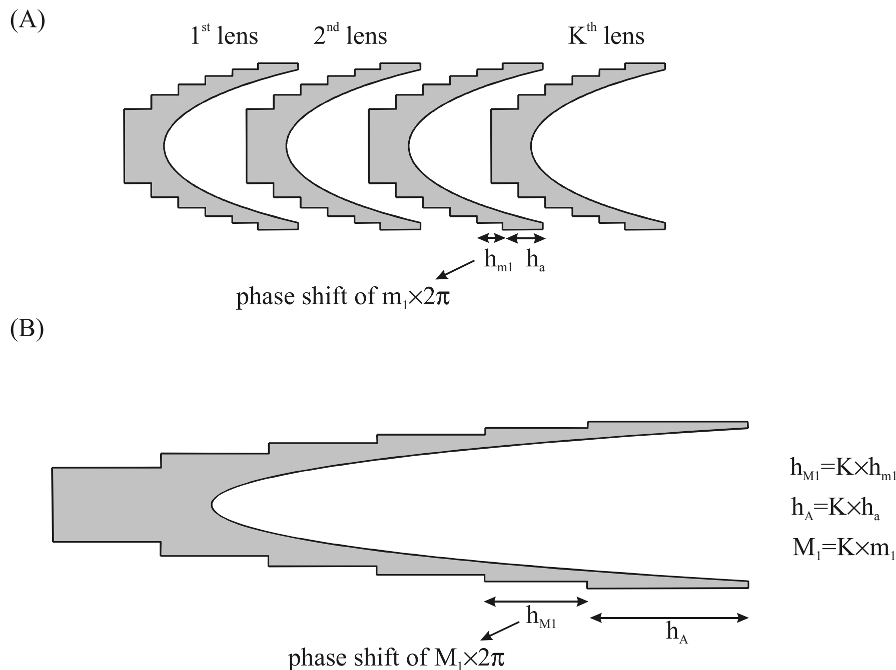

Figure 6.3: (A) Sketch of a stack of lenses using K lenses with minimized absorption in series. For each lens bars of thickness h_{ml} and h_a are removed and added, respectively. (B) Equivalent lens to (A), having basically the same optical properties as the lens in Figure A. Due to the small deflection angles of the x-ray beam the optical effects of individual lenses in a lens simply add up.

Finally, one has to consider that there are certain limitations to the applicability of the design considerations made in this chapter.

Up to now it has been assumed that the wave properties of x-rays do not play a direct role, meaning that any diffraction at the sharp edges of a lens with minimized absorption is negligible. Note, that such a lens can be seen as a diffractive lens with a minimal grating period b_{min} given by the minimal width of the outermost lens sector. One has $h_{M1} \approx h_A$ and therefore $b_{min} \approx d_{min}$, meaning that this minimal grating period is in the order of a few microns.

In order to estimate the influence of diffraction one can consider two beams, travelling in the directions of two neighbouring diffraction orders (e.g. the 0th and 1st order), whereas the two beams coincide at the beginning of the lens. If the separation of the two beams after passing the lens (after a distance L) is significantly less than the minimal grating period b_{min}, one can expect that diffraction only has a minor effect on the performance of the lens. This leads to the condition

$$L < b_{\min}{}^{2} / \lambda \qquad (6.4)$$

Assuming reasonable values of the length and the minimal period (L=1cm, b_{min}=4µm) we find that the condition (6.4) is always fulfilled for x-rays in the hard x-ray region, so that diffraction at the sharp edges of the lenses odes not play a role. However, for lenses with high numerical aperture, leading to lens length L in the cm range, one is already close to violating this condition. Condition (6.4) may be too rigid if it is applied to a stack of lenses with a large distance between individual lenses. It was mentioned above that it should be of advantage to use an integer value for the parameter m_1, as otherwise the wave exiting the lens shows jumps in phase. If the distance to the next lens within the stack is large, these inhomogeneities of the phase will propagate and influence the whole wave front, leading to pronounced diffraction of the original wave. Using integer values for m_1 circumvents inhomogeneities of the wave exiting a lens so that the distance between individual lenses of the stack should not play a role.

So far it was assumed that the deflection of the rays propagating through a stack of lenses is negligible. In reality the incoming beam is gradually deflected each time it passes one of the lenses within the stack. The numerical aperture of the lens determines the maximum deflection of the beam. Using a similar argument as above one finds, that the deflection is negligible if the displacement between an idealized non-deflected beam and the real deflected beam remains smaller than the minimal grating period within the whole stack of lenses. This leads to

$$NA \times L < b_{\min} \qquad (6.5)$$

The largest numerical apertures realized for refractive lenses within this work were of the order of 10^{-4}. Assuming a length L of 1 cm one find that the minimum tolerable grating period is about 1 µm, which is significantly less than the minimal grating periods b_{min} that have been realized. It should be noted that the finite beam deflection within a stack of lenses could be taken into account in the design of the lenses with minimal absorption. Instead of a plane wave, one would have to assume a cylindrical wave approaching one of the lenses within the stack. In consequence concentric rings - instead of rectangles - causing a multiple of 2π in phase shift would have to be removed from this lens. However, the resulting lens design would be very complicated and different for each lens within a stack, making e-beam lithography of the corresponding etch-mask a complex and elaborate task.

6.1.3 Influence of shape error

For refractive lenses any deviation of the ideal lens shape will lead to a decrease of the optical performance of the lens. There are two types of deviations one can distinguish. On the one hand one finds a certain roughness of the lens surface. The feature size of these deviations is typically much smaller than the diameter of the lens and leads to diffraction of the x-ray beam passing the lens and consequently to a widely spread background of stray light in the focal plane of the lens. On the other hand one always has a certain shape error of the lens. One often finds that such a shape error either continuously increases or continuously decreases from the center of the lens. This leads to a slight change of the refraction angles in comparison to a lens with ideal lens shape and therefore to a certain broadening of the focal spot formed with such a lens.

Due to mask erosion and under-etching during the fabrication process of diamond lenses and silicon lenses, lens shape errors strongly influence the performance of refractive x-ray lenses. It is therefore useful to consider the influence of such shape errors for this special case of refractive x-ray lenses and to quantitatively estimate the resulting lens aberrations. Figure 6.4 shows a schematic sketch of a planar refractive lens, illustrating the two different types of deviations from the ideal lens profile.

On the one hand under-etching and mask erosion will lead to some kind of shape error, meaning that there is a certain distance Δu between the surface of the ideal and the actual lens profile. Considering the simplest case, that the under-etching Δu is the same for the whole lens, this will result in a distortion of the ideal elliptic surface and consequently lead to aberrations and a broadening of the resulting line focus. On the other hand an imperfect etch process will lead to non-vertical sidewalls of a planar refractive lens and consequently to a certain slope error α. Such a slope error causes an unintended refraction in the vertical direction (z-direction) and therefore leads to additional aberrations of the lens.

To first order the influences of the two types of lens errors Δu and α can be considered independently. It will be shown in the following that due to a shape error Δu a light ray passing a certain point of the lens will no more be refracted into the focal line but have a certain horizontal displacement Δy. A slope error α causes an unintended deflection in vertical direction and therefore leads to a displacement Δz in z-direction relative to the position of the light ray in case of an ideally shaped lens (see Figure 6.5).

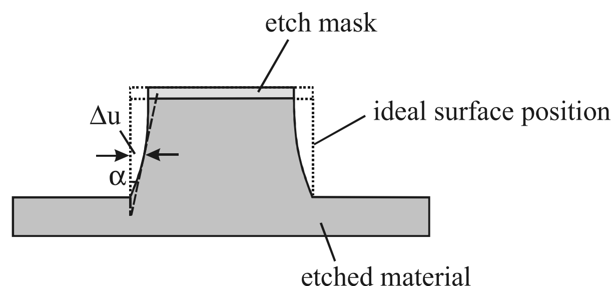

Figure 6.4: Schematic of an etched structure of a planar refractive lens, illustrating the two parameters describing deviations from the ideal lens surface. The actual lens surface has a position dependent distance Δu to the ideal one. In addition one finds a deviation α from the ideally vertical orientation of the sidewall. Although the shape error Δu and the slope error α are related to each other, for a particular point on the lens any combination of values Δu and α is possible. Consequently both of them are needed for the full characterisation of the deviations from the ideal lens shape.

Taking into account the peculiarities of refractive lenses in the x-ray range it is relatively simple to find approximate relationships between the displacements Δy and Δz and the underlying lens errors Δu and α.

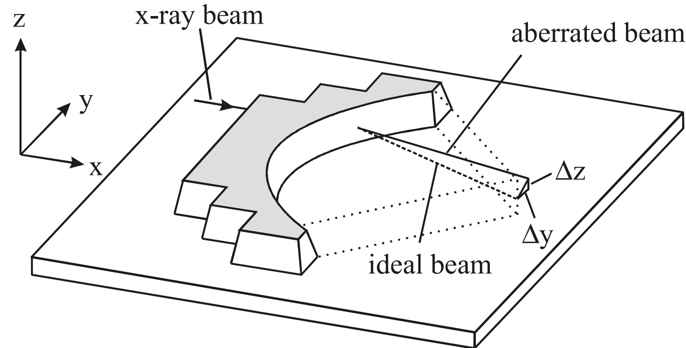

Figure 6.5: Schematic of a planar refractive lens with deviations from the ideal lens shape. The lens errors Δu and α lead to a displacement from the ideal beam position in horizontal (Δy) and vertical direction (Δz).

Figure 6.6 shows a cross section of a refractive lens in horizontal direction (in the x,y-plane) and illustrates the influence of a certain under-etching Δu. The aberrations due to under-etching are determined by the difference in light path between the ideal and the actual lens profile. For the center of the lens this difference is simply equal to Δu, and therefore comparatively small. At the edges of the lens the difference in light path is much bigger due to the typically very larger slope of the lens shape utilized for refractive x-ray lenses. Consequently the resulting aberrations will be strong in the region close to the edge of the lens.

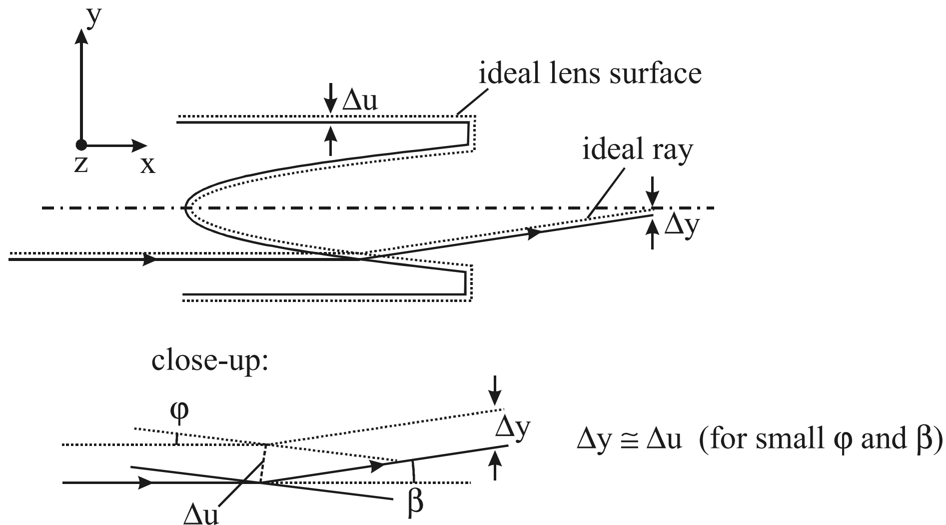

Figure 6.6: Horizontal cross-section through a lens with a shape error Δu (see also Figure 6.5). Due to this shape error the refracting surface is shifted by a distance Δu, but the refraction angle at this position remains the same. The lower graph illustrates that for lens regions with large slopes of the lens surface (small φ) the displacement Δy of an x-ray beam is almost equal to the shape error Δu.

An under-etching shifts the refracting surface a distance Δu but in first order does not change the refraction angle at the corresponding position. For regions with large slope of the lens shape this shift occurs in a direction normal to the incoming beam. For regions with large slope a ray passing the lens is therefore shifted by Δu in comparison to an ideal lens, so that the displacement Δy of the beam is given by

$$\Delta y \cong \Delta u \tag{6.6}$$

Therefore, the broadening of the focal line, which is induced by Δy, is more or less equal to the shape error Δu of the planar refractive lens.

If the under-etching is constant within the lens, the displacement Δy will be constant for regions with large slope. In consequence the focal line formed by these regions of the lens will be shifted but not broadened compared to the focal line of an ideal lens. Consequently, by using only parts of a lens having large slope - which normally only excludes a small region in the lens center - it should be possible to circumvent any broadening of the focus due to under-etching. However, the shift of the focal line will have opposite sign for the left and the right part of the lens. Consequently only one part of the lens can be used as otherwise two focal lines having a distance 2×Δy would be obtained. In any case one has the problem that Δy is not constant within the entire lens. In fact Δy typically varies significantly even if only one horizontal cross-section (in the x,y-plane) of a planar refractive lens is considered. It is therefore not useful to follow such an approach in order to reduce lens aberrations caused by shape errors. Nevertheless, for diamond as well silicon lenses a faint double feature of a focal line could be observed in the experiment, which can be understood as the result of the "doubled" focal line mentioned above.

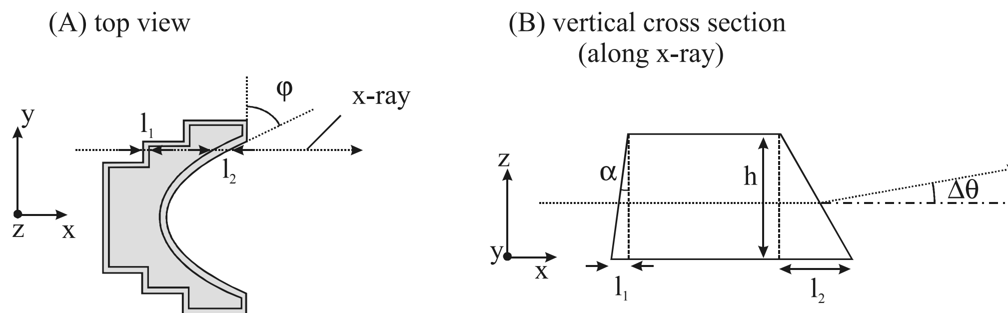

Figure 6.7: Schematic of a planar refractive lens illustrating the relationship between a slope error α and the resulting unintended deflection Δθ of the x-ray beam in the vertical direction. For reasons of simplicity a constant slope error is assumed for the entire lens. The deflection Δθ originates from the prismatic shape of the lens. Figure 6.7 shows that for regions with large slopes of the lens shape (angle φ close to 90^0) a strong prismatic behaviour can be expected. As a consequence considerable deflection angles Δθ are found near the edge of the lens.

For the estimation of the ray displacement Δz in vertical direction similar arguments can be applied in order to obtain a quantitative relationship between Δz and the slope error α. Figure 6.7 B shows a vertical cross-section of a planar refractive lens, illustrating the deflection Δθ caused by a certain slope error within the lens α. Note, that the light paths of the two x-rays passing the lens at the bottom and the top of the lens are different. The resulting difference Δl in light path is given by

$$\Delta l \cong (l_2 + l_1)\delta$$

This leads to a change in the direction of the incoming wave, i. e. a deflection $\Delta\theta$ in z-direction, given by

$$\Delta\theta \cong \Delta l / h$$

The slope error α is relatively small and consequently for the center of the lens there is only little difference in light path between the top and the bottom of the lens. However, the situation is different for positions close to the edge of the lens. Due to the large slopes of the curved lens-surface as small difference between the lens thickness at the bottom and the top of the lens results in a large difference in light path. In consequence the maximum deflection $\Delta\theta_{max}$ occurs at the edge of the lens and is mainly determined by the length l_2 (see also Figure 6.7). This leads to

$$\Delta\theta_{\max} \cong l_2\delta / h$$

At the same time we have

$$\alpha \cong l_1 / h \quad \text{and} \quad l_2 \cong l_1 \tan\varphi$$

Combining these results and using equation (6.1) we obtain

$$\Delta\theta_{\max} \cong \frac{D}{2f}\alpha \tag{6.7}$$

The maximum displacement Δz_{max} in vertical direction of an x-ray beam is therefore given by

$$\Delta z_{\max} = f \times \Delta\theta_{\max} \cong \frac{D}{2}\alpha \tag{6.8}$$

For silicon refractive lenses one finds a slope error of about 1/50 for the high quality regions of the lenses. Assuming a diameter of 400 µm this leads to a maximum displacement in z-direction of about 4 µm. This displacement in vertical direction only shifts the position of the line focus but does not result in a broadening of the focus. However if two crossed lenses are used in series, the displacement will influence the focusing in the vertical direction, performed by the second lens. This leads to an additional aberration and therefore an additional broadening of the focal spot. Such a broadening was found in the experiment as will be discussed in chapter 6.3.3.

6.2 Diamond refractive lenses

The following two chapters deal with the fabrication and optical testing of diamond lenses. In chapter 6.2.1 the fabrication process of diamond lenses is discussed, including the main fabrication difficulties and possible strategies to overcome these. In chapter 6.2.2 the results from measurements at BM05 of the ESRF are reported showing the performance of the diamond lenses.

6.2.1 Fabrication of diamond refractive lenses

The fabrication of planar refractive lenses consists of two steps. In a first step an etch mask having the desired lens shape is formed on a substrate. In a second this etch mask is then transferred into the substrate using reactive ion etching, leading to the formation of a planar refractive lens.

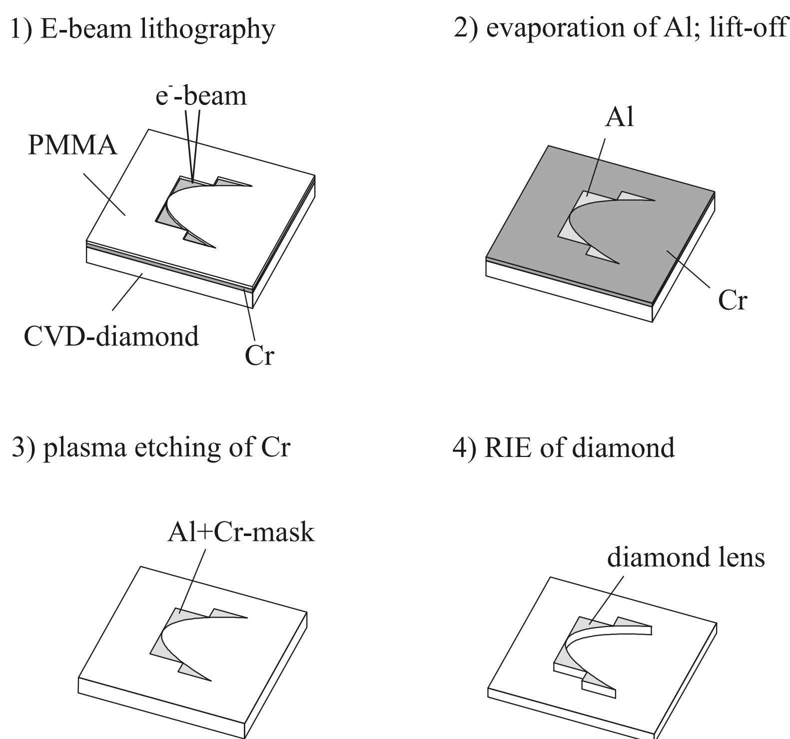

Figure 6.8: Principle of the fabrication of planar refractive diamond lenses.

Figure 6.8 shows the details of the process used for the fabrication of diamond refractive lenses. The lenses are fabricated on approximately 200 µm thick CVD diamond substrates. In the first step the lens patterns are written in a 150 nm thick layer of PMMA by e-beam lithography. Using a chlorine based plasma etch the Al-layer in the next step acts as an etch-mask for the patterning of a 2 µm thick Cr-layer, that has been deposited on the diamond substrate by thermal evaporation. The resulting Al/Cr-structures then can be used as a hard mask for the reactive ion etching of the diamond in an oxygen plasma, finally leading to the formation of diamond refractive lenses.

In the following the different steps of the fabrication process and the resulting difficulties and problems are discussed in more detail.

One key part of the fabrication process is the e-beam lithography of the desired lens pattern in a PMMA-layer. The possibility to expose continuous Bezier-lines using the LION-LV1 electron-lithography tool makes it comparatively easy to generate the corresponding data for the exposure. The boundary of a lens pattern defining a lens with minimized absorption consists of several straight lines and one single ellipse defining the curved surface of the lens. According to the considerations in chapter 3.1.2 both of them can be easily described using the Bezier-data format. In a first step of the e-beam lithography the boundary was therefore defined using the corresponding Bezier-lines. The boundary lines were exposed using an electron beam with zero defocus and maximum speed of the sample stage (2 mm/s), so that the finite width (approximately 200 nm) of the exposed lines had a negligible influence on the shape of the lens pattern. In a second step the remaining inner part of the lens was filled with lines, all of them oriented parallel to the optical axis of the lens. Again the maximum speed of the sample stage was used, but a slight defocus was employed so that a larger area of the lens could be exposed with one single line, minimizing the required time for the exposure of the lens. At the same time special care was taken, that the defocus was sufficiently small so that the filling lines close to the boundaries of the lens had no influence on the shape of the lens.

The required data for these two exposure steps were generated by means of a turbo pascal program, which takes into account the optical properties of the lens material - basically the value of δ at the design photon energy of the lens - and automatically calculates the respective Bezier-data for the lens. For each lens the lens parameters are previously specified within the program (e.g. the values of the focal length, the lens diameter, the parameters M_1, m_1, and the number K of lenslets within the stack forming the whole lens).

After the development (HAMATECH, MIBK:IP=1:1, 60 sec) of the exposed PMMA layer a short oxygen plasma etch step was used to remove remaining rests of PMMA in exposed regions. In a next step a 5nm thick chromium-adhesion layer and a 50 nm thick aluminium layer was then thermally evaporated onto the sample, and partially removed again using a lift-off process with acetone. The resulting aluminium mask could have been directly used as an etch mask for the fabrication of diamond refractive lenses. However, due the small thickness of the aluminium layer the durability against the diamond etch process was insufficient for achieving a sufficient height of the diamond lenses. Therefore the Al-layer was transferred into a 2 μm thick, thermally evaporated chromium layer by means of a chlorine based plasma etch.

Due to the high resistivity of aluminium against this etch process even thicker chromium layers could have been processed. However, a thickness of about 2 μm proved to be the upper limit, as for thicker chromium layers the considerable strain causes a peeling of the chromium layer due to an insufficient adhesion on the diamond substrate.

In the next step the resulting Al/Cr-layer is used as a hard mask for the deep reactive ion etching of the diamond in an oxygen plasma. It is known from the literature, that the achievable etch rates of diamond in an oxygen plasma are very small [94, 95, 96] and of the order of a few microns per hour. For our RIE processes we found etch rates of about 1-2 μm/h.

Due to the limited number and high cost of the diamond substrates, it was not possible to test a large range of different etch parameters. However, several etch tests varying the supplied RF-power were performed, showing that the RF-power has a relatively moderate influence on the etch rate. Keeping all other parameters constant (RIE system: Alcatel GIR300, gas pressure 50 mTorr, gas flow 5sccm O_2, electrode distance 5 cm) the etch rate was found to change from about 0.700 μm/h to 2 μm/h by increasing the power from 80 Watt to 180 Watt.

All etch processes sooner or later lead to the formation of grass on the etched surface of the diamond, i. e. a dense assembly of tiny vertical diamond needles formed on the surface. Typically the first few microns of the diamond could be etched without getting a significant roughness. Then the formation of grass started. As a consequence, further etching led to a removal of diamond, but only in regions in between the grass. This resulted in an increase of the height of the diamond needles, but did not significantly change the level of the upper surface of the etched diamond (formed by the top parts of the diamond needles). Once the grass had reached a height of about 5-10 microns the etch rate was significantly decreased so that at a certain point any further etching of the diamond was inhibited.

However, this problem could be solved by means of an ultra-sonic treatment of the sample. Once the grass had reached a height of about 10-15 microns the individual diamond needles became very fragile, so that the upper parts of the grass could be removed by putting the diamond sample in water and exposing it to ultra-sound. In comparison to the diamond needles the lens structures where much more rigid, so that damage of the lens structures was only observed using maximum power of the ultra-sonic bath and for very thin test lenses, having a lateral thickness of about 2 microns and below.

The structuring of diamond was therefore performed using a multi-step process. In a first step the diamond was etched until a grass height of about 10 μm was reached. A process with large RF-power was used (180 Watt RF-power, 5 sccm of O_2 at 50 mTorr), resulting in a high self-bias voltage (approx. 820 Volt) and an etch rate of about 2 μm/h. Afterwards the grass was partially removed exposing the sample for a few minutes to ultra-sound. The further structuring process then consisted of subsequent steps of RIE-etching and ultra-sonic treatment of the sample. A RIE-step of 2.5 hours was used, leading each time to an additional removal of about 5 μm of diamond. Before and after the ultra-sound bath the height of the grass as well as the total etch-depth was monitored using a profilometer (Tencor Alpha-step 200). The remaining height of the grass after the ultra-sonic treatment was typically between 5-10 microns. The remaining grass was also much more rigid than the grass right after the etch process.

Applying this multi-step process we could fabricate diamond lenses with a maximum structure height of 40 microns. The erosion of the chromium mask, which after about 20 hours of RIE-etching was nearly completely removed, prevented a further structuring of the diamond.

Figure 6.9 and Figure 6.10 show SEM-pictures of the resulting diamond lenses. Figure 6.9 A gives an example for a diamond lens with a large light collecting power, where 12 lenses in series are used in order to achieve a focal length of 500 mm at 12.4 keV photon energy for a lens diameter of 500 μm. Figure 6.9 B shows a set of lenses, each of them having a diameter of 100 μm and a focal length of 250 mm at the design energy of 12.4 keV. The lenses only differ with respect to the value of M_1, which increases from the left to the right of Figure 6.9 B (M_1=3, 6, 12, 24, 48). Figure 6.9 C shows a similar set of lenses, all of them having an aperture of 100 μm. The curvature of the refracting surfaces increases from left to right, while the number of lenslets put in series decreases accordingly, so that the focal length of all five devices is 250 mm for the design energy of 12.4 keV photon energy.

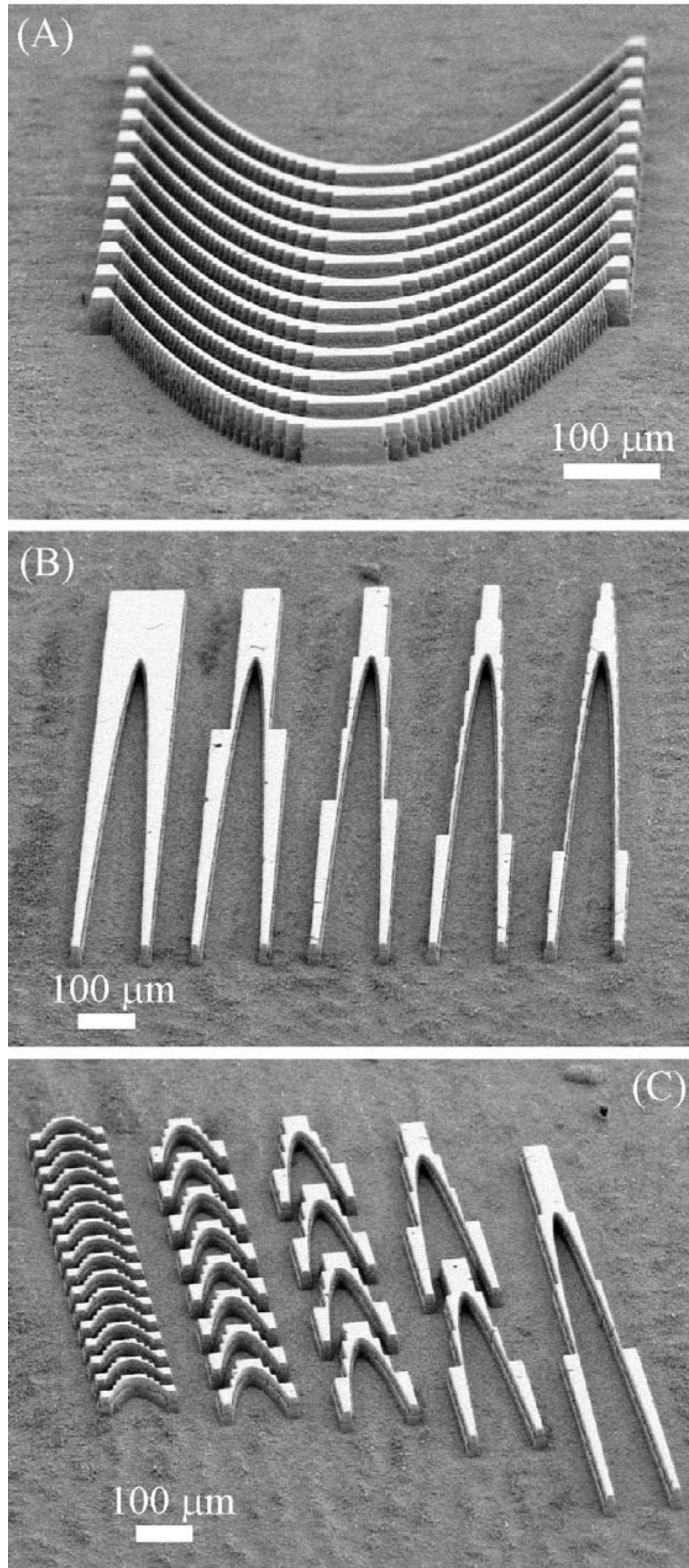

Figure 6.9: SEM-viewgraphs of various planar refractive diamond lenses. (A) Lens with large light collecting power, using 12 lenslets of 500 µm diameter in series in order to achieve a focal length of 500 mm at the design energy of 12.4 keV. (B-C) Diamond lenses with different designs having the same diameter (100 µm) and the same focal length (250 mm) at the design energy of 12.4 keV.

Figure 6.10 shows a close-up of a diamond lens, revealing the limitations of the used etching process. All etched lenses showed a considerable surface roughness. Figure 6.10 also shows a kind of 'wrapping paper' structure around the lenses, causing a step of about one micron between the upper and the lower part of the lens. These kinds of effects appeared in all etched samples and can be explained by lateral erosion of the chromium mask during the reactive ion etching of the diamond.

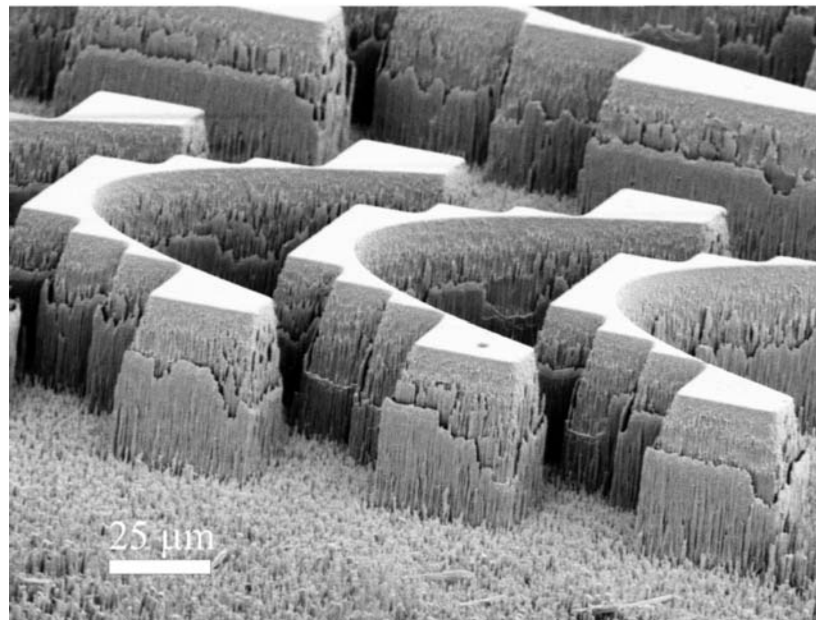

Figure 6.10: Close-up of a diamond refractive lens

The phase shift introduced by this kind of roughness is much smaller than 2 π so that the optical influence of these local deviations from the ideal lens shape should be small. However, for lenses with large slope of the lens shape the phase shift introduced by this roughness can be strongly increased. As a consequence this roughness can lead to significant diffraction losses within a stack of lenses, especially if many lenses are used in series in order to achieve large numerical apertures.

Besides these local deviations from the ideal lens surface, a considerable shape error Δu and slope error α is found for the lens surface. The lower half of the lens appears to be of relatively good quality having vertical sidewalls, whereas the upper half shows strong deviations from the ideal surface with a slope error of about 1/6 rad. Such an etch behaviour is known in micro-fabrication technology as faceting [see e.g. 97] and can be explained by a lateral erosion of the chromium hard mask during the etching process.

Besides deviations from the ideal lens shape, the comparatively small height of 40 microns of the diamond lenses is presently the main factor limiting the applicability and performance of these lenses. Both problems are directly related to the applied fabrication process and it should be possible to overcome these by further optimisation of the etch process and using more durable mask materials.

6.2.2 Measurements on diamond lenses

6.2.2.1 Experimental set-up

All measurements were performed at the BM05 optics beamline of the ESRF (second part of experiment MI-563, March 2002). The experimental set-up was identical to the one, used for the testing of multilevel diffractive gratings and zone plates.

Figure 6.11 recapitulates the corresponding set-up. Like the zone plates the diamond lenses were fixed in such way that focusing in vertical direction was achieved. In a first step the lenses were aligned with respect to the beam. To achieve optimal performance of the lenses the diamond sample surface has to be perfectly parallel to the incoming x-ray beam. The corresponding adjustment of the angle θ_1 was first performed coarsely using the x-ray camera. Then slit1 was closed down in horizontal direction (horizontal gap = 10 μm) in such way, that only about one half of the resulting x-ray beam passed the diamond sample, whereas the other half was absorbed within the diamond substrate. A variation of the tilt angle θ_1 changed the amount of x-rays passing the diamond sample and therefore the measured diode signal. Maximum diode signal is achieved for perfect alignment of the diamond surface with respect to the beam. Using this method θ_1 could be aligned with an accuracy better than 1/2000 rad. Given the length of the diamond sample along the x-ray beam (about 1cm), this corresponds to a maximal deviation from the ideal surface position of less than 3 microns. This is much smaller than the height of the diamond lenses so that blocking of the x-rays due to a bad alignment of θ_1 can be considered to be negligible.

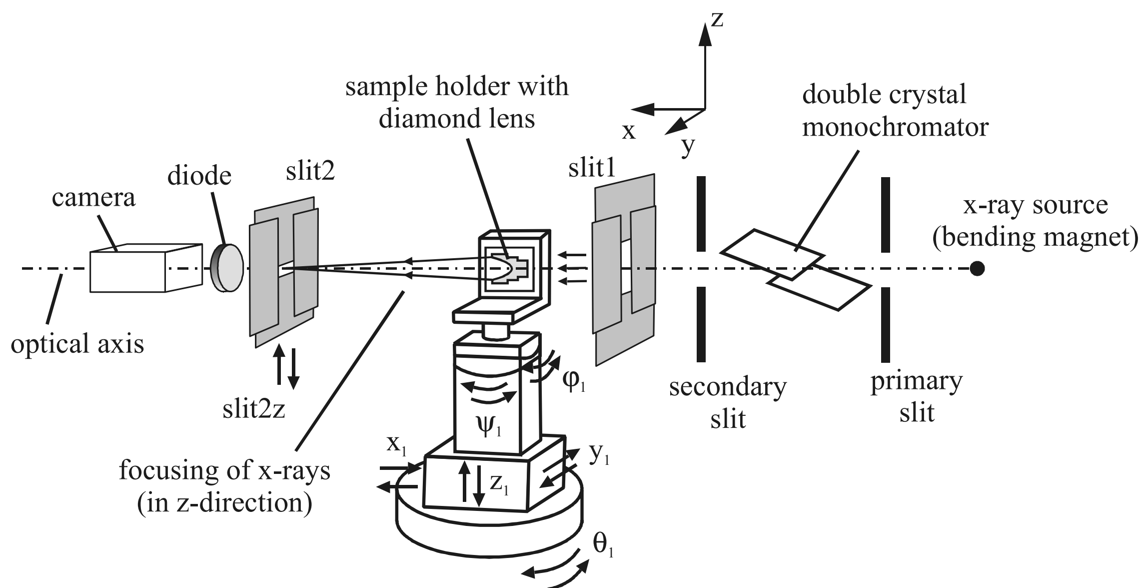

Figure 6.11: Sketch of the set-up used for the optical testing of diamond refractive lenses

Optimal performance of the diamond lenses also requires that the axis of symmetry of the lenses (their optical axes) is parallel to the incoming x-ray beam. The adjustment of the corresponding angle ψ_1 was performed using an alignment mark, which had been fabricated in addition to the diamond lenses on the sample. The alignment mark consisted of a 6 mm long and 20 microns wide non-etched rectangular line parallel to the optical axes of the diamond lenses. The alignment mark was clearly visible in the x-ray camera and by changing ψ_1 in small steps and minimizing the size of its projected x-ray image in vertical direction, we could align the optical axes with respect to the x-ray beam. An alignment accuracy of ψ_1 better than about 1/1000 could be achieved. Making simple ray tracing calculations one finds

that this should be more than sufficient to prevent any lens aberrations caused by a misalignment of ψ_1.

Like for the measurements on diffractive optics, slit1 was used to define the x-ray beam for the illumination of the diamond lenses, whereas slit2 was used to investigate the intensity distribution behind one of these lenses - yielding basically their resolution as well as their efficiency. For both types of measurements the position of slit2 should coincide with the position of the focal plane of the considered lens. In principle the corresponding distance can be set with sufficient accuracy using a tape measure and taking into account the theoretically calculated focal length for the used photon energy. However, the experimentally determined distance leading to a minimal width of the focus was found to be significantly (typically about 5%) larger than the theoretical one. Consequently, it was necessary to optimise the distance between the sample and slit2. For this purpose slit2 was closed down in vertical direction (vertical gap between 1-4 µm) and then scanned vertically (motor slit2z) through the focus of the lens. The FWHM of the obtained signal is directly linked to the width of the focal line of the lens, making it possible to experimentally determine the distance leading to a minimal width of the focus.

One can think of two possible reasons for the observed discrepancy between the theoretical and experimentally determined position of the focal plane of a diamond lens.

One possible reason are lens shape errors. For diamond lenses the shape error is positive for all parts of the lens, i. e. a diamond lens is always thinner than the corresponding ideal lens having no shape errors. Taking into account the considerations in chapter 6.1.3 one therefore finds, that the x-rays stemming from different parts of lens intersect the optical axis in a larger distance than for an ideal lens. Consequently a minimal width of the focus is also achieved at a larger distance form the lens, which is in agreement with the observation that the experimentally determined focal length is larger than the theoretical one.

Another possible reason for the discrepancy between experimental and theoretical position of the optimal focus is the fact, that the material properties of the CVD-diamond - and in particular its refractive index - are not precisely known. For x-rays the decrement of the refractive index δ is directly proportional to the density of the material and to first approximation one can assume that the density should be about the same as the density of mono-crystalline diamond, which is found to be about 3.51g/cm^3. But density measurements showed, that the density of CVD-diamond is about 2 % smaller. The density was determined by measuring the thickness, the area and the weight of several samples and was found to be 3.44 g/cm^3 with an uncertainty of about 0.5 %. However, the measured difference of 2% in density between mono-crystalline and CVD-diamond has been taken into account for the design of the diamond lenses so that the observed difference in experimental and theoretical focal length of the diamond lenses can only be partly explained by the uncertainty of the knowledge of the CVD-diamond material properties.

6.2.2.2 Efficiency measurements

The efficiency of the diamond lenses was measured applying the same method as for the diffractive multilevel lenses (see chapter 5.1.2).

The slit in front of the lens (slit1) was used to illuminate a well-defined part it. Consequently, In vertical direction the gap of slit1 was set such that the full lens was illuminated. In horizontal direction the gap was set to very small values (in the order of 10 microns) so that only a part of the lens was fully illuminated. The center position of the horizontal gap was chosen such that maximal flux in the focus was obtained. Note, that if the horizontal gap is larger than the height (40 µm) of the diamond lenses, some x-rays will pass the lens without being refracted and therefore disturb the efficiency measurement. It was found that for vertical gap values between 5-10 µm the measured efficiencies were independent of the gap size, whereas measurements for a gap size of 20 µm and beyond yielded significantly smaller efficiencies. The horizontal gap size was therefore set to 10 µm.

The efficiency was then determined by scanning slit2 through the focal line of the lens (motor slit2z). As before the horizontal gap of slit2 was chosen significantly larger than the horizontal gap of slit1 so that in horizontal direction the full x-ray beam was collected. A vertical gap of slit2 of 20 and 50 µm was chosen for the measurements on lenses with small (100 µm) and large aperture (500 µm), respectively. The acquired data were then evaluated in the same way as for the diffractive lenses, basically using the integrated flux in the focal line and the reference signal in a region close to the lens to calculate the diffraction efficiency (see chapter 5.1.2). Efficiencies up to 70 and 79 % could be achieved for photon energies of 12.4 and 17.5 keV, respectively.

Figure 6.12 shows the measured efficiencies of a set of 5 different lenses, all of them having the same aperture (100 µm) and the same focal length (250 mm) at the design energy of 12.4 keV. The lenses only differed with respect to the parameter M_l, meaning that a different amount of material was "removed" starting from the same refractive lens. Values of 3, 6, 12, 24 and 48 were chosen for M_l leading to lenses consisting of 16, 8, 4, 2 and 1 segment, respectively. The lens with M_l=48 is a normal refractive lens, whereas for the lens with M_l=3 a large part of the lens is "removed", minimizing the absorption within the lens (see also Figure 6.9 B, showing a set of lenses with very similar design). Figure 6.12 shows the efficiencies η_m measured at the design energy of 12.4 keV. For comparison the theoretical efficiency η_{theor}, which was calculated using equation (2.112) and (2.113), and also the difference between the theoretical and the measured efficiency are depicted. According to theory the absorption losses decrease using lenses with a larger number of segments and as a consequence the lens efficiency should increase with the number of lens segments. This was found experimentally, provided that only lenses having a comparatively small numbers of segments were considered. However, for lenses with a strong segmentation the efficiency is decreasing with the number of segments. This behaviour can be explained by the larger number of edges and the increased surface area of such a lens, leading to increased scattering losses caused by the surface roughness of the lens. For the lenses described in Figure 6.12 it is therefore not useful to have more than about 4 lens segments. Obviously, in general it is rather the number of segments per lens diameter than the number of segments themselves that influence the scattering losses. Alternatively to the number of segments per lens diameter one can also consider the minimal width b_{min} of the segments at the edge of the lens. For the lenses described in Figure 6.12 having 4, 8 and 16 segments the minimal widths of the outermost segments are 6, 3 and 1.5 microns, respectively. Consequently it makes no sense to use lens designs where the minimal width of the segments is significantly smaller than about

5 microns, as otherwise the increase in scattering losses exceeds the gain in lens transmission, leading to an overall smaller efficiency of the lens.

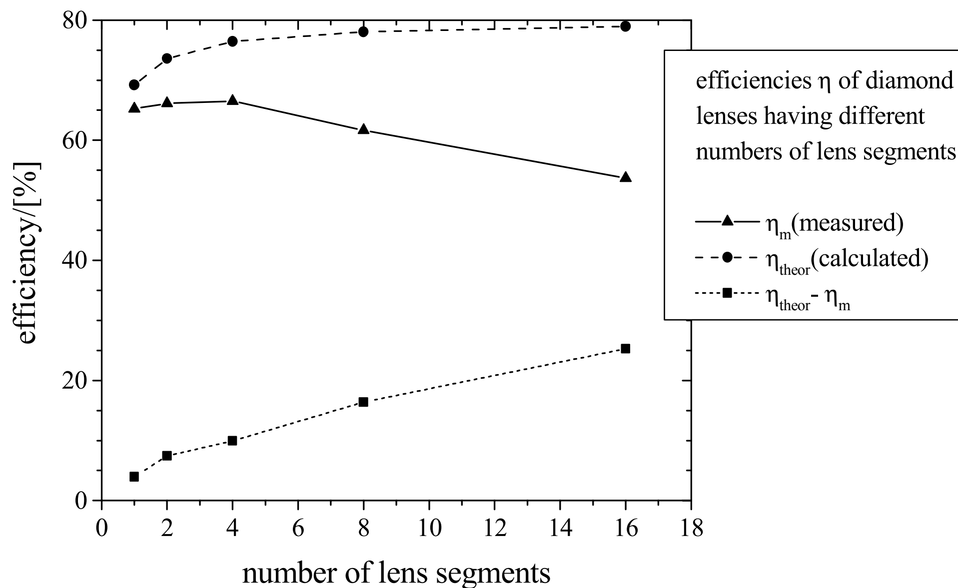

Figure 6.12: Efficiency of diamond lenses of 100 µm diameter and with 250 mm focal length at the design energy of 12.4 keV. The lenses differ only differ in the value of M_l so that each lens has a different number of lens segments. The average lens thickness decreases with the number of lens segments. Consequently, lenses with a strong segmentation theoretically yield higher efficiencies. However the measurements show a decrease in efficiency for large numbers of lens segments. This can be explained by the increased scattering losses due to the larger number of edges and the larger surface area of these lenses.

Similar results were found for measurements at a different photon energy (17.5 keV) and for lenses with large diameter where the efficiency of different lens regions could be directly determined by scanning an x-ray beam with constant flux across the lens and comparing the resulting flux within the focus. All measurements showed a significant decrease of the overall efficiency for lenses with a segment width smaller than about 5 microns. In consequence this minimal width can be seen as an experimentally determined limit, which - as the underlying scattering losses are influenced by deviations from the ideal lens shape - is characteristic for the used diamond etch process within this work.

Figure 6.13 illustrates the effect of using different numbers of lenses in series in order to achieve a certain focal length. Besides the number K of lenslets all other lens parameters were identical, i. e. all lenses had the same aperture (100 µm), the same parameters M_l (M_l=12) and the same focal length of 250 mm at the design energy of 12.4 keV (see also Figure 6.9 C, showing an SEM-picture of the resulting lenses). Theoretically all lenses should have the same efficiency and that is in fact what is found in the experiment. Measurements at another photon energy (17.5 keV) and for lenses with larger diameter lead to the same result. Consequently, as to lens efficiency it does not play a role, whether many or few lenses are used in series in order to achieve a certain focal length.

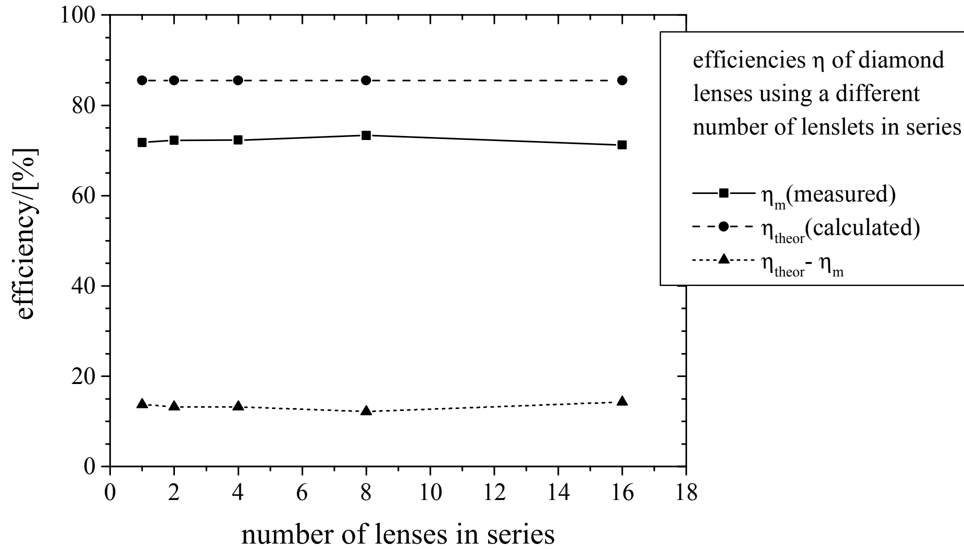

Figure 6.13: Measured efficiencies of diamond lenses consisting of a different number lenslets in series. All other lens parameters such as the focal length, the aperture and the parameter M_l are identical (see also Figure 6.9 C, showing an SEM-picture of the five different lenses). Within the experimental error all lenses were found to have the same efficiency.

6.2.2.3 Resolution tests

The resolution tests were performed with the same set-up as for the efficiency measurements. Slit1 in front of the lens was used to generate a well-defined x-ray beam. The width of the line-focus of a diamond lens was then investigated by scanning slit2 through the focus, whereas the vertical gap of slit2 was set to very small values (in the order of one micron and below). The resulting diode signal therefore closely resembles the intensity profile across the line focus. In order to maximize the measured diode signal the horizontal gap of slit2 was normally chosen to be larger than horizontal size of the x-ray beam, so that the intensity within the focus is averaged along the line focus - i.e. in horizontal direction. Consequently, the width of the measured intensity peak represents the average width of the line-focus.

Figure 6.14 shows two typical examples, which were obtained doing measurements on the first lens depicted in Figure 6.9 B on the left. The intensity profile in Figure 6.14 A was obtained using a distance between the lens and slit2 equal to the theoretical image distance. Note, that a faint double peak can be seen in the intensity profile. It was discussed in chapter 6.1.3 that such a double peak can be qualitatively understood by assuming a constant shape error Δu so that the left and the right part of the lens yield two line foci which are shifted a distance Δu to the left and to the right relative to the ideal position of the focus. Figure 6.14 B shows the resulting intensity profile after increasing the distance between the lens and slit2 by 20 mm, which was found to be the distance leading to minimum width of the line focus. The peak in Figure 6.14 B has a width (FWHM) of about 5 µm. As the vertical gap of slit2 was set to a relatively large value (3 µm), the measured intensity profile is somewhat broadened in comparison to the real intensity profile.

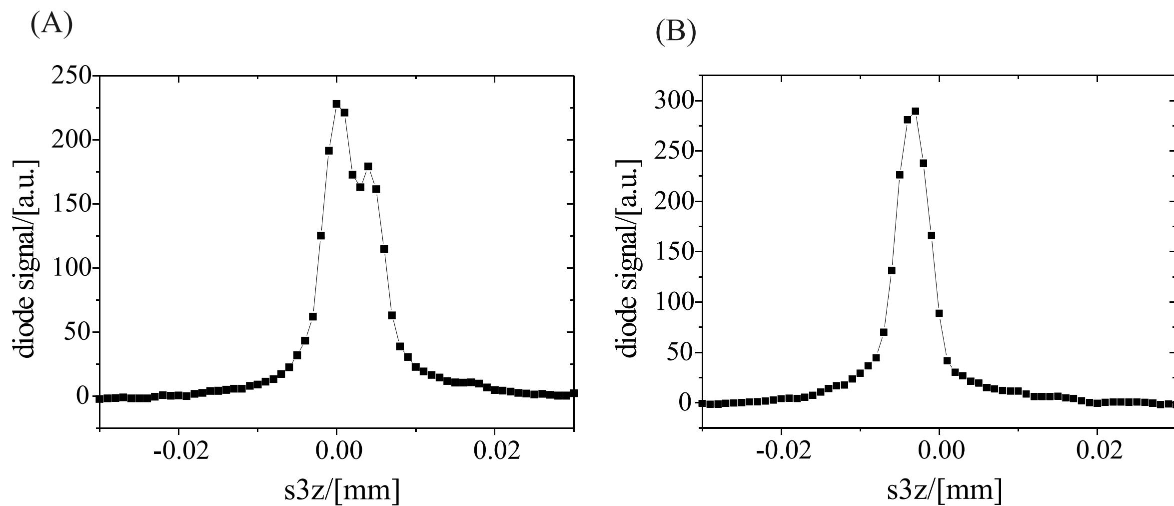

Figure 6.14: Intensity distribution across the line-focus of a diamond lens. (A) Intensity distribution measured in the theoretical image plane of the lens, which was calculated taking into account the focal length and the distance between the lens and the x-ray source. (B) Intensity distribution measured in a plane 20 mm downstream of the theoretical image plane, resulting in minimal width of the line focus.

Measurements on other lenses and at another photon energy (17.5 keV) led to similar results. For all tested lenses the distance between the lens and slit2 leading to minimal width of the line focus was found to be 5-10 % larger than the optimal theoretical distance. For all foci the minimum width was found to be in the range between 3 and 5 µm.

In order to obtain more detailed information about the focal line formed by a diamond lens, additional measurements were performed using slit2, whereas the gaps in vertical but also in horizontal direction were set to very small values. By scanning the resulting small pinhole through the image plane of a lens, it was possible to obtain a 2-dimensional map of the intensity distribution within the focus. The horizontal and vertical gaps of slit1 were set to large values in order to ensure a homogenous illumination of the full lens. Figure 6.15 shows an example of a resulting image taken at 17.5 keV photon energy. The corresponding diamond lens had an aperture of 500 µm and 3 lenslets were put in series so as to obtain a focal length of 1m.

A line focus of about 15 microns length was obtained. Note, that this is significantly less than the etched height of the lens (40 microns). This mismatch presumably originates from the special topography of the diamond lenses. Resuming the SEM-pictures of diamond lenses shown in Figure 6.9 one finds that the upper part of the diamond lenses is of comparatively bad quality and has non-vertical sidewalls. Consequently, this upper part of the lens acts like a prism, which not only focuses in the vertical direction but also causes a deflection in the horizontal direction. According to the considerations in chapter 6.1.3 this deflection occurs in the direction away from the diamond surface and therefore leads to the faint, elongated left part of the line focus (see Figure 6.15). The main contributions to the right part of the line focus supposedly originate from the lower part of the diamond lens having a comparatively high quality. All diamond samples have a considerable roughness of the order of a few micrometers, originating from the diamond etch process. This roughness leads to scattering and therefore the loss of part of the x-ray beam close to the sample surface and therefore is another reason for the observed mismatch between the lens height and the length of the line focus.

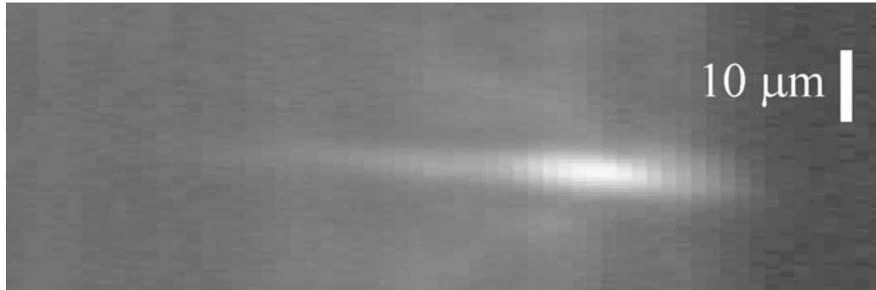

Figure 6.15: Intensity distribution within a focal line of a diamond lens, obtained by measuring the flux through a pinhole scanned through the image plane.

The vertical width of the line focus, taken in the region of maximum intensity of Figure 6.15 is 3.2 μm. For an ideal, aberration-free lens this width is given by a convolution between the geometrical source image (2.0 μm), the vertical pinhole size (0.5 μm) and the diffraction limited width of the focus (140 nm). This leads to a theoretical FWHM of the line focus of about 2.1 μm.

The observed discrepancy between the measured and the theoretical widths can be explained by deviations from the ideal lens shape originating from the imperfect etch process. According to the considerations in 6.1.3 the broadening is caused by the shape error Δu of different regions of the lens. From the SEM-viewgraphs of the diamond lenses the shape error is found to be in the order of 1-3 microns, depending on the lens region. It is therefore reasonable to expect a broadening of the line focus of approximately the same magnitude, which is in good agreement with the experimentally observed broadening.

In chapter 2.3.2 it was shown that optimum performance of a refractive lens with minimized absorption is restricted to certain photon energies given by equation (2.102). Applying Raleigh's quarter wavelength rule it was found that these photon energies have to be matched with considerable accuracy $\Delta E/E$ in order to achieve a diffraction-limited width of the focus. Applying equation (2.104) we find that an accuracy $\Delta E/E$ of about 1/3000 is required for the lens of Figure 6.15. According to equation (2.105) the refractive index and the density ρ of the diamond must also be known with this accuracy. This is beyond the capabilities of the density measurements we performed on our CVD diamond substrate, yielding an accuracy of about 1/200. The accuracy given by condition (2.104) is required in order to achieve a diffraction limited spot size. However, for the experimental situation leading to the line focus shown in Figure 6.15 the theoretical spot size is mainly determined by the size of the geometrical source image and about a factor 15 larger than the diffraction limited spot size. As a consequence the accuracy requirements for $\Delta\rho/\rho$ and $\Delta E/E$ are much less stringent. Nevertheless, some of the observed broadening of the line focus may result from a mismatch of the chosen energy.

Using the same method as before an efficiency of 67 % was found for the lens. In addition the gain of the lens was obtained by determining the ratio of the peak intensity in the focal spot and the intensity in regions unaffected by the lens. A gain of 26 was found evaluating the data shown in Figure 6.15.

6.3 Silicon refractive lenses

Chapter 6.3 deals with the fabrication and optical testing of silicon lenses. In the first part (chapter 6.3.1) the fabrication process of silicon lenses is discussed. The second part (chapter 6.3.3) reports on the results from measurements made at ID22 of the European Synchrotron Radiation facility during a commissioning time in June 2002, showing the performance of silicon lenses with respect to their efficiency and resolution.

6.3.1 Fabrication

The silicon lenses were fabricated in a very similar way to the diamond lenses. Figure 6.16 shows the principle of the respective fabrication process. The first steps are identical to the ones used to fabricate diamond lenses. E-beam lithography and a lift-off process are used to form an aluminium mask having the desired lens shape. Using a chlorine based plasma etch the resulting 50 nm thick aluminium mask is then transferred into a 100 nm thick chromium layer, which has been deposited on the silicon substrate by thermal evaporation. Contrary to the case of diamond lenses the resulting combined Al/Cr-mask is not directly used to structure the silicon sample itself, but to structure a thermally grown 2 µm thick SiO_2-layer on the silicon substrate. The SiO_2-layer was etched with a standard recipe of our group used for the anisotropic etching of SiO_2 (Oxford; 10 sccm O_2, 10 sccm CHF_3, 100 mTorr, 200 Watt - resulting bias voltage = 420 Volt, Temp.= 300K; etch time: 55min). Afterwards the sample was dipped into a buffered-oxid-etch (BOE) solution, consisting of hydrofluoric acid and ammonium fluoride for typically 1-3 minutes in order to remove remaining SiO_2 in etched sample regions. The BOE-step was several times interrupted and the silicon sample rinsed with water, enabling a monitoring of the cleaning process, as the complete removal of SiO_2 can be clearly seen by the change from a hydrophilic to a hydrophobic behaviour of the substrate surface. In a next step the remaining chromium and aluminium is removed by wet-etching. This removal of the Al/Cr-mask enables a compatibility with standard deep reactive ion etching (DRIE) processes [75] where in many cases metals are avoided and only SiO_2 or photo resist masks are used in order to guarantee reproducible etching processes. The silicon lenses are then finally formed by DRIE, which is described in more detail in following section.

The etching of the silicon lenses was performed in cooperation with the IBM research center in Rüschlikon (Switzerland), using and advanced Deep Reactive Ion Etching-model from STS (Surface Technology Systems). Such DRIE-systems utilize a sophisticated plasma etch process in order to obtain high etch rates together with a high anisotropy of the etch process. The principle of this so-called Bosch process [75] is to use a multi-step approach, where in one step the silicon is etched and in the following step a polymer passivation layer is formed, protecting the sidewalls of the etched structures during subsequent etch steps. Contrary to conventional RIE-systems, which normally use one step etch processes, this offers the possibility of an independent optimisation, so that for one step very high etch rates and for the other step a very effective generation of the polymer protection layer can be obtained. By adjusting the etch recipe - in particular the duration of the etch and the passivation steps - it is possible to achieve a high control of the side-wall slope, so that silicon structures with almost perfectly vertical sidewalls can be obtained. Using appropriate etch gases (SF_6, O_2, C_4F_8) it is also possible to achieve a very high selectivity of the DRIE-process, meaning that the etch rate of the silicon is much higher than the etch rate of SiO_2 and photo resist, which are the two standard etch mask materials used for DRIE.

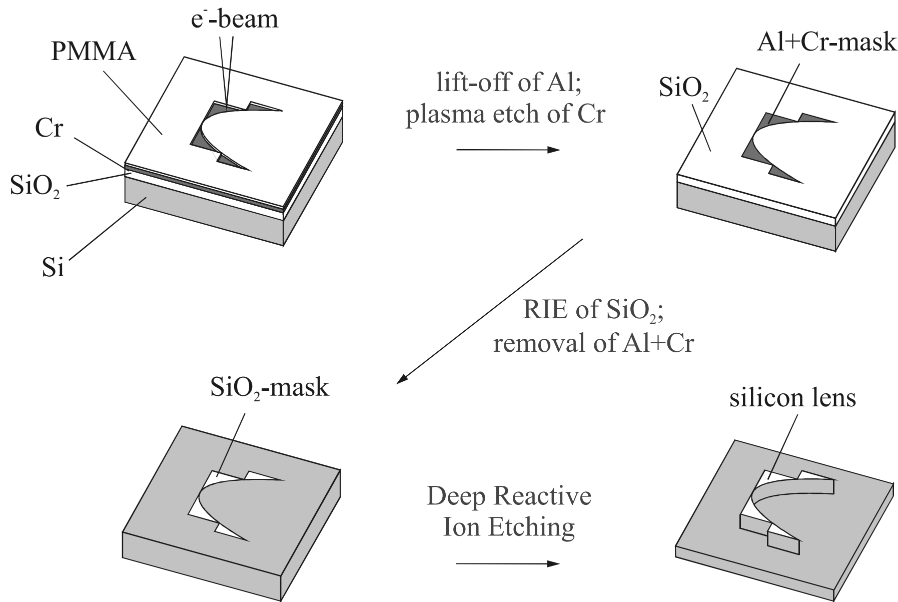

Figure 6.16: Fabrication process of planar refractive silicon lenses.

Figure 6.17 shows cross-sections of a part of a silicon lens, revealing the typical etch profile obtained using Deep Reactive Ion Etching of silicon. One characteristic of the DRIE-process is the fact that there is a considerable difference in the etch behaviour for large trenches - i. e. large regions without an etch-mask - and the etch behaviour for small trenches (see Figure 6.17 A). Next to large regions without a mask a strong under-etching is observed, especially in the lower parts of the lens. For narrow trenches the under-etching is small in the upper regions of the lens, whereas for large etch depths the width of the trench gradually decreases and goes to zero. One also finds that the etch rate for narrow trenches is significantly lower than for large trenches, so that the etch depth within the small trenches shown in Figure 6.17 A is about 50 μm smaller than etched height of the lens structure.

The right SEM-picture reveals the high quality of the etched silicon surface, showing a roughness below about 200 nm. For the upper half of the lens the under-etching is small (approx. 2 microns) and the sidewalls are almost vertical, with a slope error α in the order of 1/50.

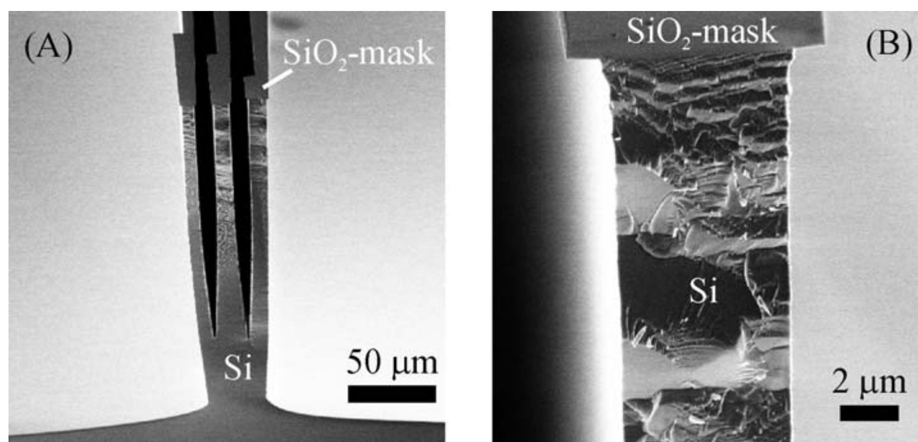

Figure 6.17: Cross-sections of a part of a silicon lens showing the typical etch profile obtained using Deep Reactive Ion Etching of silicon.

Figure 6.18 - Figure 6.20 give some examples of silicon lenses formed by Deep Reactive Ion Etching. All shown lenses have an etch-depth of about 250 μm.

Figure 6.18 shows a small test-lens revealing the high lens quality as regards to surface roughness. At the same time Figure 6.18 also shows that there is a significant under-etching of the lens. Consequently, a special lens design has to be used in order to prevent a collapsing of the etched lens structures. It was discussed before that the under-etching is particularly strong next to large regions without an etch mask. The thinnest - and therefore weakest - regions of a lens with minimized absorption are the ones close to the edge of the lens. This was the reason to use the additional bars on the left and on the right side of the lens array shown in Figure 6.18. Despite of these protection bars there is a strong under-etching for the lenslets on top and at the bottom of the array. The top and the bottom lenslet were therefore chosen to be thicker than the other lenslets within the array, which was accomplished by using a larger parameter $h_{a,thick}$ for the top and the bottom lens than the corresponding parameter h_a of all other lenses (see also Figure 6.3).

Figure 6.19 shows a SEM-viewgraph of a lens with large light collection capabilities, having a diameter of 600 μm and a focal length of 1400 mm at the design energy of 35.07 keV. Fourteen lenslets with parameters M_1=28 and m_1=2 are used in series.

Figure 6.20 shows an SEM-picture of three silicon refractive lenses with increasing apertures (200, 400 and 800 μm) and focal lengths (350, 700 and 1400 mm) from the left to the right, so that in the end all lenses have the same numerical aperture. All three lenses consist of 24 lenslets in series, have the same parameter M_1 (M_1=48) and are designed for the same photon energy (50 keV).

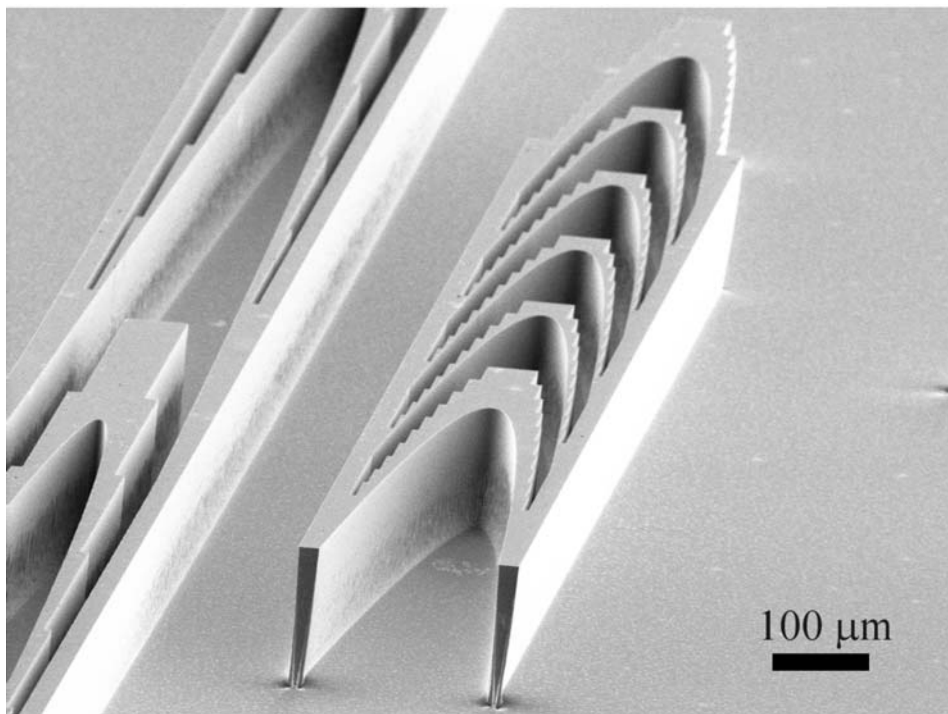

Figure 6.18: SEM-viewgraph of a small silicon test-lens showing the typical design of the silicon refractive lenses fabricated within this work. In order to prevent collapsing of the lens structures due to under-etching a special lens design was used, featuring additional bars at the left and right side of a lens array, and thicker top and bottom lenses compared to the other lenses within the stack.

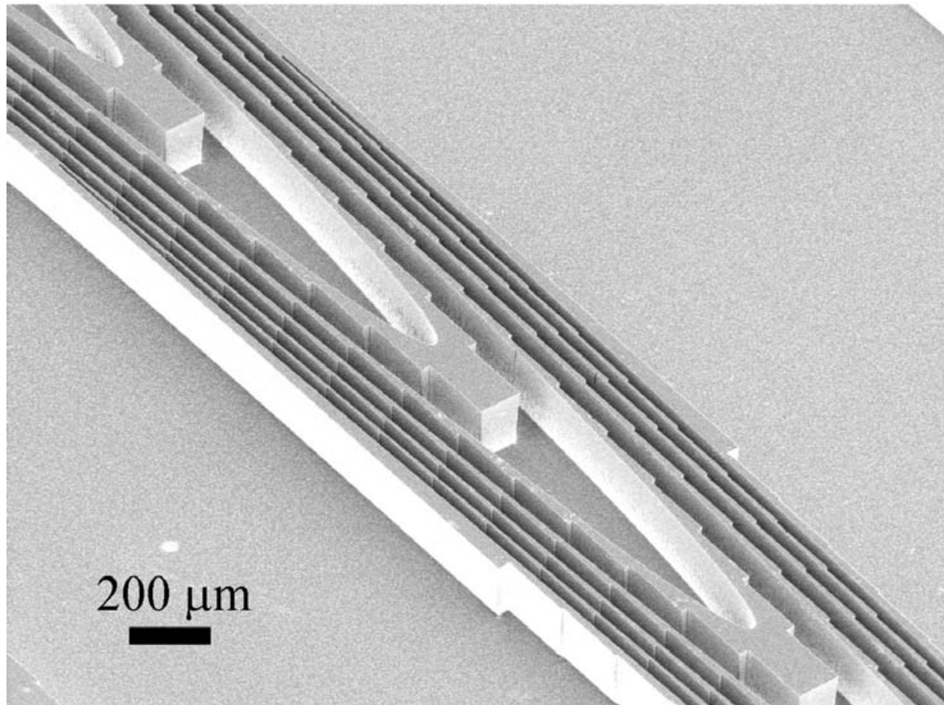

Figure 6.19: Part of a silicon refractive lens with 600 µm diameter, consisting of 14 lenses in series in order to achieve a focal length of 1400 mm at the design energy of 35.07 keV.

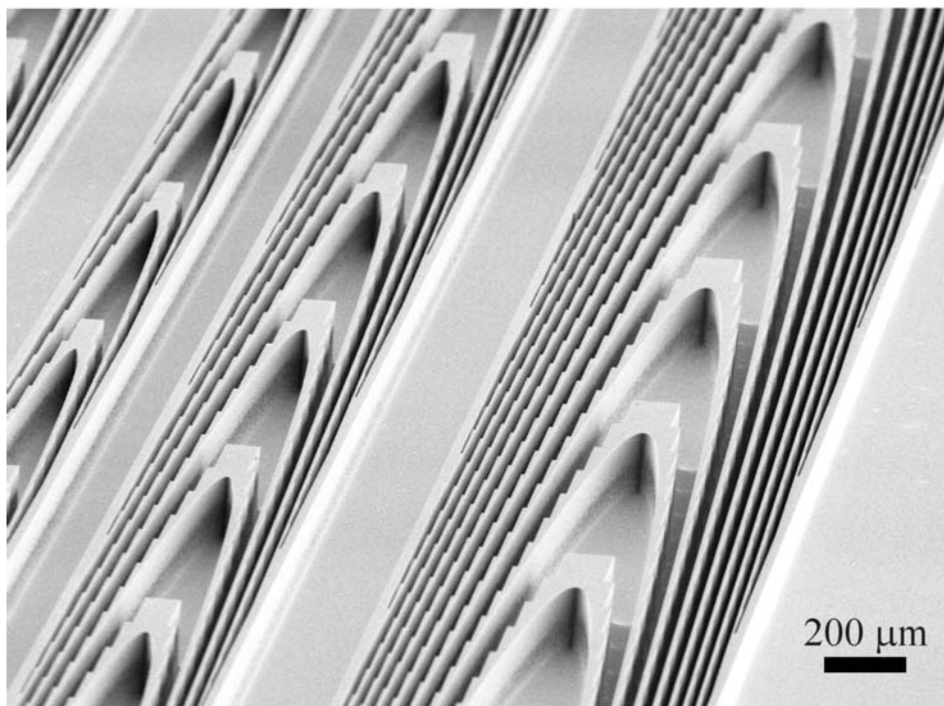

Figure 6.20: SEM-viewgraph showing three lenses with 200, 400 and 800 µm diameter and focal lengths of 350, 700 and 1400 mm at the design energy of 50 keV.

6.3.2 Stacking of silicon lenses

Figure 6.17 and Figure 6.18 showed a significant shape error Δu and slope error α for silicon refractive lenses formed by DRIE-processes. According to the considerations in chapter 6.1.3 the resulting aberration errors are directly proportional to Δu and α. Consequently, it should be possible to significantly decrease the total lens aberrations by combining two lenses with opposite sign for the shape error Δu and the slope error α. Figure 6.21 shows a scheme to compensate for the aberrations caused by a slope error, which is accomplished by stacking two identical lenses. Note that by flipping a lens by 180^0 the sign of the slope error is reversed, so that the aberrations resulting from a slope error α should be significantly reduced using such a scheme. If the slope error is constant within the overlap region of the two lenses then the corresponding aberrations are fully cancelled out.

Flipping a lens does not reverse the sign of the shape error Δu. The corresponding aberrations could only be cancelled out using a lens pattern that compensates for the under-etching and the resulting shape error. However, such a compensation of the under-etching is difficult, as the shape error strongly varies with the position on a lens and also with the etch depth. Using the stacking scheme shown in Figure 6.21 should somewhat average the shape error Δu as for example the top part of one lens - which according to Figure 6.17 has a comparatively small shape error - will overlap with the bottom part of the second lens, having a comparatively large shape error.

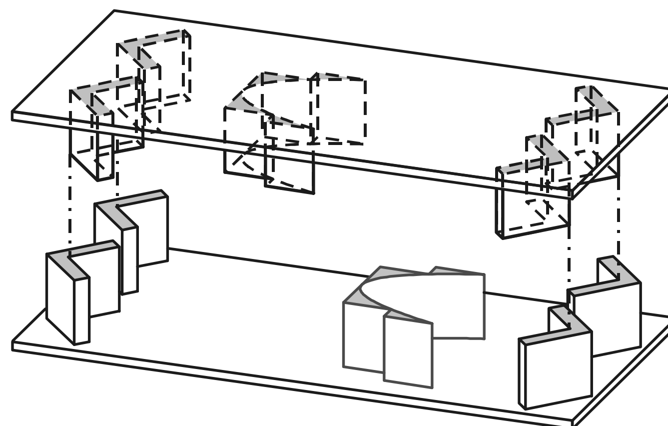

Figure 6.21: Scheme to reduce lens aberrations by stacking two identical lenses. Micro-mechanical alignment structures on the top and the bottom sample are used to facilitate the required alignment of the two lenses.

Figure 6.21 shows several micro-mechanical alignment structures, used to facilitate the alignment of the two mutually compensating lenses. Figure 6.22 depicts the realisation of such a stacking for silicon lenses. Different types of alignment marks are used in order to allow an easy first contact between the samples (marks B being pushed into the angle of marks A) and a self-finding stacking mechanism (marks C and D) when the top sample is moved down. Figure 6.23 A is a close-up of one alignment mark (type A), whereas Figure 6.23 B shows two alignment marks (type A and B) for the case that the two samples are stacked together. The gap between the top and the bottom sample is larger than the etched height of the silicon structures. However, this is due to a loose mounting within the SEM-sample holder and under normal circumstances - if one of the samples is forced down by gravity - the gap is equal to the height of the silicon structures. Figure 6.17 showed that only the upper part of a planar silicon lens close to the etch mask can be considered to be of high quality. In order to achieve a good performance of a pair of stacked lenses the lenses should

overlap in regions of high quality, which requires a distance between the stacked samples that is larger than the etched structure height. This could be achieved by putting appropriately thick spacers between the two samples.

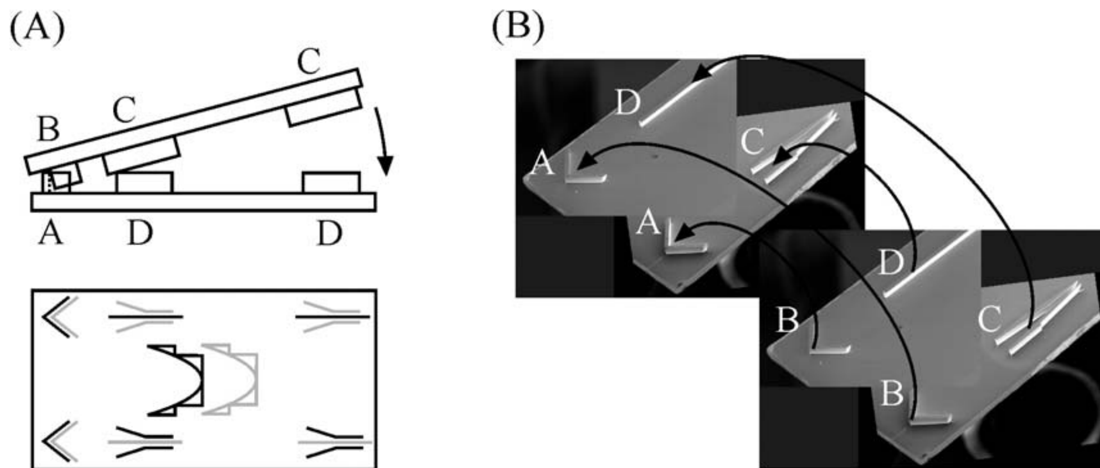

Figure 6.22: Realisation of a stacking mechanism for silicon lenses, which is used for the compensation of lens aberrations resulting from deviations from the ideal lens shape.

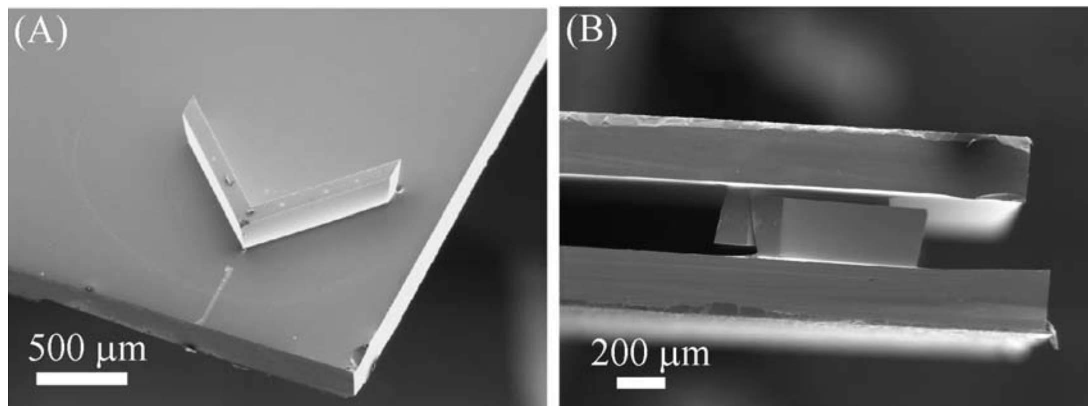

Figure 6.23: (A) Close-up of a micro-mechanical alignment structure on a silicon sample. (B) SEM-viewgraph of two alignment structures for the case that the top and the bottom silicon sample are stacked together.

The alignment marks shown in Figure 6.22 and Figure 6.23 prove to be very robust and only break if strong forces are applied. The stacking process itself is simple, does not require any special devices besides a pair of tweezers and is also reversible, so that the two samples can be easily separated again by lifting up one of the samples.

The approach of stacking lenses improves the lens performance, but it is difficult to estimate the gain in resolution. Unfortunately the duration of the beam time used for the testing of planar silicon lenses was too short to allow for the testing of stacked lenses. Consequently additional beam time would be required to enable a final judgment if using mechanically stacked lenses offers a significant advantage in comparison to conventional planar refractive lenses.

Obviously the stacking technique is not restricted to lenses but can be used for the simple alignment of two arbitrary silicon devices with accuracies in the order of a few microns, making the technique interesting for all MEMS-applications (Micro Electro Mechanical Systems) that involve the assembly of silicon substrates.

6.3.3 Measurements

Chapter 6.3.3 contains the experimental results on planar refractive silicon lenses, which were obtained at ID22 of the ESRF during three days of commissioning time in June 2002. In chapter 6.3.3.1 the corresponding experimental set-up is described. Chapter 6.3.3.2 and chapter 6.3.3.3 report about the efficiency measurements and resolution tests on silicon lenses, respectively.

6.3.3.1 Experimental set-up and general considerations

Figure 6.24 shows the experimental set-up used for the testing of planar refractive silicon lenses. Besides minor differences it is very similar to the one used for the measurements on planar refractive diamond lenses. Like the diamond lenses also the silicon lenses were fixed in such way that focusing in vertical direction was achieved. A slit in front of the lenses (slit1) was used to define the x-ray beam for the illumination of a certain silicon lens on a sample. For the efficiency measurements another slit (slit2) was placed in the image plane of the lens. The resolution of the lenses was determined by knife-edge scans with a gold test sample, which is commonly used for this purpose at the beamline ID22. At ID22 an undulator is used for the generation of an x-ray beam, which is monochromatized using a silicon double monochromator. The experiments were performed at 49.6 and at 35.07 keV photon energy, using the (311) and the (111) reflections of the silicon crystal, respectively. The silicon lenses were mounted onto a built-in stage of ID22 allowing the movement in x,y and z-direction (motors x_1, y_1 and z_1) as well as a rotation of the sample around the y- and the z-axis (motors ψ_1 and θ_1).

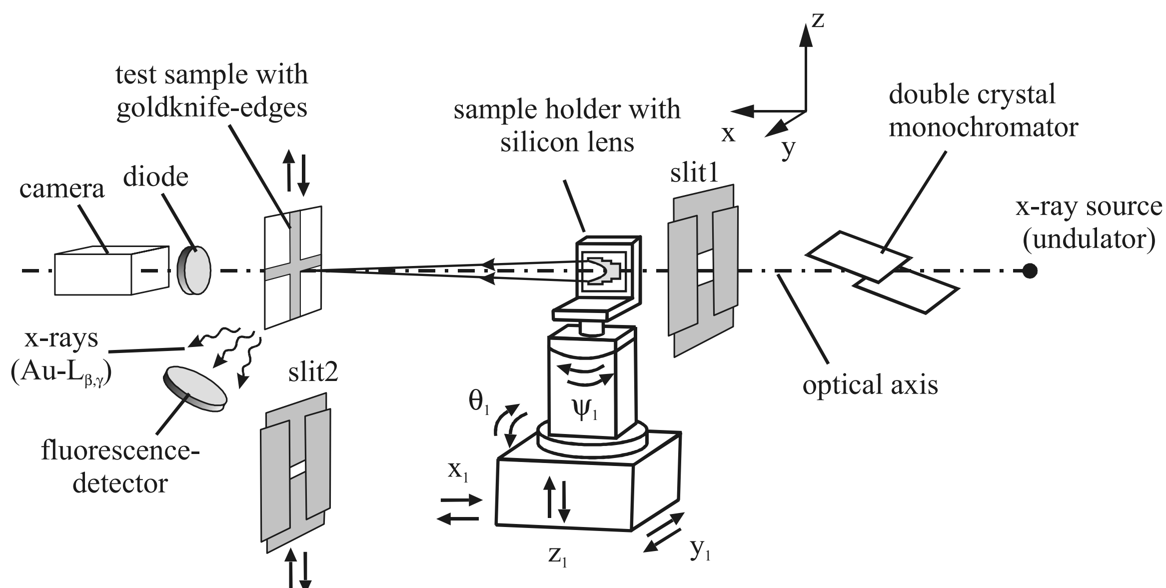

Figure 6.24: Schematic sketch of the experimental set-up for the optical testing of planar refractive silicon lenses. A slit (slit2) and a test sample with a gold knife-edge are used to measure the efficiency and the resolution of the lens, respectively.

In a first step the orientation of the silicon lenses was aligned with respect to the incoming beam (tilt angles ψ_1 and θ_1). This was performed in the same way as for the diamond lenses using built in alignment structures on the sample. For the silicon lenses two comparatively short, line-shaped alignment marks with a distance of about 4 cm were fabricated on the silicon sample. The alignment marks could be clearly seen in an x-ray camera and at the same time transmitted a considerable part of the x-rays due to the high penetration depth in silicon at the used photon energies. For the alignment the tilt angles ψ_1 and θ_1 were adjusted until the images of the two marks in the x-ray camera exactly overlapped. Due to the large distance of the alignment marks an accuracy of about 10^{-4} could be reached in both directions. This is sufficient to prevent any blocking of x-rays due to a sample surface that is not parallel to the incoming beam. The accuracy is also sufficient to prevent any lens aberrations due to a misalignment of ψ_1, as it was experimentally found that a misalignment of below 5×10^{-4} between the optical axis and the x-ray beam caused no significant increase of the width of the line focus.

6.3.3.2 Efficiency measurements

The efficiency of the silicon lenses was measured with two different methods. One of them was identical to the technique that had already been applied for the measurement on multilevel zone plates and diamond lenses, using a slit that is scanned through the image plane of the lens. Like for the zone plates and diamond lenses the slit in front of the silicon lens (slit1) was used to produce a well-defined beam for the testing of the lens. The horizontal gap of slit1 was set to values smaller than the height of the lens (gap size of 50-100 µm) in order to ensure that the whole beam undergoes focusing by the lens. For the second efficiency measurement technique the slit1 in front of the lens was used to illuminate a well-defined part of the lens. The flux within the spot was then collected with the slit placed in the image plane (slit2) and compared to the total flux passing slit1 after moving the silicon lens out of the beam. Consequently the ratio of the two signals yielded the efficiency of the lens. Within an experimental error of about 2% both efficiency measurement techniques yielded the same results.

Table 6.1: Measured and theoretical efficiencies of planar refractive silicon lenses

aperture [µm]	focal length [m]	photon energy [keV]	efficiency (measurement)	efficiency (theory)
400	1400	49.6	31 %	46.1 %
800	1400	49.6	17 %	24.8 %
600	1400	35.1	19 %	29.5 %

In total three different lenses were tested using the lens design energies of 35.07 and 49.6 keV. Table 6.1 gives a table of the obtained efficiencies. In all three cases the measured values are significantly lower than the theoretically calculated ones using equation (2.112).

The observed discrepancy can be explained by scattering losses due to deviations from the ideal lens shape and diffraction at the sharp edges of the lens structures. As for the diamond lenses it was found that the efficiency of a lens region depends on the width of the lens segments in the considered region. Comparing the flux in the focus originating from different

lens regions it was found that the lens efficiency strongly decreases for segment widths below about 5 µm. As for the diamond refractive lenses it therefore makes no sense to use lens designs with minimal segment widths that are significantly smaller than 5 µm. Due to our experience with diamond lenses this kind of design limit had already been anticipated and considered for the design of the silicon lenses so that all lenses described in Table 6.1 had minimal segment widths of approximately 4 µm.

6.3.3.3 Resolution tests

To test the resolution of silicon lenses knife-edge scans were made using a gold-test sample with knife-edges in horizontal and vertical direction (see also Figure 6.24). Slit2 was placed approximately 20 cm upstream from the gold-test sample and used as a clean-up aperture, meaning that it was used to cut out most of the unwanted photon flux outside of the line focus formed by a silicon refractive lens. For this purpose the vertical gap of slit2 was centred with respect to the focus and closed as much as possible without getting a reduction of the flux within the focus. In this way the background signal stemming from diffraction losses within the lens structures was greatly reduced. The horizontal gap of slit2 was typically set to values of about 20 µm and used to select a certain part of the line focus for the resolution testing.

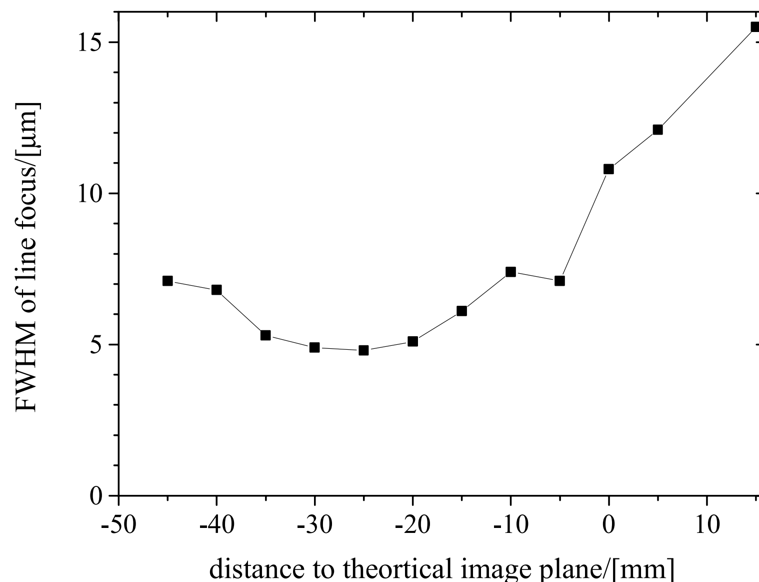

Figure 6.25: Measured FWHM of a line focus depending on the distance from a silicon refractive lens, obtained at 35.07 keV photon energy. Like for diamond refractive lenses minimal width of the focus is obtained in a distance, which is larger than the theoretically calculated image distance. However, the observed discrepancy between the optimal image distance in theory and in praxis is smaller (approx. 2%) than in the case of diamond lenses.

The knife-edge scans were evaluated in the same way as discussed for the multilevel zone plates (see chapter 5.2.2), measuring the gold fluorescence (Au-L_β and L_γ line) from the test-sample and forming the derivate of the obtained signal. The resulting peak represents the intensity distribution across the line-focus and was fitted with a Gauss-curve, yielding the FWHM-width of the peak. Figure 6.25 shows the measured widths, which were obtained at the design energy of 35.07 keV (see Table 6.1 and Figure 6.19 for the measured efficiency, a SEM-picture and the lens data). For all depicted measurements the same, upper part of the lens close to the SiO2-etch mask was selected. The FWHM- width of the line focus was then determined for different distances between the lens and the resolution test object. The zero

position in Figure 6.25 corresponds to the theoretical position of the image plane. The corresponding theoretical image distance between the lens and the focused source image was calculated to be 1.557 m, taking into account the focal length (1.4 m) and the distance between the lens and the x-ray source (41 m). As for the diamond lenses the practical image distance leading to minimal width of the line focus is a little bit (about 2%) larger than the theoretical imaging distance. Again this can be explained by a positive under-etching of the lens structures. According to the considerations in chapter 6.1.3 such a positive under-etching will on average shift the position, where the x-rays cross the optical axis, in a direction downstream from the theoretical position of the focus.

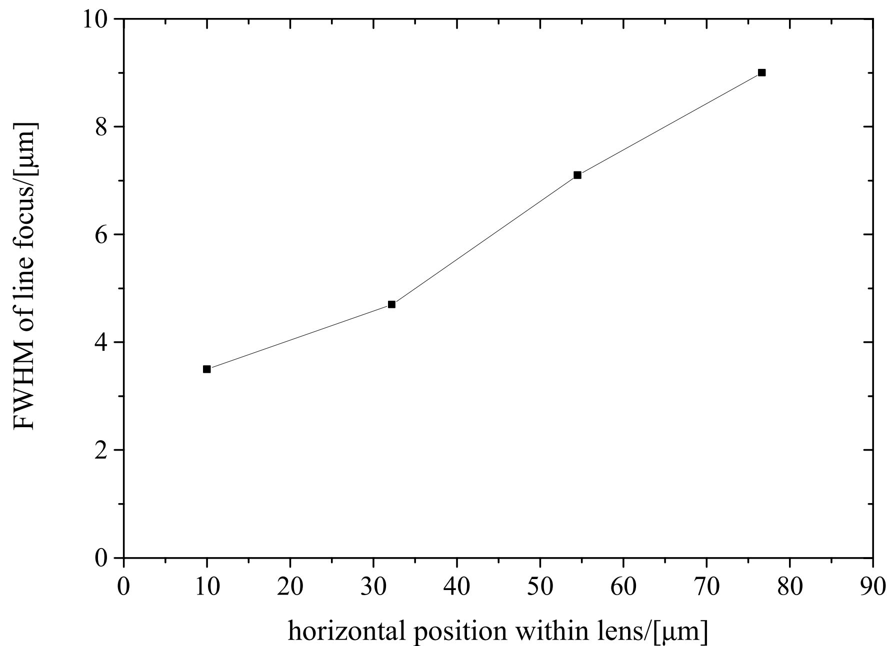

Figure 6.26: Measured widths of a line focus at 35.07 keV photon energy, which were obtained using only a certain small height region of a planar silicon refractive lens for the focusing. As the under-etching of the lens structures strongly varies within the full height of the structures the observed FWHM-width of the line focus depends on the considered height region of the lens.

Figure 6.17 and Figure 6.18 showed that the shape error caused by a non-perfect etch process strongly depends on the considered height region of the lens. Consequently, also the FWHM-width of the line-focus formed by different height regions of a planar refractive lens should be different. In fact this was observed in the experiment as shown in Figure 6.26. The corresponding measurements were performed with the same lens as for the data presented in Figure 6.25, using the design photon energy of 35 keV and the practical imaging distance that had lead to minimal width of the line focus. For the upper parts of the lens close to the etch mask a line width down to 3.5 µm is observed, whereas in lower regions of the lens a line width up to 9 µm was found. For most applications it is obviously not possible to obtain line widths as small as 3.5 µm as this would require using only a very small part of the line focus. According to the data shown in Figure 6.26 one can expect to achieve a mean width of the line focus of about 7 µm across the full height of the lens.

In any case most applications require 2-dimensional focusing of an x-ray beam. This can be achieved using two crossed planar refractive lenses in series, forming a micro-focusing device analogous to the one described for multilevel zone plates in chapter 5.2. In the experiment such a micro-focusing device was realised by replacing slit2, that had been used

as an order selecting aperture for the resolution test on single lenses, by a second lens, which was then used for the horizontal focusing of the x-ray beam. The second lens had a four time smaller diameter and focal length (D=150µm, f=350mm) than the lens in front, used for the vertical focusing. This made it possible to partially compensate for the asymmetry of the undulator source, having a FWHM size of 700µm×30µm in horizontal and vertical direction, and at the same time to collect a relatively large area of the incoming x-ray beam. Note, that the diameter of the horizontally focusing lens is in any case limited by the structure height of the vertically focusing lens to a maximal value of about 200 µm.

In a first step the two lenses were aligned using the projected images of the two lenses in the x-ray camera. In the vertical direction the two lenses were centred whereas in horizontal direction the overlap region between the two lenses was chosen in such way that the upper part of the vertically focusing lens contributed to the focusing. The distance between the second, horizontally focusing lens and the resolution test-object was first set to the theoretical imaging distance in horizontal direction (353 mm) using a tape measure. Afterwards the position of the horizontally focusing lens was adjusted in such a way that a minimal horizontal width of the micro-focus was achieved. Again a small difference of 5 mm between the theoretical and the practical optimal position was found. However, the observed difference can also be attributed to the uncertainty in determining the width of the focal spot, as a change of 5mm in the position does not cause a significant broadening of the spot.

For the optimal positions of both lenses the micro-focus was found to have a width of 13µm×8µm in the horizontal and vertical directions, respectively. Theoretically a size of the geometrical source image of 6µm×1µm is expected, taking into account the source size of 700µm×30µm and its distance from the focusing device (41 m). Obviously in both directions the focal spot is strongly broadened due to lens aberrations. The experimentally observed size of the focal spot can be understood as the convolution between the geometrical source image and the aberration limited focal spot, which one would obtain for an infinitely small x-ray source. Assuming Gauss-distributions the aberration limited focal spot is found to have a size of 12µm×8µm. The broadening due to deviations from the ideal lens shape is different in the two directions, although the shape error and the slope error should be the same for both lenses, as both lenses were processed together. This difference can be explained by the aberrations due to slope errors, which according to equation (6.8) are not only proportional to the slope error but also proportional to the lens diameter. As a consequence the corresponding aberrations introduced by the first lens with large diameter - which lead to a broadening in horizontal direction - will be larger than the aberrations introduced by the second lens.

In order to demonstrate the capabilities of the obtained micro-focusing set-up a test sample consisting of a gold mesh was placed in the image plane and scanned through the micro-focus. The resulting gold x-ray fluorescence gives a measure of the gold concentration within the focal spot, so that a fluorescence image of the gold mesh is obtained by scanning the sample (see Figure 6.27).

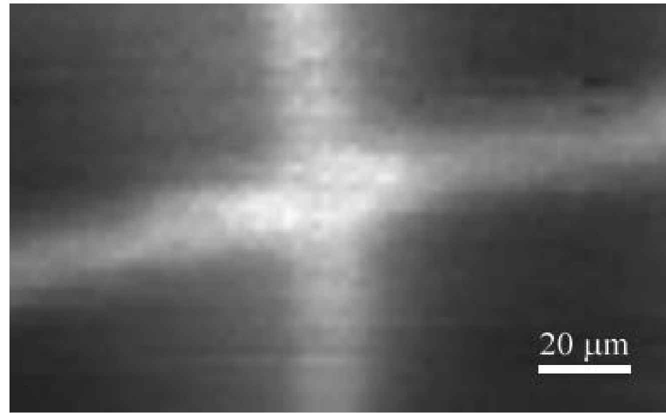

Figure 6.27: X-ray fluorescence image of a gold mesh obtained by scanning the mesh with a focal spot that was formed with a pair of two crossed silicon planar refractive lenses. The micro-focus had a size of about 13µm × 8µm in horizontal and vertical directions respectively, at a photon energy of 35.07 keV.

The same set-up can be used for the determination of the concentration of basically any type of element within a sample, provided that a suitable fluorescence line can be excited with the given photon energy. In a more recent experiment at ID22 in December 2002 the same set-up could therefore be used to measure the iodine, bromine and chlorine fluorescence of various geological samples [98]. Due to the limited time for building up the focusing device it was not possible to fully optimise the set-up with respect to the obtained size of the micro-focus. Nevertheless, a spot of 15µm ×15 µm with a photon flux of about 6×10^9 photons/s at 35.07 keV could be achieved. The resulting strong fluorescence signal was then used to investigate the iodine content of inclusion fluids trapped in minerals containing 3.5 billions years old seawater (North Pole, Australia, see Figure 6.28).

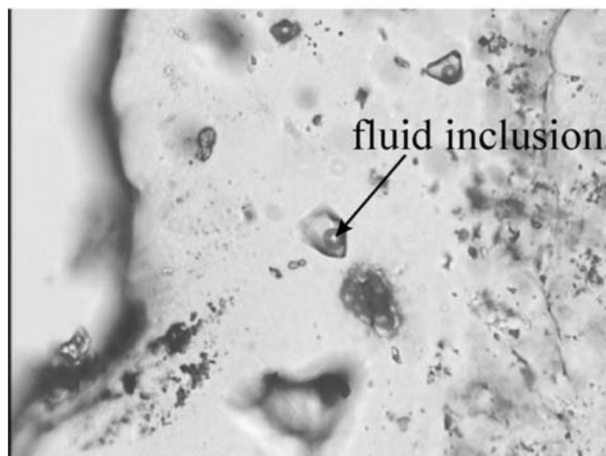

Figure 6.28: Light microscope image of a mineral with fluid inclusions containing 3.5 billion years old seawater. The inclusion was investigated using the micro-focus formed by two crossed planar refractive silicon lenses. The resulting iodine fluorescence gave a measure of the iodine concentration within the fluid inclusion and therefore gives information about the composition of archaean sea water in comparison to the composition nowadays.

Additional measurements have been performed on melt inclusions preserved in olivine crystals (Etna volcano, Sicilia) and on fluid inclusions from high pressure rocks that have been subducted to 100 km depths and that are currently exposed on the Earth's surface (Dora Maira, European Alps; Dabie Shan, China; see also [98]).

6.4 Conclusions and Outlook

The chapters 6.2 and 6.3 about diamond and silicon planar refractive lenses showed that there are many similarities in the behaviour and optical properties of these lenses. For both lenses very similar fabrication processes are used and in both cases the optical performance is mainly influenced by deviations from the ideal lens shape, which are the result of a non-ideal processing of the lenses. The considerations in chapter 6.1.3 showed that two types of deviations are at the origin of the observed lens aberrations: the shape error Δu, describing deviations from the ideal surface position, and the slope error α, describing the deviation from the ideally vertical orientation of the lens sidewalls. Although there is no direct link between these two lens errors, for realistic etch profiles one can assume that the maximal shape error Δu_{max} is of the order of $h\times\alpha_{max}$ where h is the height (etch depth) of the lens and α_{max} the maximal slope error within the lens. According to equations (6.6) and (6.8), the aberration caused by the shape error is then of the order of $h\times\alpha_{max}$, and the aberration caused by the slope error of the order of $D\times\alpha_{max}$, with D denoting the aperture of the lens. As a consequence the maximal slope error α_{max} represents a characteristic parameter that describes the accuracy of the chosen fabrication process and at the same time determines the minimal size of a focus that can be achieved with planar refractive lens.

For planar refractive silicon lenses it was shown that values of α_{max} of the order of 1/50 can be reached for the high quality regions of the lenses, which is enabled by the extreme anisotropy and selectivity of the used Deep Reactive Ion Etch process. Assuming a lens diameter and height in the order of 100 microns this leads to a size of the focus in the micron range. In the case of silicon lenses it is obviously a difficult task to further decrease the slope error, as the deep reactive ion etching process used within this work already represents a highly optimised and developed technique. Nevertheless by optimising the process specifically for the fabrication of the silicon lenses a further gain in lens quality should be possible. It was shown above that the lens aberrations caused by slope and shape errors of the lens are directly proportional to the height and diameter of a planar refractive lens. Consequently, a different possibility to improve the resolution is to use lenses with smaller diameters and etch depths. Applying this approach a micro-focus as small as 400 nm× 200 nm at 25 keV photon energy could be achieved recently [84], using two crossed silicon planar refractive lenses with an effective aperture of about 10µm×10µm. However, the restriction to small effective apertures inevitably has the disadvantage that only a very small part of the x-ray beam can be collected, leading to a very small photon flux within the focal spot.

For diamond lenses the maximal slope error is - in comparison to silicon refractive lenses - relatively large. Even for high quality regions of the lens the slope error α_{max} is in the order of 1/10. It is therefore realistic to expect an improvement of the lens quality and the resolution by optimising the diamond fabrication process. One possibility is the search for more durable etch masks than the chromium mask used within this work. This should greatly reduce the faceting effect in the upper part of the diamond lenses (see e.g. Figure 6.10) and therefore also minimize the extension of this region with strongly non-vertical sidewalls. Further improvement of the etch process and the etch parameters with respect to etch rate and anisotropy should also enable a significant increase of the quality and optical performance of diamond lenses. However, in comparison to silicon the etch rates of diamond reported in literature are much lower and diamond is much more difficult to structure. Consequently, diamond lenses will be most appropriate for special applications were the unique material properties of diamond play an essential role.

One mayor advantage of diamond is its very low absorption in the hard x-ray region. Contrary to silicon lenses, which due to absorption losses are restricted to photon energies

above about 20 keV, diamond lenses display absorption losses in the order of a few percent, even for photon energies as low as 10 keV. It was already discussed in chapter 5.2.3 that there are many competitors for this lower part of the hard x-ray range, like binary and multilevel zone plates, x-ray mirrors and parabolic compound refractive lenses. Some of these lenses achieve a resolution in the 100 nm range and at the same time high efficiencies, making it difficult to compete with their performance using diamond refractive lenses. However, besides its very low x-ray absorption diamond also has some other unique material properties, like an extremely high thermal conductivity, a low thermal expansion coefficient and a high thermal stability. In connection with the special geometry of planar refractive lenses, which enables effective heat dissipation, diamond planar refractive lenses are therefore able to sustain very large heat loads [99]. This is of high importance in the context of X-ray free electron lasers, as no conventional x-ray lens is likely to sustain the intense beam. Due to the special properties of diamond, planar refractive lenses made from diamond lenses are therefore one of the very few promising candidates for optical systems at X-FELs.

Using silicon for the fabrication of planar refractive lenses one can benefit from the highly sophisticated structuring techniques available, which enable the fabrication of lenses with high surface quality and with extreme aspect ratios and structure heights. Due to the comparatively large x-ray absorption it is difficult to obtain high efficiencies using silicon lenses for photon energies below about 30 keV. Again, there are many competing types of x-ray lenses for this lower part of the hard x-ray region. Planar refractive silicon lenses are therefore best suited for applications in the very hard x-ray range above about 30 keV, where only very few other types of lenses are available. The results presented in chapter 6.3.3.3 showed that the resolution of planar refractive lenses is relatively low. However, it was already discussed before that the obtainable focal spot size is directly related to the size of the aperture, so that the actual resolution one can reach can be strongly improved by using lenses with smaller apertures. Chapter 6.3.3.3 showed that a focal spot of the order of 10 µm×10 µm can be achieved, if at the same time a large area of the incoming beam (600×150µm^2) is collected. By further improvement and optimisation of the etch process - e.g. by compensating some of the observed under-etching using an improved mask design - even smaller spot sizes should be feasible. The main potential application of silicon lenses, which has also been described in chapter 6.3.3.3, is its use for micro-X-ray fluorescence investigations on geological, biological and historical samples. Measurement of the x-ray fluorescence enables the determination of the distribution of different elements within a sample (element mapping). The resolution of this technique is restricted by the size of the micro-spot and for many applications a spot size in the micron range - which is feasible with planar refractive silicon lenses - is already sufficient.

An alternative type of lens applicable for the use in the hard x-ray range above 30 keV is the parabolic compound refractive lens made of a material such as nickel [100], which has the potential to reach sub-micron resolution. However, compound refractive lenses require the use of many lenses in series so as to achieve reasonable focal lengths. For extremely high x-ray energies these devices then become impracticably long.

Another type of focusing device applicable for use above 30 keV is the focusing mirror, which should also be capable of reaching sub-micron resolution. However, especially at these extreme photon energies x-ray mirror optics have the disadvantage that very small incidence angles are required to reach a sufficiently high reflectivity, making it difficult to align these lenses with respect to beam and to prevent shape-error induced lens aberrations.

In comparison to compound refractive lenses and mirror optics, planar refractive silicon lenses have the advantage that they are very compact devices and comparatively easy to use.

Even for photon energies as high as 50 keV one can easily reach numerical apertures above 10^{-4}, with compact devices having lengths in the centimetre range. With the use of built-in alignment marks on the silicon sample the alignment with respect to the x-ray beam is a simple and fast procedure. Planar refractive silicon lenses are therefore best suited for applications in the very hard x-ray range above 30 keV, which do not require a high resolution. This allows then to profit from their compactness and relative simple handling for practical applications.

References

[1] W. C. Röntgen, *"Über eine neue Art von Strahlung"*, Sitzungsberichte der physikalisch-medizinischen Gesellschaft Würzburg, pp. 132-141, (1895)

[2] C.G. Barkla, *"Polarization in secondary Röntgen radiation"*, Proceedings of the Royal Society of London, Series A, Vol. **77**, pp. 247-255 (1906)

[3] W. Friedrich, P. Knipping, and M. von Laue, *"Inteferenzerscheinungen bei Röntgenstrahlen"*, Sitzungsbericht der mathematisch Physikalischen bayrischen Akademie der Wissenschaften, pp. 303-322, (1912)

[4] G. Stokes, *"On the nature of the Röntgen rays"*, Memoirs and Proceedings of the Manchester Literary and Philosophical Society, Part IV, Vol. **41**, pp. 1-28 (1896-1897)

[5] J.J. Thomson, *"A theory of the connection between cathode and Röntgen rays"*, The London, Edinburgh, and Dublin philosophical magazine and journal of science, Series 5, Vol. **45**, pp. 172-183 (1898)

[6] C.G. Barkla, *"Polarised Röntgen radiation"*, Philosophical Transactions of the Royal Society of London, Series A, Vol. **204**, pp. 467-479 (1905)

[7] W. Duane, and F.L. Hunt, *"On x-ray wave-lengths"*, Physical Review, Vol. **6**, No. 2, pp. 166-171, (1915)

[8] A. Einstein, *"Über einen die Erzeugung und Verwandlung des Lichtes betreffenden heuristischen Gesichtspunkt"*, Annalen der Physik **17**, pp. 132-149 (1905)

[9] C.G. Barkla, and C.A. Sadler, *"Homogeneous secondary Röntgen radiations"*, The London, Edinburgh, and Dublin philosophical magazine and journal of science, Series 6, Vol. **16**, pp. 550-584 (1908)

[10] N. Bohr, *"On the constitution of atoms and molecules"*, The London, Edinburgh, and Dublin philosophical magazine and journal of science, Series 6, Vol. **26**, pp. 1-25, (1913)

[11] H. G. K. Moseley, *"The high frequency spectra of the elements"*, The London, Edinburgh, and Dublin philosophical magazine and journal of science, Series 6, Vol. **26**, pp. 1024-1034 (1913)

[12] A. H. Compton, *"A quantum theory of the scattering of x-rays by light elements"*, The Physical Review, Vol. **21**, No. 5, pp. 483-502(1923)

[13] G. C. Baldwin, *"Origin of synchrotron radiation"*, Physics Today **28**(1), pp. 9-10, (1975)

[14] A. Liénard, *"Champ électrique et magnétique produit par une charge électrique"*, L 'Éclairage Électrique, Vol. **16**, pp. 5-14, 53-59, 106-112 (July 1898)

[15] G. A. Schott, "*Electromagnetic radiation"*, Cambridge University Press, (1912)

[16] J. Schwinger, *"On the classical radiation of accelerated electrons"*, Physical Review **75**(12), pp. 1912-1925 (1949)

[17] R. Chasman, G. Green, E. M. Rowe, *"Preliminary design of a dedicated synchrotron radiation facility"*, IEEE Transactions on Nuclear Science, **NS-22(3)**, pp. 1765-1767 (1975)

[18] S. S. Hasnain, H. Kamitsubo, D. M. Mills, *“New synchrotron radiation sources and the next-generation light sources”*, Journal of Synchrotron Radiation **8**, pp. 1171 (2001)

[19] G. Materlik, T. Tschentscher, *“The X-ray Free Electron Laser”*, TESLA Technical Design Report, Part V, Report DESY 2001-01, ECFA 2001-209, TESLA Report 2001-23, TESLA-FEL 2001-05, Hamburg, March 2001.

[20] H. D. Nuhn, et al., “*Linac Coherent Light Source (LCLS) conceptual design report*”, SLAC-R-593, UC-414, Stanford, (April 2002); Can be downloaded from the website http://www-ssrl.slac.stanford.edu/lcls. See in particular Chapter 3: “Scientific Experiments”.

[21] B. Goss Levi, *“An energy recovery linac is seen as a bright idea”*, Physics Today **55**(3), pp. 23-25(2002)

[22] O. Hignette, P. Cloetens, W. K. Lee, W. Ludwig, G. O.Rostaing, “*Hard x-ray microscopy with reflecting mirrors status and perspectives of the ESRF technology”*, ”, Journal de Physique IV **104**, pp. 231-234 (2003)

[23] P. Cloetens, O. Hignette, S. Bohic, E. Pereiro, C. Ch. Morawe, W. Ludwig, *“Hard x-ray phase contrast microscopy and fluorescence mapping with KB optics”*, Presented at the SRI 2003 (Eighth International Conference on Synchrotron Radiation Instrumentation), San Francisco, 25-29 August (2003); for an online-presentation see http://www.sri2003.lbl.gov/html/presentations.html

[24] G. E. Ice, J. Chung, J. Z. Tischler, A. Lunt, L. Assoufid, *“Elliptical x-ray microprobe mirrors by differential deposition”*, Review of Scientific Instruments **71**(7), pp. 2635-2639 (2000)

[25] A. Snigirev, V. Kohn, I. Snigireva, B. Lengeler, *“A compound refractive lens for focusing high-energy x-rays”*, Nature, **384**, pp. 49-51 (1996)

[26] B. Lengeler, C. G. Schroer, B. Benner, A. Gerhardus, T. F. Günzler, M. Kuhlmann, J. Meyer, C. Zimprich, *“Parabolic refractive x-ray lenses“*, Journal of Synchrotron Radiation **9**, pp. 119-124 (2002)

[27] V. Aristov, M. Grigoriev, S. Kuznetsov, L. Shabelnikov, V. Yunkin, T. Weitkamp, C. Rau, I. Snigireva, A. Snigirev, M. Hoffmann, E. Voges, *“X-ray refractive planar lens with minimized absorption”*, Applied Physics Letters **77**(24), pp. 4058-4060 (2000)

[28] G. Schneider, T. Schliebe, H. Aschoff, *“Cross-linked polymers for nanofabrication of high-resolution zone plates in nickel and germanium”*, Journal of Vacuum Science and Technology B **13**(6), pp. 2809-2812 (1995)

[29] S. J. Spector, C. J. Jacobsen, D. M. Tennant, *“Process optimization for production of sub-20 nm soft x-ray zone plates*”, Journal of Vacuum Science and Technology B **15**(6), pp. 2872-2876 (1997)

[30] E. H. Anderson, D. L. Olynick, B. Harteneck, E. Veklerov, G. Denbeaux, W. Chao, A. Lucero, L. Johnson, D. Attwood, *“Nanofabrication and diffractive optics for high-resolution x-ray applications”*, Journal of Vacuum Science and Technology B **18**(6), pp. 2970-2975 (2000)

[31] C. David, B. Kaulich, R. Medenwaldt, M. Hettwer, N. Fay, M. Diehl, J. Thieme, G. Schmahl, *“Low-distortion electron-beam lithography for fabrication of high-resolution germanium and tantalum zone plates”*, Journal of Vacuum Science and Technology B **13**(6), pp. 2762-2766 (1995)

[32] A. G. Michette, *“Optical systems for soft- x-rays”*, (Plenum Press, New York, 1986)

[33] P. Dhez, P. Chevallier, T. B. Lucatorto, C. Tarrio, *“Instrumental aspects of x-ray microbeams in the range above 1 keV”*, Review of Scientific Instruments **70**(4), pp. 1907-1920 (1999)

[34] J. Kirz, C. Jacobsen, M. Howells, *"Soft x-ray microscopes and their biological applications"*, Quarterly Reviews of Biophysics **28**(1), pp. 33-130 (1995)

[35] *"Selected papers on zone plates"*, edited by J. Ojeda-Castañeda and C. Gómez-Reino, SPIE milestone series, Vol. **128** (Bellingham, Washington USA, SPIE Optical Engineering Press, 1996)

[36] B. Nöhammer, C. David, J. Gobrecht, H. P. Herzig, *"Optimized staircase profiles for diffractive optical devices made from absorbing materials"*, Optics Letters **28**(13), pp. 1087-1089 (2003)

[37] B. Nöhammer, J. Hoszowska, H.P. Herzig, C. David, *"Blazed silicon zone plates for hard x-rays with ultra-high diffraction efficiencies"*, Journal de Physique IV **104**, pp. 193-196 (2003)

[38] B. Nöhammer, J. Hoszowska, A. Freund, C. David, *"Diamond planar refractive lenses for third- and fourth-generation x-ray sources"*, Journal of Synchrotron Radiation **10**, pp. 168-171 (2003)

[39] B. Nöhammer, C. David, J. Hoszowska, A. Freund, A. Somogyi, A. Simionovici, *"Focusing of hard x-rays using diamond and silicon refractive lenses"*, Journal de Physique IV **104**, p. 223-226 (2003)

[40] B. Nöhammer, C. David, H. Rothuizen, J. Hoszowska, A. Simionovici, *"Deep reactive ion etching of silicon and diamond for the fabrication of planar refractive hard x-ray lenses"*, Microelectronic Engineering **67-68**, pp. 453-460 (2003)

[41] C. David, B. Nöhammer, E. Ziegler, *"A wavelength tunable diffractive transmission lens for hard x-rays"*, Applied Physics Letters **79**, pp. 1088-1090 (2001)

[42] C. David, E. Ziegler, B. Nöhammer, *"Wet etched diffractive lenses for hard x-rays"*, Journal of Synchrotron Radiation **8**, pp. 1054-1055 (2001)

[43] C. David, B. Nöhammer, H.H. Solak, E. Ziegler, *"Differential x-ray phase contrast imaging using a shearing interferometer"*, Applied Physics Letters **81**(17), pp. 3287-3290 (2002)

[44] M. Born, E. Wolf, *"Principles of Optics"*, (Cambridge University Press, Cambridge U.K., seventh edition, 1999)

[45] B. L. Henke, E. M. Gullikson, J. C. Davis, *"X-ray interactions: photoabsorption, scattering, transmission, and reflection at E=50-30000 eV, Z=1-92"*, Atomic Data and Nuclear Data-Tables **54**(2), pp. 181-342 (1993)

[46] C. T. Chantler, *"Theoretical form factor, attenuation and scattering tabulation for Z=1-92 from E=1-10 eV to E=0.4-1.0 MeV"*, Journal of Physical and Chemical Reference Data **24**(1), pp. 71-643 (1995)

[47] O. Klein, Y. Nishina, *"Über die Streuung von Strahlung durch freie Elektronen nach der neuen relativistischen Quantendynamik nach Dirac"*, Zeitschrift für Physik, Vol. **52**, pp. 853-868 (1929)

[48] A. C. Thompson, D. Vaugham, *"X-ray Data Booklet"*, (Lawrence Berkeley National Laboratory, Berkeley California, second edition, 2001; available free of charge at http://xdb.lbl.gov/)

[49] J. H. Hubbell, W. J. Veigele, E. A. Briggs, R. T. Brown, D. T. Cromer, R. J. Howerton, *"Atomic form factors, incoherent scattering functions, and photon scattering cross sections"*, Journal of Physical and Chemical Reference Data **4**(3), pp. 471-538 (1975)

[50] M. Young, *"Zone plates and their aberrations"*, Journal of the Optical Society of America **62**(8), pp. 972-976 (1972)

[51] M. V. Miles, T. E. Furtak, *"Optics"*, (John Wilsey & Sons, New York, second edition, 1986)

[52] O. E. Meyers (Junior), *"Studies of transmission zone plates"*, American Journal of Physics **19**(6), pp. 359-365 (1951)

[53] D. J. Stigliani, R. Mittra, R. G. Semonin, *"Resolving power of a zone plate"*, Journal of the Optical Society of America **57**(5), pp. 610-613 (1967)

[54] P. D. Kearney, A. G. Klein, *"Resolving power of zone plates"*, Journal of Modern Optics **36**(3), pp. 361-367 (1989)

[55] Jing-Ao Sun, Anni Cai, *"Archaic focusing properties of Fresnel zone plates"*, Journal of the Optical Society of America A **8**(1), pp. 33-35 (1991)

[56] Y. Vladimirsky, H. W. P. Koops, *"Moire method and zone plate inaccuracies"*, Journal of Vacuum Science and Technology B **6**(6), pp. 2142 2146 (1988)

[57] H.P. Herzig, *"Micro-optics"*, (Taylor&Francis, London, 1998)

[58] G. Schneider, *"Zone plates with high efficiency in high orders of diffraction described by dynamical theory"*, Applied Physics Letters **71**(16), pp. 2242-2244 (1997)

[59] D. Hambach, G. Schneider, E. M. Gullikson, *"Efficient high-order diffraction of extreme-ultraviolet light and soft x-rays by nanostructured volume gratings"*, Optics Letters **26**(15), pp. 1200-1202 (2001)

[60] R. Tatchyn, P.L. Csonka, and I. Lindau, *"Optimization of planar metallic nonrefracting transmission-grating profiles for mth-order intensity maximization in the soft-X-ray range"*, Journal of the Optical Society of America **72**(12), pp. 1630-1639 (1982)

[61] E. Aarts, J.K. Lenstra, *"Local search in combinatorial optimisation"*, (John Wilsey&Sons, Chichester U.K., 1997)

[62] S. Suehiro, H. Miyaji, H. Hayashi, *" Refractive lens for x-ray focus"*, Nature **352**, pp. 385-386 (1991)

[63] Tomie T., Japanese Patent No. 06045288 (1994), US Patent No. 5594773 (1997), German Patent No. DE199595433 (1998)

[64] V. V. Aristov, M. Grigoriev, S. Kuznetsov, L. Shabelnikov, V. Yunkin, C. Rau, A. A. Snigirev, I. Snigireva, T. Weitkamp, M. Hoffmann, E. I. Voges, *"Silicon planar parabolic lenses"*, Advances in X-Ray Optics, San Diego USA 3-4 August 2000, edited by A.K. Freund et al., Proceedings of SPIE **4145**, pp. 285-293 (2001)

[65] S. M. Sze, *"VLSI Technology"*, (McGraw-Hill, New York, 1988)

[66] G. Farin, *"Curves and surfaces for computer-aided geometric design: a practical guide"*, (Academic Press, San Diego, 1996)

[67] C. David and D. Hambach, *"Line width control using a defocused low voltage electron beam"*, Microelectronic Engineering **46**, Issues 1-4, pp. 219-222 (1999)

[68] D. Meyerhofer, *"Characteristics of resist films produced by spinning"*, Journal of Applied Physics **49**(7), pp. 3993-3997 (1978)

[69] B. N. Chapman, *"Glow discharge processes: sputtering and plasma etching"*, (John Wiley & Sons, New York, 1980)

[70] E. Di Fabrizio, F. Romanato, M. Gentili, S. Cabrini, B. Kaulich, J. Susini, R. Barrett, *"High-efficiency multilevel zone plates for keV X-rays"*, Nature **401**, pp. 895-898 (1999)

[71] W. Yun, B. Lai, A. A. Krasnoperova, E. Di Fabrizio, Z. Cai, F. Cerrina, Z. Chen, M. Gentili, E. Gluskin, "*Development of zone plates with a blazed profile for hard x-ray applications"*, Review of Scientific Instruments **70**(9), pp. 3537-3541 (1999)

[72] E. Di Fabrizio, M. Gentili, L. Grella, M. Baciocchi, A. Krasnoperova, F. Cerrina, W. Yun, B. Lai, and E. Gluskin,*"High-performance multilevel blazed x-ray microscopy Fresnel zone plates: fabricated using x-ray lithography"*, Journal of Vacuum Science and Technology B **12**(6), pp. 3979-3985 (1994)

[73] PCT CH0100578

[74] C. David, *"Fabrication of stair-case profiles with high aspect ratios for blazed diffractive optical elements"*, Microelectronic Engineering **53**, Issues 1-4, pp. 677-680 (2000)

[75] R. B. Bosch Gmbh, U.S. Pat. 4855017, U.S. Pat. 4784720, Germany Pat. 4241045C1, (1994)

[76] *"Handbook of optical constants of solids"*, edited by E. D. Palik, p. 565 (Orlando, Academic Press, 1985)

[77] *"Properties of strained and relaxed SiGe"*, edited by E. Kasper, EMIS Datareview Series No. **12**, p. 123 (INSPEC, IEE, 1995)

[78] C. David, A. Souvorov, *"High-efficiency Bragg-Fresnel lenses with 100 nm outermost zone width"*, Review of Scientific Instruments **70**(11), pp. 4168-73 (1999)

[79] B. Golosio, A. Simionovici, A. Somogyi, C. Camerani, B. M. Steenari, *"X-ray fluorescence tomography of individual waste fly ash particles"*, Journal de Physique IV **104**, pp. 647-650 (2003)

[80] M. Chukalina, A. Simionovici, L. Lemelle, C. Rau, L. Vincze, P. Gillet, *"X-ray fluorescence tomography for non-destructive semi-quantitative study of microobjects"*, Journal de Physique IV **104**, pp. 627-630 (2003)

[81] B. Golosio, A. Simionovici, A. Somogyi, L. Lemelle, M. Chukalina, A. Brunetti, *"Internal elemental microanalysis combining x-ray fluorescence, Compton and transmission tomography"*, Journal of Applied Physics **94**(1), pp. 145-156 (2003)

[82] M. Feser, C. Jacobsen, P. Rehak, G. DeGeronimo, *"Scanning transmission x-ray microscopy with a segmented detector"*, Journal de Physique IV **104**, pp. 529-534 (2003)

[83] C. G. Schroer, B. Benner, T. F. Günzler, M. Kuhlmann, C. Zimprich, B. Lengeler, C. Rau, T. Weitkamp, A. Snigirev, I. Snigireva, J. Appenzeller, *"High resolution imaging and lithography with hard X-rays using parabolic compound refractive lenses"*, Review of Scientific Instruments **73**(3), pp. 1640-1642 (2002)

[84] C. G. Schroer, M. Kuhlmann, U. T. Hunger, T. F. Günzler, O. Kurapova, S. Feste, F. Frehse, B. Lengeler, M. Drakopoulos, A. Somogyi, A. S. Simionovici, A. Snigirev, I. Snigireva, C. Schug, W. H. Schröder, *"Nanofocusing parabolic refractive x-ray lenses"*, Applied Physics Letters **82**(9), pp. 1485-1487 (2003)

[85] G. Kostorz, *"Small-angle scattering studies of phase separation and defects in inorganic materials"*, Journal of Applied Crystallography **24**(5), pp. 444-456 (1991)

[86] P. Fratzl, *“Small-angle scattering in materials science - a short review of applications in alloys, ceramics and composite materials”*, Journal of Applied Crystallography **36**(3), pp. 397-404 (2003)

[87] M. J. Zwanenburg, J. H. H. Bongaerts, J. F. Peters, D. Riese, J. F. van der Veen, *“Focusing of coherent X-rays in a tapered planar waveguide”*, Physica B **283**(1-3), pp. 285-288 (2000)

[88] M. J. Zwanenburg, J. H. H. Bongaerts, J. F. Peters, D. O. Riese, J. F. van der Veen, *“X-ray waveguiding studies of ordering phenomena in confined fluids”*, Physical Review Letters **85**(24), pp. 5154-5157 (2000)

[89] F. Pfeiffer, C. David, M. Burghammer, C. Riekel, T. Salditt, *“Two-dimensional x-ray waveguides and point sources”*, Science **297**(5579), pp. 230-234 (2002)

[90] J. H. H. Bongaerts, C. David, M. Drakopoulos, M. J. Zwanenburg, G. H. Wegdam, T. Lackner, H. Keymeulen, J. F. van der Veen, *“Propagation of a partially coherent focused x-ray beam within a planar x-ray waveguide”*, Journal of Synchrotron Radiation **9**, pp. 383-393 (2002)

[91] Y. Kohmura, M. Awaji, Y. Suzuki, T. Ishikawa, Yu. I. Dudchik, N. N. Kolchevsky, F. F. Komarov, *“X-ray focusing test and x-ray imaging test by a microcapillary x-ray lens at an undulator beamline”*, Review of Scientific Instruments **70**(11), pp. 4161-4167 (1999)

[92] B. Lengeler, C. Schroer, J. Tümmler, B. Benner, M. Richwin, A. Snigirev, I. Snigireva, M. Drakopoulos, *“Imaging by parabolic refractive lenses in the hard x-ray range”*, Journal of Synchrotron Radiation **6**, pp. 1153-1167 (1999)

[93] C. G. Schroer, M. Kuhlmann, B. Lengeler, T. F. Günzler, O. Kurapova, B. Benner, C. Rau, A. S. Simionovici, A. A. Snigirev, I. Snigireva, *“Beryllium parabolic refractive x-ray lenses”*, Design and Microfabrication of Novel X-Ray Optics, Seattle USA 9 July 2002, edited by D. C. Mancini, Proceedings of SPIE **4783**, pp. 10-18 (2002)

[94] S. Kiyohara, Y. Yagi, K. Mori, *“Plasma etching of CVD diamond films using an ECR-type oxygen source”*, Nanotechnology **10**(4), pp. 385-388 (1999)

[95] P. W. Leech, G. K. Reeves, A. Holland, *“Reactive ion etching of diamond in CF_4, O_2, O_2 and Ar-based mixtures”*, Journal of Materials Science 36(14), pp. 3453-3459 (2001)

[96] F. Silva, R. S. Sussmann, F. Benedic, A. Gicquel, *“Reactive ion etching of diamond using microwave assisted plasmas”*, Diamond and Related Materials **12**(3-7), pp. 369-373 (2003)

[97] R. J. Schutz, in: *“VLSI Technology”*, edited by S. M. Sze (McGraw-Hill, New York, 1988)

[98] D. Molinari, P. Philippot, J. Cauzid, J. Foriel, B. Ménez, A. Somogyi, B. Nöhammer, *“Br and I content of HP saline aqueous brines from Dabie Shan and the Alps”*, to be published in Geochimica et cosmochimica acta

[99] A. A. Snigirev, V. Yunkin, I. Snigireva, M. Di-Michiel, M. Drakopoulos, S. Kouznetsov, L. Shabel'nikov, M. Grigoriev, V. Ralchenko, I. Sychov, M. Hoffmann, E. I. Voges, *“Diamond refractive lens for hard x-ray focusing”*, Design and Microfabrication of Novel X-Ray Optics, Seattle USA 9 July 2002, edited by D. C. Mancini, Proceedings of SPIE **4783**, pp. 1-9 (2002)

[100] C. G. Schroer, J. Tümmler, B. Lengeler, M. Drakopoulos, A. Snigirev, I. Snigireva, *“Compound refractive lenses: high-quality imaging optics for the X-FEL”*, X-Ray FEL Optics and Instrumentation, San Diego 30-31 July 2000, edited by M. Mills, H. Schulte-Schrepping and J. R. Arthur, Proceedings of SPIE **4143**, pp. 60-68 (2001)